HOT STREAK CHARACTERIZATION IN SERPENTINE EXHAUST NOZZLES

DISSERTATION

Darrell S. Crowe, Major, USAF

AFIT-ENY-DS-14-D-32

DEPARTMENT OF THE AIR FORCE
AIR UNIVERSITY

AIR FORCE INSTITUTE OF TECHNOLOGY

Wright-Patterson Air Force Base, Ohio

AFIT-ENY-DS-14-D-32

HOT STREAK CHARACTERIZATION IN SERPENTINE EXHAUST NOZZLES

DISSERTATION

Presented to the Faculty

Graduate School of Engineering and Management

Air Force Institute of Technology

Air University

Air Education and Training Command

in Partial Fulfillment of the Requirements for the

Degree of Doctoral of Science in Aeronautical Engineering

Darrell S. Crowe, B.S.A.E., M.S.A.E.

Major, USAF

December 2014

AFIT-ENY-DS-14-D-32

HOT STREAK CHARACTERIZATION IN SERPENTINE EXHAUST NOZZLES

DISSERTATION

Darrell S. Crowe, B.S.A.E., M.S.A.E.
Major, USAF

Approved:

_____//signed//_____   ____24 Nov 14____
Christopher L. Martin, Jr., PhD (Chairman)   Date

_____//signed//_____   ____5 Dec 14____
Robert B. Greendyke, PhD (Member)   Date

_____//signed//_____   ____3 Dec 14____
Lt Col Brian K. McBee, PhD (Member)   Date

_____//signed//_____   ____1 Dec 14____
Gregory A. Addington, PhD (Member)   Date

Accepted:

_____   _____
Adedeji B. Badiru   Date
Dean, Graduate School of Engineering and Management

AFIT-ENY-DS-14-D-32

Abstract

Modern aircraft of the United States Air Force face increasingly demanding cost, weight, and survivability requirements. Serpentine exhaust nozzles within an embedded engine allow a weapon system to fulfill mission survivability requirements by providing denial of direct line-of-sight into the high-temperature components of the engine. Recently, aircraft have experienced material degradation and failure along the aft deck due to extreme thermal loading. Failure has occurred in specific regions along the aft deck where concentrations of hot gas have come in contact with the surface causing hot streaks. The prevention of these failures will be aided by the accurate prediction of hot streaks. Additionally, hot streak prediction will improve future designs by identifying areas of the nozzle and aft deck surfaces that require thermal management. To this end, the goal of this research is to observe and characterize the underlying flow physics of hot streak phenomena. The goal is accomplished by applying computational fluid dynamics to determine how hot streak phenomena is affected by changes in nozzle geometry. The present research first validates the computational methods using serpentine inlet experimental and computational studies. A design methodology is then established for creating six serpentine exhaust nozzles investigated in this research. A grid independent solution is obtained on a nozzle using several figures of merit and the grid-convergence index method. An investigation into the application of a second-order closure turbulence model is accomplished. Simulations are performed for all serpentine nozzles at two flow conditions. The research introduces a set of characterization and performance parameters based on the temperature distribution and flow conditions at the nozzle throat and exit. Examination of the temperature distribution on the upper and lower nozzle surfaces reveals critical information concerning changes in hot streak phenomena due to changes in nozzle geometry.

To My Wife and Family

Acknowledgements

I'd first like to thank Dr. Christopher Martin for his willingness to pursue this research topic with me even with a late start, his time and direction even during his deployment, and his unfailing positive support throughout this effort. I'd also like to thank Dr. Robert Greendyke, Lt Col Brian McBee, and Dr. Greg Addington for serving on my committee and Dr. Ronald Coutu for serving as the Dean's representative. Their expertise has been critical in defining the direction of this research and strengthening this document. The support from the sponsor, especially the efforts of Michael Bartowitz and Dave Schwartz, was instrumental in defining the research goals and keeping the project on course. Doug Essman essentially created the research topic via his hot streak "manifesto". Ryan Baker and Chad Winkler provided key guidance and expertise concerning nozzle design. Dave Doak and Don Bodle provided clutch Linux and supercomputing support.

Above all else, I'd like to thank my wife for her love and support. I wouldn't have made it through three months, much less three years, of this program without her constant encouragement.

<div align="right">

Darrell S. Crowe

</div>

Table of Contents

List of Figures

Figure   Page

List of Tables

List of Symbols

Symbol	Definition
a	speed of sound (m/s) or combustion pre-multipler or grid point distance (m)
A	area (m^2)
AR	ratio of throat width to height
b	combustion pre-multipler or grid point distance (m)
BPR	ratio of bypass to core mass flow rate
c	grid point distance (m)
C	coefficient or carbon
C_{ij}	convection of Reynolds stresses
C_P	specific heat at constant pressure (J/(kg · K))
C_V	specific heat at constant volume (J/(kg · K))
CO_2	carbon dioxide
d	combustion pre-multipler
D	nozzle diameter (m)
$D_{L,ij}$	molecular diffusion of Reynolds stresses
$D_{T,ij}$	turbulent diffusion of Reynolds stresses
D_ω	cross-diffusion blending function
DC	distortion coefficient
De	Dean number
e	approximate relative error
E	total energy (J)
f	force per mass (N/kg) or empirical function or combustion pre-multipler or figure of merit
F	force (N) or blending function
F_g	gross thrust (N)

Symbol	Definition
G	generation due to turbulence
h	height (m)
H	hydrogen
H_2O	water vapor
I	turbulent intensity
J	diffusive flux $(1/(m^2 \cdot s))$
k	coefficient of thermal conductivity $(W/(m \cdot K))$
K	turbulent kinetic energy (J/kg)
l	length (m)
L/D	ratio of length (mixing plane to throat) to entrance diameter
m	mass (kg)
M	Mach number
$\mathcal{M}$	molar mass (g/mol)
Mag	magnitude of hot flow
n	unit normal (m)
N	extensive fluid property or number
N_2	diatomic nitrogen
O_2	diatomic oxygen
p	order of convergence or grid point
P	pressure (Pa) or wetted perimeter (m)
P/P_{i_0}	non-dimensional static pressure
P_{ij}	stress production of Reynolds stresses
P_i/P_{i_0}	non-dimensional stagnation pressure
P_{T_2}/P_{T_0}	non-dimensional freestream total pressure
PAV	average ring total pressure (Pa)

Symbol	Definition
PAVLOW	average ring total pressure below PAV (Pa)
Pr	Prandtl number
q	*Q* per mass (J/kg) or order of convergence quantity
Q	heat (J)
r	radius (m) or refinement ratio
R	specific gas constant (J/(kg · K))
R^2	goodness-of-fit parameter
s	arc length (m)
S	source term or modulus of mean strain rate tensor
$\mathbb{S}$	serpentinity
t	time (s) or thickness (m)
T	temperature (K)
TAV	average total temperature (K)
TAVHI	average total temperature of probe above *TAV* (K)
TAVHOT	average total temperature of hot flow (K)
TFAV	average total temperature of probes (K)
u	axial, 1D, or primitive velocity (m/s)
U	speed (m/s)
v	3D velocity (m/s) or primitive vertical velocity (m/s)
V	volume (m^3)
w	primitive lateral velocity (m/s) or width (m)
W	work (J)
x	axial position (m)
y	distance to wall (m) or vertical distance (m)
Y	dissipation due to turbulence

Symbol	Definition
z	lateral position (m)

0	initial state
1	first or inner state or fine grid
2	second or outer state or medium grid
3	third state or coarse grid
5	station 5, nozzle core entrance
6	station 6, mixing plane
8	station 8, throat
9	station 9, nozzle exit
15	station 15, nozzle bypass entrance
21	medium-fine grid comparison
32	coarse-medium grid comparison
amb	standard atmospheric conditions
b	body
back	leeward face of control volume
cc	curvature correction
d	discharge
e	bulk fluid
eff	effective
exit	divergent section
ext	extrapolated
f	skin friction
fine	fine grid

Symbol	Definition
$front$	windward face of control volume
g	gross thrust
h	hydraulic
hot	above threshold temperature (880K)
i	axial computational coordinate or first index or ring number
j	vertical computational coordinate or second index
k	lateral computational coordinate or third index
l	liner
med	medium grid
min	minimum
mix	mixture
mp	mixing plane
$prod$	combustion products
r	rotation
s	secondary
st	static
$\mathcal{S}$	modified by serpentinity
t	turbulent or tailcone or total
T	turbulent eddy
u	universal
w	wall
x	axial Cartesian direction or number of carbon atoms
y	vertical Cartesian direction or number of hydrogen atoms
z	lateral Cartesian direction

Symbol	Definition

Superscripts

Symbol	Definition
21	medium-fine grid comparison
32	coarse-medium grid comparison
^	unit vector or RSM constant
→	vector
.	rate (1/s)
$\overline{(...)}$	average
$\overline{\overline{(...)}}$	tensor
′	fluctuating
~	mass-weighted (Favre) average
″	mass-weighted (Favre) fluctuating
+	positive or wall coordinate
∞	freestream
*	auxiliary turbulent constant or throat

Greek Letters

Symbol	Definition
α	damping coefficient or angle or under-relaxation factor
β_i	auxiliary turbulent model constant
β_∞	auxiliary turbulent model constant
γ	ratio of specific heats
Γ	effective diffusivity
$\hat{\gamma}$	auxiliary RSM constant
δ	infinitesimal change or boundary layer height (m)
δ_{ij}	Kroniker Delta
ε	figure of merit change

Symbol	Definition
ε_{ij}	viscous dissipation of Reynolds stresses
η	*N* per mass
κ	auxiliary turbulent model constant
λ	bulk viscosity (kg/(m · s))
μ	dynamic viscosity (kg/(m · s))
ρ	density (kg/m^3)
σ	turbulent Prandtl number
τ	stress (N)
ϕ	auxiliary blending function or equivalence ratio or circumferential location
ϕ_{ij}	pressure strain of Reynolds stresses
χ	auxiliary RSM constant or mole fraction
ω	vorticity (1/s) or turbulent dissipation rate (J/(kg · s))
Ω	modulus of vorticity tensor

Math

∇	differential operator

List of Acronyms

Acronym	Definition
AFIT	Air Force Institute of Technology
AIAA	American Institute of Aeronautics and Astronautics
AIP	aerodynamic interface plane
AMG	algebraic multigrid
ARD	Aerospace Resource Document
ARSM	Algebraic Reynolds Stress Model
CDC	circumferential distortion coefficient
CDI	circumferential distortion intensity
CFD	computational fluid dynamics
CFL	Courant-Friedrichs-Lewy
DES	Detached Eddy Simulation
DSRCs	Department of Defense Supercomputing Resource Centers
FRANS	Favre- and Reynolds-averaged Navier Stokes
GCI	grid-convergence index
GE	General Electric
GRC	NASA Glenn Research Center
ILU	Incomplete Lower Upper
JPC	Joint Propulsion Conference
LES	Large Eddy Simulation
MUSCL	Monotone Upstream-Centered Schemes for Conservation Laws
NACA	National Advisory Committee for Aeronautics
NASA	National Aeronautics and Space Administration
OML	outer mold lines

Acronym	Definition
PAW	Propulsion Aerodynamics Workshop
PBCS	pressure-based coupled solver
PNS	parabolized Navier-Stokes
RANS	Reynolds-averaged Navier-Stokes
RDI	radial distortion intensity
RSM	Reynolds Stress Model
SAE	Society of Automotive Engineers
SST	shear stress transport
UAV	unmanned aerial vehicles
UCAV	unmanned combat aerial vehicles
USAF	United States Air Force

HOT STREAK CHARACTERIZATION IN SERPENTINE EXHAUST NOZZLES

I.   Introduction

Modern aircraft of the United States Air Force (USAF) face increasingly demanding cost, weight, and survivability requirements. These requirements are met by seeking technological improvements in every component of the aircraft, including the propulsion system. The embedded engine concept allows a weapon system to fulfill mission survivability requirements while providing additional cost and weight savings via airframe/propulsion integration. The exhaust nozzle systems of this type of engine are typically complex in design. The cross-sectional shape of the nozzle transitions from round at the turbine exit to a more rectangular shape for tactical advantages such as thrust vectoring. Also, the flowpath is curved or serpentine in shape to provide denial of direct line-of-sight into the high-temperature components of the engine. The B-2 is one example of a current USAF aircraft that utilizes a serpentine exhaust nozzle. On the B-2, an area of the fuselage called the aft deck is placed downstream of the exhaust exit to provide further line-of-sight denial and thermal management (see Figure 1.1). These design features create a complex flow path for the exhaust gas, as seen in Figure 1.2.

Recently, USAF aircraft have experienced material degradation and failure along the aft deck due to extreme thermal loading. Failure has occurred in specific regions along the aft deck where concentrations of hot gas have come in contact with the surface causing hot streaks. The design and materials used in the construction of aft decks are highly advanced, and the replacement or repair of these components is time-consuming and expensive [2]. Preventative steps could be taken if the magnitude and location of hot streaks were known

1

before they became a maintenance concern. Therefore, the prediction of hot streaks is of utmost importance to the sustainment of systems employing a serpentine exhaust nozzle.

For the design of future propulsion systems, the high-temperature environment of embedded serpentine engines will require complex cooling schemes along the aft deck. These schemes typically use cooling air redirected from the engine—so there exists a trade-off between cooling the hot aft section of the aircraft and maximizing the available thrust. Also, the use of exotic materials for thermal management must be minimized due to weight and cost concerns. The accurate prediction of hot streaks enables tailored thermal management of affected aft deck sections and is therefore critical to the design of systems employing a serpentine exhaust nozzle. As a step towards accurate hot streak predictions, this research attempts to understand the complex nature of the flow leaving an embedded serpentine engine and define a set of analytic parameters for investigation of this unique aero-thermal environment.
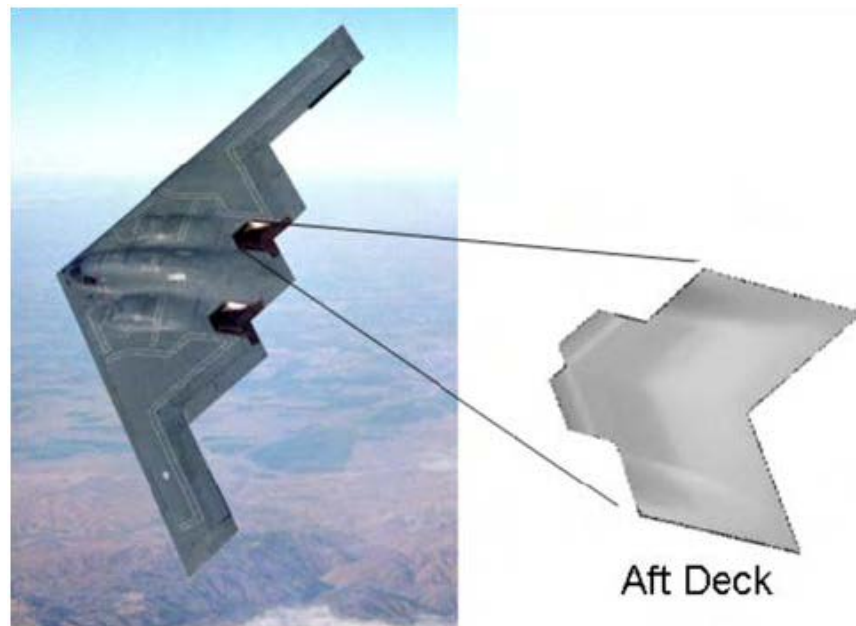
Figure 1.1: Location of the aft deck on the B-2.[28]
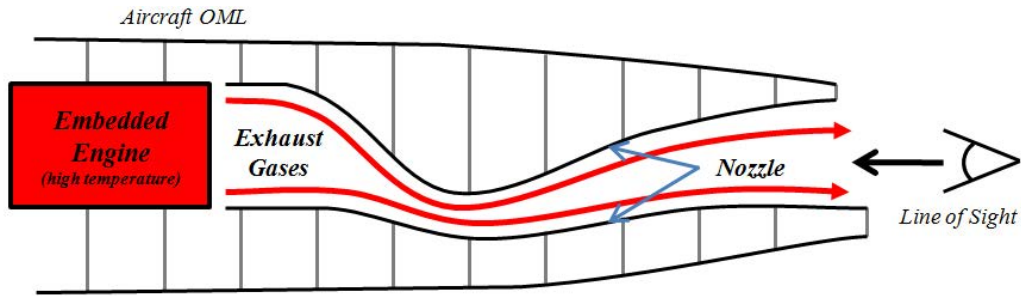
Figure 1.2: Embedded engine and serpentine exhaust nozzle concept.[19]

1.1 Turbofan Engines

The propulsion systems of interest to this research are turbofan engines. In general, a turbofan consists of an inlet, a fan, a core section (compressor, combustor, and turbine), and an exhaust nozzle. The inlet directs air to a fan, which is larger in diameter than the core of the engine, so that some of the air flows into a bypass duct and some to the core section. The core air is compressed, mixed with fuel and ignited in the combustor, then expanded through the turbine so that usable work is extracted to turn the spool. For high-performance engines like those in modern USAF aircraft (see Figure 1.3), the hotter core flow combines with the cooler bypass flow in the exhaust nozzle, where it is mixed with additional fuel and ignited (i.e., afterburning), thus increasing thrust. The final section of a high-performance turbofan consists of a convergent-divergent (C-D) nozzle, which also increases available thrust. Here, the flow is accelerated to sonic velocity in the convergent portion, then further accelerated as the flow expands in the divergent section. The function of an exhaust nozzle extends beyond afterburning and accelerating the flow to include [38]:

- matching exit and atmospheric pressures

- wall cooling

- mixing core and bypass streams

- suppressing jet noise and infrared radiation

- allowing for thrust vectoring
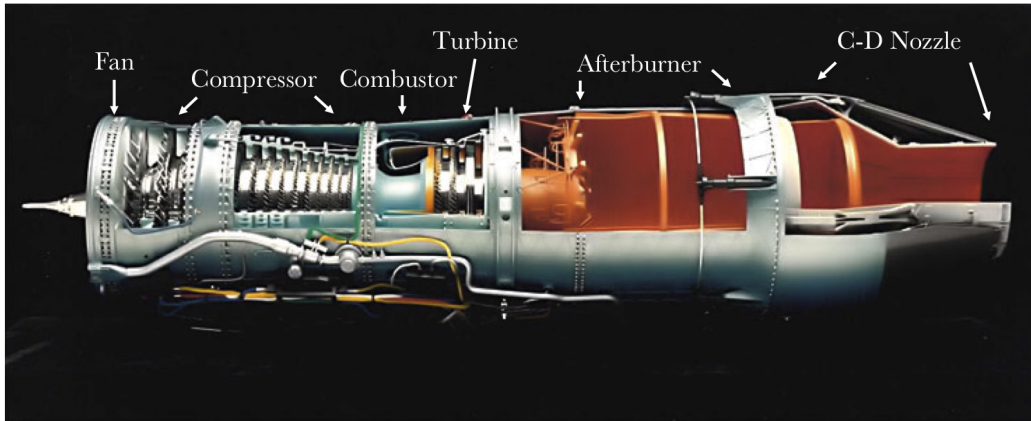
Figure 1.3: High-Performance Turbofan Engine Used by USAF.

1.2 Exhaust Nozzle System

Figure 1.4 shows a representation of the complex exhaust system of interest. A numbering scheme will be used throughout this document consistent with conventional aircraft engine nomenclature. The entrance of the exhaust nozzle is the exit of the turbine and is denoted Station 5. Station 6 is called the "mixing plane", where the liner that separates the core and bypass flow terminates, and the two streams begin to mix. For the engines considered in this research, the tailcone (i.e., end of the engine spool) also terminates at Station 6. The serpentine section begins at Station 6 and is of the "two-turn" type, meaning the flow experiences both a downward and upward bend before exiting the nozzle. The location of minimum nozzle area (i.e., end of convergent section), called the throat, is at Station 8. The exit of the exhaust nozzle (i.e., end of divergent section) is at Station 9. Some important features are defined below and shown in Figure 1.4:

- bypass ratio (*BPR*) — ratio of bypass section mass flow rate to core section mass flow rate

4

- aspect ratio (AR) — ratio of throat width to height

- length-to-diameter ratio (L/D) — ratio of nozzle length from Station 6 to Station 9 to Station 6 diameter (D_6)

- offset — minimum and maximum vertical position of nozzle expressed as percentage of D_6

- direction of vertical displacement — initial direction of serpentine centerline from axial at Station 6 (e.g. down-first or up-first)

- swirl angle — tangential flow component of turbine exit velocity vector
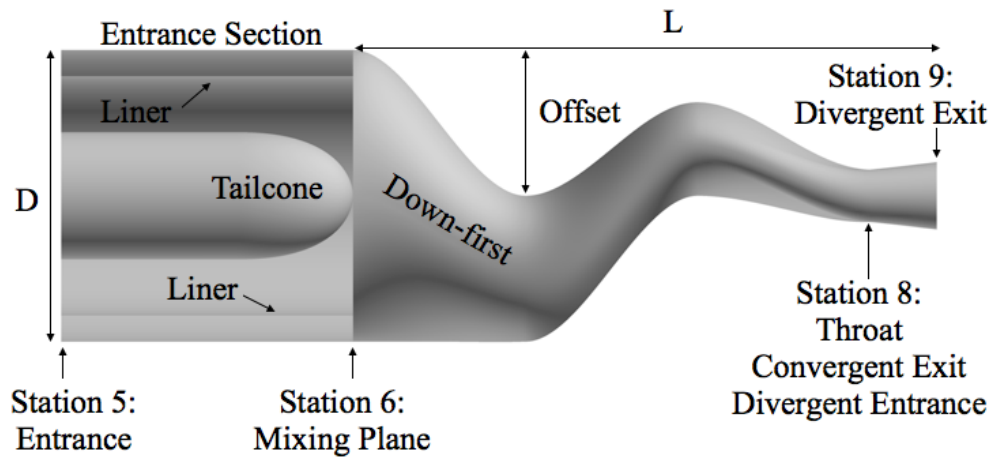
Figure 1.4: Representative Nozzle Showing Important Features.

1.3   Research Goal

The goal of this research is to observe and characterize the underlying flow physics of hot streak phenomena. This goal will be accomplished by applying computational fluid dynamics (CFD) to calculate the flowfield within a set of serpentine exhaust nozzles created from parametrized flowfield and geometry definitions. The primary question to be answered is thus—how is hot streak phenomena in serpentine exhaust nozzles affected by changes in nozzle geometry? Therefore, the critical outcome of this effort is determining the relationship between quantifiable changes in the nozzle temperature distribution and changes in nozzle shape.

This research involves a complex flowpath encompassing supersonic nozzle flow, flow through transition ducts, and flow through serpentine ducts. It will be noted in the literature review that past research has established a good understanding of the underlying physics for each situation. However, no work has been published to show what flow features result when the configurations are combined in a turbofan engine—dual-temperature streams mixing throughout an exhaust nozzle that is transitioning, serpentine, and accelerating the flow to supersonic speeds. This research will provide insight into that unique flow environment. It is this novel perspective that can be considered the contribution of this effort to the field of propulsion aerodynamics.

1.4   Research Objectives

While the number of design parameters that can vary from engine to engine is vast, three have been identified for initial study: *AR*, *L/D*, and swirl angle. The first two parameters are related to nozzle geometry, while swirl angle is a flow condition deemed important to simulating a realistic turbofan engine flowfield. Table 1.1 lists the parameter values used in this research. Table 1.1 equates to 6 different nozzle shapes for each swirl condition, for a total of 12 configurations. A new parameter, *serpentinity*, is introduced that combines the effects of varying *AR* and *L/D* and allows for a direct comparison of

6

Table 1.1: List of Design Parameters

Parameter	Values
AR	4, 10
L/D	2, 3, 4
Swirl	0°, 10°

different nozzle shapes. Serpentinity is a measure of the "degree of turning" within a serpentine nozzle and is defined in Chapter 3. Using the parameters in Table 1.1, the following research objectives will be met:

1. Perform CFD simulations to test and validate the computational methods proposed to accomplish the research goal.

2. Establish a design methodology for the serpentine exhaust nozzles used in this research. Isolate the internal flow of the exhaust system by excluding the aft deck from the initial design. Test this methodology with a preliminary nozzle design and CFD simulations; adjust the design as necessary.

3. Perform a grid convergence study on one nozzle. Obtain a grid-independent CFD solution and determine the appropriate grid resolution for the remaining configurations. Quantify the error and uncertainty in the simulations.

4. Investigate the application of an advanced second-order closure turbulence model to the research problem.

5. Design the remaining 5 nozzles and perform the remaining 11 CFD simulations. Describe the flow physics involved in two-stream mixing through serpentine exhaust nozzles.

6. Establish criteria for identifying and characterizing hot regions of flow and analyze exit temperature distribution based on these criteria. Draw conclusions about the impact of changing design parameters on the temperature distribution and the formation of hot streaks.

1.5 Chapter Outline

This work begins with a discussion of the relevant background concerning basic exhaust nozzle flow, flow through ducts with transitioning cross-sectional area, and flow through serpentine ducts. The remainder of Chapter 2 is devoted to the theory behind the computational methods used in this research. The discussion includes a derivation of the pertinent discretized equations from governing principles. Special attention is given to turbulence modeling because of the highly complex flowpath examined in this work. Chapter 3 discusses the design methodology used to create the nozzles, including how preliminary simulations affected design choices. Grid generation techniques are then covered. Chapter 3 also discusses the specific computational methods applied to this research, including the choice of CFD code, ANSYS Fluent. Chapter 4 first presents results of the validation study, then describes the results of the grid convergence study. The chapter continues with results for the remaining nozzles and describes the relationship between nozzle geometry, the flow features observed in the nozzles, and the temperature distribution at the nozzle exit. Chapter 5 draws conclusions that support the research goal and makes recommendations for future study.

II. Background & Theory

This chapter begins with the general principles of C-D nozzle flow. Next, previous research is reviewed involving relevant flow features: transition duct flows, serpentine duct flows, flows over spheres and spheroids (similar to the engine tailcone), and dual-temperature duct flows. Finally, since this research uses numerical simulations to achieve the research goal, a discussion of the pertinent numerical methods and turbulence models used in the simulations is presented as a conclusion to this chapter.

2.1 Basic Exhaust Nozzle Flow

The primary purpose of an exhaust nozzle is to increase the velocity of the exhaust gas before discharge into the freestream. High exit velocity is required to supply the thrust needed for an aircraft to maintain flight. The exhaust nozzle supplies this high exit velocity by expanding the exhaust gas in a process which requires a decrease in static pressure, since fluid tends toward regions of lower pressure. The relationship between static pressure and velocity is demonstrated for an inviscid flowfield by Euler's equation, shown in a simple quasi-one-dimensional differential form in Equation 2.1 [4]:

$$dP = -\rho u du \tag{2.1}$$

Equation 2.1 shows that an increase in velocity (positive du) must correspond to a decrease in static pressure (negative dP). The relationship between static pressure and velocity is physically necessary due to Bernoulli's principle. Some of the random molecular motion of the fluid must be converted into kinetic energy to accelerate the fluid forward. Since static pressure is due to random molecular motion, an increase in velocity corresponds to a decrease in pressure. Therefore, if flow is to pass through a duct, the static pressure at the exit of the duct must be lower than that at the entrance. A static pressure gradient is

certainly present in aircraft exhaust systems, where the static pressure at the exit of the turbine can be several times higher than that of the ambient air at the nozzle exit.

2.2 Flow Through C-D Nozzles

A typical high-performance aircraft engine exhaust nozzle contains a C-D section. This section is necessary to produce high amounts of thrust through the acceleration and expansion of the flow to ambient pressure. If the flow is incompressible (approximately Mach number (M) < 0.3), the continuity equation is just

$$\dot{m}_1 = \dot{m}_2 = u_1 A_1 = u_2 A_2 \tag{2.2}$$

Therefore, if an increase in velocity is desired ($u_2 > u_1$), Equation 2.2 requires a decrease in area ($A_2 < A_1$). This flow regime would indicate a low-thrust engine and would utilize a convergent-only nozzle to increase thrust [38].

For compressible flow, the continuity equation must account for changes in density. Since $\rho u A$ is constant, the differential form of the continuity equation becomes

$$d(\rho u A) = 0 \tag{2.3}$$

or from the product rule

$$\frac{d\rho}{\rho} + \frac{du}{u} + \frac{dA}{A} = 0 \tag{2.4}$$

Rearranging Equation 2.1 yields

$$\frac{dP}{\rho} = \frac{dP}{d\rho}\frac{d\rho}{\rho} = -u\,du \tag{2.5}$$

Using the definition of speed of sound, $dP/d\rho = a^2$, gives

$$a^2\frac{d\rho}{\rho} = -u\,du \tag{2.6}$$

or

$$\frac{d\rho}{\rho} = -\frac{u\,du}{a^2} = -\frac{u^2 du}{a^2 u} = -M^2\frac{du}{u} \tag{2.7}$$

10

Thus by the presence of the negative sign in the above equation, an increase in velocity (such as that desired in an exhaust nozzle) equates to a decrease in density (negative $d\rho$). Equation 2.7 can be rearranged to

$$\frac{d\rho}{du} = -M^2\frac{\rho}{u} \tag{2.8}$$

It can be observed from this equation that in subsonic flow, u will increase faster than ρ decreases since (for unit velocity and density) $d\rho/du$ will be less than unity, and for $M > 1$, ρ will decrease faster than u increases. Applying this fact to the continuity equation ($A = \dot{m}/\rho u$) gives the familiar result from the incompressible flow discussion above that for $M < 1$, area must decrease to achieve an increase in velocity, and for $M > 1$, area must *increase* to achieve an increase in velocity.

An alternative view on the difference between subsonic and supersonic nozzle flow can be seen by substituting Equation 2.7 into Equation 2.4 to get a relationship between Mach, area, and velocity

$$\frac{dA}{A} = \left(M^2 - 1\right)\frac{du}{u} \tag{2.9}$$

from which the same conclusions and be reached concerning the relationship between velocity and area change in a nozzle. Equation 2.9 also gives the result that for sonic flow ($M = 1$), $dA/A = 0$. Sonic conditions correspond to a minimum in the area distribution, which is called the throat.

If the difference in pressure at the entrance of the nozzle and ambient pressure is high enough that the velocity will be supersonic when the gas is expanded to ambient conditions (for maximum thrust, as determined by Euler's equation), the gas will need to first pass through a convergent section until it reaches sonic speeds at the throat, then pass through a divergent section until the desired ambient pressure is reached. This design is called a C-D nozzle. If during the isentropic expansion process the pressure at the nozzle exit is below ambient pressure, the flow is said to be overexpanded. The flow will increase in pressure to match the ambient conditions via an oblique shock downstream of the nozzle. If the

pressure at the exit is above ambient pressure, the flow is said to be underexpanded. In this situation the flow will equalize with ambient conditions via expansion waves downstream of the nozzle [4].

2.3   Flow Through Ducts with Transitioning Cross-Sectional Area

One important geometric feature of the exhaust nozzles created for this research is a cross-sectional area that transitions from circular at Station 6 to the rounded-rectangle discussed in Chapter 3. Prior research has been fairly conclusive as to the flow features that arise from ducts with transitioning cross-sectional area. The earliest work in this area was performed nearly 75 years ago by Mayer at the National Advisory Committee for Aeronautics (NACA) [39]. His early experimental work characterized the velocity and pressure field distortions created by the change in duct shape along the primary flow axis. He showed pressure-driven crossflows create secondary flow features, that is, vortical flow. He also showed that the length of the transition duct had an effect on the flow profile development. Also, Mayer found that rounded corners reduce the strength of the vortices, which is a feature used in modern aircraft exhaust system and will be applied to this effort, as discussed in Chapter 3. While the *AR* of the rectangular exit in Mayer's work was 2, which falls below the range of this research, his work was the foundation for many efforts that followed at the National Aeronautics and Space Administration (NASA).

Modern work in transition nozzle research for aerospace propulsion applications came about due to thrust vectoring requirements for fifth-generation fighter aircraft, and began at NASA Glenn Research Center (GRC) [12, 42]. Malechi and Lord [37] were the first to utilize numerical simulation for circular-to-rectangular transition duct research. Their results showed the ducts produced a pair of counter-rotating vortices. While important, their results would be considered low-fidelity by today's standards, since they used a parabolized Navier-Stokes (PNS) code, which required accurate inlet boundary-layer profiles to accurately calculate the fixed-input static pressure field. The PNS code used a

$K - \varepsilon$ turbulence model, and they discovered the turbulent eddy viscosity was numerically suppressed in the vortex core.

Benchmark experimental results were presented by Davis and Gessner with support from GRC [18]. Their work focused on incompressible turbulent flow with $L/D = 4.5$ and $AR = 3.0$. The duct's inlet and outlet cross-sectional areas were the same, although there was slight expansion and contraction of the flow in the duct, so that the flow would remain attached, as demonstrated by previous experiments at GRC. They showed that lateral skewing of the near-wall flow at the diverging side walls induced a transverse pressure gradient, causing the formation of vortices near the side walls. The pressure near the side walls increased as the vertical edges of the circular cross-section diverged to form the rectangular shape, so that the pressure along the upper and lower portions of the duct was lower than along the sides. This pressure gradient encouraged the flow along the sides to migrate toward the upper and lower surfaces. The flow was then turned inward as it met the high-pressure fluid in the near-wall region at the upper and lower surfaces. These counter-rotating vortices met at the semimajor axis and deflect one another toward the interior, where they were deflected outward again by the high-momentum fluid at the duct core. Direct measurement of the Reynolds stresses confirmed this phenomenon. However, the experiment did not allow for measurement directly at the wall, so the behavior was observed for $y^+ > 80$ at some stations and $30 \leq y^+ \leq 80$ at other stations. Since wall function behavior was only valid for $y^+ > 400$ in the experiment, they recommended wall functions be used with caution for any numerical simulation comparisons. This statement drove the first applications of CFD to the Davis and Gessner transition duct.

Sotiropoulos [51] was the first to attempt to resolve the Davis and Gessner transition duct all the way to the wall using a second-order closure model. Previous attempts using a $K - \varepsilon$ model and a Reynolds Stress Model (RSM) (with wall functions) failed to adequately capture the strength of the secondary flow. The mesh used by Sotiropoulos resulted in

13

$y^+ \cong 0.5$ so that the near-wall region was well-resolved. The results showed remarkable agreement with the experimental data of Davis and Gessner, with values of vorticity differing by less than 5% at the exit of the duct, giving credence to the use of an RSM to accurately capture the secondary flow features. The comparison of Reynolds stresses also showed good agreement at the end of the transition section. This work also examined the differences in normal Reynolds stresses to determine the levels of anisotropy in the flow. It found anisotropy levels consistence with measured values, giving further reasons for the use of a turbulence model that does not employ the Boussinesq approximation.

Other interesting aspects of the Sotiropoulos research included the realization that the Reynolds stress equations are more stability-limited than the momentum equations, resulting in a reduction of the maximum Courant-Friedrichs-Lewy (CFL) number that can be used to advance the solution to convergence. Also, Sotiropoulos found the Reynolds stress field to be fairly insensitive to grid refinement.

On the practical side of applying transition ducts to high-performance aircraft engine exhaust systems, two efforts were carried out to determine flow separation limits on L/D and AR combinations. While flow separation is not optimal in exhaust nozzles due to the inherent loss in kinetic energy (and thus a decrease in thrust), a balance must be struck between keeping the flow attached and minimizing the length of the transition section. To this end, Wu, et al. [63] studied optimum length transition ducts with the support of GRC and compared their computational results with experiments at General Electric (GE) Aircraft Engines. They used the CFD code PEPSI-G, a three-dimensional, subsonic, PNS flow solver. Again, by today's standard a PNS code would be considered low-fidelity, especially with the use of a mixing-length turbulence model and in the treatment of flow separation. The PEPSI-G code did not allow for reverse flow but instead substituted a small positive value for any cells where flow is detected opposite to the primary flow direction. In fact, if massive separation occurred for a particular problem, no solution was obtained, and

this issue was used to create a chart for limits on *L/D* and *AR* combinations (reproduced in Figure 2.1). This chart provides a rough guide of the *L/D* and *AR* ratios (or "slope" of the line) where some separation is expected to occur. From this data, a ratio of 0.42 − 0.77 would cause flow separation. The work of Abbott, et al. [3] produced a similar chart, with *L/D* and *AR* ratios from 0.5 − 0.83 producing separated flow. It is reproduced in Figure 2.2, which also gives a good visual representation of various circular-to-rectangular transition ducts. In both cases, a smaller ratio than the lower bound of the ranges would result in separation. Based on these charts, separation due to area transition could occur in the ducts created for this research which have *AR* = 10.
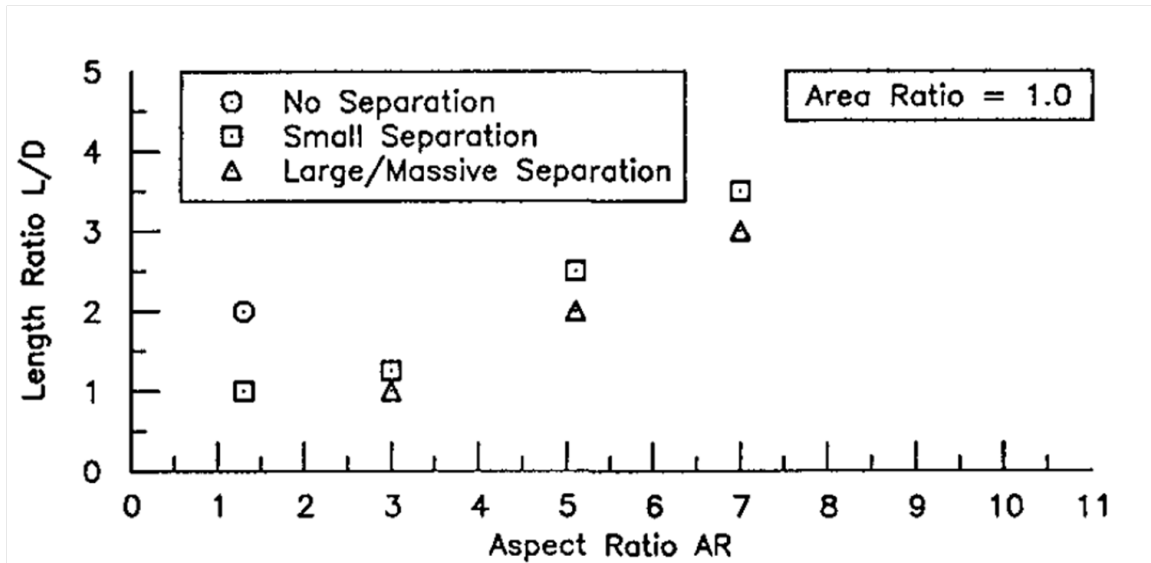
Figure 2.1: Separation prediction of transition ducts from Wu, et al. [63]

Due to the application of transition ducts aft of turbomachinery, the effects of swirl were considered early in NASA research efforts. Reichert and Hingst [46] performed experiments using the Davis duct with a swirl angle of 15.6°. They observed an additional pair of counter-rotating vortices near the side walls at the semi-major axis via oil film visualization. Significantly, they concluded that the presence of swirl suppressed the formation of vortices within the duct. Later, Cavicchi [13] performed CFD comparisons

15
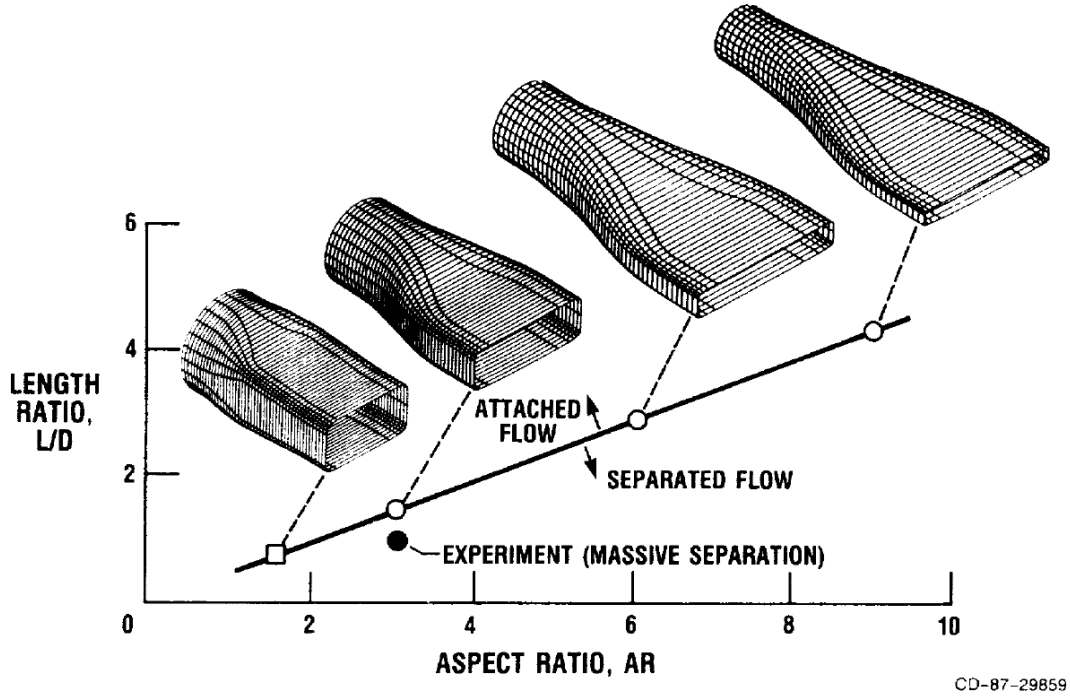
Figure 2.2: Separation prediction of transition ducts from Abbott, et al. [3]

with the Reichert and Hingst experiments that predicted the pairs of vortices. However, the comparisons are wrought with issues, as no experimental data was available directly adjacent to the walls (where CFD predicted the location of the vortices), but the CFD simulations used a mixing-length eddy viscosity turbulence model, and no information was reported on wall functions or y^+.

Miau, et al. [41] performed more detailed experiments on transition ducts with swirling flow, to include measurement of the Reynolds stresses, for a duct with $AR = 2$ and $L/D = 0.54, 0.92$, and 1.08. Significantly, they tested flows with Reynolds number up to two orders of magnitude difference (2.8×10^3 and 4.4×10^5) and found it did not play a critical role in varying the flow features. Their results also showed that swirl introduced a skewed velocity distribution at the duct exit. This was caused by the cross-stream velocity being aided in the upper left and lower right corners of the duct (looking upstream) by the counter-clockwise swirl-induced velocity. The curvature-induced cross-

16

stream velocity worked against the swirl in the opposite corners (lower left and upper right), thus reducing the intensity of the vorticity. Corresponding asymmetry in the pressure distribution was observed. Finally, they noted the $\overline{v'w'}$ Reynolds stress played a significant role in transporting streamwise vorticity outwards from the center of the duct.

For most applications of transition ducts to the aero-propulsion environment (including this research), the flow entering the duct is leaving a section of the engine that contains a centerbody, as depicted in Figure 1.4, representing the end of the engine spool. Thus, this type of duct can be considered an annular-to-rectangular transition. Prior research into the effect of this centerbody on transition duct flow features is surprisingly minimal, with only the early work of Sobota and Marble [50] represented in the literature. The combined experimental and computational effort used a duct with an area ratio of 3.6 and $AR = 5$. Swirl was introduced at 15° and 30°. They also used split blades, where the blade angle for the inner and outer annular sections could be set independently. For this experiment, the inner half was set to 0° and the outer half to 30°.

Interesting results from their experiments include the presence of a large vortex in the center of the exit plane due to the swirl near the centerbody increasing as the radius of the centerbody decreases downstream in order to conserve angular momentum. A similar central vortex could be expected for the swirl cases of the current research. The relative strength of the vortex, however, may be reduced because of the smaller swirl angles.

A pair of vortices rotating in the opposite direction of this main vortex were also present asymmetrically about the main vortex. The vortex generation occurred for both the 15° and 30° swirl cases. These were attributed to the boundary layer separation that occured on the outer walls due to the pressure gradient established by the strong central vortex. The vorticity of the central vortex was of opposite sense to the vortex pair. The pair was entrained into the main stream as the nozzle contracted. For the split blade cases, the center vortex was eliminated since the inner portion of the annulus had little vorticity,

17

and two vortices were present symmetrically at the exit. Flow separation was reduced, and two additional smaller vortices were formed in opposite corners of the exit (upper left and lower right), where the movement of the boundary layer fluid to the sidewalls was in the direction of the swirl.

The numerical portion of the study used the incompressible, finite-difference INS3D code. No turbulence model was used (i.e., laminar flow assumed), and because the code had difficulty with flow separation, the centerbody was changed from the experiment to a more gradually tapering conical tip. The computational results displayed the basic flow features of the experiment, but no conclusions could be drawn from the relatively low-fidelity simulations. Thus, the current research could provide the first high-fidelity computational results for a duct with centerbody and swirl.

2.4   Flow Through Serpentine Ducts

Another important geometric feature of the nozzles designed for this research is the serpentine flowpath. As with transition ducts, basic flow through serpentine ducts was described early on, then extended to aero-propulsion applications. These applications tend to focus on aircraft inlets, with very little research focused on the two-turn ducts like those used in the current effort, and no published research is found involving a two-stream flow like that of a turbofan engine.

The dominant characteristics of flow through a curved pipe were described by Prandtl [44]. The relationship for the centrifugal effects when fluid flows in curved lines is

$$\frac{v^2}{r} = \frac{1}{\rho}\frac{\partial P}{\partial s} \tag{2.10}$$

where ∂s is an element of arc in the normal direction, P is pressure, r is the radius of curvature, ρ is density, and v is velocity. Equation 2.10 shows that for flow traversing the same arc length along the inner and outer portions of a curve, the pressure gradient on the outer portion of the curve will be greater than the inner portion by the amount $\rho v^2/r$. This

18

provides the conditions for flow separation at the outer region of the curve, where the lower velocity due to increased pressure may not overcome the frictional forces and backward flow may develop.

Prandtl also described the formation of secondary flow in curved pipes as originating from the lateral displacement of the flow parallel to the boundaries of the pipe. When this occurs, a centrifugal force is generated on the core flow, causing it to accelerate. With lower static pressure near the center of the duct, the low energy boundary layer flow migrates inward, where the merging flow is pushed away from the wall and back towards the outside of the bend. Therefore the flow with the lower velocity (near the walls) is displaced more than the flow further away (at the core). So the core flow tends to go straight ahead due to its greater velocity, while the flow at the edges is deflected and tends toward the inner edges (for a "down-first" duct, the "outer" edge is at the top of the duct). Thus the main flow has superimposed on it a secondary motion normal to it, where the outer flow tends towards the inner edge of the curve. It then meets the counter-rotating flow from the symmetry plane and is deflected outward once again. These flow features are shown in Figure 2.3. Prandtl termed this type of skew-induced formation "secondary flows of the first kind". He also classified "secondary flows of the second kind" as stress-induced, originating from non-uniformities in wall turbulence, which occur primarily in non-circular ducts or in the boundary layer formed at the corner or edge of a surface [9].

Research into understanding the flow features of serpentine ducts for aerospace applications began in the 1970s as modern aircraft of the time began to feature curved ducts in dorsal and wing-root intakes. Bansod and Bradshaw [7] were first to accurately explain the physical mechanism behind the non-uniform total pressure distribution observed at the exit plane of an S-duct by means of experiment. Their experiment used various round serpentine ducts with $L/D \cong 3.5$, which is within the range of the current research. The Reynolds number was 5×10^5 (which is lower than the current research), however, the

19
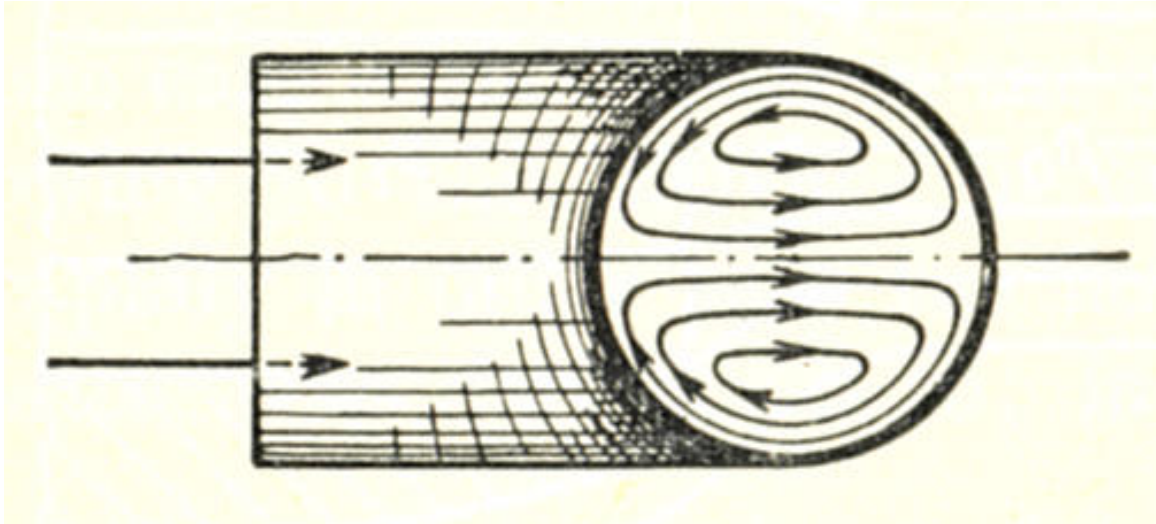
Figure 2.3: Secondary flow features in a curved pipe as described by Prandtl [44]

qualitative results are still useful. The direction of vertical displacement was "down-first" and attempted to approximate the dorsal intake of the Lockheed TriStar aircraft (see Figure 2.4), highlighting the aerospace interest at the time.
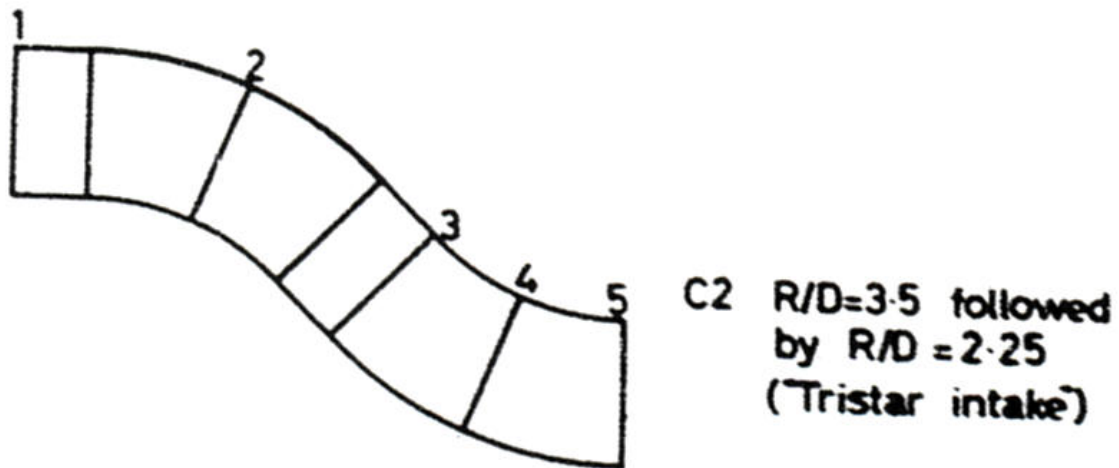
Figure 2.4: "TriStar" serpentine duct used by Bansod [7]

The most important result was the appearance of a region of low pressure at the bottom of the exit. The mechanism that caused this non-uniform pressure distribution was

20

attributed to the expulsion of boundary layer fluid by a pair of counter-rotating vortices in the boundary layer. The vortices were produced by lateral deflection of the boundary layer flow in the first bend, followed by vortex stretching in the longitudinally-accelerating flow towards the end of the second bend, viz., a pair of counter-rotating vortices were embedded in the "bottom" boundary layer at the exit and expelled low-velocity fluid toward the center of the duct. An important distinction was made in that the mechanism does not involve an instability of the flow, so that the vortices can be expected whether or not separation is present. Also, the mechanism that produced the low-total-pressure region at the outside of the second bend (in a down-first duct) was an inviscid one. Interestingly, the results also showed that the flow was not quite symmetric about the vertical center plane.

Key conclusions from the research of Bansod and Bradshaw concern the mechanism of vortex formation. The pressure gradients which deflect the inviscid core of the flow around a bend tend to produce a larger deflection in the slower-moving boundary layer fluid. After the first bend, the boundary layer thickness at the bottom of the duct starts to increase rapidly, indicating the formation of a pair of counter-rotating vortices. The pressure gradient reverses sign as the fluid moves through the second bend and tends to make the boundary layer fluid migrate towards the center of the duct. However, the fluid near the bottom does not migrate circumferentially because the pressure gradient near the bottom has negligible circumferential component and cannot overcome the buildup of boundary layer fluid from the first bend. The appearance of concentrated vortices is assisted by a favorable longitudinal pressure gradient starting near the middle of the second bend, which causes the flow near the surface to accelerate, thus stretching and intensifying the existing longitudinal vortex.

Bansod and Bradshaw also note that the eruption of fluid from the bottom surface would occur even in irrotational flow in order to satisfy continuity, but the vortices assist the process. They postulate that a short duct (shorter than any used in their research) could

21

avoid extensive flow separation because the secondary flow thins the top boundary layer, reducing its tendency to separate, and providing a "built-in vortex generator" in the bottom boundary layer.

More recent benchmark experimental data was produced by Wellborn [59]. His experiments involved a down-first diffusing S-duct at Mach 0.6 and Reynolds number of 2.6×10^6 with an L/D within the range of the current research. The results showed a region of streamwise flow separation with the development of counter-rotating vortices through curvature-induced, pressure-driven secondary flows. These vortices convected low momentum fluid from the boundary layer toward the center of the duct, degrading the uniformity and magnitude of the total pressure exit profile, which is a primary interest to aircraft intake researchers.

The diffusing S-ducts had curvature of the centerline and an increase of cross-sectional area. Cross-stream pressure gradients, resulting from the curvature, produced significant secondary flows, as expected. These flows convected boundary-layer fluid from the duct surface to the center, creating nonuniform cross-stream total pressure profiles, similar to Bansod and Bradshaw. Additionally, the adverse streamwise pressure gradient caused by the increasing cross-sectional area led to more dramatic flow separation.

Wellborn gives the progression of the flow physics in the diffusing S-duct are as follows: first, the curvature deflected the incoming flow downward, which caused the flowfield to deviate from traditional developing pipe flow through the development of cross-stream static pressure gradients, which were a direct result of the core flow adjusting to duct geometry and the resulting streamline curvature. In the middle of the first bend, the maximum static pressure existed at the top of the duct and the minimum at the bottom because the curvature induced a streamwise pressure gradient, which accelerated the flow near the bottom of the duct, and decelerated the flow near the top. In order to maintain equilibrium, the lower momentum fluid near the top of the duct was directed

circumferentially downward. In the second bend, the static pressure distribution was reversed, so that the lowest static pressure was near the top and the highest was near the bottom. At the second bend, the accumulation of low momentum fluid in the bottom of the duct was caused by the convection of the boundary-layer fluid toward the lower surface and also by the reversed flow and the adverse streamwise pressure gradient upstream of the second bend. By the exit, a pair of counter-rotating vortices located in the lower half of the duct had formed. The region of low momentum fluid extended above the centerline, which the author notes had been difficult to compute numerically. Wellborn's results for static pressure (a), total pressure (b), streamwise velocity (c), and transverse velocity (d) are given in Figure 2.5 where the slices roughly correspond to the stations in Figure 2.4.

Computational investigation of serpentine ducts began in earnest around the same time as that of transition ducts, both being important to modern aircraft research at the time. Towne and Anderson's early work at GRC involved CFD simulations of flow in a diffusing S-duct with elliptical-to-circular transition, for application to the F-16 inlet. While this early work wouldn't be considered high fidelity by today's standards (the aforementioned PEPSI-G code was used with a first-order marching scheme and one-dimensional pressure field correction), some results and hypotheses are helpful to the current research. First, in the case of a circular duct flow with no transition, counter-rotating vortices were produced in a similar manner as the experimental work discussed above. For the ducts with cross-sectional transition, it was hypothesized that the effect of the change in cross-section shape was much more important in this flow than the effect of the centerline curvature. This conclusion was supported by the results from the F-16 inlet, which had a low degree of curvature. The secondary flow patterns were not produced in the simulations, but this could be due to the fidelity of the code. The results showed the boundary layer became so thin near the converging sides of the duct that the boundary layers in the top and bottom halves of the inlet were essentially isolated from each other. It was postulated that the low

23
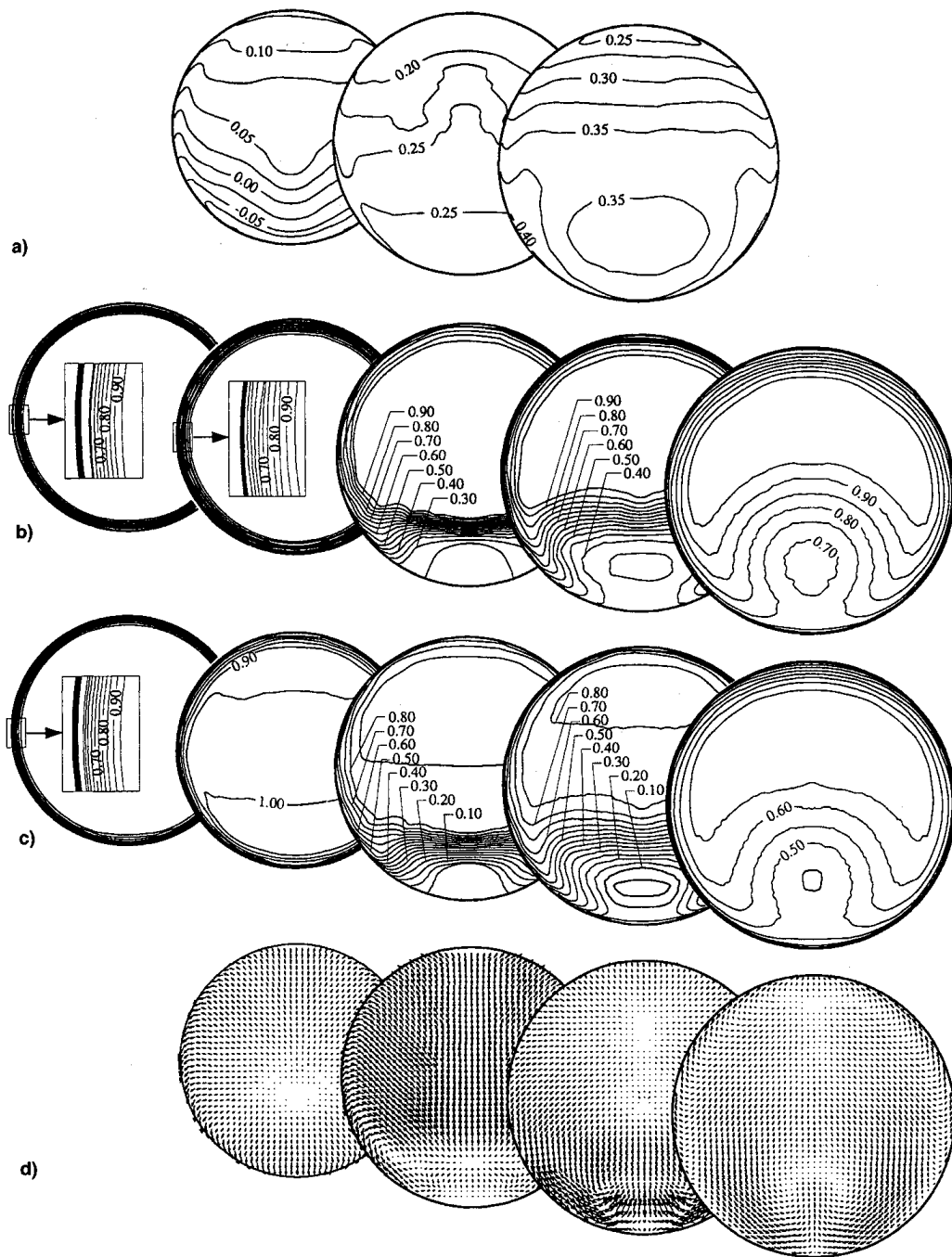
Figure 2.5: Serpentine Duct Results of Wellborn [59]

24

energy boundary layer fluid could not migrate through the thin boundary layer region and therefore could not form secondary flow patterns.

Later work from GRC provided more insight into S-duct flows. Harloff, et al. [29], performed simulations of flow through S-ducts (non-diffusing and diffusing, down-first with an offset of one diameter) using the PARC3D code with an algebraic turbulence model. The main contribution of this work is that the inviscid contributions to the secondary flows were quantified, supporting the hypothesis of Towne and Anderson.

For these simulations, the inlet Mach number was 0.6 and L/D was approximately 4. The flowfield for the non-diffusing S-duct showed secondary flow features developing very rapidly in the second bend. As stated previously, the secondary flow formation was due to the curvature-induced cross-stream pressure gradient. For the non-diffusing duct, $y^+ = 19$, while $y^+ = 10$ for the diffusing duct, which the authors note could be an issue for the wall functions used in the turbulence model. As a result, the simulations predicted a larger inviscid core region than experiments.

In order to quantify the inviscid contributions of the secondary flow and examine the magnitude of the viscous effects, the Euler equations were solved for irrotational and rotational inflow conditions. The computed inviscid, irrotational flow results showed no secondary flow development, which is consistent with classical theories. Likewise, the inviscid, rotational flow accounted for a significant portion of the secondary flow present in the fully viscous case. The algebraic turbulence model was found inadequate to properly predict secondary flow patterns when compared to experimental data, but two counter-rotating vortices at the S-duct exit were predicted. The rotational Euler solutions showed that the development of the secondary flow was driven by inviscid phenomena.

A computational parametric study of serpentine inlets was performed at the Air Force Institute of Technology (AFIT) to determine the effect of changing the duct shape on engine performance [52]. The serpentine ducts had an elliptic-to-circular transition. A design-

of-experiments framework was used to produce a response surface by varying geometric factors. The response surface was used to determine the most important factors in pressure recovery at the exit of serpentine ducts, many of which are the same factors that will vary in the current effort (L/D and AR). This work used the CFD code Fluent with a $K - \varepsilon$ turbulence model and special wall treatments. The results of the study concluded that the most important factors affecting the pressure recovery were (in rank order): throat Mach number, offset, area ratio, L/D, and AR. The rank order for pressure uniformity was: offset, L/D, AR, Mach, and area ratio.

For the current research, the serpentine duct has a nearly rectangular cross-section. Past research on this type of configuration is limited, but recently Reynolds [47] conducted experimental and computational work at AFIT to determine the effects of changing AR on a rectangular serpentine duct. The duct was tested and simulated in a horizontal and vertical configuration so that the aspect ratios were the inverse of one another. Important results from the horizontal case include the identification for two strong counter-rotating vortices in the upper half of the exit plane, with a region of high velocity at the lower portion of the duct. Important results from the vertical case include the identification of four vortices at the exit plane. The two vertical pairs rotated outward, while the two horizontal pairs rotated toward one another. The vertical duct displayed a larger region of separation after the second bend than the horizontal duct.

The CFD simulations were performed using Fluent with a third-order convective flux scheme and both the $K - \varepsilon$ and RSM turbulence models. The $K - \varepsilon$ model matched the experimental data poorly, due to the dissipative nature of the scheme and poor handling of separated flows. The RSM simulations matched the experimental data well, and gave credence to the conclusion that flow through serpentine ducts (especially the formation of secondary flow features) is highly dependent upon aspect ratio.

Finally, the literature reveals a few sources of information on computational research pertaining to two-turn ducts for propulsion application. The work of Gerolymos [24] assessed two versions of an RSM and compared the results to a standard $K - \varepsilon$ model and experimental data for an aircraft engine serpentine inlet duct with elliptical-to-circular transition. The duct centerline began and ended at the same vertical station, similar to the current effort. The simulations showed the two forms of the RSM were superior to the two-equation turbulence model at accurately predicting two high-loss, counter-rotating vortices, and two smaller secondary vortices at the exit plane. The primary vortices formed as a result of the large portion of separated flow that occurred after the first bend, while the secondary vortices formed from the boundary layer flow on the sides of the duct separating around the second bend. The two systems interacted strongly at the exit plane.

Other recent efforts were concerned specifically with unmanned aerial vehicles (UAV) and unmanned combat aerial vehicles (UCAV). An inlet that could be considered slightly "two-turn" was investigated using an algebraic RSM with a standard $K - \omega$ component [56]. The ducts in this research were fairly short (L/D ranged from 1 to 2.75), so separation tended to dominate the flow. There were two regions of flow separation corresponding to the two bends of the duct. At the exit, a region of low-velocity fluid was present in the upper region due to separation in the second bend, and two counter-rotating vortices were present in the lower region due to the flow migration at the first bend. CFD results compared favorably to experiment in determining pressure recovery and also demonstrated the dominance of flow separation over secondary flow formation in the upper region at the exit.

Another effort that demonstrated the significance of flow separation in a two-turn inlet is the UCAV work of Brear, et al. [10]. This research included experimental and CFD results using the NASA CNS code and a $K - \omega$ turbulence model. The curvature of the second bend is very slight at the bottom and more abrupt at the top before a diffusion

section begins. For this reason, the pair of vortices at the bottom of the exit is hardly identifiable, while the top pair of vortices are stronger, confined to the region just upstream of the exit, and are a result of the flow separation at the second bend.

The authors' primary focus was on the unsteady nature of the flow separation. They hypothesized that the separation within the duct was strongly unsteady and may respond to freestream disturbances. They described the difficulty of Reynolds-averaged Navier-Stokes (RANS) CFD codes to accurately model flow separation. The difficulty was demonstrated by a stagnation pressure which was lower than experimental data within separated regions, which is often observed in steady RANS models. The turbulence model predicted levels of turbulent viscosity within the separated region several orders of magnitude greater than the laminar viscosity. Brear, et al., showed the entropy generation per unit volume is directly proportional to the turbulent viscosity [11]; therefore, the turbulence model was predicting the primary sources of loss generation within the separation as the Reynolds stresses. Laminar stresses were less significant and therefore because the numerical prediction is steady, increased entropy was manifested as reduced stagnation pressure. The authors also mention that the Reynolds stresses can be computed to be much higher than experiment in attached boundary layers. However, the CFD results do match the experimental pressure recovery well, pointing to the overall utility of RANS codes. This research also concluded that the flow separation created large, coherent structures with a characteristic frequency and which convect downstream to the exit. Thus, the same mechanism (separation) produces both a reduction of inlet pressure recovery and an increase in inlet unsteadiness.

Several efforts focused on the STRICT inlet duct for use on next-generation UCAVs. The STRICT duct has an L/D of 2.5, an AR of 4, a bi-convex entrance section followed by a dual-turn offset section and diffusing, elliptical-to-circular exit section. Rabe [45] was first to publish work on this design, which included experimental and CFD simulations using the Lockheed Martin Falcon code. The experimental results showed two pairs of

28

counter-rotating vortices at the exit. The lower pair were generated by the first bend via the mechanisms described in above sections. These vortices were considerably dissipated at the exit. The second bend produced the upper pair of vortices, which rotated in the opposite sense as the first. The two pairs interacted along the vertical symmetry plane and were seen to slightly cancel each other. The CFD results lacked accuracy in predicting the vortex dissipation.

Another experimental and CFD investigation of the STRICT duct used the Texas A&M code UNS3D and Fluent [33]. Similar flow features to the work of Rabe were observed. Comparison between results showed the UNS3D solver did better than Fluent at matching experimental pressure recovery and separation locations, although this was mostly attributed to grid quality. The work of Hamstra [27] focused on flow control. Like Rabe, this effort used the Falcon code, and the lack of accuracy of the turbulence model at matching the experimental data was noted.

2.5   Flow Over Spheres and Spheroids at High Reynolds Number

A review of flow over spheres and spheroids must be accomplished since this is a major feature of nozzles designed for this research, and the work of Sobota and Marble [50] was the only source found to describe nozzle flow with a centerbody. Since flow over spheres and spheroids has received extensive attention for many decades, the following discussion is limited to high Reynolds number ($\mathcal{O}(10^6)$) flows like those seen in this research.

Taneda [53] was first to visualize high Reynolds number flow past a sphere. He used surface oil flow, smoke injected into the wake, and fabric tufts downstream of the sphere. The surface oil flow method acts under the combined action of gravity and air flow skin friction, so that the resulting pattern provides information about the distribution of skin friction on the surface. One of the most important features he observed was a Ω-shaped line prior to turbulent separation. The spirals represent the foci and lift-off point of two counter-

rotating vortices. The pattern is formed from the rollup of the vortex sheet off the surface, as shown in his drawing in Figure 2.6. Asymmetry was seen on the surface and further observed in the smoke and tuft results, where the wake oscillated slowly and irregularly, which means the sphere was subjected to a side force (a well-known phenomenon). Taneda notes that the asymmetry is heavily influenced by small perturbations of the sphere shape, such as seams and bumps, and small obstructions in the wake.
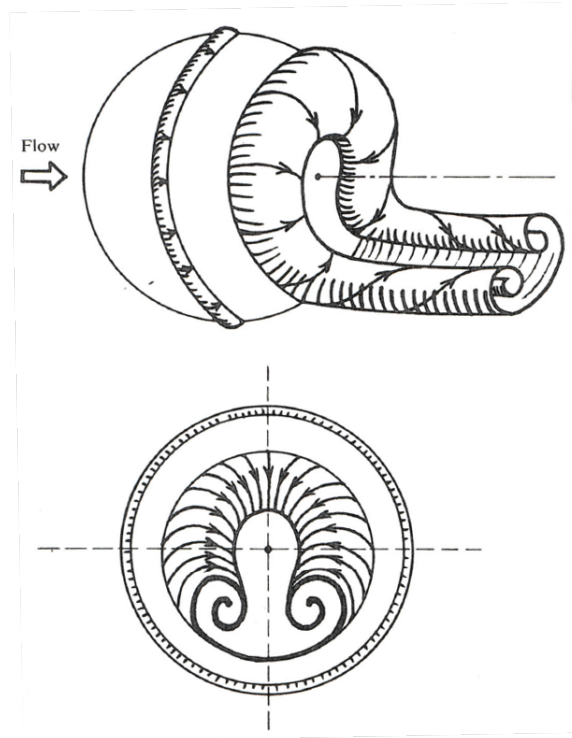
Figure 2.6: Vortex structure of separation from sphere at high Reynolds number. [53]

Constantinescu [16, 17] performed several time-accurate numerical studies on spheres and spheroids at high Reynolds number. The flow structures changed dramatically from lower Reynolds number cases, and asymmetry was seen in the wake vortical structures. As observed by Taneda, a counter-rotating vortex pair was present in the spherical studies. The vortices originated above the horizontal centerline and rotated about the centerline axis. Similar flow structures were seen in spheroid simulations, where coherent streamwise

30

vortices dominated the wake. While no direct comment is made on the symmetry of the separated flow structures, the azimuthal distribution of skin friction coefficient indicates non-axisymmetric behavior.

2.6   Thermally Stratified Shear Layers

In the nozzles designed for this research, the termination of the bypass liner at the mixing plane creates a thermally stratified shear layer between the bypass and core flows. For most high-performance propulsion applications the static pressure at the mixing plane is matched to promote mixing of the two streams for afterburning. Classic plane mixing layer theory [60] would apply only briefly due to the geometric changes in the nozzle beginning at the mixing plane. At the high Reynolds numbers seen in engine exhaust nozzles, this shear layer will generate vorticity, which can have a strong influence on mass, momentum, and heat transfer[64]. Thermally stratified flows are the topic of much research in the environmental community, where the flows of interest primarily involve natural convection and are at low Reynolds number. The literature does not provide much insight on the behavior of thermally stratified mixing layers in ducts (curved or otherwise). The lack of previous research for propulsion applications can be attributed to the presence of forced mixers in most modern high-performance gas turbine engines.

2.7   Literature Review Conclusions

The conclusions from the literature review are thus:

- Flow separation is common in S-ducts and transition ducts.

- Vortex pairs are evident in the exit plane of S-ducts and transition ducts.

- Vortex formation is due to secondary flows structures induced by centrifugal pressure gradients and in some cases flow separation.

- A pair of counter-rotating vortices should be expected to originate from flow separation off the tailcone and could have some degree of asymmetry.

- Reynolds stress models are better suited for computation of secondary flows in S-ducts and transition ducts than two-equation turbulence models.

- No published work was found for the application of serpentine ducts to aircraft engine exhaust systems; therefore, little attention is given in the literature to thermal mixing and temperature distribution in transition or serpentine ducts.

2.8   Computational Methods

The goal of CFD is to model a continuous medium with a set of discrete points via numerical methods. The continuum assumption (Knudsen number << 1) allows the application of physical laws to each point in the solution space. These laws define important physical quantities such as density, velocity, pressure, and energy which describe the state of the fluid at a particular location in the solution space. The applicable physical laws to fluid dynamics are: conservation of mass (mass is not created nor destroyed), conservation of momentum (Newton's second law), and conservation of energy (first law of thermodynamics). These laws are developed into a set of governing equations in the following sections, known collectively as the Navier-Stokes equations. Necessary closure equations are then discussed. The development of the K-ω shear stress transport (SST) and Reynolds stress turbulence models completes this chapter.

2.8.1   General Conservation Law.

The following development uses the finite volume method to arrive at the Navier-Stokes equations. A useful mathematical tool in the derivation of this form of the equations is the Reynolds transport theorem. Consider a system that contains a fixed control volume of fluid. Let N be any extensive property of the fluid (a property that is dependent upon mass). The Reynolds transport theorem states that the rate of change of N within the system

is equal to the rate of change of N within the control volume (due to sources of generation or destruction) plus the net change of N through the control surface due to the convective flux (bulk motion of the flow) and the diffusive flux (random molecular motion, or changes of the fluid at rest):

$$\frac{DN}{Dt} = \frac{\partial}{\partial t} \int_V \eta \rho \, dV + \oint_A \eta \rho \, (\vec{v} \cdot \hat{n}) \, dA + \oint_A \left(\vec{J} \cdot \hat{n} \right) dA \qquad (2.11)$$

Where η is N per unit mass, ρ is density (mass per volume), $\vec{v}$ is velocity, V is volume, $\hat{n}$ is the unit normal, $\vec{J}$ is the diffusive flux, and A is area. The extensive property can be considered conserved if it obeys the conservation law:

Rate of change of η within V + flux of η through $A =$

Production of η within V + Production of η on A

A general conservation law can be then expressed by the following:

$$\frac{\partial}{\partial t} \int_V \eta \rho \, dV + \oint_A \eta \rho \, (\vec{v} \cdot \hat{n}) \, dA + \oint_A \left(\vec{J} \cdot \hat{n} \right) dA = \int_V S_V \, dV + \oint_A \left(\vec{S}_A \cdot \hat{n} \right) dA \qquad (2.12)$$

where $\eta \rho$ is the conserved quantity, S_V is the volume sources, and S_A is the surface sources.

2.8.2 Continuity Equation.

If the extensive property is mass, $N = m$, so that in Equation 2.11, $\eta = 1$, and the conserved quantity is density. Turning to Equation 2.12, there is no diffusive flux since mass cannot vary without motion, so that only convective fluxes contribute to a change in mass over time within the control volume. Also, there are no sources since mass cannot be created or destroyed. The continuity equation is thus given by

$$\frac{Dm}{Dt} = \frac{\partial}{\partial t} \int_V \rho \, dV + \oint_A \rho \, (\vec{v} \cdot \hat{n}) \, dA = 0 \qquad (2.13)$$

2.8.3 Momentum Equation.

Within the context of the finite volume method, Newton's second law states that the net force acting on the control volume is equal to its mass times acceleration, which is the

33

time rate of change of momentum. If the extensive property is momentum, $N = m\vec{v}$, then $\eta = \vec{v}$ and the conserved quantity is momentum. Summing the forces in the control volume and using Equation 2.12 yields

$$\frac{D(m\vec{v})}{Dt} = \frac{\partial}{\partial t} \int_V \rho\vec{v}\,dV + \oint_A \rho\vec{v}(\vec{v} \cdot \hat{n})\,dA = \sum \vec{F} \tag{2.14}$$

There is no diffusive flux since there can be no diffusion of momentum for a fluid at rest. The sum of the forces on the control volume equates to the source terms in Equation 2.12. The volume sources are body forces acting on the control volume and can be represented as:

$$\vec{F}_b = \int_V \rho\vec{f}_b\,dV \tag{2.15}$$

and can include gravitational, buoyancy, centrifugal, Coriolis, or electromagnetic forces [8]. The surface forces include the pressure, P, acting on the control volume from the surrounding fluid and the viscous forces from the friction between the surrounding fluid and the control volume surface. These forces can be expressed in the form of a stress tensor, $\bar{\bar{\tau}}_{ij}$. In the case of a Cartesian control volume $\bar{\bar{\tau}}_{ij}$ is

$$\bar{\bar{\tau}}_{ij} = \begin{bmatrix} \tau_{xx} & \tau_{xy} & \tau_{xz} \\ \tau_{yx} & \tau_{yy} & \tau_{yz} \\ \tau_{zx} & \tau_{zy} & \tau_{zz} \end{bmatrix} \tag{2.16}$$

In general, the normal forces are not equal for the front and back of the control volume, $\tau_{xx_{front}} \neq \tau_{xx_{back}}$. Rather, $\tau_{xx_{front}} = \tau_{xx_{back}} + \frac{\partial \tau_{xx}}{\partial x}dx$. This is also true for the y and z directions. Therefore, the net force in the x direction is

$$dF_v = \left(\tau_{xx_{front}} - \tau_{xx_{back}}\right) dy\,dz = \frac{\partial \tau_{xx}}{\partial x}dx\,dy\,dz = \frac{\partial \tau_{xx}}{\partial x}dV \tag{2.17}$$

and similarly for the other eight terms of $\bar{\bar{\tau}}_{ij}$. Summing the x, y, and z forces gives

$$dF_{v_x} = \left(\frac{\partial \tau_{xx}}{\partial x} + \frac{\partial \tau_{xy}}{\partial y} + \frac{\partial \tau_{xz}}{\partial z}\right)dV \tag{2.18}$$

$$dF_{v_y} = \left(\frac{\partial \tau_{yx}}{\partial x} + \frac{\partial \tau_{yy}}{\partial y} + \frac{\partial \tau_{yz}}{\partial z} \right) dV \tag{2.19}$$

$$dF_{v_z} = \left(\frac{\partial \tau_{zx}}{\partial x} + \frac{\partial \tau_{zy}}{\partial y} + \frac{\partial \tau_{zz}}{\partial z} \right) dV \tag{2.20}$$

Therefore, $d\vec{F}_v = \left(\nabla \cdot \bar{\bar{\tau}}_{ij} \right) dV$. Integration using the divergence theorem yields the total force:

$$\vec{F}_v = \begin{bmatrix} \tau_{xx} n_x + \tau_{xy} n_y + \tau_{xz} n_z \\ \tau_{xy} n_x + \tau_{yy} n_y + \tau_{yz} n_z \\ \tau_{xz} n_x + \tau_{yz} n_y + \tau_{zz} n_z \end{bmatrix} \tag{2.21}$$

Each term in the stress tensor can be represented by three components:

1. Thermodynamic pressure normal to the surface,

2. Linear dilation—change in shape of the control volume, and

3. Volumetric dilation—rate of change of volume, i.e. change in density.

Stokes derived the following expression for a Newtonian fluid, given in index notation:

$$\bar{\bar{\tau}}_{ij} = -\delta_{ij} P + \mu \left(\frac{\partial u_i}{\partial x_j} + \frac{\partial u_j}{\partial x_i} \right) + \delta_{ij} \lambda \nabla \cdot \vec{v} \tag{2.22}$$

where δ_{ij} is the Kroniker Delta, μ is dynamic viscosity, and λ is second, or bulk viscosity. Stokes also introduced the hypothesis that the mechanical pressure equals the thermodynamic pressure. If the mechanical pressure can be defined as the average of the normal stresses, then from Equation 2.22, $\vec{\tau}_{ii}$ is given by

$$\tau_{xx} = -P + \mu \left(\frac{\partial u}{\partial x} + \frac{\partial u}{\partial x} \right) + \lambda \nabla \cdot \vec{v} = -P + 2\mu \frac{\partial u}{\partial x} + \lambda \nabla \cdot \vec{v} \tag{2.23}$$

$$\tau_{yy} = -P + \mu \left(\frac{\partial v}{\partial y} + \frac{\partial v}{\partial y} \right) + \lambda \nabla \cdot \vec{v} = -P + 2\mu \frac{\partial v}{\partial y} + \lambda \nabla \cdot \vec{v} \tag{2.24}$$

$$\tau_{zz} = -P + \mu \left(\frac{\partial w}{\partial z} + \frac{\partial w}{\partial z} \right) + \lambda \nabla \cdot \vec{v} = -P + 2\mu \frac{\partial w}{\partial z} + \lambda \nabla \cdot \vec{v} \tag{2.25}$$

and taking the average yields

$$\bar{P} = -\frac{1}{3}\left(\tau_{xx} + \tau_{yy} + \tau_{zz}\right) = -\frac{1}{3}\left[-3P + 2\mu\left(\frac{\partial u}{\partial x} + \frac{\partial v}{\partial y} + \frac{\partial w}{\partial z}\right) + 3\lambda\nabla\cdot\vec{v}\right]$$

$$= P - \frac{2}{3}\mu\nabla\cdot\vec{v} - \lambda\nabla\cdot\vec{v} = P - \left(\lambda + \frac{2}{3}\mu\right)\nabla\cdot\vec{v} \quad (2.26)$$

Equating $\bar{P}$ and P in Equation 2.26 (and thus eliminating them) yields the now-famous final form of Stokes' hypothesis:

$$0 = -\left(\lambda + \frac{2}{3}\mu\right)\nabla\cdot\vec{v} \Rightarrow \boxed{\lambda = -\frac{2}{3}\mu} \quad (2.27)$$

Applying Stokes' hypothesis to Equation 2.22 gives

$$\bar{\bar{\tau}}_{ij} = -\delta_{ij}P + \mu\left[\frac{\partial u_i}{\partial x_j} + \frac{\partial u_j}{\partial x_i} - \frac{2}{3}\delta_{ij}\nabla\cdot\vec{v}\right] \quad (2.28)$$

The final form of the momentum equation can thus be written as

$$\frac{D\left(m\vec{v}\right)}{Dt} = \frac{\partial}{\partial t}\int_V (\rho\vec{v})\,dV + \oint_A \rho\vec{v}(\vec{v}\cdot\hat{n})\,dA = \int_V \rho\vec{f}_b\,dV + \oint_A \left(\bar{\bar{\tau}}_{ij}\cdot\hat{n}\right)dA \quad (2.29)$$

2.8.4 Energy Equation.

The first law of thermodynamics states the change of total energy, E, in the control volume is equal to the heat, Q, added to the volume plus the work, W, done on the volume by surface and volume sources. It is commonly expressed for an arbitrary system as

$$dE = \delta Q + \delta W \quad (2.30)$$

If the extensive property is the total energy (internal plus kinetic), $N = E = me + \frac{1}{2}m\left|\vec{v}\right|^2$, then $\eta = e + \frac{1}{2}\left|\vec{v}\right|^2$ and the conserved quantity is the intensive total energy per volume. Applying Equation 2.11:

$$\frac{DE}{Dt} = \frac{\partial}{\partial t}\int_V \rho\left(e + \frac{1}{2}\left|\vec{v}\right|^2\right)dV + \oint_A \rho\left(e + \frac{1}{2}\left|\vec{v}\right|^2\right)(\vec{v}\cdot\hat{n})\,dA = \frac{\delta Q}{dt} + \frac{\delta W}{dt} \quad (2.31)$$

The two terms on the right hand side of Equation 2.31 are the rates of heat exchange and work produced, respectively. The rate of heat exchange in the control volume can be represented by body heating (due to combustion or radiation) and surface heating (due

to conduction), which equate to the portion of volume sources due to heat transfer and the diffusive flux, respectively, in Equation 2.12. Applying Fourier's law of heat conduction to the surface heating term gives

$$\frac{\delta Q}{dt} = \int_V \rho \dot{q}_b \, dV + \oint_A (k\nabla T \cdot \hat{n}) \, dA \tag{2.32}$$

where $\dot{q}_b$ is the rate of body heating, k is the coefficient of thermal conductivity, and T is temperature. The other portion of the volume sources in Equation 2.12 is the work done by the body forces, $\rho \vec{f}_b \cdot \vec{v}$. The work rate term in Equation 2.31 corresponds to the surface sources in Equation 2.12, and is equal to the work done by the pressure as well as the shear and normal stresses on the control volume. Applying the concept of the stress tensor as in the momentum equation yields

$$\frac{\delta W}{dt} = \oint_A \left[\left(\bar{\bar{\tau}}_{ij} \cdot \vec{v} \right) \cdot \hat{n} \right] \, dA \tag{2.33}$$

The final form of the energy equation can be obtained by combining equations 2.31, 2.32, and 2.33:

$$\frac{DE}{Dt} = \frac{\partial}{\partial t} \int_V \rho \left(e + \frac{1}{2} \left| \vec{v} \right|^2 \right) dV + \oint_A \rho \left(e + \frac{1}{2} \left| \vec{v} \right|^2 \right) (\vec{v} \cdot \hat{n}) \, dA$$
$$= \int_V \rho \dot{q}_b \, dV + \int_V \rho \vec{f}_b \cdot \vec{v} \, dV + \oint_A (k\nabla T \cdot \hat{n}) \, dA + \oint_A \left[\left(\bar{\bar{\tau}}_{ij} \cdot \vec{v} \right) \cdot \hat{n} \right] dA \tag{2.34}$$

2.8.5 *Closure Equations.*

Several assumptions can be made about the fluid of interest in order to close the Navier-Stokes equations. First, the fluid is assumed to be a calorically perfect gas, so that the ideal gas law ($P = \rho R T$) can be applied. Next, the dynamic viscosity of the gas is assumed to depend strongly on temperature and weakly on pressure, so that Sutherland's formula may be applied:

$$\mu = \frac{C_1 T^{3/2}}{C_2 + T} \tag{2.35}$$

where C_1 and C_2 are empirically derived constants. Finally, the thermal conductivity is defined as:

$$k = C_P \frac{\mu}{Pr} \tag{2.36}$$

where Pr is the Prandtl number, usually assumed to be 0.72 for air. The definitions of the specific gas constants ($R = C_P - C_V$) and the ratio of specific heats ($\gamma = C_P/C_V$) are used to close out the equations.

2.8.6 Vorticity Equation.

As described in the literature review, vorticity is expected to play a significant role in the development of secondary flow in the serpentine exhaust nozzles used in the current research. While not one of the conserved variables solved in the Navier-Stokes equations, examination of the vorticity transport equation can be a useful exercise in determining the sources of vorticity in the nozzles. Vorticity is a kinematic property of a flow that describes the local spinning motion of a fluid element and is defined as twice the local angular velocity, which is the curl of the velocity vector: $\vec{\omega} = \nabla \times \vec{v}$ [60]. Therefore, the transport equation for vorticity can be obtained by taking the curl of the momentum equation:

$$\frac{\partial \vec{\omega}}{\partial t} + (\vec{v} \cdot \nabla)\,\vec{\omega} = (\vec{\omega} \cdot \nabla)\,\vec{v} - \vec{\omega}\,(\nabla \cdot \vec{v}) + \frac{1}{\rho^2}\nabla\rho \times \nabla P + \nabla \times \left(\frac{\nabla \cdot \bar{\bar{\tau}}_{ij}}{\rho} \right) + \nabla \times \vec{f_b} \tag{2.37}$$

The terms on the left hand side represent the rate of change of vorticity and the convective term. The first term on the right hand side represents vortex stretching due to velocity gradients. Vortex stretching is the mechanism by which turbulent kinetic energy is transferred to smaller scales and is present in almost all high-Reynolds-number flows. Therefore this term has obvious implications to the current research. The second term represents vortex stretching due to compressibility. The negative sign indicates that in an expanding flow (positive $\nabla \cdot \vec{v}$), this term will reduce the vorticity, and vice versa. This term could have an impact in vortex transport for the current research due to the compressible nature of the flow within a C-D nozzle. The third term is the baroclinic term and represents

the change in vorticity due to unequal acceleration when pressure and density gradient are misaligned. While this term is sometimes ignored in aerodynamics (but remains important in atmospheric and environmental fluid models), it could have an impact on the flows in an exhaust nozzle due to the presence of the thermally stratified shear layer at the mixing plane, as discussed in Section 2.6. The fourth term represents the diffusion of vorticity due to viscosity. It shows that vorticity tends to diffuse in the flow due to viscosity. At high Reynolds number, the effect of this term tends to be small compared to the other mechanisms in the vorticity transport equation [40]. Therefore, the formation of large-scale vortical structures tend to be independent of viscosity, as noted in Section 2.4 in the important early work of Bansod and Bradshaw[7]. The final term in the vorticity transport equation represents the generation of vorticity due to external body forces, of which centrifugal forces are expected to play an important role due to the curvature of the nozzle (see Equation 2.10 for an example of such a source term).

2.8.7 *Reynolds- and Favre-Averaging of the Navier-Stokes Equations.*

Special treatment of the Navier-Stokes equations must be given in situations that involve turbulent flow. Reynolds proposed a methodology by which the flow variables are decomposed into mean and fluctuating components (e.g., $\eta = \bar{\eta} + \eta'$), where the averaging can take one of three forms: temporal, spatial, or ensemble. This decomposition is then substituted into the original equations, and simplifications are made concerning the average of fluctuating terms (e.g., $\overline{\eta'} = 0$). For incompressible flows, the result is the RANS equations. For compressible flows, it is more convenient to apply a mass-weighted decomposition (proposed by Favre) to the velocity, internal energy, and temperature terms (e.g., $T = \tilde{T} + T''$). Reynolds-averaging is reserved for the density and pressure terms. This form is known as the Favre- and Reynolds-averaged Navier Stokes (FRANS) equations, although "RANS" is often used for both compressible and incompressible flows. After similar simplifications as for the RANS equations, the final form can be written in the

following index notation [8]:

$$\frac{\partial \overline{\rho}}{\partial t} + \frac{\partial}{\partial x_i}\left(\overline{\rho}\tilde{v}_i\right) = 0 \tag{2.38}$$

$$\frac{\partial}{\partial t}\left(\overline{\rho}\tilde{v}_i\right) + \frac{\partial}{\partial x_j}\left(\overline{\rho}\tilde{v}_j\tilde{v}_i\right) = -\frac{\partial \overline{p}}{\partial x_i} + \frac{\partial}{\partial x_j}\left(\tilde{\tau}_{ij} - \overline{\rho}\widetilde{v_i''v_j''}\right) \tag{2.39}$$

$$\frac{\partial}{\partial t}\left(\overline{\rho}\tilde{e}\right) + \frac{\partial}{\partial x_j}\left[\overline{\rho}\tilde{v}_j\left(\tilde{e} + \frac{\overline{p}}{\overline{\rho}}\right)\right] = \frac{\partial}{\partial x_j}\left(\tilde{k}_t\frac{\partial \tilde{T}}{\partial x_j} - C_P\overline{\rho}\widetilde{v_j''T''} + \widetilde{\tau_{ij}v_j''} - \overline{\rho}\widetilde{v_j''K} + \tilde{v}_i\tilde{\tau}_{ij} - \overline{\rho}\widetilde{v_i''v_j''}\right) \tag{2.40}$$

Equation 2.40 is similar to the non-averaged Navier-Stokes equations, except for the appearance of the following new terms, which must be modeled:

- $\widetilde{\tau_{ij}v_j''} \longrightarrow$ molecular diffusion

- $\overline{\rho}\widetilde{v_j''K} \longrightarrow$ turbulent transport of turbulent kinetic energy

- $c_p\overline{\rho}\widetilde{v_j''T''} \longrightarrow$ turbulent heat flux

- $\overline{\rho}\widetilde{v_i''v_j''} \longrightarrow$ Reynolds-stress tensor, transport of mean momentum due to turbulence

The first two terms above are usually ignored. The next term is usually modeled using the Reynolds analogy

$$C_P\overline{\rho}\widetilde{v_j''T''} \approx -\frac{C_P\tilde{\mu}_t}{Pr_t}\frac{\partial \tilde{T}}{\partial x_j} \tag{2.41}$$

where Pr_t is the turbulent Prandtl number. Much work in the field of turbulence modeling concerns the last term in the above list—the Reynolds-stress tensor. The most common models are so-called *first-order closures*, which use the eddy viscosity hypothesis proposed by Boussinesq to close the FRANS equations with one or two additional transport equations. One-equation models directly employ a transport equation for the eddy viscosity (μ_T), while two-equation models relate two additional terms, the turbulent kinetic energy (K) and turbulent dissipation rate (ε or ω) to μ_T. The next section discusses the two-equation model used in this research, the $K - \omega$ SST model.

40

2.8.8 $K - \omega$ *Shear Stress Transport Model.*

The $K - \omega$ SST model is a two-equation model that blends two common turbulence models, $K - \varepsilon$ and $K - \omega$, in order to take advantage of the best qualities of each model. The $K - \omega$ model is sensitive to freestream values of ω, while the $K - \varepsilon$ model is fairly independent of freestream conditions. The $K - \omega$ model performs much better in boundary layers since wall functions are not required. The $K - \omega$ SST model uses blending functions to transition the equations from the $K - \omega$ model in the boundary layer to the $K - \varepsilon$ model in the freestream. The transport equations for this model are

$$\frac{\partial}{\partial t}(\rho K) + \frac{\partial}{\partial x_i}(\rho K u_i) = \frac{\partial}{\partial x_j}\left(\Gamma_K \frac{\partial K}{\partial x_j}\right) + \tilde{G}_K - Y_K \tag{2.42}$$

$$\frac{\partial}{\partial t}(\rho \omega) + \frac{\partial}{\partial x_i}(\rho \omega u_i) = \frac{\partial}{\partial x_j}\left(\Gamma_\omega \frac{\partial \omega}{\partial x_j}\right) + G_\omega - Y_\omega + D_\omega \tag{2.43}$$

The terms on the left-hand-side of above equations represent the time rate of change and the convective transport of K and ω, respectively. The right-hand-side components of the transport equation are described below [5]:

$$\Gamma_K \rightarrow \text{Effective diffusivity of } K \tag{2.44}$$

$$\Gamma_\omega \rightarrow \text{Effective diffusivity of } \omega \tag{2.45}$$

$$\tilde{G}_K \rightarrow \text{Generation of K due to mean velocity gradients} \tag{2.46}$$

$$G_\omega \rightarrow \text{Generation of } \omega \tag{2.47}$$

$$Y_K \rightarrow \text{Dissipation of } K \text{ due to turbulence} \tag{2.48}$$

$$Y_\omega \rightarrow \text{Dissipation of } \omega \text{ due to turbulence} \tag{2.49}$$

$$D_\omega \rightarrow \text{Cross-diffusion blending function} \tag{2.50}$$

The effective diffusivity of K, Γ_K, is

$$\Gamma_K = \mu + \frac{\mu_t}{\sigma_K} \tag{2.51}$$

where the turbulent eddy viscosity, μ_t is

$$\mu_t = \frac{\rho K}{\omega} \frac{1}{\max\left[\frac{1}{\alpha^*}, \frac{SF_2}{a_1\omega}\right]} \tag{2.52}$$

The necessary closures and constants for μ_t are

$$\alpha^* = \alpha^*_\infty \left(\frac{\alpha^*_0 + Re_t/Re_K}{1 + Re_t/Re_K}\right) \tag{2.53}$$

$$\alpha^*_\infty = 1.0 \tag{2.54}$$

$$\alpha^*_0 = \frac{\beta_i}{3} \tag{2.55}$$

$$\beta_i = 0.072 \tag{2.56}$$

$$Re_t = \frac{\rho K}{\mu\omega} \tag{2.57}$$

$$Re_K = 6.0 \tag{2.58}$$

$$S = \sqrt{2S_{ij}S_{ij}} \tag{2.59}$$

$$S_{ij} = \frac{1}{2}\left(\frac{\partial u_i}{\partial x_j} + \frac{\partial u_j}{\partial x_i}\right) \tag{2.60}$$

$$F_2 = \tanh\left(\phi_2^2\right) \tag{2.61}$$

$$\phi_2 = \max\left[2\frac{\sqrt{K}}{0.09\omega y}, \frac{500\mu}{\rho y^2\omega}\right] \tag{2.62}$$

$$a_1 = 0.31 \tag{2.63}$$

where α^* is a damping coefficient used in the low-Reynolds number correction, S is the modulus of the mean strain rate tensor (S_{ij}), F_2 is the outer blending function, and y is the distance to the nearest wall. The turbulent Prandtl number for K, σ_K, is

$$\sigma_K = \frac{1}{\frac{F_1}{\sigma_{K,1}} + \frac{1-F_1}{\sigma_{K,2}}} \tag{2.64}$$

$$F_1 = \tanh\left(\phi_1^4\right) \tag{2.65}$$

$$\phi_1 = \min\left[\max\left(\frac{\sqrt{K}}{0.09\omega y}, \frac{500\mu}{\rho y^2\omega}\right), \frac{4\rho K}{\sigma_{\omega,2}D_\omega^+ y^2}\right] \tag{2.66}$$

$$\sigma_{\omega,2} = 1.168 \tag{2.67}$$

$$D_\omega^+ = \max\left[2\rho\frac{1}{\sigma_{\omega,2}}\frac{1}{\omega}\frac{\partial K}{\partial x_j}\frac{\partial \omega}{\partial x_j}, 10^{-10}\right]$$ (2.68)

$$\sigma_{K,1} = 1.176$$ (2.69)

$$\sigma_{K,2} = 1.0$$ (2.70)

where F_1 is the inner blending function[8].

The effective diffusivity of ω, Γ_ω, is similarly defined as

$$\Gamma_\omega = \mu + \frac{\mu_t}{\sigma_\omega}$$ (2.71)

with

$$\sigma_\omega = \frac{1}{\frac{F_1}{\sigma_{\omega,1}} + \frac{1-F_1}{\sigma_{\omega,2}}}$$ (2.72)

$$\sigma_{\omega,1} = 2.0$$ (2.73)

Note that the preceding definitions of diffusivity are given with a low-Reynolds number correction [61], as discussed in Chapter 3.

The generation of K due to mean velocity gradients, $\tilde{G}_K$, is

$$\tilde{G}_K = \min\left(G_k, 10\rho\beta^*K\omega\right)$$ (2.74)

The necessary closures and constants for $\tilde{G}_K$ are

$$G_K = -\rho\overline{u_i'u_j'}\frac{\partial u_j}{\partial x_i} = \mu_t S^2$$ (2.75)

$$\beta^* = \beta_\infty^*\left[\frac{4/15 + \left(Re_t/Re_\beta\right)^4}{1 + \left(Re_t/Re_\beta\right)^4}\right]$$ (2.76)

$$\beta_\infty^* = 0.09$$ (2.77)

$$Re_\beta = 8.0$$ (2.78)

The generation of ω, G_ω, is

$$G_\omega = \frac{\alpha\rho}{\mu_t}\tilde{G}_K$$ (2.79)

43

The necessary closures and constants for G_ω are

$$\alpha = \frac{\alpha_\infty}{\alpha^*} \left(\frac{\alpha_0 + Re_t/Re_\omega}{1 + Re_t/Re_\omega} \right) \tag{2.80}$$

$$\alpha_\infty = F_1 \alpha_{\infty,1} + (1 + F_1) \alpha_{\infty,2} \tag{2.81}$$

$$\alpha_{\infty,1} = \frac{\beta_{i,1}}{\beta_\infty^*} - \frac{\kappa^2}{\sigma_{\omega,1} \sqrt{\beta_\infty^*}} \tag{2.82}$$

$$\alpha_{\infty,2} = \frac{\beta_{i,2}}{\beta_\infty^*} - \frac{\kappa^2}{\sigma_{\omega,2} \sqrt{\beta_\infty^*}} \tag{2.83}$$

$$\beta_{i,1} = 0.075 \tag{2.84}$$

$$\beta_{i,2} = 0.0828 \tag{2.85}$$

$$\beta_\infty^* = 0.09 \tag{2.86}$$

$$\kappa = 0.41 \tag{2.87}$$

$$\alpha_0 = 1/9 \tag{2.88}$$

$$Re_\omega = 2.95 \tag{2.89}$$

One unfortunate feature of eddy viscosity models like $K - \omega$ SST is an insensitivity to streamline curvature [61], which could have a large impact on this research effort. Therefore, a form of the model with a curvature correction is used. The correction is applied to the ω generation term to arrive at $G_{\omega,cc}$ via the following formulation:

$$G_{\omega,cc} = G_\omega f_r \tag{2.90}$$

$$f_r = \max \left(0, \tilde{f}_r \right) \tag{2.91}$$

$$\tilde{f}_r = \max \left[\min \left(f_{cc}, 1.25 \right), 0 \right] \tag{2.92}$$

$$f_{cc} = (1 + c_{r1}) \frac{2r^*}{1 + r^*} \left[1 - c_{r3} \tan^{-1} \left(c_{r2} \tilde{r} \right) \right] - c_{r1} \tag{2.93}$$

$$r^* = \frac{S}{\Omega} \tag{2.94}$$

$$\tilde{r} = \frac{DS_{ij}}{Dt} \frac{2}{\tilde{D}} \Omega_{ik} S_{jk} \tag{2.95}$$

$$\Omega = \sqrt{2\Omega_{ij}\Omega_{ij}} \tag{2.96}$$

44

$$\Omega_{ik} = \frac{1}{2}\left(\frac{\partial u_i}{\partial x_j} - \frac{\partial u_j}{\partial x_i}\right) \tag{2.97}$$

$$\tilde{D} = \Omega D^3 \tag{2.98}$$

$$D = \sqrt{\max\left(S^2, 0.09\omega^2\right)} \tag{2.99}$$

$$c_{r1} = 1.0 \tag{2.100}$$

$$c_{r2} = 2.0 \tag{2.101}$$

$$c_{r3} = 1.0 \tag{2.102}$$

where Ω is the modulus of the vorticity tensor, Ω_{ij}. Note that the preceding formulation does not include terms to account for system reference frame rotation [5] since this research will not include such rotation.

The dissipation of K due to turbulence, Y_K, is

$$Y_K = \rho\beta^* K\omega \tag{2.103}$$

The dissipation of ω due to turbulence, Y_ω, is

$$Y_\omega = \rho\beta_i\omega^2 \tag{2.104}$$

where β_i is

$$\beta_i = F_1\beta_{i,1} + (1 + F_1)\beta_{i,2} \tag{2.105}$$

Note that the preceding definition does not include a compressibility correction, which has been shown to apply primarily to low-Reynolds-number, strained homogeneous flows [61].

The cross-diffusion blending function arises from the transformation of the $K - \varepsilon$ model into a form based on K and ω—namely

$$D_\omega = 2\left(1 - F_1\right)\rho\frac{1}{\omega\sigma_{\omega,2}}\frac{\partial K}{\partial x_j}\frac{\partial \omega}{\partial x_j} \tag{2.106}$$

2.8.9 Reynolds Stress Model.

The Boussinesq approximation assumes a linear relationship between the Reynolds-stress tensor and the mean strain rate of the flow. However, if a flow is subject to a sudden

change in mean strain rate, the instantaneous Reynolds stresses will adjust to the changes at a rate unrelated to the mean flow. The same is true for the contrasting situation—a flow subjected to sudden changes in dilation, off-axis straining, or curvature will result in unequal normal Reynolds stresses (anisotropic flow). Due to the complex flow path of the nozzles in this research, the following situations are expected to be present in the flow and are situations were the Boussinesq approximation (and thus first-order closure models) are not appropriate [61]:

- flow over curved surfaces

- flow in ducts with secondary motions

- three-dimensional flows

Therefore, the FRANS equations must be closed by a different manner. One method is to directly solve transport equations for each of the Reynolds stresses, together with an equation for the dissipation rate. This method is called a Reynolds Stress Model. Because $\bar{\bar{\tau}}_{ij}$ is a symmetric tensor, RSMs solve an addition seven transport equations for a three-dimensional problem (six Reynolds stresses and one length scale), which is why RSMs are sometimes referred to as seven-equation turbulence models. They are also referenced as belonging to the class of *second-order closures*.

Taking higher moments of the Navier-Stokes equations yields the exact form of the transport equation of the Reynolds stresses, shown below in compressible form. For the sake of convenience and convention, the Favre-averaging symbology as been discarded for general averaging nomenclature but is assumed:

$$\frac{\partial}{\partial t}\left(\rho\overline{u_i'u_j'}\right) + \frac{\partial}{\partial x_k}\left(\rho u_k\overline{u_i'u_j'}\right) = -\frac{\partial}{\partial x_k}\left[\rho\overline{u_i'u_j'u_k'} + \overline{P\left(\delta_{kj}u_i' + \delta_{ik}u_j'\right)}\right] + \frac{\partial}{\partial x_k}\left[\mu\frac{\partial}{\partial x_k}\left(\overline{u_i'u_j'}\right)\right]$$
$$- \rho\left(\overline{u_i'u_k'}\frac{\partial u_j}{\partial x_k} + \overline{u_j'u_k'}\frac{\partial u_i}{\partial x_k}\right) + \overline{P\left(\frac{\partial u_i'}{\partial x_j} + \frac{\partial u_j'}{\partial x_i}\right)} - 2\mu\overline{\frac{\partial u_i'}{\partial x_k}\frac{\partial u_j'}{\partial x_k}}$$

$$(2.107)$$

46

Each term in Equation 2.107 is defined as follows and should be understood as applying to the Reynolds stresses, not the bulk flow (e.g., "Convection" is "Convection of the Reynolds stresses") [5]:

- $\frac{\partial}{\partial t}\left(\rho \overline{u_i' u_j'}\right) \longrightarrow$ Local Time Derivative

- $\frac{\partial}{\partial x_k}\left(\rho u_k \overline{u_i' u_j'}\right) \longrightarrow$ Convection, C_{ij}

- $\frac{\partial}{\partial x_k}\left[\rho \overline{u_i' u_j' u_k'} + \overline{P\left(\delta_{kj} u_i' + \delta_{ik} u_j'\right)}\right] \longrightarrow$ Turbulent Diffusion, $D_{T,ij}$

- $\frac{\partial}{\partial x_k}\left[\mu \frac{\partial}{\partial x_k}\left(\overline{u_i' u_j'}\right)\right] \longrightarrow$ Molecular Diffusion, $D_{L,ij}$

- $-\rho\left(\overline{u_i' u_k'}\frac{\partial u_j}{\partial x_k} + \overline{u_j' u_k'}\frac{\partial u_i}{\partial x_k}\right) \longrightarrow$ Stress Production, P_{ij}

- $\overline{P\left(\frac{\partial u_i'}{\partial x_j} + \frac{\partial u_j'}{\partial x_i}\right)} \longrightarrow$ Pressure Strain, ϕ_{ij}

- $2\mu \overline{\frac{\partial u_i'}{\partial x_k}\frac{\partial u_j'}{\partial x_k}} \longrightarrow$ Viscous Dissipation, ε_{ij}

While C_{ij}, $D_{L,ij}$, and P_{ij} can be computed directly, $D_{T,ij}$, ϕ_{ij}, and ε_{ij} must be modeled to close the equations. The modeling assumptions for these terms are the subject of many second-order closure models. The current effort uses the Stress-ω model of Wilcox [61]. The following sections describe how the Reynolds stress equation is closed using the Stress-ω model.

A simplified version of the generalized gradient-diffusion model of Daly and Harlow can be used to reduce numerical instabilities by applying a scalar turbulent diffusivity [5]:

$$D_{T,ij} = \frac{\partial}{\partial x_k}\left(\frac{\mu_t}{\sigma_k}\frac{\partial \overline{u_i' u_j'}}{\partial x_k}\right) \tag{2.108}$$

where σ_K is given a value of 0.82, which is different from the blending function used in the $K-\omega$ SST model. The turbulent eddy viscosity, μ_t, is computed in the same manner as the standard two-equation $K-\omega$ model:

$$\mu_t = \alpha^* \frac{\rho K}{\omega} \tag{2.109}$$

47

where α^* is defined the same as for the $K - \omega$ SST model in Equations 2.53-2.57 with $Re_K = 12$.

The pressure strain term, ϕ_{ij} is modeled as

$$\phi_{ij} = -\rho\omega C_1 \beta_{RSM}^* \left(\overline{u_i' u_j'} - \frac{2}{3}\delta_{ij}K\right) - \hat{a}\left(P_{ij} - \frac{1}{3}P_{kk}\delta_{ij}\right) -$$
$$\hat{\beta}\left(D_{ij} - \frac{1}{3}P_{kk}\delta_{ij}\right) - K\hat{\gamma}\left(S_{ij} - \frac{1}{3}S_{kk}\delta_{ij}\right) \quad (2.110)$$

The necessary closures and constants are

$$C_1 = 1.8\left(\frac{5/3 + Re_t/Re_K}{1 + Re_t/Re_K}\right) \quad (2.111)$$

$$\beta_{RSM}^* = \beta^* f_{\beta^*} \quad (2.112)$$

$$f_{\beta^*} = \begin{cases} 1 & \chi_K \leq 0 \\ \frac{1+640\chi_K^2}{1+400\chi_K^2} & \chi_K > 0 \end{cases} \quad (2.113)$$

$$\chi_K = \frac{1}{\omega^3}\frac{\partial K}{\partial x_j}\frac{\partial \omega}{\partial x_j} \quad (2.114)$$

$$\hat{a} = \frac{1 + \hat{a}_0 Re_t/Re_K}{1 + Re_t/Re_K} \quad (2.115)$$

$$\hat{a}_0 = \frac{8 + C_2}{11} \quad (2.116)$$

$$C_2 = 0.52 \quad (2.117)$$

$$\hat{\beta} = \hat{\beta}_0 \frac{Re_t/Re_K}{1 + Re_t/Re_K} \quad (2.118)$$

$$\hat{\beta}_0 = \frac{8C_2 - 2}{11} \quad (2.119)$$

$$D_{ij} = -\rho\left(\overline{u_i' u_m'}\frac{\partial u_m}{\partial x_j} + \overline{u_j' u_m'}\frac{\partial u_m}{\partial x_i}\right) \quad (2.120)$$

$$K = \frac{1}{2}\overline{u_i' u_i'} \quad (2.121)$$

$$\hat{\gamma} = \hat{\gamma}_0 \frac{0.007 + Re_t/Re_K}{1 + Re_t/Re_K} \quad (2.122)$$

$$\hat{\gamma}_0 = \frac{60C_2 - 4}{55} \quad (2.123)$$

where D_{ij} is the diffusion tensor, and K is computed directly (as opposed to being modeled by a transport equation as in the $K - \omega$ SST model). S_{ij} and β^* are defined the same

as in Equations 2.60 and 2.76-2.77, respectively, with $Re_\beta = 12$. Equations 2.110-2.123 are the low-Reynolds formulation of the pressure strain term with the inclusion of viscous damping.

The dissipation tensor, ε_{ij}, is modeled as

$$\varepsilon_{ij} = \frac{2}{3}\delta_{ij}\rho\beta^*_{RSM}K\omega \tag{2.124}$$

The transport equation for ω is computed similarly to the $K - \omega$ SST described above but without the cross-diffusion blending term so that it is equivalent to the standard $K - \omega$ model [61].

III. Methodology

This chapter first discusses the isentropic flow analysis used to size the two sections of the exhaust stream and compute boundary condition inputs to the CFD code. Next, a discussion of the nozzle design iterations performed during this research to arrive at the final set of geometries is presented. Aspects of the final design are then examined. Grid generation methods and techniques, to include grid convergence, are considered next. Then, specific computational methods are discussed. Finally, parameters used to characterize hot streak phenomena are given, including the introduction of a modified Dean number.

3.1 Sizing the Turbofan Sections

Table 3.1 lists the inputs to this research effort. The values are based on a notional cruise flight condition and power setting at 20,000 ft for an F110 engine. The first section of Table 3.1 gives dimensions of the nozzle entrance section. The second section shows thermodynamic properties of the flow leaving the turbine and thus act as boundary conditions to the CFD simulation. The third section lists fluid properties of the two streams with the fuel assumed to be a simplified form of JP-8. In the next section, the information in the table is used to compute the radius of the core section at the nozzle entrance (Station 15) and the resulting mass flow split.

3.1.1 Gas Properties of Core Flow.

The gas properties of the core flow are calculated according to [57]. It is assumed that complete combustion occurs upstream of the nozzle entrance; therefore, the core flow is comprised of combustion products. If the fuel is assumed to be a simple hydrocarbon, the general reaction equation for complete combustion is
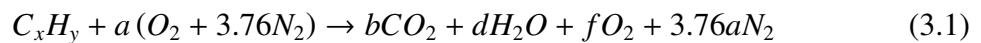
$$C_xH_y + a\,(O_2 + 3.76N_2) \rightarrow bCO_2 + dH_2O + fO_2 + 3.76aN_2 \tag{3.1}$$

Table 3.1: Given/Assumed Parameters

Parameter	Value in SI Units	Value in English Units
D, Outer Diameter	0.9906 m	39 in
D_t, Tailcone Diameter	0.4318 m	17 in
t_l, Liner Thickness	1.016×10^{-3} m	0.04 in
M_5, Mach Number	0.3	0.3
$T_{t,5}$, Core Total Temperature	977.59 K	1,300°F
$T_{t,15}$, Bypass Total Temperature	401.04 K	264°F
$P_{t,5}$, Core Total Pressure	213,737.48 N/m^2	31 psia
$P_{t,15}$, Bypass Total Pressure	213,737.48 N/m^2	31 psia
γ_5, Ratio of Specific Heats, Core	1.315	1.315
γ_{15}, Ratio of Specific Heats, Bypass	1.395	1.395 [62]
BPR, Bypass Ratio	0.8	0.8
ϕ, Equivalence Ratio	0.5	0.5
R_{air}, Gas Constant, Air	287.04 m^2/(s^2 K)	1,716.49 ft lb-f/slug °R
R_u, Gas Constant, Universal	8,314.32 (g m^2)/(s^2 mol K)	1,545.35 ft lb-f/°R lb-mol

Assuming the chemical formula of JP-8 is a form of kerosene ($C_{11}H_{21}$), the pre-multipliers representing the number of moles of each molecule are

$$a = \frac{x + y/4}{\phi} = 32.5 \tag{3.2}$$

$$b = x = 11 \tag{3.3}$$

$$d = \frac{y}{2} = 10.5 \tag{3.4}$$

$$f = (1 - \phi)(x + y/4) = 16.25 \tag{3.5}$$

where x is the number of carbon atoms and y is the number of hydrogen atoms in a molecule of the hydrocarbon fuel. From Equation 3.1, the total number of moles of combustion products is

$$N_{prod} = b + d + f + 3.76a = 159.95 \tag{3.6}$$

Individual mole fractions can then be found:

$$\chi_{CO_2} = b/N_{prod} = 0.0688 \tag{3.7}$$

$$\chi_{H_2O} = d/N_{prod} = 0.0656 \tag{3.8}$$

$$\chi_{O_2} = f/N_{prod} = 0.1016 \tag{3.9}$$

$$\chi_{N_2} = (3.76a)/N_{prod} = 0.7640 \tag{3.10}$$

Therefore, in the core section the composition of the fluid differs from that of air by the inclusion of about 14% hydrocarbons (CO_2 and H_2O) and the subsequent reduction in percentage of air components (O_2 and N_2). The molar mass of each product of combustion is given in Table 3.2. Using this information, the total molar mass of the combustion products is

$$\mathcal{M}_{prod} = \chi_{CO_2}\mathcal{M}_{CO_2} + \chi_{H_2O}\mathcal{M}_{H_2O} + \chi_{O_2}\mathcal{M}_{O_2} + \chi_{N_2}\mathcal{M}_{N_2} = 28.86 \ g/mol \tag{3.11}$$

and the gas constant for the combustion products is

$$R_{prod} = R_u/\mathcal{M}_{prod} = 288.07 \ m^2/\left(s^2 K\right) \tag{3.12}$$

Table 3.2: Molar Mass of Combustion Products

Molecule	Molar Mass
$\mathcal{M}_{CO_2}$	44 g/mol
$\mathcal{M}_{H_2O}$	18 g/mol
$\mathcal{M}_{O_2}$	32 g/mol
$\mathcal{M}_{N_2}$	28 g/mol

Thus, the molar mass and gas constant of the combustion products differ from that of air by only 0.35% due to the leanness of the mixture. At the mixing plane, the influence of combustion products on the composition of the fluid in the nozzle is further diluted due to the presence of bypass air. While the analysis in the following section will use the combustion products properties for sizing the core section, the difference in the resulting radius from using air is small (0.06%). This research effort will simplify the CFD simulations for such a lean mixture by using air as the working fluid in both sections. The effect of this simplification on the fluid properties of the exhaust gas is observed through examination of the Prandtl number, a non-dimensional parameter relating the momentum diffusivity to the thermal diffusivity:

$$Pr = \frac{C_P \mu}{k} \tag{3.13}$$

where C_P is the specific heat, μ is the dynamic viscosity, and k is the thermal conductivity. Table 3.3 [4] gives the Prandtl number for each combustion product and air at entrance conditions. The Prandtl number using air in both sections is computed using the BPR, and the Prandtl number for the mixture is computed using the mole fractions in Equations 3.7-3.10. The difference in Prandtl number for the mixture versus air is only 1.1%. The effects of simplifying the fluid mixture can be investigated in future research efforts (see Chapter

53

5). The simplification reduces computational time and resources required by eliminating the need to solve four additional species transport equations.

Table 3.3: Prandtl Number of Combustion Products and Air

Component	Prandtl Number
Air	0.714 (bypass)
	0.730 (core)
CO_2	0.723
H_2O	0.890
O_2	0.733
N_2	0.736
Pr_{mix}	0.731
Pr_{air}	0.723

3.1.2 Density Calculations.

The total density for each section is calculated using the ideal gas law:

$$\rho_{t,5} = \frac{P_{t,5}}{R_{mix} \cdot T_{t,5}} = 0.759 \frac{kg}{m^3} \tag{3.14}$$

$$\rho_{t,15} = \frac{P_{t,15}}{R_{air} \cdot T_{t,5}} = 1.857 \frac{kg}{m^3} \tag{3.15}$$

The static densities are found by isentropic relations:

$$\rho_{st,5} = \frac{\rho_{t,5}}{\left(1 + \frac{\gamma_5 - 1}{2}M^2\right)^{\frac{1}{\gamma_5 - 1}}} = 0.726 \frac{kg}{m^3} \tag{3.16}$$

$$\rho_{st,15} = \frac{\rho_{t,15}}{\left(1 + \frac{\gamma_{15} - 1}{2}M^2\right)^{\frac{1}{\gamma_{15} - 1}}} = 1.776 \frac{kg}{m^3} \tag{3.17}$$

3.1.3 Speed of Sound Calculations.

The static speed of sound for each section is found using [62]:

$$a_{st,5} = \sqrt{\frac{(R_{mix} \cdot T_{t,5} \cdot \gamma_5) / (\gamma_5 - 1)}{(M^2/2) + (\gamma_5 - 1)^{-1}}} = 604.3 \, m/s \tag{3.18}$$

$$a_{st,15} = \sqrt{\frac{(R_{air} \cdot T_{t,15} \cdot \gamma_{15}) / (\gamma_{15} - 1)}{(M^2/2) + (\gamma_{15} - 1)^{-1}}} = 397.2 \, m/s \tag{3.19}$$

3.1.4 Mass Flow Calculations.

The mass flow of each section can be calculated by solving the following system of equations:

$$\dot{m} = \dot{m}_5 + \dot{m}_{15} \tag{3.20}$$

$$BPR = \frac{\dot{m}_{15}}{\dot{m}_5} \tag{3.21}$$

3.1.5 Annular Area and Core Radius Calculations.

The radius of the core section can be computed by applying continuity and adjusting the total mass flow to ensure the outer radius is equivalent to the given design constraint. The necessary flow areas required by the continuity equation are computed using

$$A_5 = \frac{\dot{m}_5}{\rho_{st,5} \cdot a_{st,5} \cdot M} \tag{3.22}$$

$$A_{15} = \frac{\dot{m}_{15}}{\rho_{st,15} \cdot a_{st,15} \cdot M} \tag{3.23}$$

$$A_t = \pi \, (D_t/2)^2 \tag{3.24}$$

The radii are then computed by

$$r_5 = \sqrt{\frac{A_5 + A_t}{\pi}} = 0.4240 \, m \tag{3.25}$$

$$r_{15} = \sqrt{\frac{A_{15} + A_5 + A_t}{\pi}} = 0.4953 \, m \tag{3.26}$$

It is this value of r_5 that is used to create the entrance section geometry shown in Figure 1.4. When the mass flow rate is iteratively adjusted to match the computed r_{15} to the given r_{15}, the result is

$$\begin{matrix} \dot{m} = 99 \, kg/s \\ BPR = 0.8 \end{matrix} \Rightarrow \begin{matrix} \dot{m}_5 = 55 \, kg/s \\ \dot{m}_{15} = 44 \, kg/s \end{matrix} \tag{3.27}$$

The liner is a thin wall with rectangular cross-section of thickness t_l. The tailcone shape is taken from an F110 engineering drawing. The length of the entrance section is D

to allow development of the boundary layer before the flow encounters a large amount of curvature at the termination of the tailcone, which aids in code stability by reducing pressure reflections at the boundary of the solution domain.

3.2 Nozzle Design

3.2.1 Build-Up Procedure .

The first attempted design was a build-up procedure, where downstream of the entrance section the nozzle included a straight transition section followed by a serpentine section of constant cross-sectional area and C-D section. The length of the transition section was chosen as $0.5D$ based on transition section lengths for modern straight nozzles used in current USAF aircraft. The cross-sectional shape at the exit of the transition section was chosen to be rectangular with highly curved edges. The radius of curvature was chosen to be a function of the height of the exit ($r = h/2$), so that the shape was equivalent to a rectangle with a semicircle at each end. The area ratio between the mixing plane and exit of the transition section was chosen as 1. Therefore, the shape of the transition exit plane (denoted as Station 7) can be defined completely by the *AR*:

$$A_7 = h^2 \left(\frac{\pi}{4} - 1 + AR \right) \tag{3.28}$$

Figure 3.1 shows the geometry of the transition section for $AR = 4$. Flow separation was expected based on Figures 2.2 and 2.1.

The length of the serpentine section was chosen as $4D$ so the nozzle represented the largest computational domain and an upper limit on grid generation requirements could be established. The C-D section was designed using compressible flow theory to determine the exit area, primary and secondary nozzle lengths, and primary and secondary nozzle angles. The resulting C-D section is shown in Figure 3.2. The complete build-up design is shown in Figure 3.3.
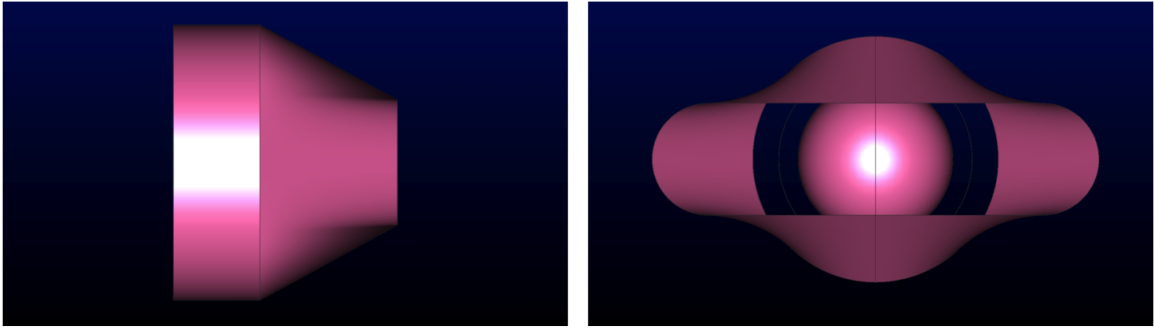
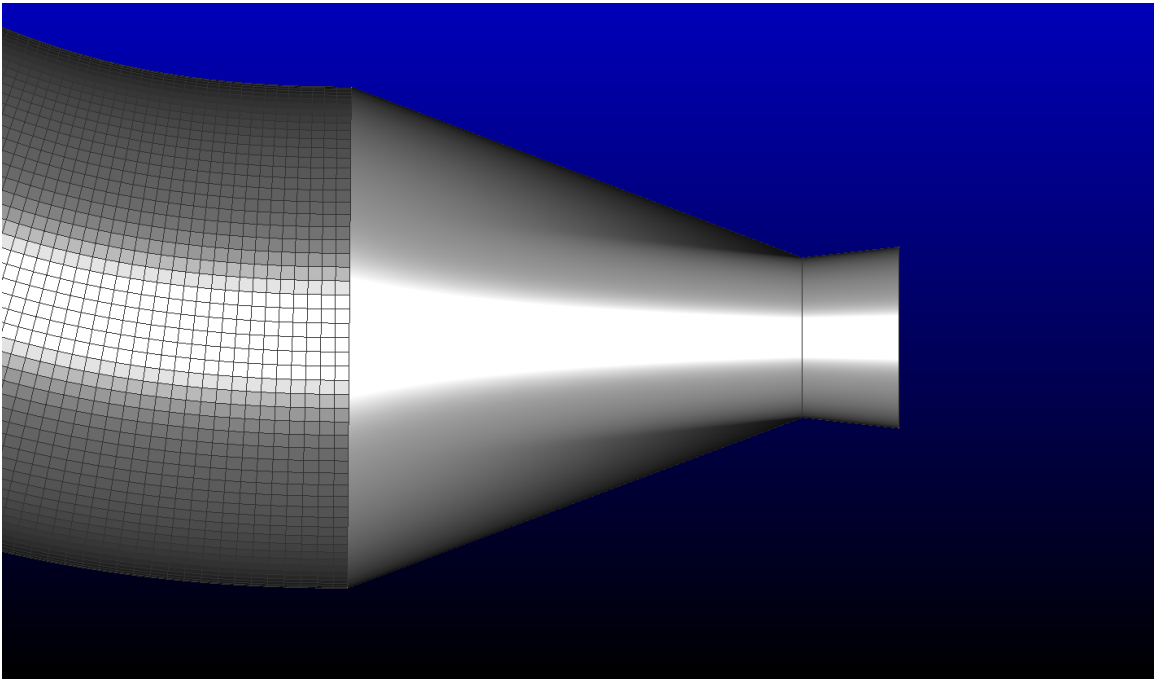Figure 3.1: Build-up transition section; $AR = 4$.

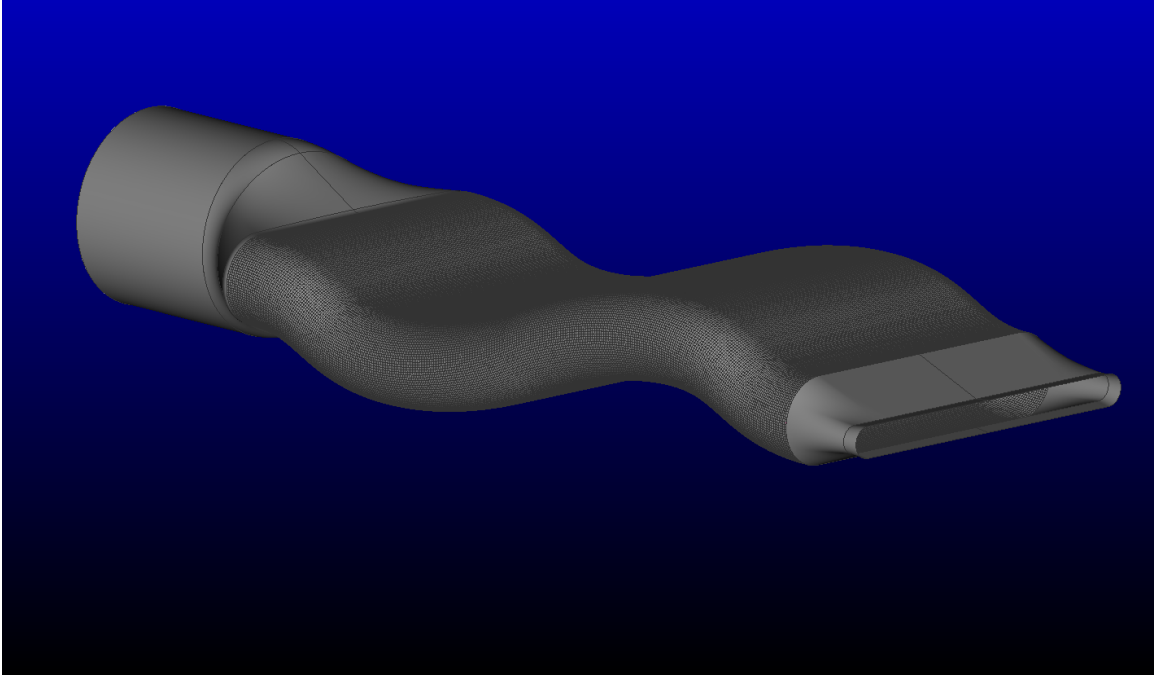Figure 3.2: Build-up C-D section.

Figure 3.3: Build-up nozzle design.

Preliminary first-order CFD simulations were performed using the methods described later in this chapter and the $K - \omega$ SST turbulence model described in Chapter 2. Large amounts of flow separation were observed in the transition section, as expected. The separation is shown via Mach contours through the horizontal center plane in Figure 3.4. The result of this separation was a pair of strong counter-rotating sidewall vortices, similar to those observed by previous researchers for the transition ducts described in Chapter 2. The vortices dominated the flow in the transition nozzle, as seen in the Mach contour slices shown in Figure 3.5. Another result of the build-up design was the rapid displacement of the bypass flow to the sidewalls due to the change in cross-sectional area. Since this displacement occurred in the presence of the flow separation, the cooler bypass flow tended to contain lower axial momentum than the core, remain at the sidewalls, and was little influenced by the nozzle curvature, as seen in Figure 3.6.
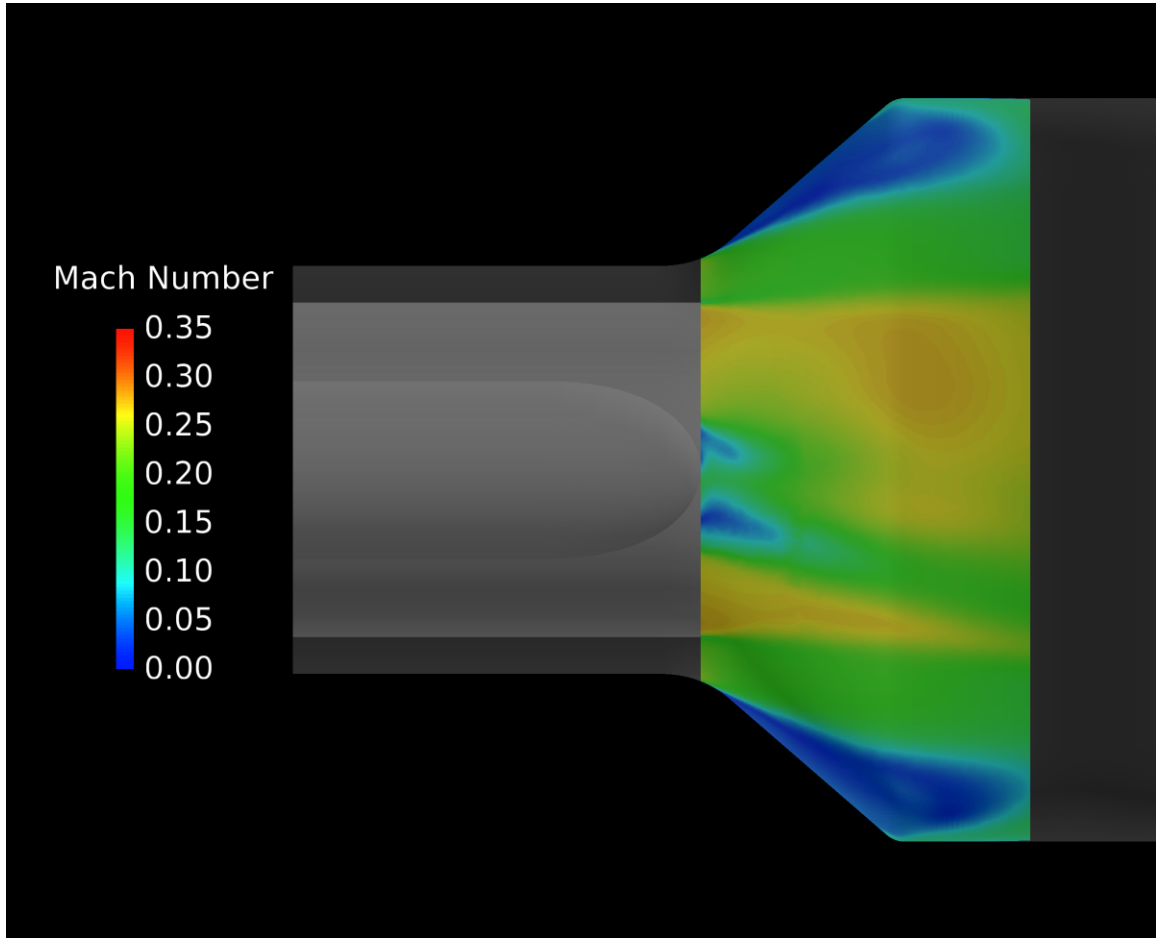
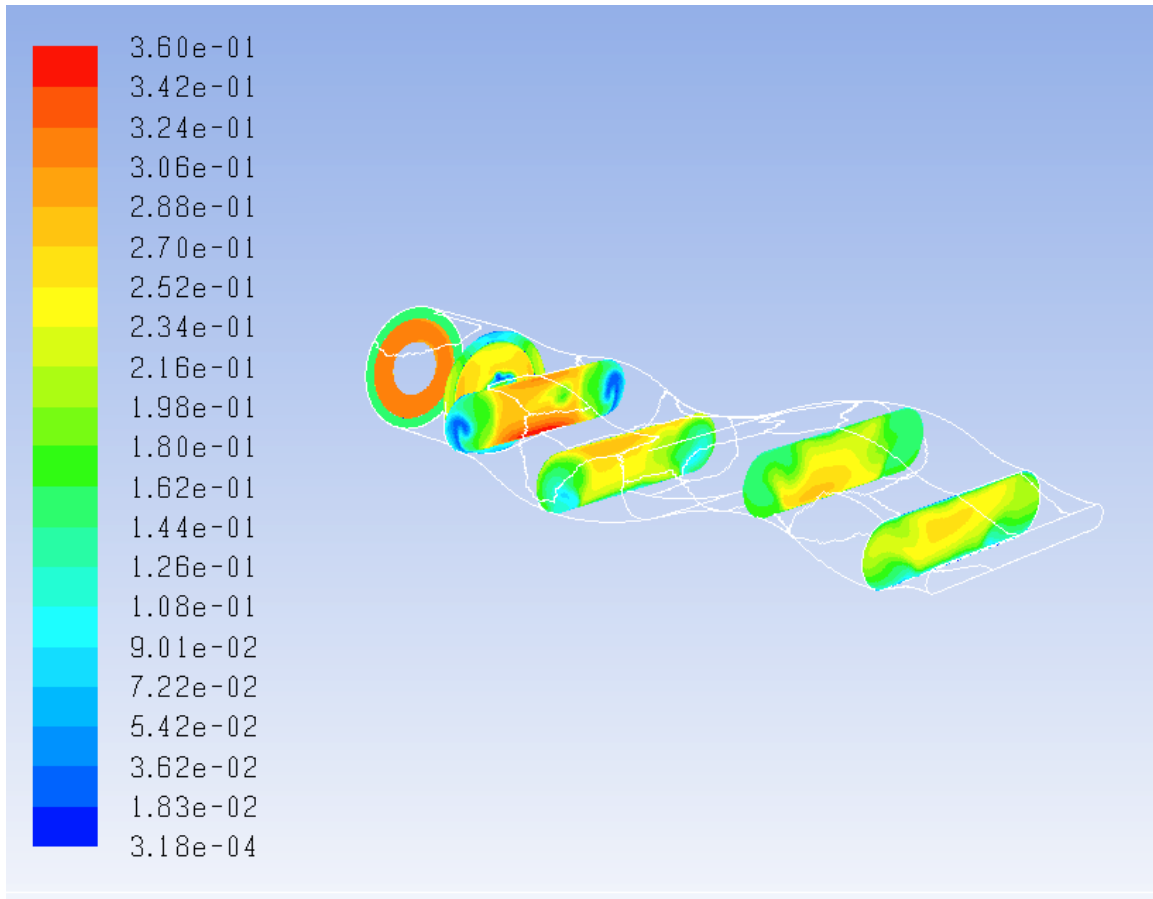Figure 3.4: Massive flow separation in the transition section.

3.60e-01	
3.42e-01	
3.24e-01	
3.06e-01	
2.88e-01	
2.70e-01	
2.52e-01	
2.34e-01	
2.16e-01	
1.98e-01	
1.80e-01	
1.62e-01	
1.44e-01	
1.26e-01	
1.08e-01	
9.01e-02	
7.22e-02	
5.42e-02	
3.62e-02	
1.83e-02	
3.18e-04	

Figure 3.5: Mach contours at various axial locations in the build-up nozzle.
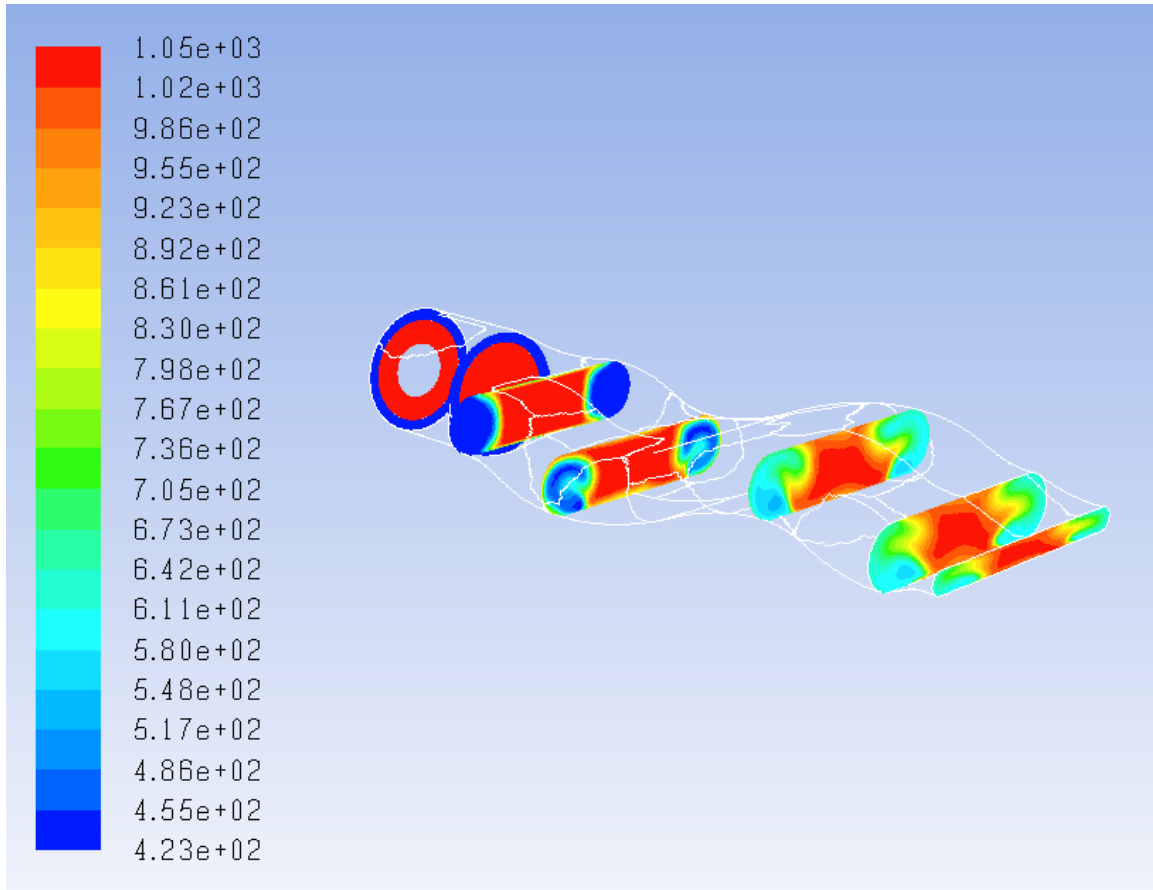
Figure 3.6: Total temperature contours at various axial locations in the build-up nozzle.

While the first-order solutions were informative as to the flow features and dominant behavior in the buildup nozzle, attempts to obtain second-order RSM solutions were unsuccessful. In the transition section, the turbulent viscosity ratio grew uncontrollably and caused the solution to diverge. This behavior, along with the observation that the transition section was driving the flow physics, resulted in reexamining the nozzle design to avoid the massive flow separation caused by the short transition section. The goal of next design iteration was to produce a nozzle more relevant to modern aircraft mission requirements, where the added length due to separating the transition, serpentine, and C-D sections of the build-up nozzle would degrade weapon system performance.

3.2.2 *Blended Design.*

The next design iteration is a blended nozzle, where downstream of the entrance section the nozzle transitions cross-sectional area while also experiencing changes to streamline curvature. The blended design allows for shorter nozzles and more gradual geometric changes when compared to the build-up design. Instead of a separate C-D section, the nozzle continuously converges to the throat, which has the same rectangular shape shown in Figure 3.1. Downstream of the throat, the nozzle expands to the exit in the vertical direction only, i.e., there is no lateral divergence of the nozzle between Stations 8 and 9. The exit shape is the same as the throat but scaled to the appropriate area. From discussions with nozzle design experts [6], it was recommended that the secondary nozzle angle (α_s) be limited to 7°. This limit comes from practical experience and the desire to reduce angularity losses. The divergent section is designed to be as short as possible while still meeting this criteria. Because L includes the length of the divergent section, the throat and exit areas must be computed first to determine the divergent section length. The rest of the nozzle can then be designed once the divergent section is sized.

The calculation of exit area required by isentropic relations is an iterative process. First, an initial guess for the exit total temperature is taken to be the mass flow-weighted

average total temperature at the mixing plane ($T_{t,9} = T_{t,6}$). The specific heat for this initial guess is used to calculate the ratio of specific heat and static temperature at the exit:

$$\gamma_9 = \frac{C_P}{C_P - R_{air}} \tag{3.29}$$

$$T_{st,9} = T_{t,6} \left(\frac{P_{st,9}}{P_{t,6}} \right)^{\frac{\gamma_9 - 1}{\gamma_9}} \tag{3.30}$$

where $P_{st,9}$ = 46,563.3 kg/(m s^2), the standard atmospheric pressure at 20,000 ft. The value of $T_{st,9}$ is used to find a new interpolated value of C_P from tabulated data [62]. The process is continued until $T_{st,9}$ does not vary between iterations. The final values are γ_9 = 1.39 and $T_{st,9}$ = 470.5 K. The exit area is then calculated using the following method:

$$a_9 = \sqrt{\gamma_9 R_{air} T_{st,9}} = 433.2 \ m/s \tag{3.31}$$

$$M_9 = \sqrt{\frac{2}{\gamma_9 - 1} \frac{P_{t,6}}{P_{st,9}}^{\left(\frac{\gamma_9 - 1}{\gamma_9} - 1 \right)}} = 1.65 \tag{3.32}$$

$$\rho_{st,9} = \frac{P_{st,9}}{R_{air} T_{st,9}} = 0.3447 \ kg/m^3 \tag{3.33}$$

$$A_9 = \frac{\dot{m}}{\rho_{st,9} a_9 M_9} = 0.4 \ m^2 \tag{3.34}$$

A similar iterative process is carried out for sonic throat conditions where $T_{t,8} = T_{t,6}$:

$$\gamma_8 = \frac{C_P}{C_P - R_{air}} = 1.375 \tag{3.35}$$

$$T_{st,8} = T_{t,8} \frac{2}{\gamma_8 + 1} = 607.438 \ K \tag{3.36}$$

$$\rho_{t,8} = \frac{P_{t,6}}{R_{air} T_{t,8}} = 1.032 \ kg/m^3 \tag{3.37}$$

$$\rho_{st,8} = \rho_{t,8} \frac{2}{(\gamma_8 + 1)^{\left(\frac{1}{\gamma_8 - 1} \right)}} = 0.6527 \ kg/m^3 \tag{3.38}$$

$$a_8 = \sqrt{\gamma_8 R_{air} T_{st,8}} = 489.7 \ m/s \tag{3.39}$$

$$A_8 = \frac{\dot{m}}{\rho_{st,8} a_8} = 0.31 \ m^2 \tag{3.40}$$

With A_8 and A_9 determined, the cross-sectional shapes can be created for each section. The width and height of the throat are found by solving the following system of equations:

$$A_8 = h_8^2 \left(\frac{\pi}{4} - 1 + AR \right) \tag{3.41}$$

$$AR = w_8 / h_8 \tag{3.42}$$

Since $w_8 = w_9$, the height at the exit can be computed directly using

$$A_9 = h_9^2 \left(\frac{\pi}{4} - 1 + \frac{w_9}{h_9} \right) \tag{3.43}$$

With the necessary heights and widths known, coordinates to create the throat and exit shapes can be easily determined. The length of the divergent section, l_{exit}, is found by

$$l_{exit} = \frac{(h_9 - h_8)/2}{\tan \alpha_s} \tag{3.44}$$

For ease of geometry creation, l_{exit} is set to 9 inches (0.2286 m) for $AR = 10$ and 15.6 inches (0.3962 m) for $AR = 4$ (with $\alpha_s = 6.7°$ and 6.5°, respectively). Because the $AR = 4$ nozzles are comparatively taller at the throat and exit than the $AR = 10$ nozzles, it is necessary to make l_{exit} comparatively longer to meet the α_s constraint. With l_{exit} defined, the remaining length for a given L/D is just $(L - l_{exit})$. It is this length that represents the design space for the blended portion of each nozzle. Therefore, the blended section of the $AR = 4$ nozzle will be 6.6 inches (0.1676 m) shorter than the $AR = 10$ nozzle.

The next design decision to be made is determining the serpentine shape along the four nozzle centerlines (upper, lower, port, and starboard). Two additional research inputs that inform this decision are a design that is down-first with a 0.5/0.5 offset, as shown in Figure 1.4. These design features necessitate the definition of two inflection points, shown in Figure 3.7, representing the denial of direct-line-of-sight into the hot section of the engine. These inflection points are equally spaced between the mixing plane and $(L - l_{exit})$. At the first inflection point, the lower centerline remains unchanged since the nozzle is down-first, while the upper centerline is placed at the axial centerline to satisfy the

first 0.5 offset requirement. At the second inflection point, the lower centerline is placed at the axial centerline to satisfy the second 0.5 offset requirement, while the upper centerline is placed vertically halfway between the entrance diameter and the axial centerline, or $D/4$. To facilitate lateral divergence of the nozzles from D to w_8, the coordinates of the lateral centerline are placed halfway between the upper and lower surfaces at each inflection point, as shown in Figure 3.8.
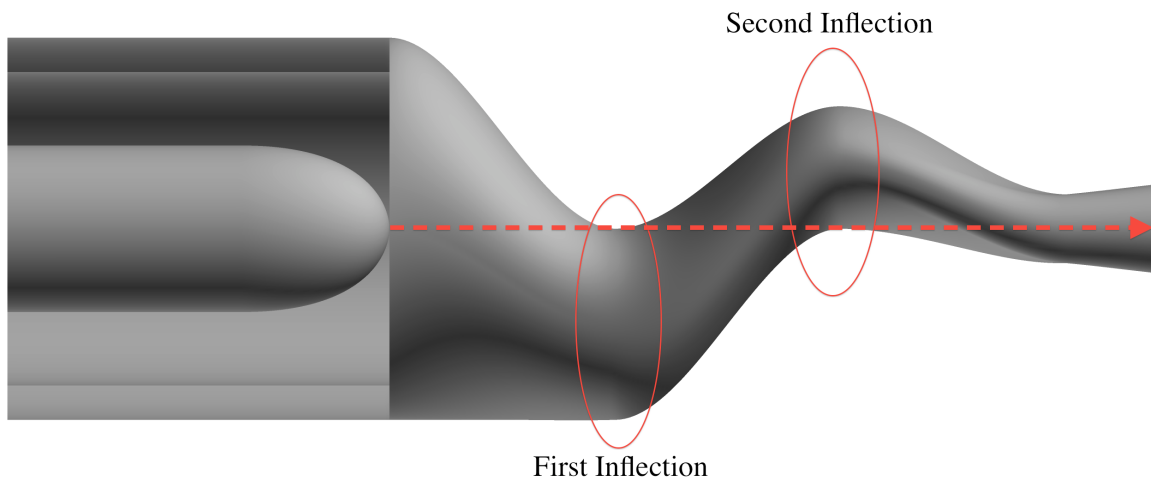

Figure 3.7: Nozzle inflection points providing denial of line-of-sight.

All centerlines are created using cubic Bézier curves (Figure 3.9) in a piecewise fashion. Each centerline is comprised of three curves to define three sections: entrance-to-first inflection, first inflection-to-second inflection, and second inflection-to-throat. The use of cubic Bézier curves allows for a smooth transition between sections and scalability between nozzle geometries via slope control of four control points [43]. Cubic Bézier curves are defined by these four points, as seen in Figure 3.9. The control points of each curve are chosen to ensure tangency with the entrance section and throat, and a smooth curve between sections.
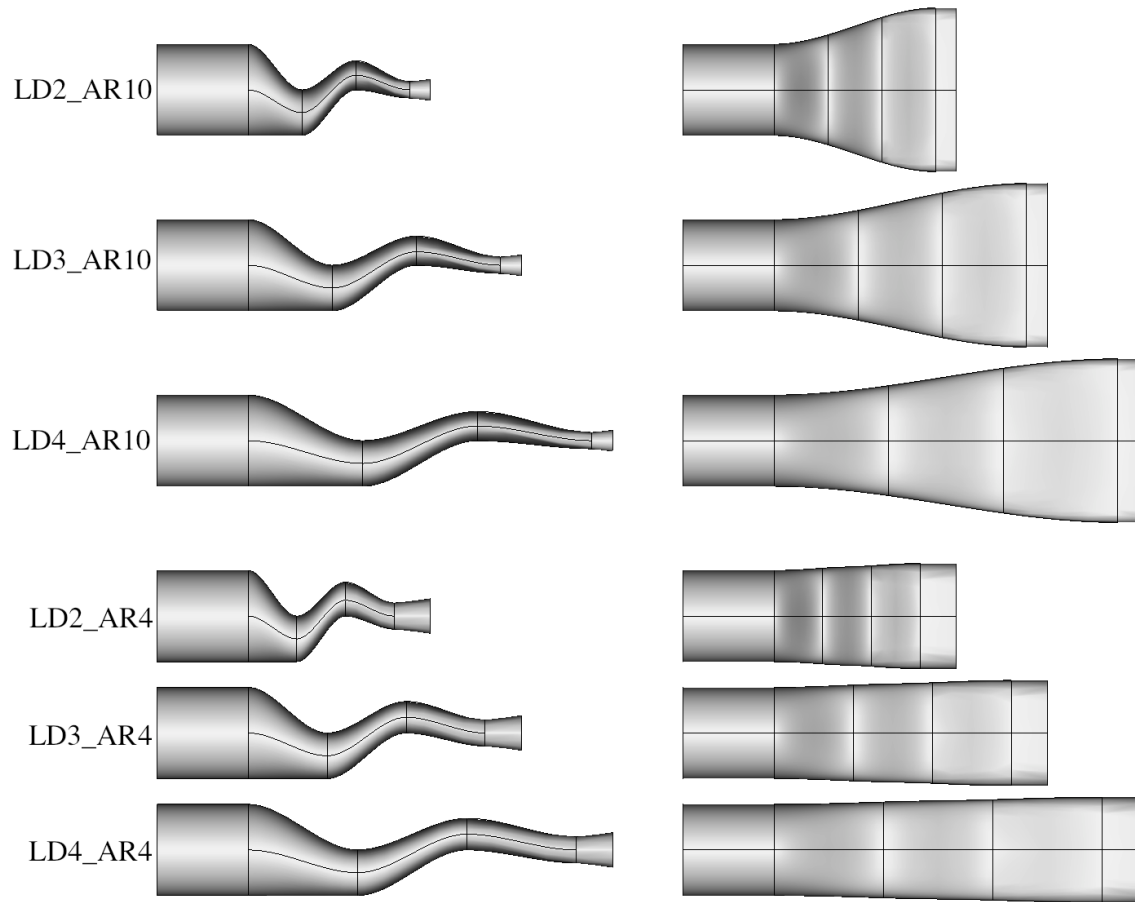
Figure 3.8: Nozzle geometries with Bézier design curves shown, side and top views.
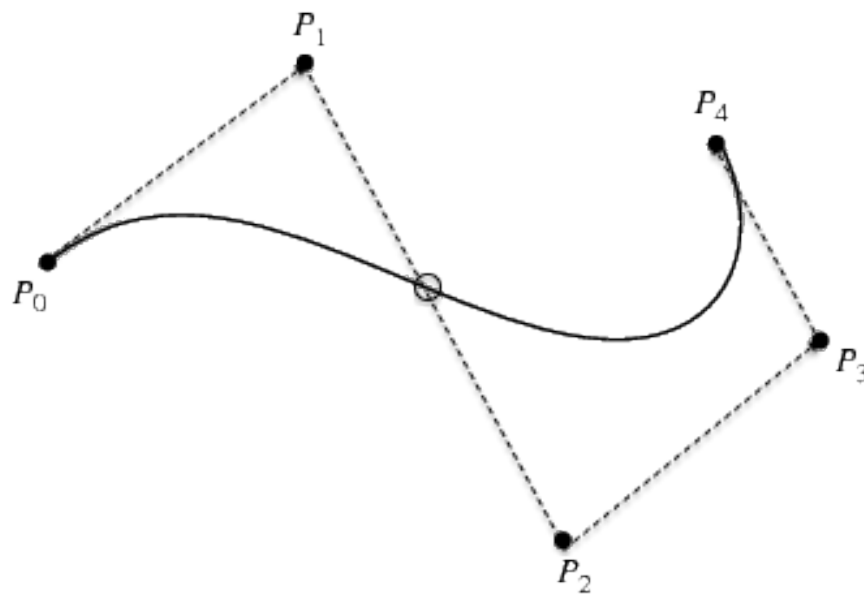

Figure 3.9: Generic Bézier curve with control points.

Surfaces are created between the curves using Coons patch manifolds to smoothly join each section [43]. All geometries were created using the commercial CFD grid generation software Pointwise. The resulting six geometries corresponding to Table 1.1 are shown in Figures 3.8 and 3.10. For the remainder of the document, each nozzle will be designated by "LDX_ARX", as shown in the figures.

Initial simulations proved to be much different than the build-up design, and second-order $K - \omega$ SST and RSM solutions were achieved. A grid convergence study was performed as described in Section 3.4. The solution at the finest grid level showed a strange feature. Wave-like structures formed between the throat and the exit of the nozzle, which was the exit of the solution domain. This phenomenon is seen in contours of total temperature through the horizontal mid-plane in Figure 3.11. Since the second-order methods used in this research tend to be dominated by numeric dispersion and not numeric dissipation [54], the source of this phenomenon was in establishing the exit of the computational domain as the nozzle exit (i.e., a completely internal flow). The pressure outlet boundary condition described in Section 3.5.4 was not compatible with supersonic flow at the exit, since the flow could not propagate numeric pressure corrections upstream of the throat due to the sonic condition. Thus a final design iteration was required to achieve successful simulations.

3.2.3   External Domain.

While the nozzle geometry did not change for the final design iteration, the computational domain was expanded to include a farfield bounding box containing quiescent flow. The bounding box allows for the exhaust flow to leave the nozzle in a physically realistic way. If the bounding box is far enough away from the nozzle exit the flow will not be supersonic, and the pressure outlet boundary condition can be appropriately applied. The bounding box for this research is shown in Figure 3.12 and has the following dimensions: $30D \times 25D \times 25D$. Generic outer mold lines (OML) around the nozzles were

LD2_AR10
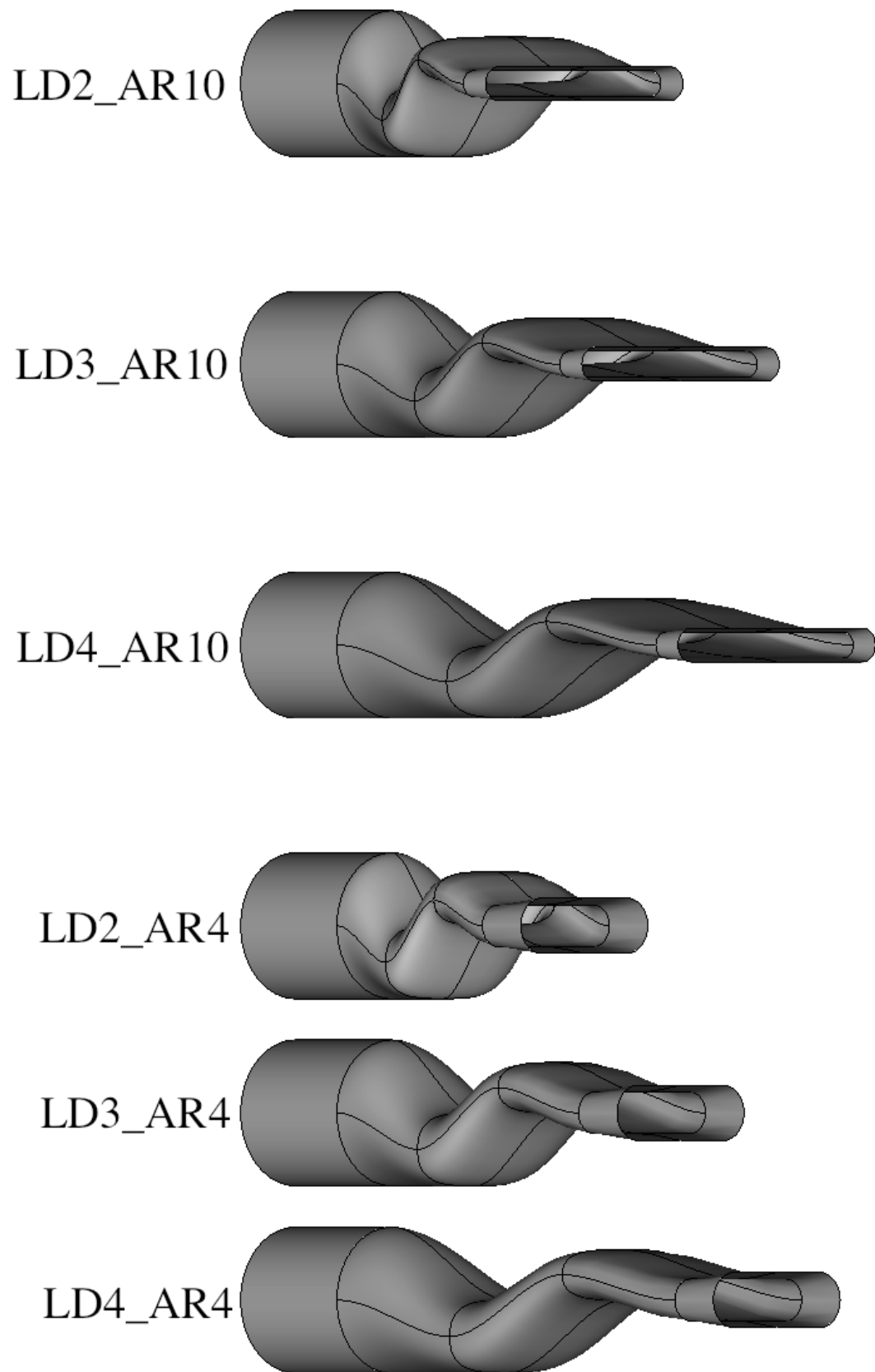
LD3_AR10

LD4_AR10

LD2_AR4

LD3_AR4

LD4_AR4

Figure 3.10: Nozzle geometries with Bézier design curves shown, rotated view.
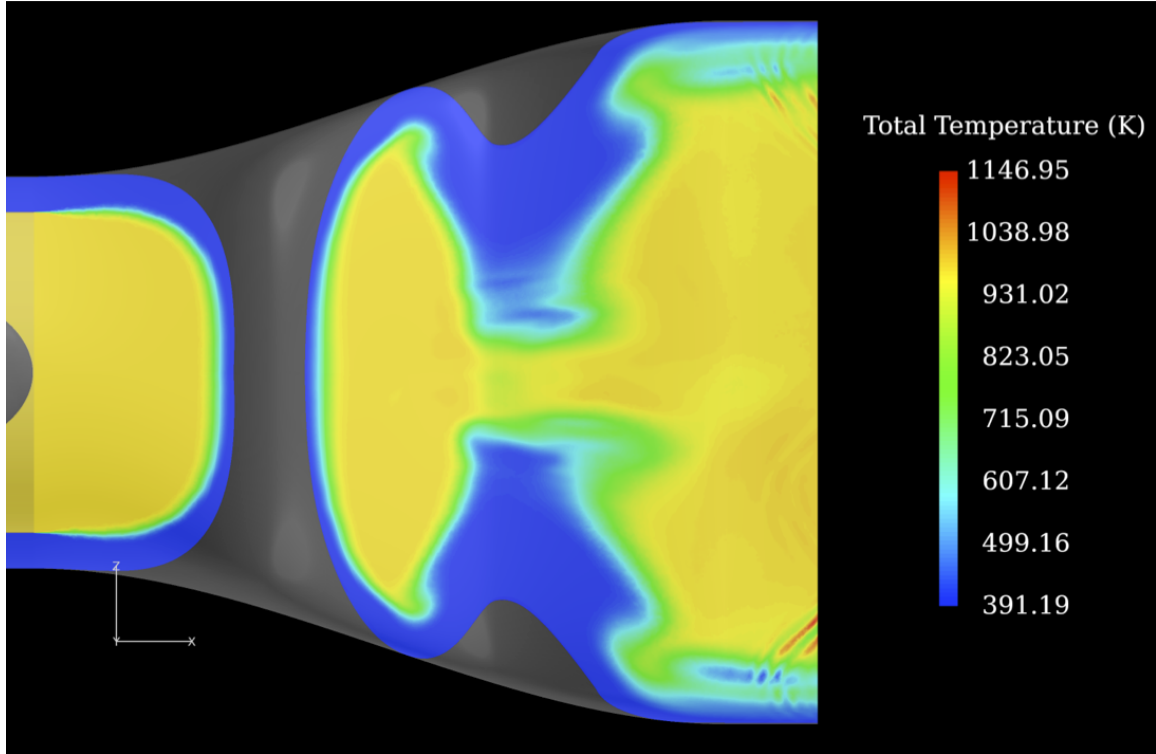
Figure 3.11: Wave-like phenomenon at exit of internal flow solution.

created due to the addition of the external flowfield and are shown in Figures 3.13 and 3.14. The OML begins as a circle of diameter $3D$ at the computational domain entrance and transitions cross-sectional area to match the rounded rectangle at the exit nozzle. The OML geometry was created in a similar fashion as the nozzles—using Bézier curves with tangent control points at the entrance and exit. Coons patches were used to generate the surface geometry. Initial simulations demonstrated a well-behaved flowfield. Therefore, this design is used for the remainder of the research. Next, methods for grid generation and performing grid convergence studies on this design are discussed.

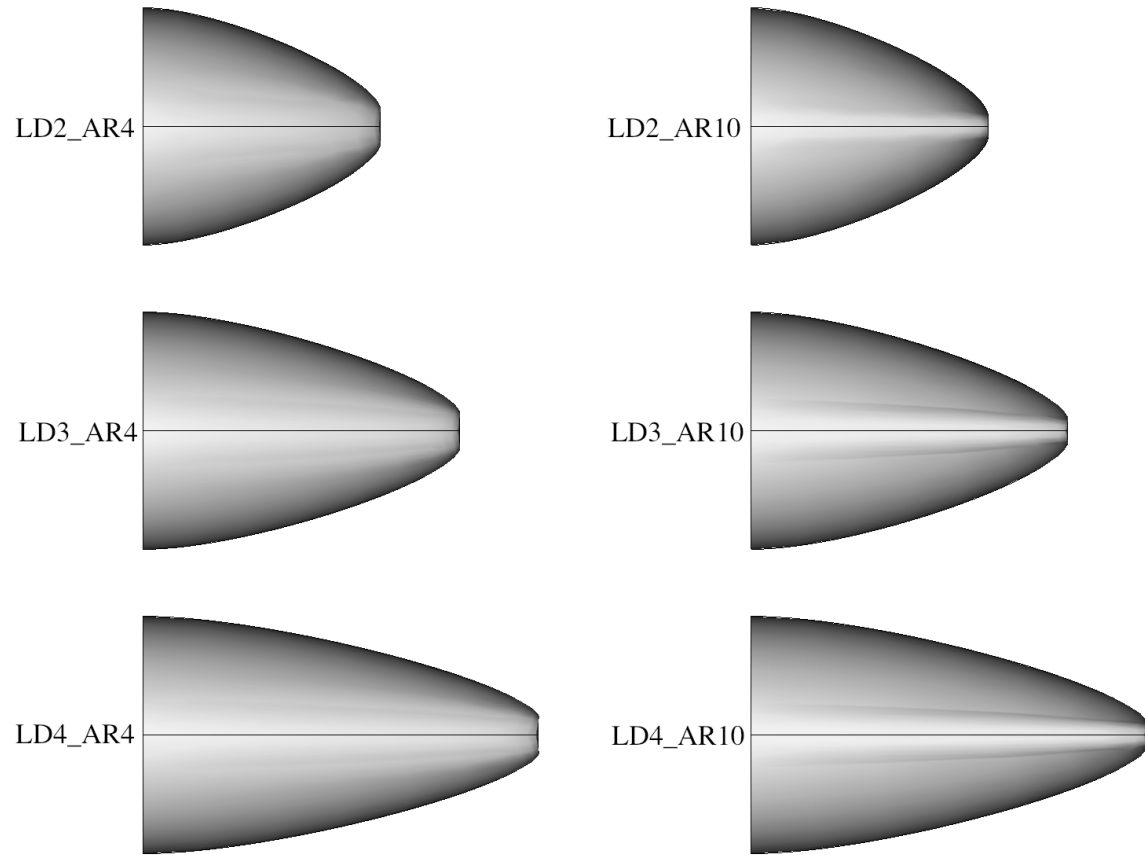Figure 3.12: External domain bounding box.

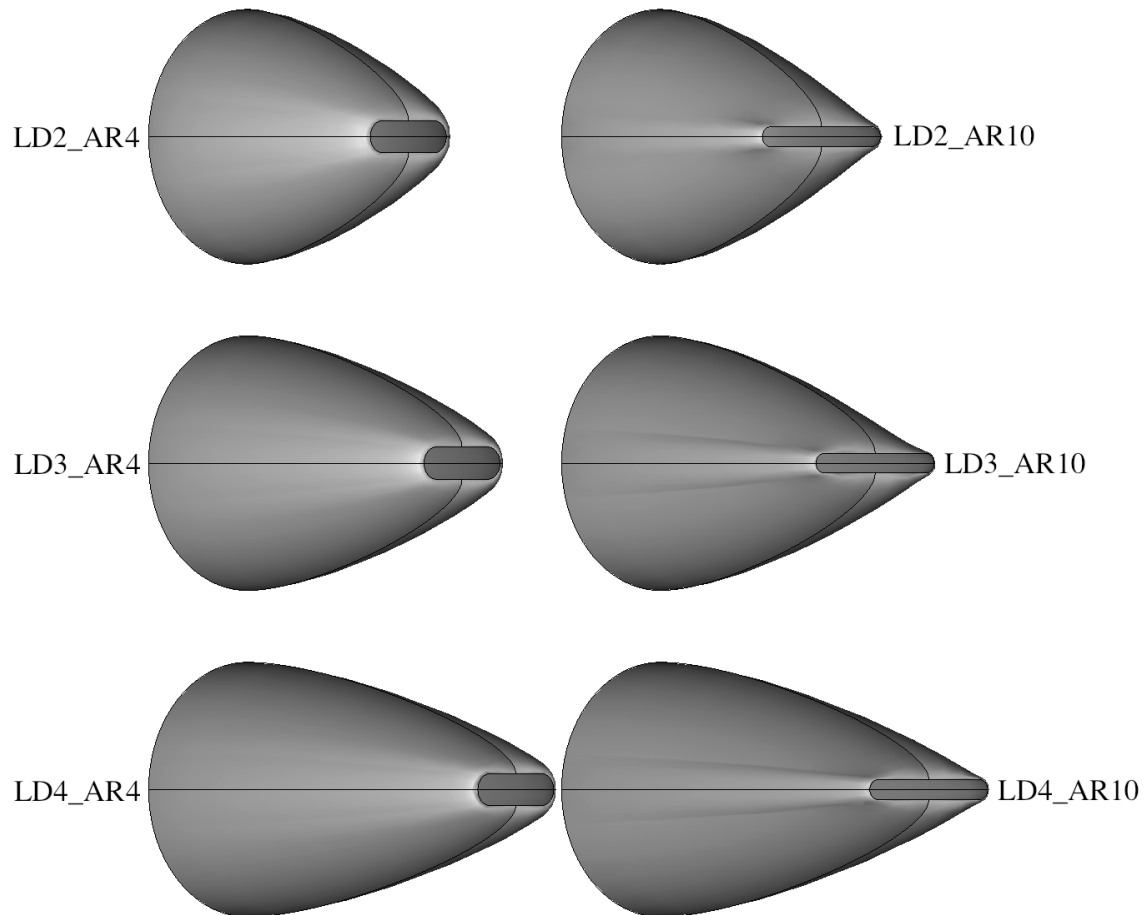Figure 3.13: OML geometries with Bézier design curves shown, side view.

Figure 3.14: OML geometries with Bézier design curves shown, rotated view.

3.3   Grid Generation

The solution domain is populated with computational grids generated by Pointwise. Hybrid grids are used in this research. Hybrid grids consist of tetrahedral, pyramidal, and hexahedral cells in the same solution domain. Hexahedral grids are used in the boundary layer because of their increased accuracy and stability in the bulk flow direction [8]. Even though secondary flow features will occur in or near the boundary layer, the streamwise component of the velocity vector will dominant the high subsonic and supersonic flow. In general, the solution will converge faster when the grid is aligned in the prominent flow direction. Grid alignment in the boundary layer is realized more easily with hexahedral grids, where high quality cells with high aspect ratios can be produced. It is also advantageous for the turbulence model near the wall to have a grid with easily definable transverse normals, which is more readily done with a hexahedral grid cell [15].

3.3.1   Boundary Layer Grids.

Because the boundary layer will experience high gradients due to viscous forces and secondary flow features, special care is taken in generating the boundary layer grids. The $K - \omega$ SST and Stress-ω form of the RSM turbulence model do not require the use of wall functions. Therefore, a non-dimensional wall distance (y^+) of 1 is desired for accurate calculation of boundary layer flows [60]. Prediction of the required first cell height off the wall can be performed with the following method. Values at the entrance section are used for the calculation. The actual y^+ value is calculated during the simulation to ensure it is 1 or less everywhere at the nozzle surface. The definition of y^+ is

$$y^+ = \frac{\rho U_\tau y}{\mu} \qquad (3.45)$$

where the desired cell height is y so that

$$y = \frac{y^+ \mu}{U_\tau \rho} \qquad (3.46)$$

73

The density and viscosity are known from Equations 3.17 and 2.35. The quantity U_τ is defined as

$$U_\tau = \sqrt{\frac{\tau_w}{\rho}} \tag{3.47}$$

where the wall shear stress, τ_w, is computed using

$$\tau_w = \frac{1}{2}C_f\rho U_\infty^2 \tag{3.48}$$

The freestream velocity is computed using Equation 3.18 or 3.19 and the entrance Mach number ($U_\infty = M_5 a$). The skin friction coefficient for internal flows is computed as

$$C_f = 0.079 Re_{D_h}^{-0.25} \tag{3.49}$$

where the Reynolds number based on hydraulic diameter is

$$Re_{D_h} = \frac{\rho U_\infty D_h}{\mu} \tag{3.50}$$

and the hydraulic diameter for each section is given by

$$D_{h,6} = 2r_5 - D_t \tag{3.51}$$

$$D_{h,16} = 2r_{15} - 2r_5 \tag{3.52}$$

The computed initial grid cell heights for each section are $y_6 = 9.09 \times 10^{-6}$ m and $y_{16} = 3.16 \times 10^{-6}$ m, with y_6 used in the boundary layer off the tailcone, and y_{16} used in the boundary layer off the liner and outer walls.

An estimate for the boundary layer height (δ) is needed to determine when to stop the extrusion of hexahedral cells from the surfaces. The $1/7^{th}$ power flat plate approximation is used to determine the boundary layer thickness at the mixing plane. The mixing plane was chosen as the plane of interest since it is the only straight section of the nozzle and thus is closest in form to a flat plate. While the boundary layer continues to grow through the nozzle, a majority of the boundary layer will be captured by the hexahedral cells. A smooth transition between hexahedral and tetrahedral cells ensures the gradients in the

outer portion of the boundary layer will be appropriately captured. The calculation of the boundary layer height for a flat plate uses the Reynolds number based on location downstream of the leading edge, or in this case the location of the mixing plane, x_{mp}:

$$Re_x = \frac{\rho U_\infty x_{mp}}{\mu} \tag{3.53}$$

$$\delta = 0.16 x_{mp} Re_x^{-1/7} \tag{3.54}$$

The computed boundary layer heights at the mixing plane for the core and bypass sections are $\delta_6 = 0.0187$ m and $\delta_{16} = 0.0160$ m. Several guidelines are used in the extrusion of the boundary layer grids [58]:

- The second cell height off the wall is equal to the first for accurate shear stress calculations.

- The growth rate is set to 1.2 in the first half of the boundary layer.

- The growth rate is set to 1 in the second half of the boundary layer to accurately capture gradients in the turbulent quantities.

A Fortran code was written to calculate the number of cells in each half of the boundary layer in order to determine when the extrusion method should switch growth rates.

3.3.2 Populating the Solution Domain with Tetrahedral Grid Cells.

After the boundary layer grids are generated, a single layer of pyramidal cells are created to transition between the hexahedral and tetrahedral cells. The solution domain is then populated with anisotropic tetrahedral cells. An advancing front technique is used with a growth rate of 1.2. The advancing front method results in a smoother transition between hexahedral and tetrahedral cells, so that large jumps in spacing are avoided. The advancing front terminates once isotropic tetrahedrons are achieved. The remainder of the solution domain is populated with tetrahedral cells using Delauney triangularization. An example of the hybrid topology at the mixing plane is given in Figures 3.15. The grid

spacing at the farfield bounding box boundaries is set to 9 inches (0.2286 m), which is h_9 for the $AR = 10$ nozzles. This rather large grid spacing facilitates a rapid coarsening of the external flowfield grid, as seen in Figure 3.16. A coarse external grid reduces the overall cell count dramatically and aids in solution stability by adding numeric dissipation to the solution in the exhaust plume region. Artificial dissipation of the plume is appropriate for this problem since the plume is not the focus of the research, and the supersonic exit plane will not be affected by grid resolution far downstream. The grid resolution of the external flowfield is shown in Figure 3.17.
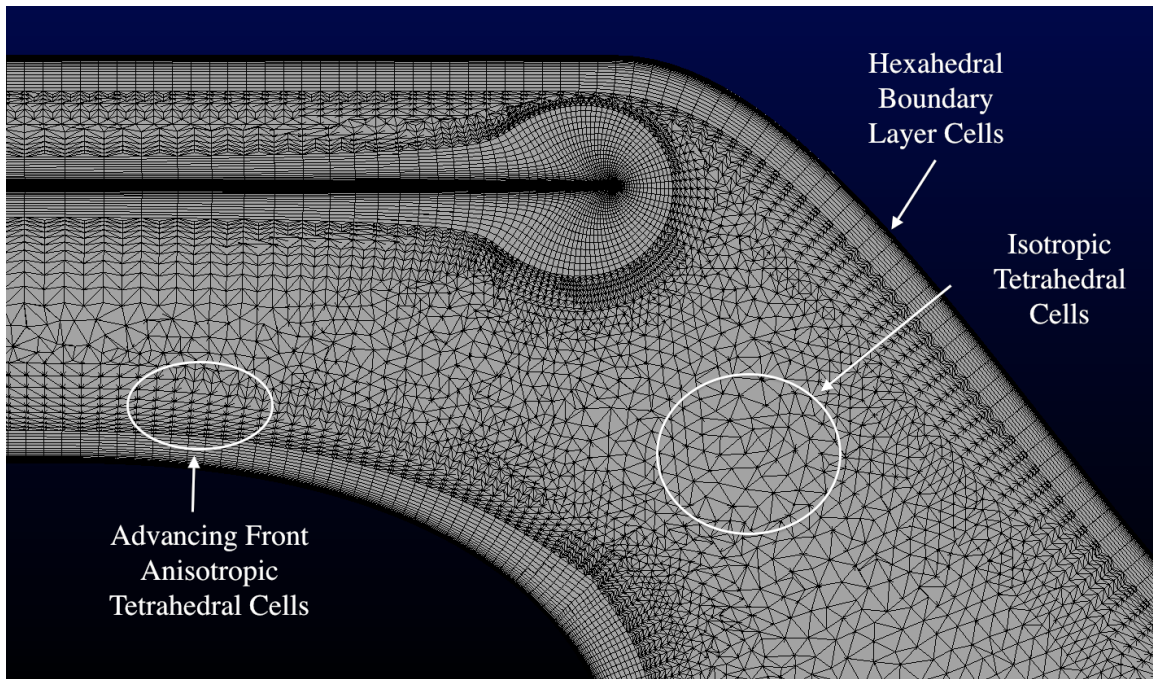
Figure 3.15: Hybrid grid topology at the mixing plane.
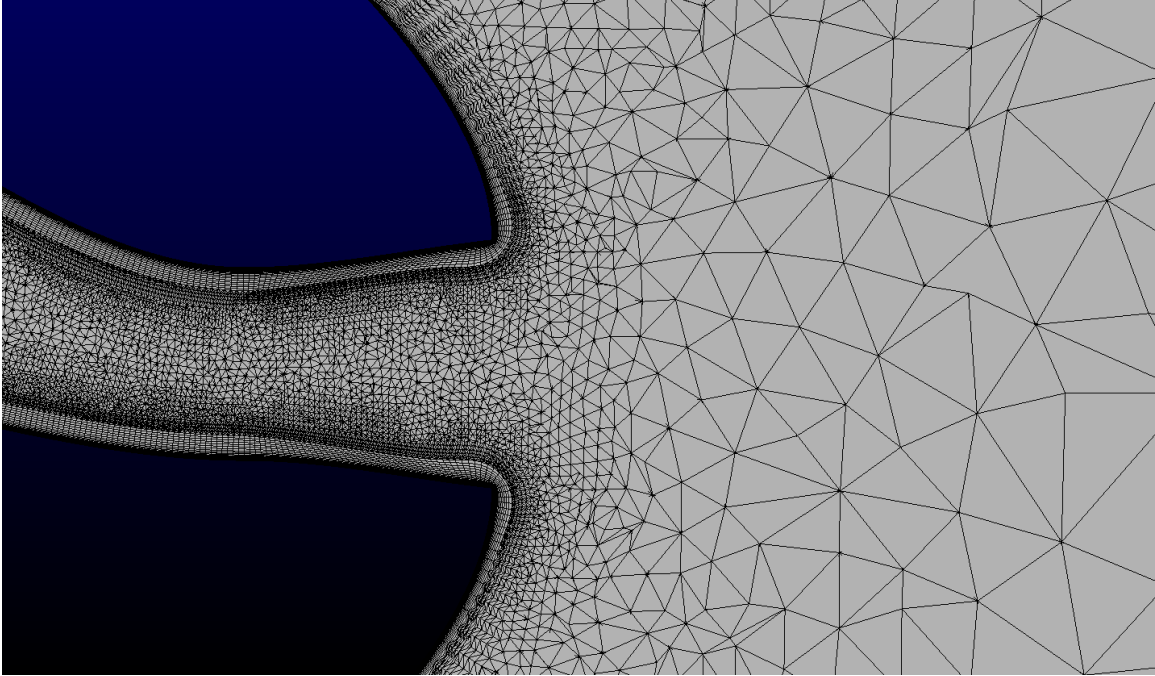
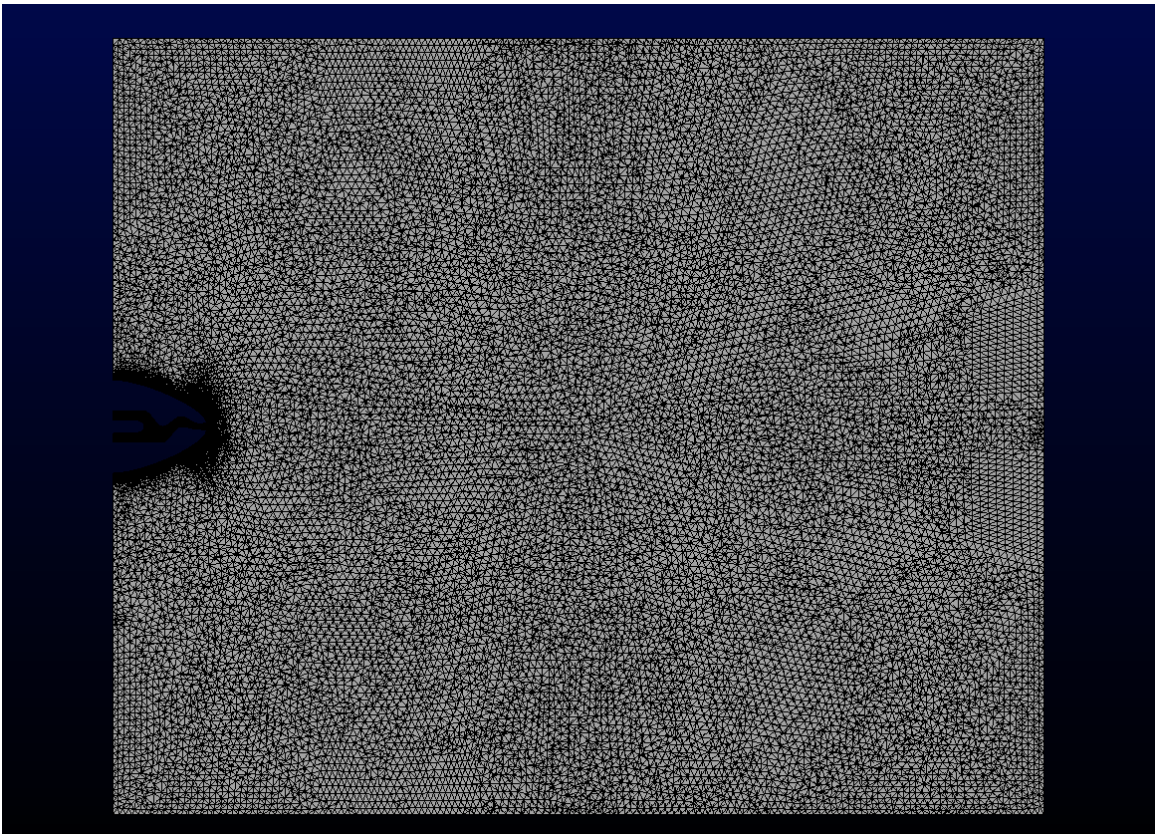Figure 3.16: Typical grid coarsening in the nozzle exhaust.

Figure 3.17: Grid resolution of the farfield bounding box.

3.4 Solution Independence and Uncertainty Quantification via Grid-Convergence Study

A grid-convergence study is performed to determine the necessary grid resolution required to achieve grid independent solutions. A grid-convergence study is necessary because a CFD solution is an approximation of the continuous, nonlinear Navier-Stokes equations. Truncation errors exist in the solution because the computational domain is discretized by grid cells, and thus the truncation error depends on the grid resolution. The goal of a grid-convergence study is to find a grid resolution that reduces the truncation error to an acceptable level while keeping the total number of grid cells to a minimum for computational efficiency. The typical process involves obtaining CFD solutions on successively finer grids and comparing a figure of merit, f in the simulation. Once the difference between the figure of merit for two grids is acceptably low, the solution is said to be "grid independent". Figures of merit and acceptable truncation errors vary by problem and depend on the specific research goals of a given CFD study. Grid-convergence studies are also a common, straightforward, and reliable technique for uncertainty quantification [48]. A method for uniform reporting of grid convergence studies called the grid-convergence index (GCI) [48] is discussed below. GCI is based on the generalized theory of Richardson Extrapolation. The following steps for performing a grid-convergence study are adapted from [14]. The results of the grid-convergence study are given in Chapter 4.

First, a representative grid size is established. Since this research uses viscous boundary layer grids, successive doubling of the grid in every direction used in traditional grid-convergence studies would result in either an unnecessarily refined boundary layer, or upon coarsening, a boundary layer that does not meet y^+ requirements. However, GCI does not require integer refinement, so any two grids of varying grid spacing can be compared. Therefore, this grid-convergence study will vary the spacing by effectively doubling the grid on the surface of the nozzle—viz., only in the axial and circumferential directions.

78

The grid spacing off the nozzle surface, on the OML surface, and at the farfield boundaries will not vary.

Next, three grids of successive refinement are created, figures of merit are established, and an acceptable error is determined. A survey of grid-convergence studies for the prior serpentine/transition duct research discussed in Chapter 2 reveals typical figures of merit and error ranges for this class of flow problem. The figures of merit ranged from pressure recovery [26], [55], [52], to minimum streamwise velocity [31], to wall static pressure distribution [24], [51], [33]. The range of acceptable error between grids for these figures of merit ranged from as small as 0.016% to as much as 20% for older work. The typical error is around 2%. A summary of grid convergence studies by Propulsion Aerodynamics Workshop (PAW) participants in given in [20]. Pressure recovery and distortion were used as figures of merit, and the best results obtained a difference of only 0.07%, but values ranged from 2-4% on average. This research uses three figures of merit related to the temperature distribution at the exit. Therefore, this grid-convergence study tends to be more restrictive than those that use only one quantity to determine grid independence. The figures of merit are discussed in Section 3.6. An acceptable error of 2.5% is established, along with an acceptable GCI of 5% to mirror the 95% confidence band used for the PAW [20]. Once the figures of merit and acceptable error levels are established, CFD simulations are performed on the three grids, and the grid-convergence calculations can be accomplished.

The apparent order p of the computational method is determined using the three levels of grid size h, where $h_1 < h_2 < h_3$:

$$r_{32} = h_3/h_2 \tag{3.55}$$

$$r_{21} = h_2/h_1 \tag{3.56}$$

$$\varepsilon_{32} = f_3 - f_2 \tag{3.57}$$

$$\varepsilon_{21} = f_2 - f_1 \tag{3.58}$$

$$s = 1 \cdot \text{sgn}\left(\varepsilon_{32}/\varepsilon_{21}\right) \tag{3.59}$$

$$q(p) = \ln\left(\frac{r_{21}^p - s}{r_{32}^p - s}\right) \tag{3.60}$$

where r is the refinement ratio, ε is the figure of merit change between grids, and the quantity q is solved iteratively for p using an initial guess equal to the anticipated order of the method (i.e., $p = 2$ for a second-order method).

The approximate relative error e and GCI are computed for each refinement ratio:

$$e^{32} = \left|\frac{f_2 - f_3}{f_2}\right| \tag{3.61}$$

$$e^{21} = \left|\frac{f_1 - f_2}{f_1}\right| \tag{3.62}$$

$$GCI_{med}^{32} = \frac{1.25e^{32}}{r_{32}^p - 1} \tag{3.63}$$

$$GCI_{fine}^{21} = \frac{1.25e^{21}}{r_{21}^p - 1} \tag{3.64}$$

The safety factor of 1.25 in the GCI equations is recommended when three or more grids are used, while a safety factor of 3 is recommended if only two grids are used [48].

Another method for estimating the order of convergence for a three-dimensional problem is to plot f versus the number of degrees of freedom (grid cells) to the -2/3 power, $N^{-2/3}$ (a two-dimensional problem would use $N^{-1/3}$), and check for linear behavior [20]. While this is usually done by visual inspection, this research combines the degrees of freedom test with the methods in [48] to arrive at an analytic approach. A theoretical "zero-grid" value for f, representing the solution using infinitely small grid spacing, is found by

$$r_{eff}^{32} = \left(\frac{N_2}{N_3}\right)^{1/3} \tag{3.65}$$

$$r_{eff}^{21} = \left(\frac{N_1}{N_2}\right)^{1/3} \tag{3.66}$$

$$f_{ext}^{32} = \left|\frac{\left(r_{eff}^{32}\right)^p (f_2 - f_3)}{\left(r_{eff}^{32}\right)^p - 1}\right| \tag{3.67}$$

$$f_{ext}^{21} = \left|\frac{\left(r_{eff}^{21}\right)^p (f_1 - f_2)}{\left(r_{eff}^{21}\right)^p - 1}\right| \tag{3.68}$$

where r_{eff} is the effective grid refinement ratio and f_{ext} is the extrapolated "zero-grid" figure of merit. A line is fit through all four values of f on a plot versus $N^{-2/3}$ and the goodness-of-fit parameter, R^2, is calculated. In general, R^2 values above 0.80 are considered acceptable for engineering applications with values above 0.95 considered an excellent fit [36].

3.5 Solution Methods and Models

After careful examination of available CFD codes, ANSYS Fluent was chosen as the best option to achieve the research goals. Fluent is widely used for aero-propulsion applications, including serpentine duct flows, as discussed in Chapter 2. One of the major conclusions from the literature review highlighted the benefits of an RSM turbulence model. Fluent is one of only a few production codes with this capability. Critical to this research effort, Fluent is available at Department of Defense Supercomputing Resource Centers (DSRCs), which were used extensively. The following sections describe various solution methods and models used in Fluent for this research.

3.5.1 Spatial Discretization .

Since a closed-form solution to the general conservation law stated in Equation 2.12 does not exist for practical flows of interest, the equation is converted into an algebraic form that can be solved numerically using a computational domain consisting of discrete points, or grid cells, as described in Section 3.3. This discretization is accomplished by assuming the control volume is constant in time and approximating the surface integrals as summations about the cell faces. The resulting discretized general conservation equation is:

$$\frac{\partial (\eta \rho)}{\partial t} + \sum_{faces} \eta \rho \left(\vec{v} \cdot \hat{n} \right) A_{face} + \sum_{faces} \left(\vec{J} \cdot \hat{n} \right) A_{face} = S_V \, V_{cell} + \sum_{faces} \left(\vec{S}_A \cdot \hat{n} \right) A_{face} \quad (3.69)$$

Fluent is a cell-centered code, where values of η are stored at the cell centroid. But as Equation 3.69 shows, the finite volume method requires the values at the cell faces. This research uses a second-order upwind scheme to achieve second-order spatial accuracy when

81

computing cell face values. This method calculates cell face values by

$$\eta_{face} = \eta + \nabla\eta \cdot \vec{r} \tag{3.70}$$

where η is the cell-centered value in the upwind cell, $\nabla\eta$ is the gradient in the upwind cell, and $\vec{r}$ is the displacement vector between the upwind cell centroid and the cell face centroid. Therefore, information must be known concerning the gradient of the upwind cell.

3.5.2 Evaluation of Gradients.

The Green-Gauss theorem is used to approximate the gradient of the scalar function η at the cell center by

$$\nabla\eta = \frac{1}{V} \oint_A \eta \hat{n} dA \tag{3.71}$$

which in discrete form yields

$$\nabla\eta = \frac{1}{V} \sum_{faces} \eta_{face} A_{face} \tag{3.72}$$

The face value of η is computed using a node-based method by finding the average node values on the face:

$$\eta_{face} = \frac{1}{N_{faces}} \sum_{faces} \eta_n \tag{3.73}$$

The node values are found from the spatially-weighted average of the surrounding cell values, since that is the information that is stored in a cell-centered code. Fluent uses a constrained minimization problem to reconstruct the exact values of a linear function at a node [5]. The gradient calculation is limited using the *minmod* function to prevent numeric oscillations in the solution which can appear in regions of discontinuity and rapid changes in the flow field. This function attempts to enforce monotonicity by preventing the face value from exceeding the minimum or maximum values in surrounding cells [8].

3.5.3 Pressure-Based Coupled Solver.

The two types of solvers available in Fluent (density- and pressure-based) were evaluated during the validation portion of this research (described in Chapter 4). It

was determined that the pressure-based solver was the more efficient choice in terms of computational time and convergence behavior. This observation follows recommendations from ANSYS PAW participants and claims that convergence rates could be increased by as much as five times [32]. The pressure-based approach used in Fluent was originally developed for use in low-speed incompressible flow problems [5] but has since been extended to the high-speed regime, to include supersonic nozzles [35], [49]. The term "pressure-based" arises from the use of primitive variables (p, u, v, w, and T) in the governing equations instead of conservative variables (ρ, ρu, ρv, ρw, and ρE).

A majority of CFD codes applied to high-speed compressible flow problems use a density-based approach to solve the Navier-Strokes equations simultaneously and determine the pressure field using an equation of state. The pressure-based solver is characterized by a method in which the momentum equations are solved using an estimate for the pressure field. The result will not satisfy the continuity equation unless the pressure term is corrected, which will change the velocity field from the previous step. This procedure is repeated until continuity is satisfied and a divergence-free velocity field is obtained [54].

This pressure-correction procedure can be performed implicitly, where the momentum and pressure-based continuity equations are solved simultaneously—in a "coupled" manner. The coupled method is opposed to a segregated approach where the momentum equations are solved sequentially. After the pressure-correction step is performed, the energy and turbulence equations are solved in a segregated fashion. The coupled approach results in faster convergence rates than a segregated approach but requires 1.5-2 times more memory to store the implicit terms [5]. The basic steps in the pressure-based coupled solver (PBCS) are:

1. Solve pressure-based continuity and momentum equations simultaneously.

2. Update mass flux at cell face.

3. Solve energy and turbulence equations.

4. Check for convergence.

5. If not yet converged, update properties and repeat.

The following is a description from ANSYS of how the nonlinear governing equations are solved in a discretized manner for the PBCS:

> *"An implicit discretization of pressure gradient terms in the momentum equations, and an implicit discretization of the face mass flux, including the Rhie-Chow pressure dissipation terms, provide fully implicit coupling between the momentum and continuity equations. This discretization yields a system of algebraic equations whose matrix depends on the discretization coefficients for momentum equations, which is then solved using the coupled algebraic multigrid (AMG) scheme. An Incomplete Lower Upper (ILU) smoother is applied to smooth the residuals between levels of the AMG* [49]*."*

Second-order central differencing is used in this research for the implicit discretization of the pressure gradient terms, and second-order upwinding is used for the implicit discretization of the face mass flux. Details on the complete system of equations for the PBCS are given in [5].

This research solves a steady-state problem for each nozzle, so that the time-dependent term in Equation 2.12 is not included. The PBCS updates the solution iteratively using explicit under-relaxation to control the change in variables from one iteration to the next in order to provide numeric stability in the solution. For the general property η in a cell, the update is

$$\eta_{new} = \eta_{old} + \alpha \Delta \eta \tag{3.74}$$

where $\Delta \eta$ is the change in η and α is the under-relaxation factor. The under-relaxation factor is applied directly to the pressure and momentum terms in the governing equations

(i.e. explicit relaxation) and is applied to other equations (i.e., implicit relaxation) via the CFL input parameter:

$$\frac{1 - \alpha}{\alpha} = \frac{1}{CFL} \tag{3.75}$$

Note this is a different definition for CFL than is used in density-based solvers.

3.5.4   Boundary Conditions .

Pressure inlet boundary conditions are applied to all external faces except the downstream face which is given a pressure outlet boundary condition. The total pressure is given in Table 3.1, but the static pressures (called "Supersonic/Initial Gauge Pressure" in Fluent) must be computed in order to initialize the problem. Static pressure is calculated using the isentropic relation

$$P_{st} = \frac{1}{P_t}\left(1 + \frac{\gamma - 1}{2}M^2\right)^{-\frac{\gamma}{\gamma-1}} \tag{3.76}$$

A small Mach number (0.05) is applied at the external inflow boundaries via P_{st} to aid in solution convergence. Uniform turbulent quantities are specified at the core and bypass boundaries by computing the turbulent length scale and turbulent intensity:

$$I = 0.16Re_{D_h}^{-1/8} \tag{3.77}$$

$$l = 0.07D_h \tag{3.78}$$

Turbulent quantities at all external pressure boundaries are established using turbulent intensity and turbulent viscosity ratio values taken from PAW measurements in a still room. Temperature for all external pressure boundaries is set to standard atmospheric temperature at 20,000 ft. A pressure outlet boundary conditions is applied to the downstream face of the farfield bounding box with the gauge pressure set to $P_{st,9}$. Since this research will not consider heat transfer, the nozzle and OML are given an adiabatic wall boundary condition, which is typical of nozzle flows [30].

3.6 Hot Streak Characterization Parameters

A set of parameters are developed in this section to aid in the research goal of *"observe and characterize the underlying flow physics of hot streak phenomena."* As stated in Section 1.3, the critical outcome of this research is quantifying how the size, magnitude, and location of hot streaks vary with when the nozzle geometry changes. The set of parameters discussed below help describe those changes quantitatively. The first set of parameters involve examination of the exit flow plane:

Threshold Temperature: The temperature above which a region of exit flow is considered "hot" is defined as 90% of the core temperature: $T_{hot} = 0.9T_6 = 880K$. Therefore, the threshold temperature is the same for all nozzles investigated in this research.

Size: The size of a hot region of flow is computed by summing the areas of all exit grid cell faces that meet or exceed the T_{hot} criteria and normalizing by A_9 such that size represents the percentage of exit area consumed by flow above T_{hot}.

Magnitude: A region of hot exit flow is assigned a magnitude using

$$Mag = \frac{TAVHOT - T_{hot}}{T_6 - T_{hot}} = \frac{TAVHOT - 880K}{98K} \tag{3.79}$$

where $TAVHOT$ is the average temperature of the hot region.

Location: The location of a hot region of flow at the exit is found by computing the temperature-weighted centroid of the hot region.

3.6.1 Temperature Distortion.

In addition to these parameters, the distortion of the temperature field is used to understand how the temperature distribution varies with nozzle geometry and (especially) swirl. The Society of Automotive Engineers (SAE) Aerospace Resource Document (ARD) 50015 defines temperature distortion of aircraft engine inlets with circular cross-sections

[1]. This research extends the concepts in SAE ARD 50015 to a non-circular nozzle exit. The three distortion parameters used in this research are radial distortion intensity (RDI), circumferential distortion intensity (CDI), and circumferential distortion coefficient (CDC). The concepts in SAE ARD 50015 were developed for experimental testing where the distortion parameters are computed using discrete temperature measurements at the engine inlet aerodynamic interface plane (AIP). For these experiments, the measurements are usually taken using a circular total temperature rake, the most common consisting of 5 rings of 8 probes each (see Figure 4.3). Therefore, the definitions of RDI, CDI, and CDC were formulated on the basis of having discrete rake values. For the CFD simulations in this research, a similar concept is used, where the exit plane is probed at 40 discrete locations, which are divided into the 5 rings shown in Figure 3.18 for each aspect ratio. The "probe" locations are based on the outermost ring, which is at the nozzle surface. The solution is probed at the horizontal and vertical centerlines, and the corner locations of the semicircles. Subsequent rings are scaled proportionally from the outer surface to the exit center. Using the nomenclature in SAE ARD 50015, the rings are numbered 1-5 from inner to outer ring.

The intensity parameters RDI and CDI are computed on a per-ring basis. RDI relates the average ring total temperature to the average total temperature of the rake and thus is a measure of how the total temperature varies from the average in the radial direction:

$$RDI_i = \frac{TAV_i - TFAV}{TFAV} \tag{3.80}$$

where TAV_i is the average total temperature of the 8 probes in the i-th ring, and $TFAV$ is the average total temperature of all 40 probe locations. CDI relates the average ring total temperature to probes of total temperature above the average and thus is a measure of how the total temperature varies in the circumferential direction:

$$CDI_i = \frac{TAVHI_i - TAV_i}{TAV_i} \tag{3.81}$$

87

(a) $AR = 4$

(b) $AR = 10$
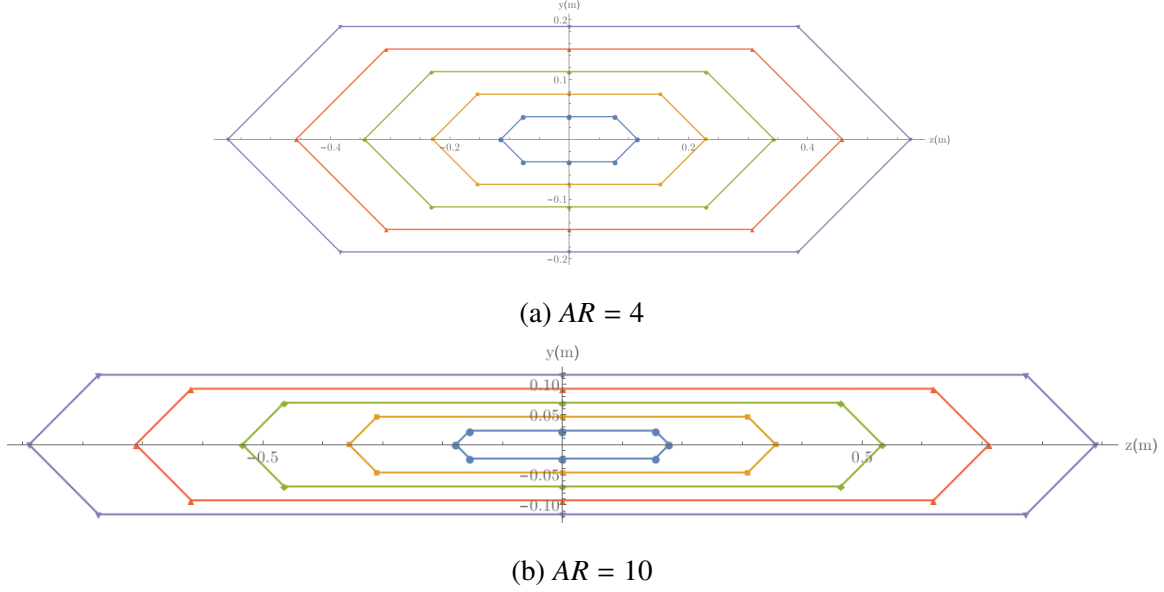
Figure 3.18: Temperature rakes used for distortion calculations.

where $TAVHI_i$ is the average total temperature of any probe locations in the i-th ring above TAV_i. CDC is the average of the 5 CDI values and thus is a global measure of circumferential distortion at the exit plane.

3.6.2 Performance Parameters.

The effect of nozzle geometry changes on performance is important for integration of serpentine exhaust nozzles into aircraft weapon systems. Trade-offs between performance requirements and mission capability provided by serpentine exhaust nozzles could drive a design choice. Two performance parameters are computed for each simulation: discharge coefficient, C_d, and thrust coefficient, C_{F_g}. Discharge coefficient is used to determine nozzle choking and to size the nozzle throat area. Thrust coefficient accounts for losses due to velocity vector angularity, boundary layer viscosity, and flow non-uniformities [38]. These parameters are defined as [34]:

$$C_d = \frac{\oint_{A_9} (\rho_9 U_9) \; dA_9}{\rho_i U_i A_9} \tag{3.82}$$

88

$$C_{F_g} = \frac{\oint_{A_9} \left[\rho_9 U_9^2 + (P_{st,9} - P_{amb}) \right] \, dA_9}{U_i \oint_{A_9} (\rho_9 U_9) \, dA_9} \tag{3.83}$$

where ρ_9, U_9, and $P_{st,9}$ are the density, axial velocity, and static pressure integrated over the exit plane, and P_{amb} is the standard atmospheric static pressure at 20,000 ft. The "ideal" density and velocity, ρ_i and U_i, are computed from the isentropic relations in Equations 3.31-3.33.

3.6.3 Modified Dean Number and Serpentinity .

Finally, a parameter is introduced to compare the various nozzles used in this research. In general, curved ducts are classified in terms of the Dean number [47]:

$$De = \frac{\rho U D_h}{\mu} \left(\frac{D_h}{2R} \right)^{1/2} = Re \left(\frac{D_h}{2R} \right)^{1/2} \tag{3.84}$$

where R is the radius of curvature and the second term represents the square root of the curvature ratio. For the nozzles designed in this research effort, the radius of curvature constantly varies through the duct. Therefore, a modified Dean number is proposed for use in this research:

$$De_{\mathcal{S}} = \frac{\rho_8 U_8 D_{h,8}}{\mu} \left(\frac{D_{h,8}}{2R_{min}} \right)^{1/2} = Re_{D_{h,8}} \mathcal{S} \tag{3.85}$$

where $D_{h,8}$ is the hydraulic diameter at the throat, which for a non-circular shape is defined as

$$D_h = \frac{4A}{P} \tag{3.86}$$

where A is the cross-sectional area and P is the wetted perimeter. For the two aspect ratios considered in this research, $P = 102.8$ inches (2.61 m) for $AR = 4$, and $P = 148$ inches (3.76 m) for $AR = 10$. The hydraulic diameters for each aspect ratio are 18.7 inches (0.475 m) for $AR = 4$ and 13 inches (0.330 m) for $AR = 10$. The denominator in Equation 3.85 is termed *serpentinity*, defined as

$$\mathcal{S} = \left(\frac{D_{h,8}}{2R_{min}} \right)^{1/2} \tag{3.87}$$

where R_{min} is the minimum radius of curvature along along any of the centerlines (upper, lower, port, or starboard), which can be considered a "global" radius of curvature for the

nozzle [25]. Therefore, serpentinity attempts to capture the relationship between highest degree of curvature in the nozzle and the exit throat shape. Equation 3.85 is beneficial in that when the modified Dean number is applied to a duct of constant curvature and cross-section, the original Dean number is recovered. For a centerline comprised of discrete grid points, the radius of curvature R_i at each point i is computed using elementary geometry where any three points (p_{i-1}, p_i, p_{i+1}) in space define a unique circle which has a radius

$$r = \frac{cba}{4A} \tag{3.88}$$

where c is the distance between p_{i-1} and p_i, b is the distance between p_i and p_{i+1}, and a is the distance between p_i and p_{i+1}. The area of the triangle created by the three points is

$$A = \frac{1}{2} ca \sin\theta_{ab} \tag{3.89}$$

where θ_{ab} is the angle between the vectors made by a and b and is found by the law of cosine ($c^2 = a^2 + b^2 - 2ab \cos\theta$). The radius of curvature at each point simplifies to

$$R_i = b \left(2 \sqrt{1 - \frac{(a^2 + b^2 - c^2)^2}{4a^2b^2}} \right)^{-1} \tag{3.90}$$

IV.   Results

This chapter first describes a validation effort for the application of Fluent to a serpentine duct. Next, the results of a grid convergence study are presented. Then, the flowfield features and hot streak phenomena observed for each nozzle are described and discussed. The characterization parameters are then investigated for trends related to the altering of flowfield physics due to changes in nozzle geometry and swirl. Finally, nozzle surface temperatures are analyzed to determine the impact of altering nozzle geometry on hot streak formation.

4.1   Serpentine Flow Validation Using Fluent

An effort to validate the numerical models, methods, and tools proposed for the current research is described in this section. An extensive search of the available literature failed to yield any useful data pertaining to serpentine exhaust nozzles. Therefore, the validation study is based on a circular diffusing serpentine duct investigated at the first American Institute of Aeronautics and Astronautics (AIAA) PAW, which was held in 2012 and whose results were reported at the AIAA Joint Propulsion Conference (JPC) in 2013. The workshop compared CFD solutions from various government and industry participants to experimental data taken at the ONERA wind tunnel (Modane-Avrieux, France) in 2006.

The geometry of the test configuration is shown in Figure 4.1. Boundary layer thickness was measured at three circumferential locations ($0°$, $90°$, $180°$) at $s/D_1 = -0.575$, where s is the centroid arc length and D_1 is the inlet diameter. Surface static pressure data was taken along three circumferential locations ($0°$, $90°$, $180°$) and three axial locations ($s/D_1 = 2$, $s/D_1 = 3$, $s/D_1 = 4$). The location of the experimental data points on the surface are shown in Figure 4.2. Total pressure measurements were taken at the AIP using

a 40-probe unsteady total pressure rake to determine pressure recovery and distortion. The location of the probe measurements are shown in Figure 4.3.
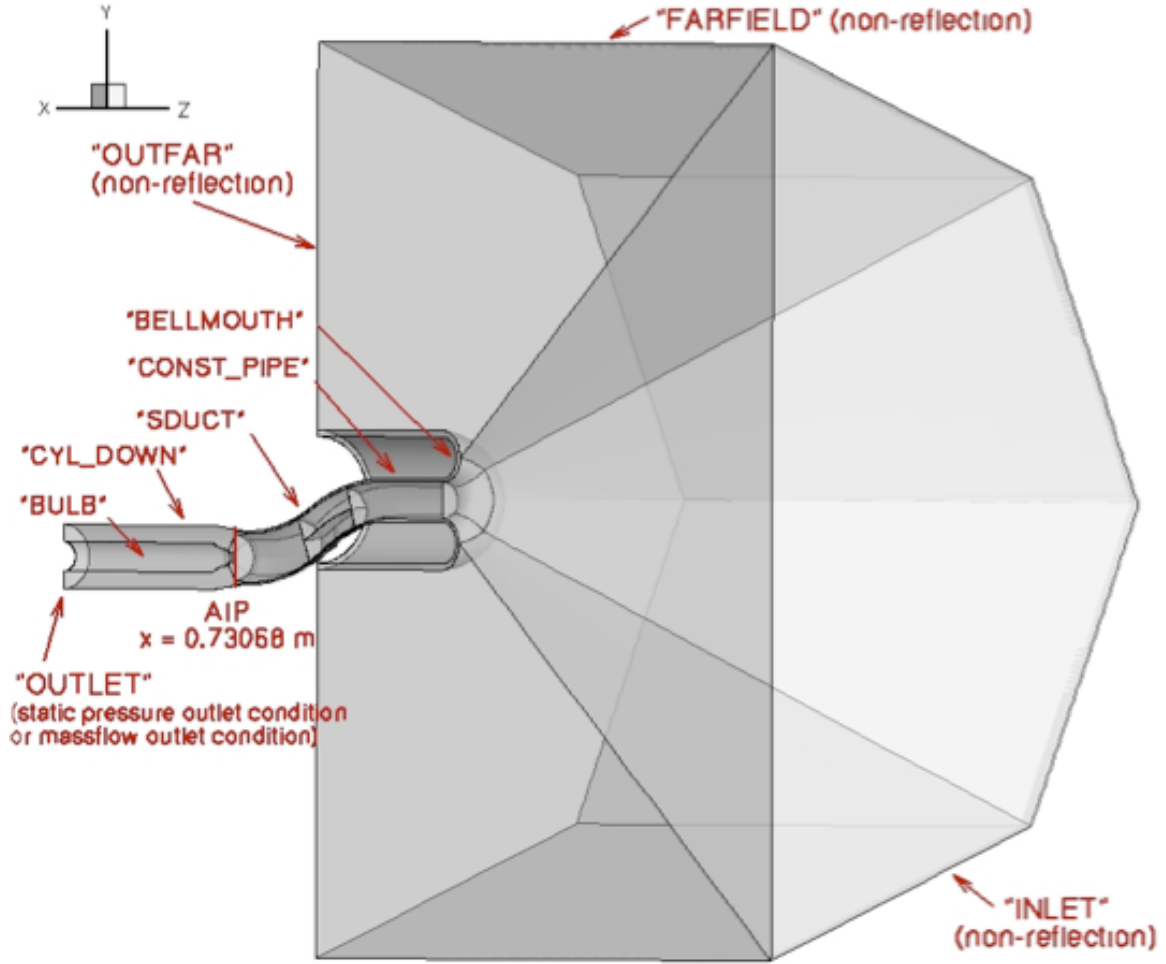
Figure 4.1: Test case geometry [20].

Two flow configurations were tested, and the flow conditions (ambient total pressure, P_t; ambient total temperature, T_t; mass flow at the nozzle exit, $\dot{m}$; average Mach number at the AIP, M_{AIP}) are listed in Table 4.1. Details about the experimental facility, instrumentation, and measurement techniques are given in [20]. CFD comparisons for Test 1 were performed and reported by PAW participants in [21], [22], [23], [34]. Of special note is the participation of ANSYS [34], who develops the Fluent CFD code.

92
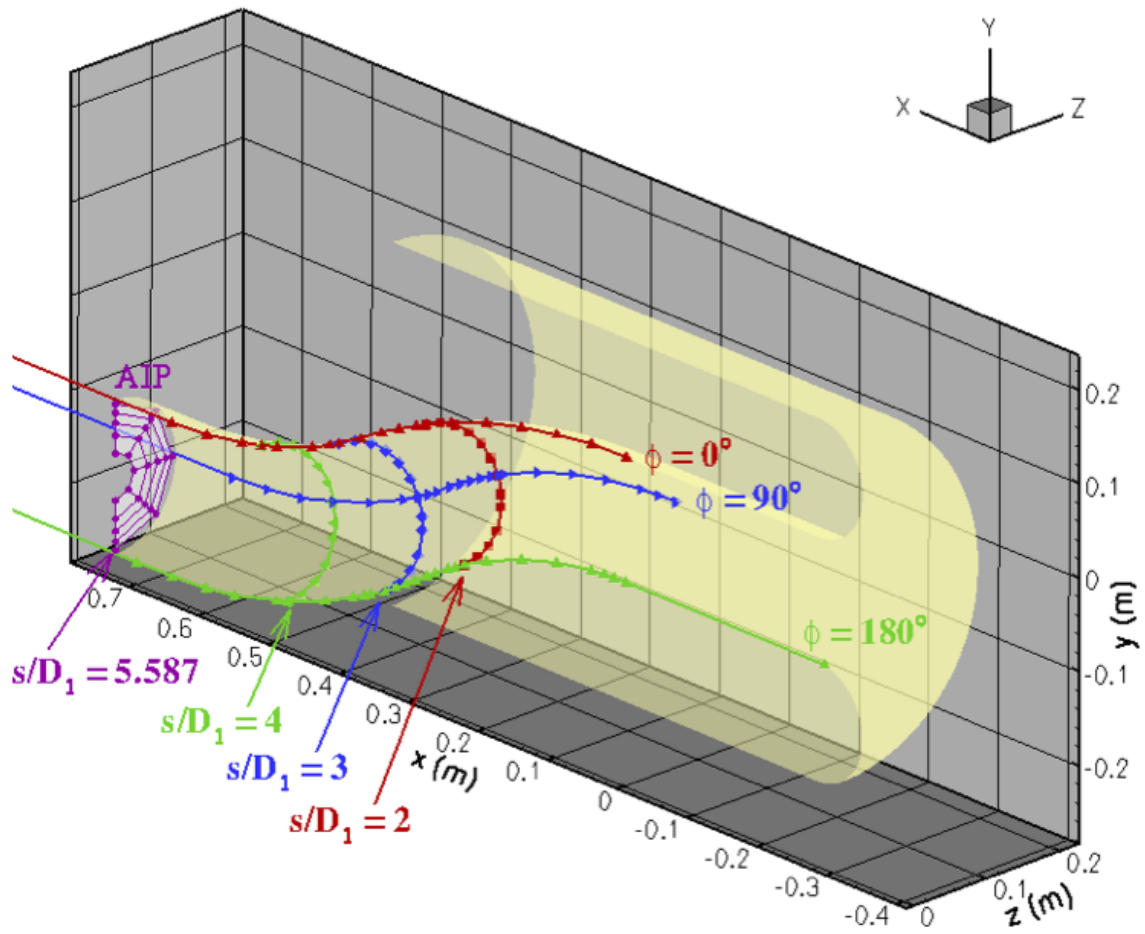
Figure 4.2: Location of static and total pressure measurements [20].
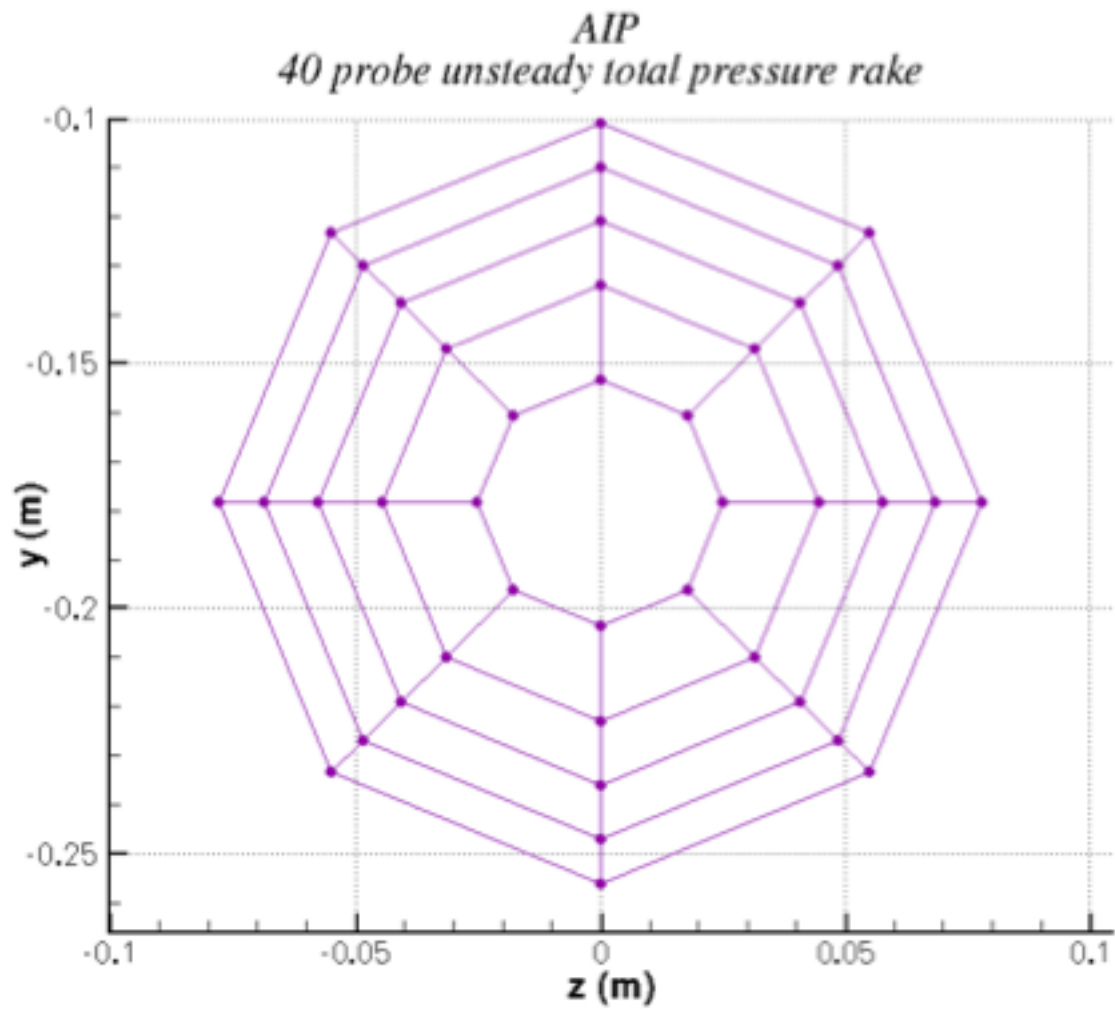
Figure 4.3: Location of unsteady total pressure measurements at the AIP [20].

Table 4.1: Validation Experiment Conditions [20]

Condition	Test 1	Test 2
P_t	88744 Pa	88731 Pa
T_t	286.2 K	286.3 K
$\dot{m}$	2.427 kg/s	1.356 kg/s
M_{AIP}	0.3549	0.1819

4.1.1 Computational Methods for Validation.

The computational models and methods used in the validation effort mirror those proposed for the research effort in Chapter 3. Within Fluent, the pressure-based coupled solver is employed. Air is modeled as an ideal gas with viscosity defined using Sutherland's law. Specific heat and thermal conductivity are computed by interpolating from standard atmospheric tables. While the temperature does not vary appreciably for the validation study, the variation of specific heat and thermal conductivity with temperature is employed to ensure proper function for the research effort where the temperature will vary greatly. In contrast, the ANSYS PAW participants used constant air properties at default ambient conditions in the code, not the conditions listed in Table 4.1.

Grids were provided by the PAW Committee for comparing CFD results with the experiment. While some PAW participants generated additional grids to perform grid convergence studies, this study only uses the provided structured grid. The results described here can thus be compared to the "baseline" structured results in [34], which used the same structured grid.

The computational domain is shown in Figure 4.4 and includes a portion of the room where the experiment was conducted and the bellmouth of the experimental nozzle inlet. The grids were generated using a symmetry plane. The various boundary conditions used in the study are shown in Figure 4.4, where the walls are modeled as adiabatic no-slip surfaces, the pressure inlet boundaries (all sides of the "farfield" domain) are given a

turbulent intensity of 0.4% based on experimental data [20], and the mass flow rate for the mass-flow inlet boundary is half the experimental value due to the symmetry plane.

The computational methods used in Fluent for this validation effort are almost identical to those described in [34], except for the aforementioned variable air properties. The pressure-based solver is employed with second-order upwinding used for all convection terms of each transport equation. It should be noted that solutions using third-order Monotone Upstream-Centered Schemes for Conservation Laws (MUSCL) extrapolation for all convection terms were completed for Test Case 1 and negligible difference was found between the two discretization schemes, while achieving the MUSCL solution required many more computational hours and increased the solution residuals. The Stress-ω formulation of RSM is used for modeling turbulence.
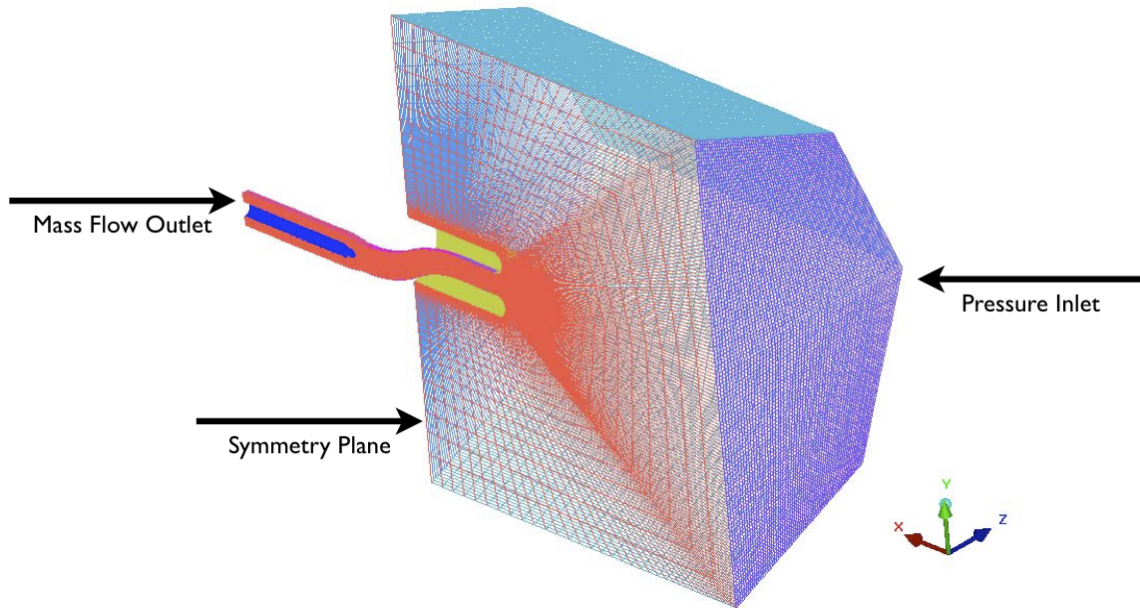
Figure 4.4: Computational domain and boundary conditions [20].

4.1.2   Results.

In contrast to most PAW participants, both test cases were accomplished for this validation study. Three types of data were provided by the PAW organizers: boundary layer profiles at the duct entrance, surface pressures at the locations shown in Figure 4.2, and performance calculations (pressure recovery and distortion coefficient at the AIP). Results are discussed in this order for each test case.

4.1.2.1   Test Case 1 – Flow Features and Development.

As shown in Table 4.1, the experimental average Mach number is given as 0.3549. The average Mach number from the CFD simulation is 0.3603, or a difference of 1.53%. Figure 4.5 shows Mach contours along the symmetry plane. The flow is accelerated to a maximum Mach number of 0.68 at the entrance. Flow separation occurs around the first bend at the lower surface due to the high degree of turning in the duct. To a lesser extent, flow separation occurs at the upper and lower surfaces just upstream of the AIP due to a sharp edge in the geometry. Figure 4.6 shows the development of the flow through the S-duct at the s/D_1 experimental locations. The non-uniformity of the flow at the AIP (which will be quantified by recovery and distortion) is demonstrated in this figure. Also clearly seen is the region of low-momentum fluid downstream of the first bend at $s/D_1 = 3$ and $s/D_1 = 4$, a feature discussed in Chapter 2 for other S-ducts.
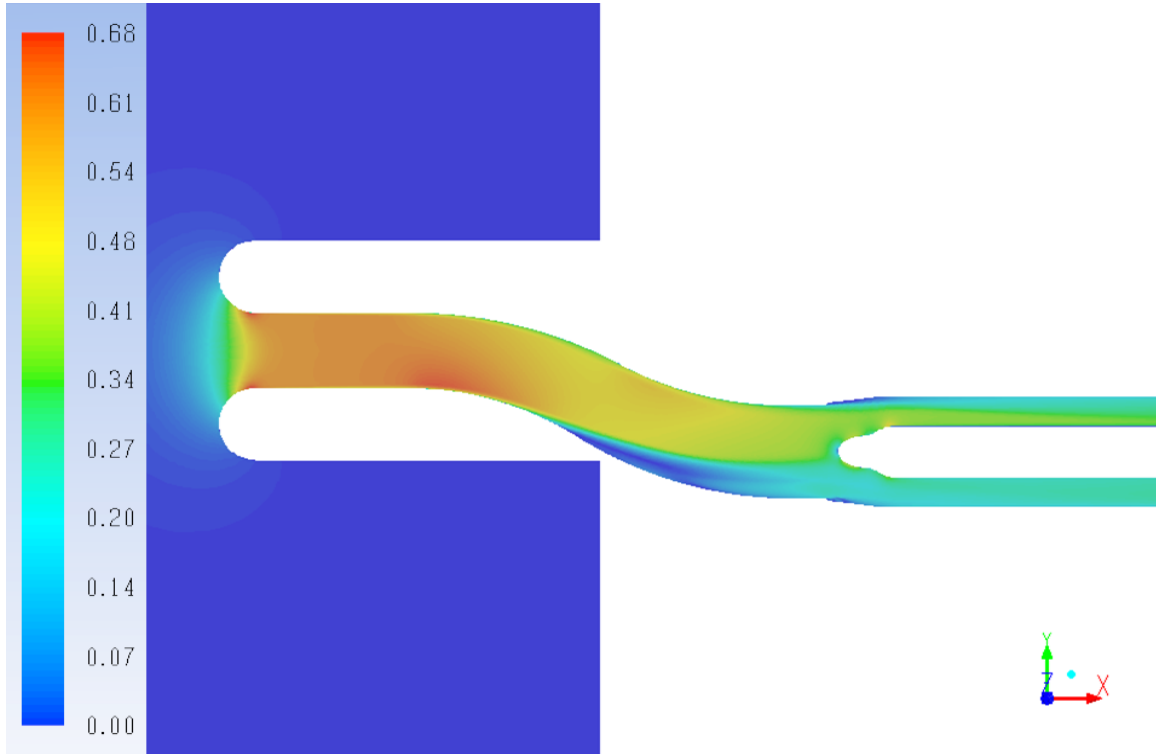
Figure 4.5: Test Case 1 Mach number along symmetry plane.
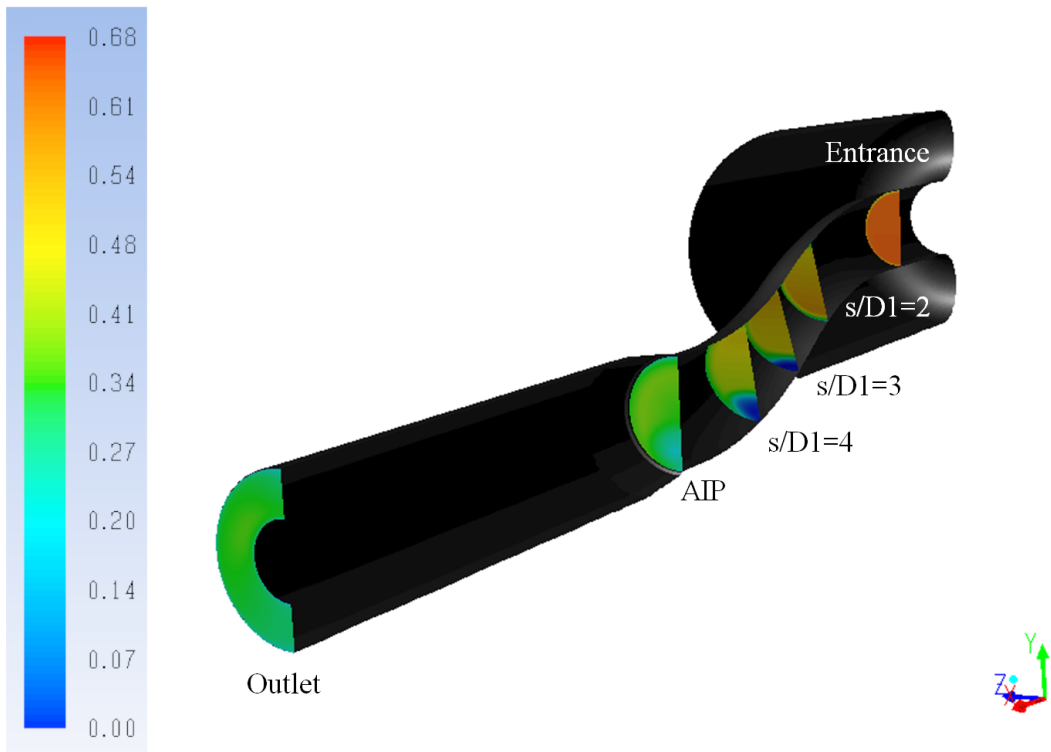
Figure 4.6: Test Case 1 Mach number at cross-sections throughout duct.

4.1.2.2   Test Case 1 – Boundary Layer Profiles.

Boundary layer profiles of non-dimensional stagnation pressure (P_i/P_{i_0}) along three radial lines at circumferential locations $\phi = 0°$, $90°$, and $180°$ are shown in Figure 4.7. Numerical simulations are symmetric at all locations, while the experimental data differs slightly at the sidewall ($\phi = 90°$) from the other two locations. The differences in the experimental data could be attributed to installation features not present in the simulation geometry. A difference between the two data sets is also observed near the wall, where the values associated with the experimental data are greater, which can be attributed to the inability of the boundary layer probes to obtain data very close to the wall (less than 0.2 mm) [20]. Numerical and experimental data for $\phi = 90°$ match almost exactly up to 2 mm. The differences after 2 mm are small (less than 1%) until the data converges to freestream values. In this region of the provided grid $y^+ < 1$, so confidence is gained from the boundary layer profile comparisons that the methods used for the simulation can accurately predict near-wall properties.

4.1.2.3   Test Case 1 – Surface Pressure Distributions.

The PAW organizers provided (x, y, z) locations of the surface pressure taps; however, these did not match the provided geometry and grid (e.g., some experimental locations were well into the domain of the provided grid or outside the computational domain altogether). For the current effort, the provided location was extrapolated down to the nearest wall grid cell by identifying the closest cell in Pointwise and averaging the surrounding nodal values. The averaged values are used for comparison with experimental surface pressures.

Streamwise non-dimensional static pressure (P/P_{i_0}) distribution comparisons with experimental data are shown in Figure 4.8 in accordance with the experimental data locations shown in Figure 4.2. The dominant trends are present in the CFD plots, except for capturing the constant-pressure region (indicative of flow separation) in the $\phi = 180°$ and $90°$ distributions. PAW participants did not match this region either [20]. The results
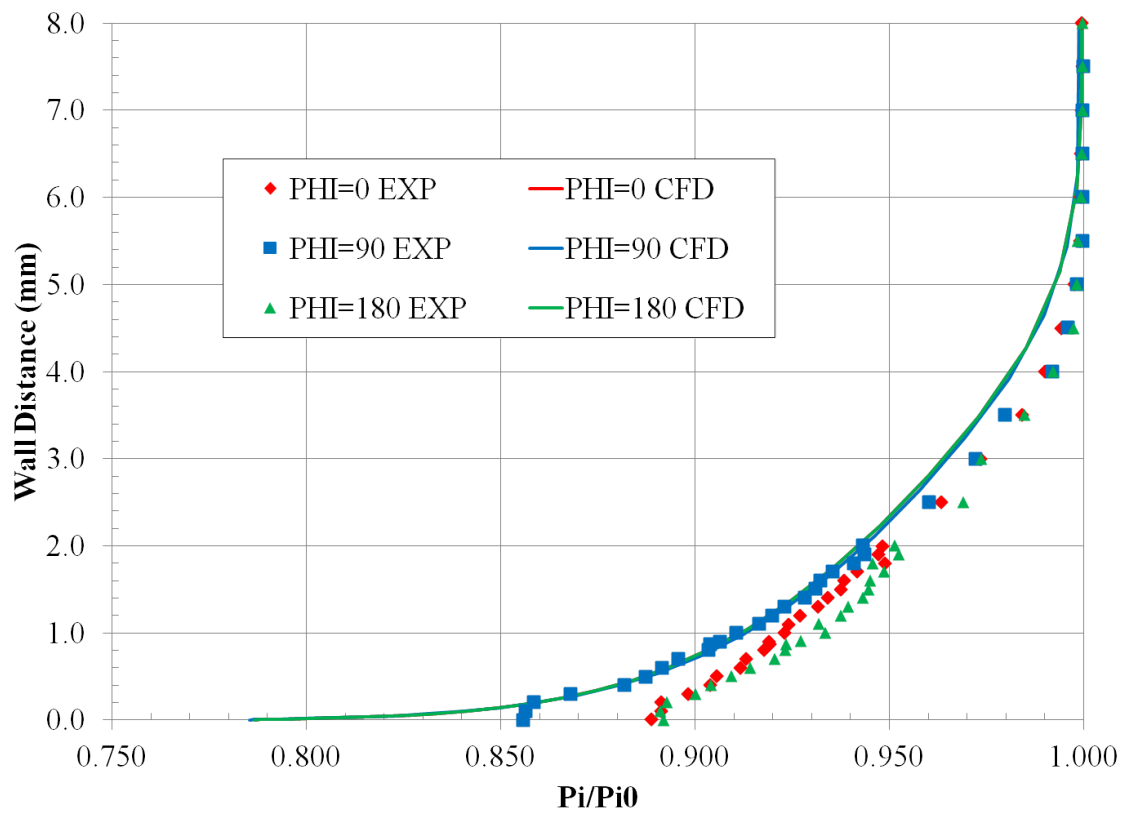
Figure 4.7: Test Case 1 boundary layer profile comparison.

reported here are very similar to those reported in [34]. The maximum error for $\phi = 0°$ is 1.68% and for $\phi = 90°$ the maximum error is 2.15%. The first few data points for $\phi = 180°$ do not match experimental data as well, with maximum errors between 2.64% and 5.76%. Similar deviation in this region of flow acceleration was seen by PAW participants [20].

Circumferential non-dimensional static pressure (P/P_{i_0}) distribution comparisons with experimental data are shown in Figure 4.9 in accordance with the experimental data locations shown in Figure 4.2. The location at the start of the separated region ($s/D_1 = 2$) has the largest difference compared to experiment, a maximum error of 2.22%. Downstream of the onset of separation, the CFD simulation matches experiment well, with maximum error of 1.67% for $s/D_1 = 3$ and 0.40% for $s/D_1 = 4$.
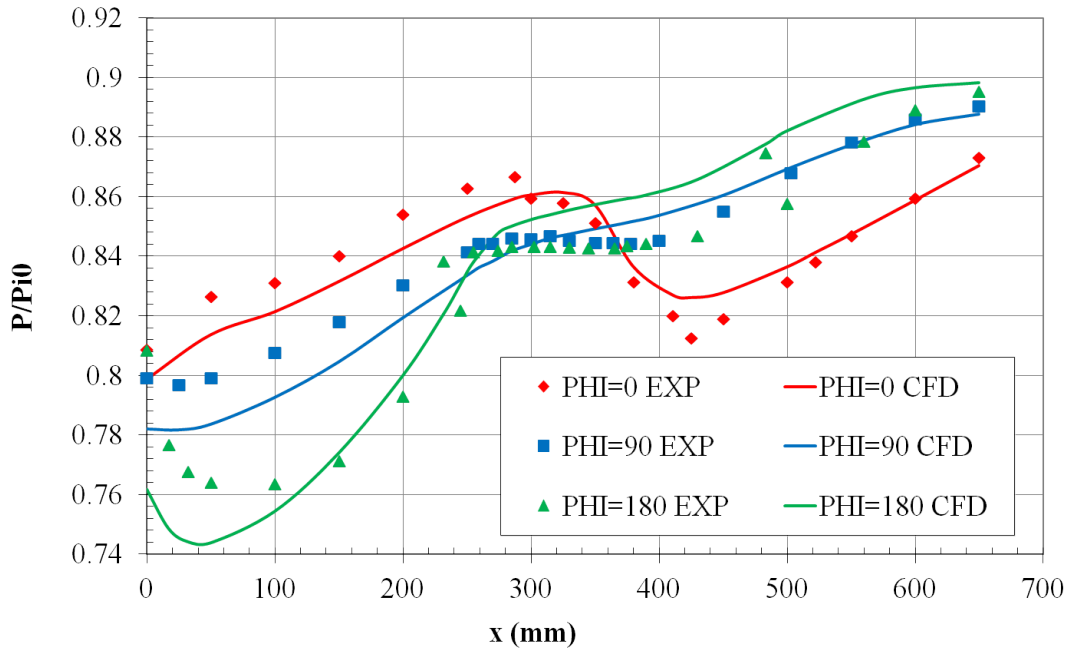
Figure 4.8: Test Case 1 streamwise pressure distribution comparison.
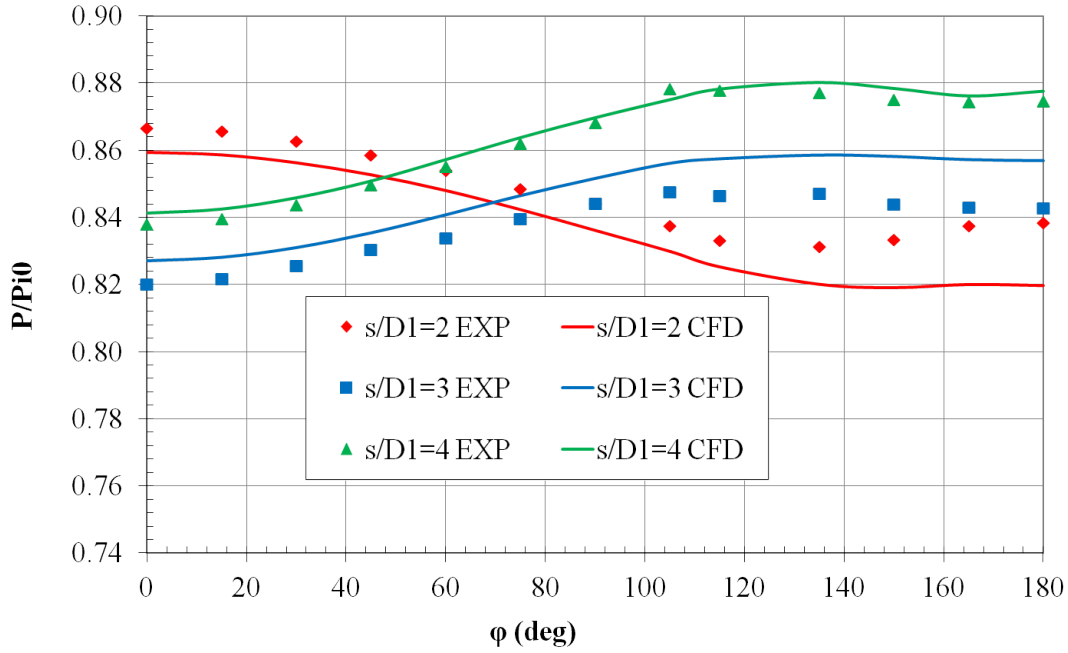
Figure 4.9: Test Case 1 circumferential pressure distribution comparison.

4.1.2.4   *Test Case 1 – Performance Calculations.*

Two performance indicators were provided by the PAW organizers – pressure recovery and distortion at the AIP. Pressure recovery is defined as the ratio of the average total pressure at the AIP and the non-dimensional freestream total pressure ((P_{T_2}/P_{T_0}) in [20]). The provided experimental value is 0.9711. The computed value from the CFD simulation is 0.9707, a difference of only 0.05%. This small difference was seen by many PAW participants [20]. ANSYS reported a recovery of 0.9699 on the baseline grid (0.12% difference) [34], so the changes in fluid properties used in this validation study seem to provide a slightly better comparison with experiment.

Distortion coefficient is defined as

$$DC = \frac{1}{N} \sum_{i=1}^{N} \frac{PAV_i - PAVLOW_i}{PAV_i} \tag{4.1}$$

102

where N is the number of circumferential rings in the measurement device, PAV_i is the average total pressure at ring i, and $PAVLOW_i$ is the average total pressure of all measurement points below PAV_i at ring i. As shown in Figure 4.3, 40 measurements were taken using eight rakes with five locations per rake, so that five rings of data were obtained ($N = 5$). Because of the symmetry plane in the CFD grid, data from the three rakes not along the $z = 0$ axis are counted twice.

The provided experimental value of distortion coefficient is 0.0195. The computed value from the CFD simulation is 0.0286. A higher value of distortion was reported by every PAW participant, and in some cases the values were as high as 0.036. ANSYS reported a distortion coefficient on the baseline structured grid of 0.0317 [34], so again the current simulation does better than the baseline ANSYS case. It is noted in [20] that Fluent with RSM turbulence model does the best job overall of matching measured distortion values and modeling the separated flow region at the lower portion of the AIP compared to all other codes in the study.

4.1.2.5   *Test Case 2 – Flow Features and Development.*

As shown in Table 4.1, the experimental average Mach number for Test Case 2 is given as 0.1819. The average Mach number from the CFD simulation is 0.1845, or a difference of 1.43%. Figure 4.10 shows Mach contours along the symmetry plane. Similar to Test Case 1, the acceleration of the flow to a maximum Mach number of 0.3189 at the entrance is observed, along with a region of separation downstream of the first bend at the lower surface. Flow separation is also seen to a lesser extent at the upper and lower surfaces at the edge just upstream of the AIP. Figure 4.11 shows the development of the flow through the S-duct at the s/D_1 experimental locations. The non-uniformity of the flow at the AIP is demonstrated in this figure, although to a lesser extent than Test Case 1, as expected.
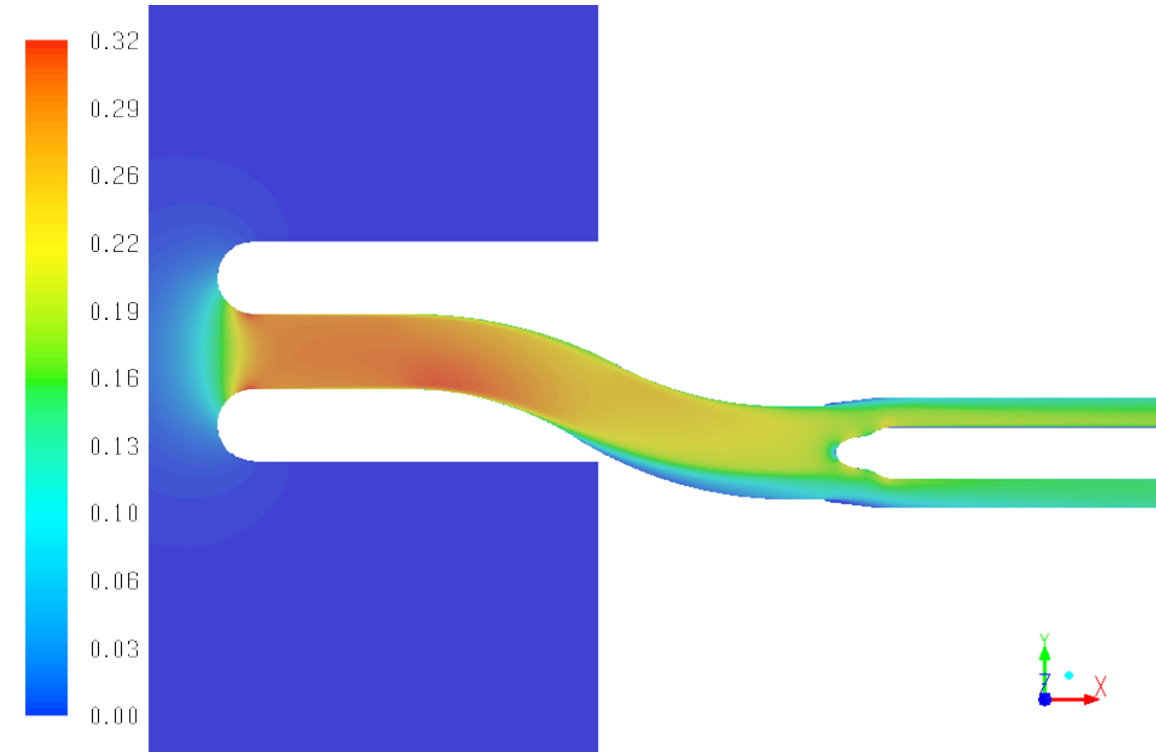
Figure 4.10: Test Case 2 Mach number along symmetry plane.
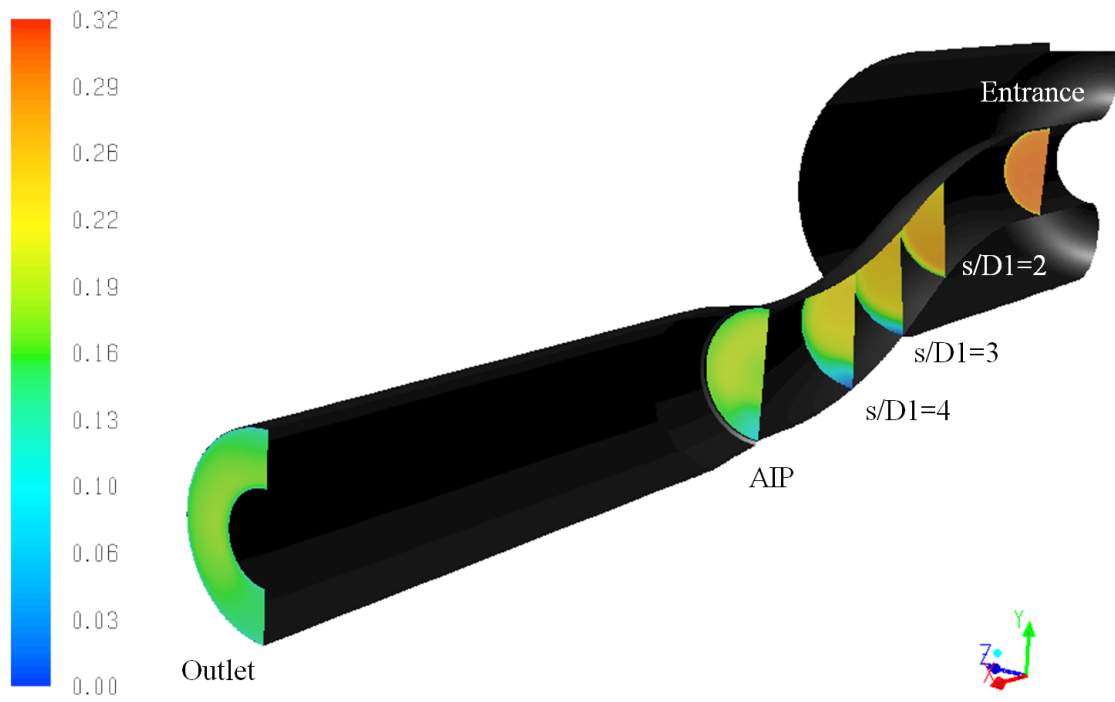
Figure 4.11: Test Case 2 Mach number at cross-sections throughout duct.

4.1.2.6   Test Case 2 – Boundary Layer Profiles.

Boundary layer profiles of total pressure ratio along three radial lines at circumferential locations $\phi = 0°$, $90°$, and $180°$ are examined in Figure 4.12. Unlike Test Case 1, the CFD simulation does not reach freestream pressure in the same boundary layer region, although the differences in the numerical simulation and the experimental data are small (maximum error < 1%). The only PAW participant to report data on Test Case 2 was [21], who used a two-equation $k - kl$ turbulence model that closely matched the boundary layer profile. The simulations in this study and in [34] did not use a low-Reynolds number option in the Stress-ω formulation of RSM because the option consistently resulted in an unstable solution. This option, which affects all terms in the turbulence model containing the turbulent Reynolds number, has the potential to increase the accuracy of the solution in the viscous sublayer, as described in Chapter 2. The probable cause of the instability can be attributed to the provided grids not being fine enough to capture the large gradients in and around the separated flow region.

The CFD simulation displays symmetry at all locations, while the experimental data differs slightly at the sidewall ($\phi = 90°$) from the other two locations. Similar to Test Case 1, the differences in the experimental data can be attributed to installation features not present in the simulation geometry. A difference between the two data sets is also observed near the wall, where the experimental data is greater, which can again be attributed to the inability of the boundary layer probes to obtain data very near the wall.

4.1.2.7   Test Case 2 – Surface Pressure Distributions.

Streamwise pressure distribution comparison with experimental data is shown in Figure 4.13 in accordance with the experimental data locations shown in Figure 4.2. The dominant features are present in the CFD distributions, except again for capturing the constant-pressure region in the $\phi = 180°$ and $90°$ distributions. However, even in the
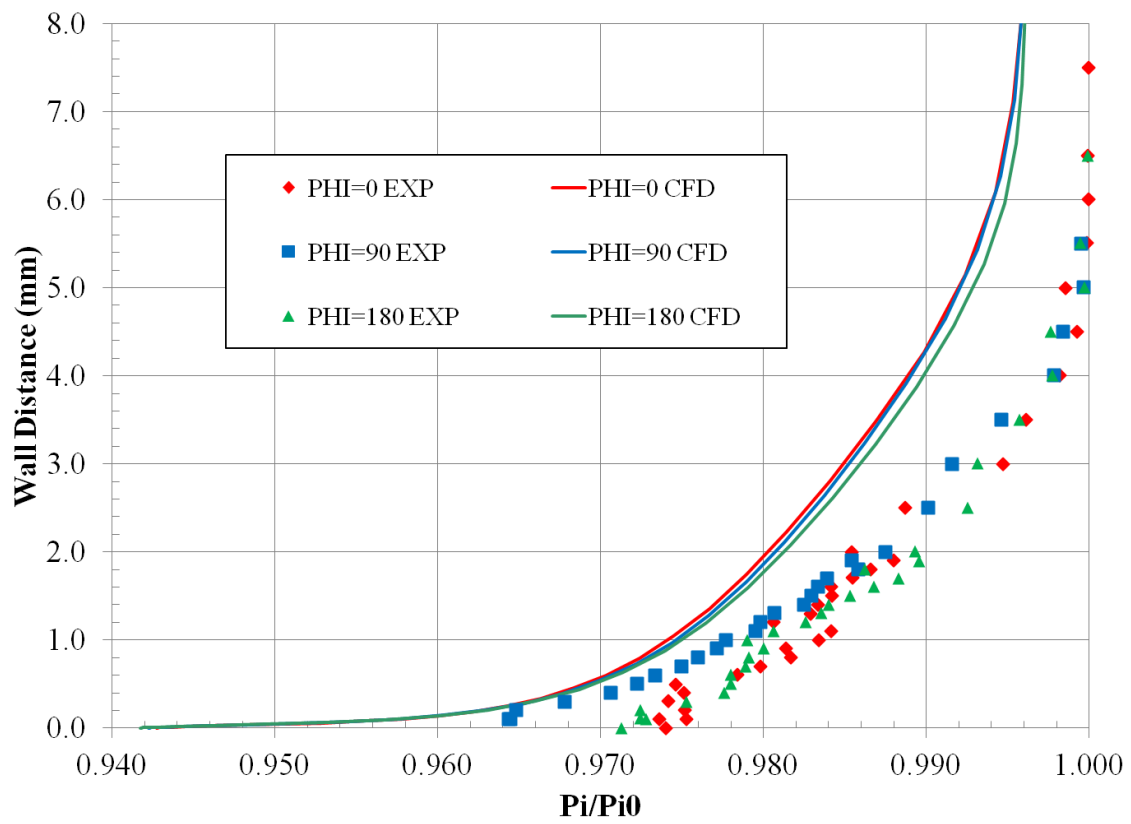
Figure 4.12: Test Case 2 boundary layer profile comparison.

regions of separated flow the maximum error is small: 0.71% for $\phi = 0°$, 0.77% for $\phi = 90°$, and 1.58% for $\phi = 180°$.

Circumferential pressure distribution comparison with experimental data is shown in Figure 4.14 in accordance with the experimental data locations shown in Figure 4.2. The location at the start of the separated region ($s/D_1 = 2$) has the largest error compared to experiment, but the maximum error is only 1.16%. Downstream of the onset of separation, the CFD simulation matches experiment very well, with a maximum error of 0.38% for $s/D_1 = 3$ and 0.20% for $s/D_1 = 4$.
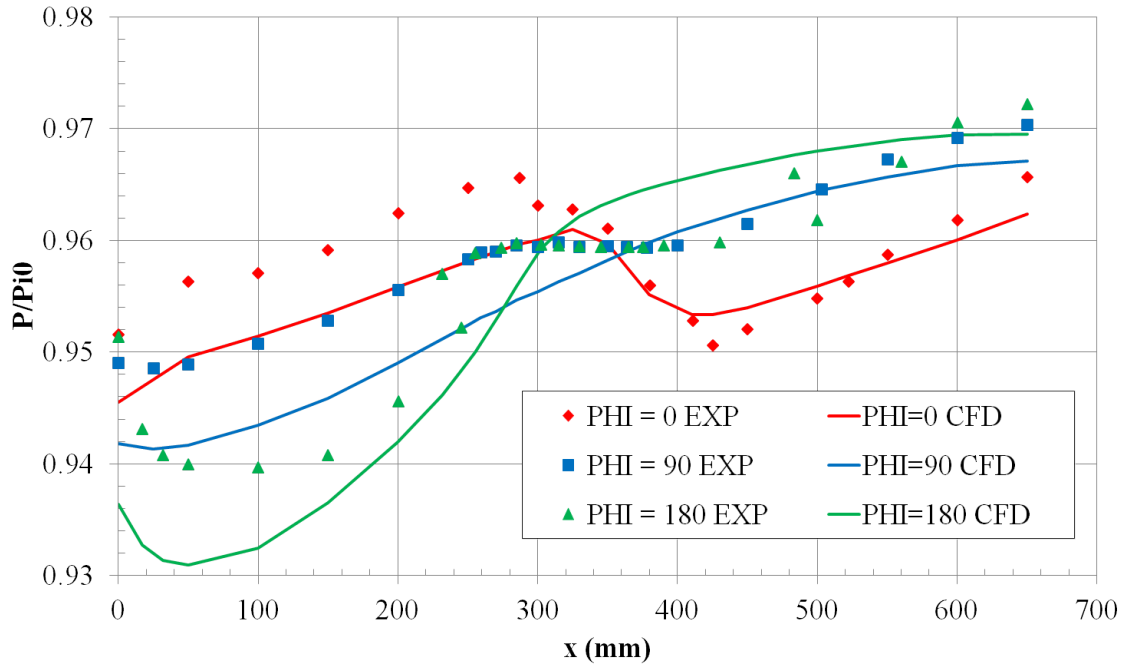
Figure 4.13: Test Case 2 streamwise pressure distribution comparison.

4.1.2.8   Test Case 2 – Performance Calculations.

The provided experimental value for recovery is 0.9931. The computed value from the CFD simulation is 0.9918, a difference of only 0.13%. The provided experimental value of distortion coefficient is 0.0051. The computed value from the CFD simulation is 0.0041,

107
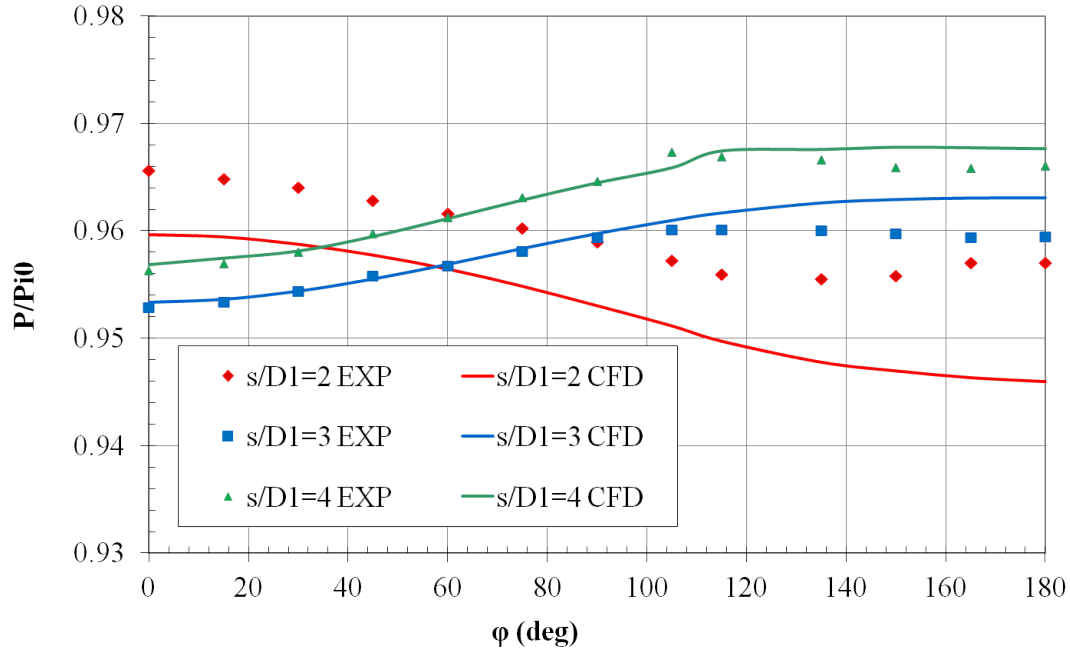
Figure 4.14: Test Case 2 circumferential pressure distribution comparison.

which is a closer match than for Test Case 1 due to the less severe flow separation and thus more uniform flowfield at the AIP.

4.1.3   Conclusions from the Validation Study.

The accuracy of results from the validation study meet or exceed those achieved by PAW participants. The near-wall behavior matches experimental data well. The average surface pressure error for Test Case 1 is 1%, while the average surface pressure error for Test Case 2 is only 0.4%. However, the simulation in the region of separated flow could be improved. To this end, the low-Reynolds number turbulence model option is used henceforth with an appropriately resolved grid, described in the next section.

4.2   Grid-Convergence Study

This section reports the results of a grid-convergence study performed using the methods discussed in Section 3.4. In contrast to many of the grid-convergence studies

reviewed in Section 3.4 that use a single figure of merit to determine convergence, three figures of merit are used which are related to the characterization parameters: size, $TAVHOT$, and $TFAV$. Hot streak size is a characterization parameter of interest, $TAVHOT$ is used in calculating hot streak magnitude and location, and $TFAV$ is used in calculating the distortion.

The LD2_AR10 nozzle is chosen for the study since it was the first nozzle designed for this research and has one of the highest degrees of turning. The small L/D and large AR should result in higher gradients compared to nozzles with less severe flowpaths (e.g., the LD4_AR4 nozzle, see Figures 3.8 and 3.10). Therefore, if grid independence is found the LD2_AR10, the other nozzles should display similar convergent behavior since they should contain lower gradients. Three levels of grid refinement are investigated for the LD2_AR10 nozzle. As stated in Section 3.4, the three grids are created by subsequently doubling the spacing on the nozzle surface in the axial and circumferential directions from an initial mesh. The three grids are denoted as "coarse", "medium", and "fine", with "coarse" being the initial mesh. An example of the three refinement levels at the nozzle exit is shown in Figure 4.15. The average surface spacing in meters, h, and the resulting number of grid cells in millions, N, for each refinement level are given in Table 4.2.

Table 4.2: Grid Resolution Parameters

Grid	$h(m)$	$N(M)$
Coarse	0.0119	36
Medium	0.0079	60
Fine	0.0052	106

The results of the grid-convergence study are given in Table 4.3. Hot streak size is the limiting figure of merit because the error of the medium grid (e^{32}) is above the desired threshold of 2.5%. The error of the fine grid (e^{21}) is below this threshold, and therefore,
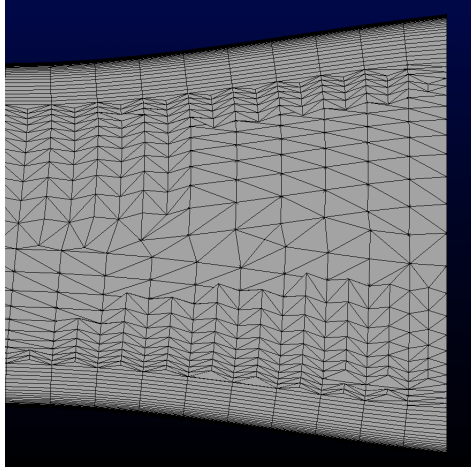
(a) Coarse
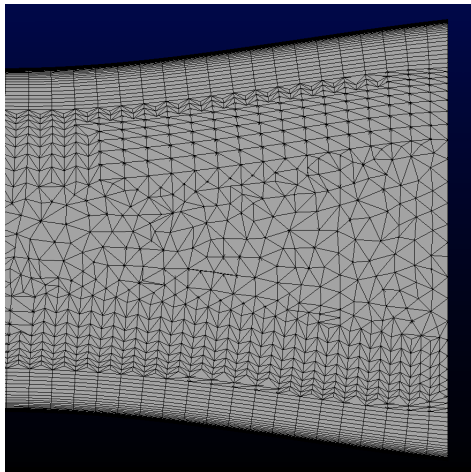
(b) Medium
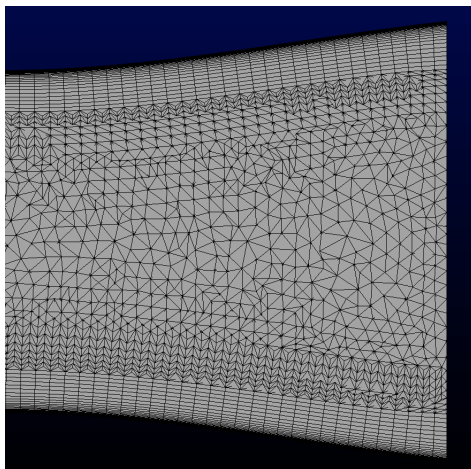
(c) Fine

Figure 4.15: Grid Density at Nozzle Exit for Grid-Convergence Study

the fine grid spacing is chosen for the remainder of the nozzles. The GCI for the fine grid is also reported in the table, with size having the largest uncertainty at 4.45%. All figures of merit display near or above second-order convergence in p. Second order convergence is also displayed in the "zero-grid" linearity tests shown in Figure 4.16, which all exhibit near-linear behavior. The goodness-of-fit parameter, R^2, for each curve fit is given in Table 4.3 and confirms the linear behavior.

Table 4.3: Grid Resolution Study Results

Parameter	e^{32}	e^{21}	GCI^{21}_{fine}	p	R^2
Size	3.61%	2.35%	4.45%	2.69	0.98
TAVHOT	0.32%	0.47%	1.60%	1.67	0.97
TFAV	0.72%	1.27%	2.55%	2.57	0.98
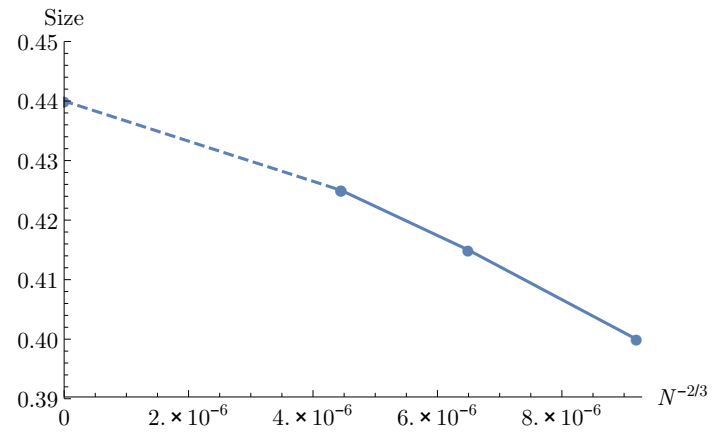
(a)
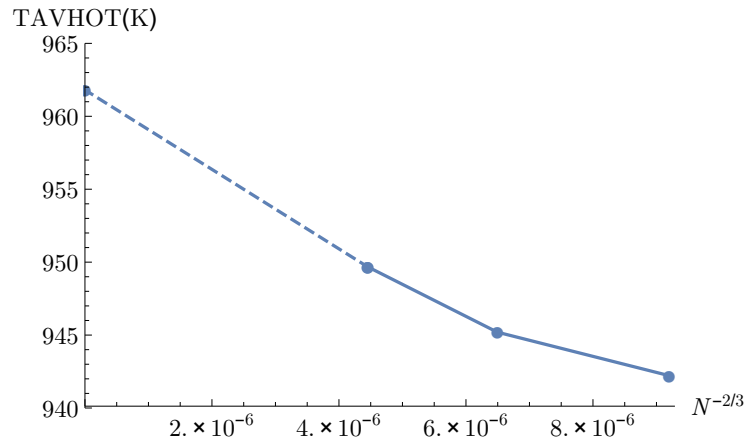
(b)
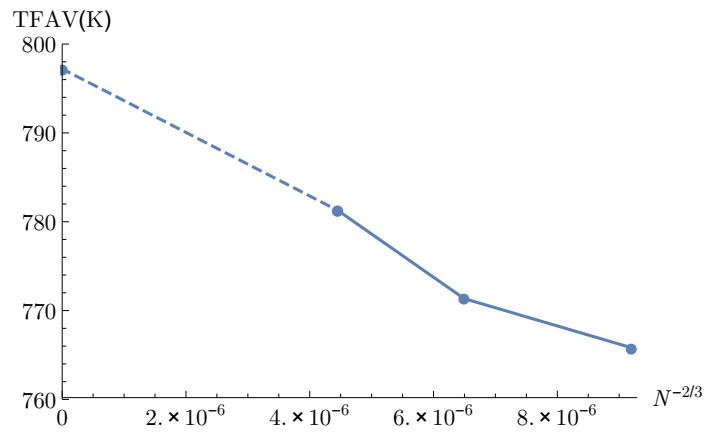
(c)

Figure 4.16: Grid Convergence Study Linearity Plots

4.3 Nozzle Solutions

This section includes an in-depth examination of each nozzle solution computed using the methods discussed in Section 3.5 with the K-ω SST turbulence model. The no-swirl and swirl cases for each nozzle are examined in turn. The section begins with the LD2_AR10 nozzle (the first designed for this research) and continues with each $AR = 10$ nozzle. The $AR = 4$ nozzles are discussed next in order of increasing L/D. Centerline Mach contours, centerline surface pressure, and surface flows are computed for each case. Streamwise vorticity and total temperature contour cross-sections are computed at the mixing plane, the two inflection points, midway between the second inflection point and the throat (denoted as "Nearing Throat" in the following figures), the throat, and the exit. These streamwise locations are shown in Figure 4.17. Thorough examination of the flowfield reveals a connection between the flow physics within the nozzle and the resulting exit temperature distribution and how altering the nozzle geometry affects this relationship.
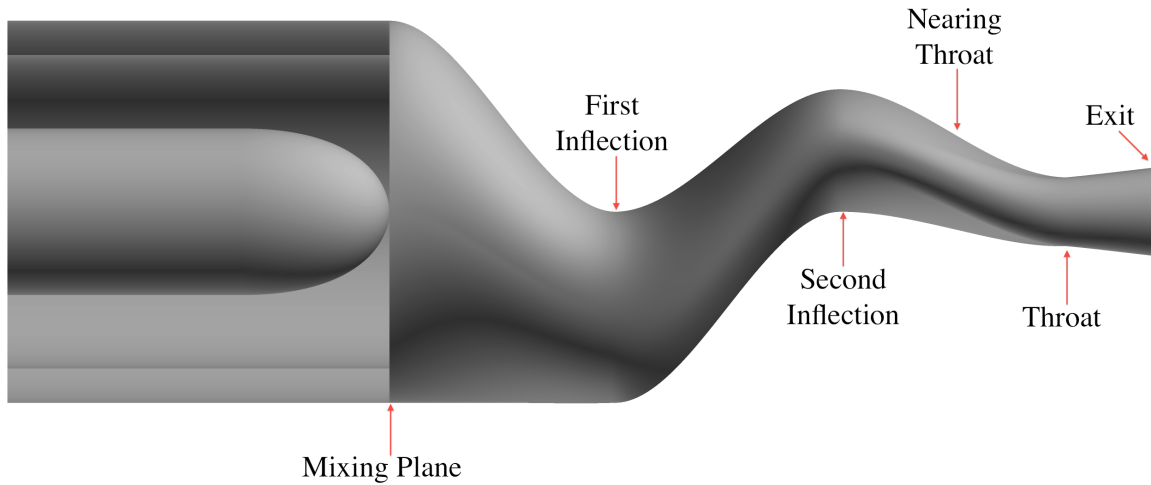
Figure 4.17: Streamwise location of cross-sections.

4.3.1   *LD2_AR10, No-swirl.*

Important flow features for the LD2_AR10 nozzle can be seen in Figure 4.18. The difference in Mach between the two streams is observed in the entrance section due to matching the inflow pressure boundary condition at different temperatures. Flow separation off the tailcone is also shown by a region of low Mach at the surface and just downstream of the tailcone. The flow is accelerated around the first upper curve, as well as the second lower curve. Due to the large amount of streamline curvature, an area of flow separation occurs downstream of the first curve, with a reattachment point that "jumps over" the second upper bend. The flow becomes supersonic very near the designed throat location at the bottom surface and slightly upstream of the throat on the upper surface. The slanted throat is due to the final contraction of the nozzle occurring primarily near the upper surface as the radius of curvature at the second inflection point is larger at the upper surface than the lower surface. The flow behavior is confirmed by examination of non-dimensional static pressure ($P_{st}/P_{st,amb}$) at the surface along the upper and lower centerlines in Figure 4.19. Flow acceleration due to streamline curvature is represented by decreases in the surface pressure, while flow separation is represented by the region of constant pressure near $x/L = 0.5$. At the exit $P_{st}/P_{st,amb} < 1$ which means the nozzle is slightly overexpanded.

As discussed in the literature review, the transition of cross-sectional area and change in streamline curvature induces secondary flow in ducts and nozzles. The development of secondary flow through the nozzle can be seen in Figure 4.20 via contours of streamwise vorticity. All contours plots in this and the following sections are aft-looking-forward. The progression of the flowfield begins at the mixing plane, where a pair of high-vorticity regions of opposite sense originate from the flow separation off the tailcone. These regions represent a pair of counter-rotating vortices. The flow separation is asymmetric, as shown by the tailcone surface flow in Figure 4.21. Asymmetry in separation off spheres and spheriods at high Reynolds number, such as the nozzle tailcone, is discussed in Section
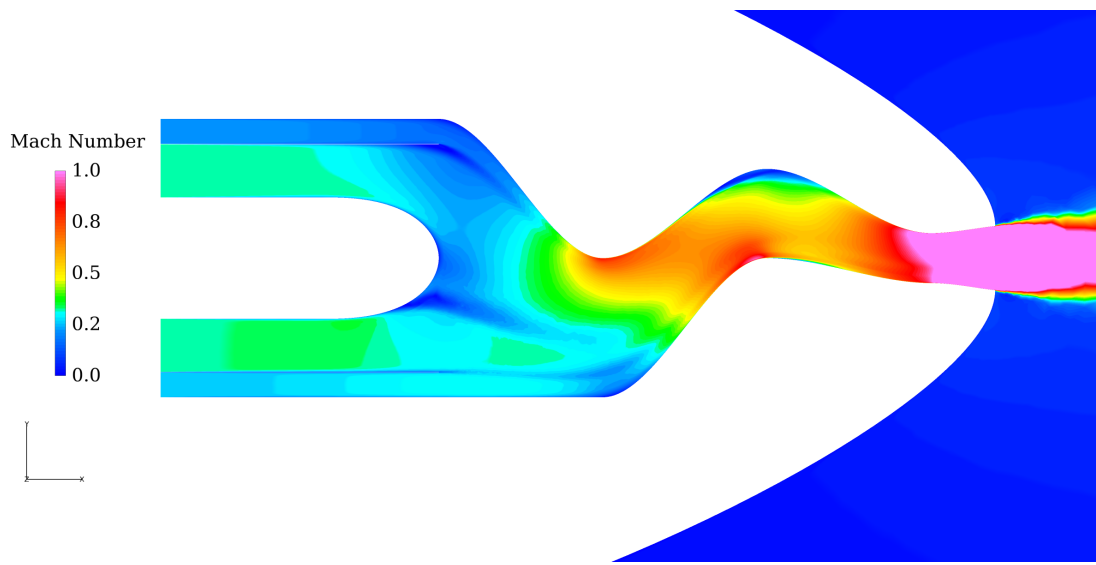
Figure 4.18: Centerline Mach number contours, LD2_AR10.
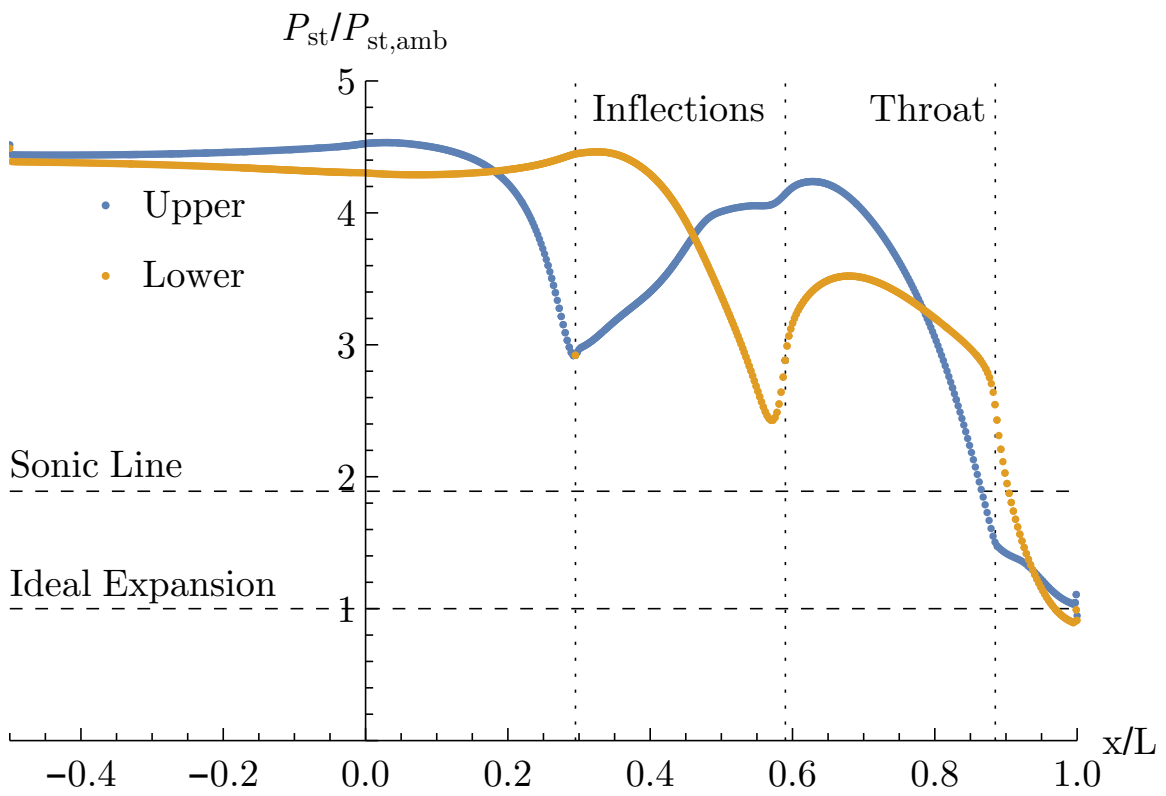
Figure 4.19: Centerline surface $P_{st}/P_{st,amb}$, LD2_AR10.

2.5. Vorticity is also generated near the inner surface of the liner due to the influence of backpressure from the upper curvature as it pushes the flow away from the centerline. The opposite direction of vorticity on either side indicates the dominance of the v_z component of the streamwise vorticity:

$$\omega_x = \hat{i}\left(\frac{\partial v_z}{\partial y} - \frac{\partial v_y}{\partial z}\right) \tag{4.2}$$

At the first inflection point, flow from the upper portion of the nozzle migrates down the sides due to the change in streamline curvature at the upper surface. This motion generates vorticity at the sidewalls, where the sign indicates dominance of the v_y component in Equation 4.2. Weaker vorticity of the opposite sense continues due to the mixing plane shear layer and is spread out from the mixing plane due to the lateral divergence of the cross-sectional area. Residual vorticity from the outer portion of the liner has an opposite sense as the inner liner, which indicates the downward trajectory of that region of flow caused by the upper curvature dominates the vorticity. The pair of counter-rotating vortices is clearly observed in the center of the plane but is shifted from the centerline due to the asymmetric separation. At the second inflection point, the dominant vorticity features are two pairs of counter-rotating vortices at the upper sidewalls. These are formed due to the roll-up and separation of flow just upstream of the second inflection point. This phenomenon is shown in the surface flow in Figure 4.22 as pairs of spiraling foci. The shear layer and tailcone vortices persist at the second inflection point. Downstream of the second bend a complex flow has developed. The tailcone vortex pair are still strongly influencing the flowfield. At the sidewalls, the original pair of counter-rotating vortices are present, but one vortex emerges as the stronger of the pair. On the port side this is the vortex of negative sense, while on the starboard side, the positive vortex is stronger. The opposing sense of the two vortices is due to an interaction between the vortex and the changing geometry: as the nozzle contracts, conservation of angular momentum increases the strength of rotating flow—a phenomenon known as vortex stretching. The nozzle is also experiencing lateral

116

divergence, which pulls the vortices to the sidewalls. So the vortex which is spinning in the direction of the lateral divergence is strengthened due to vortex stretching, while the vortex spinning in the opposite direction is weakened as it competes with the direction of the pull. At the throat, the tailcone vortex pair persist but are separated due to lateral divergence. At the sidewalls the dominant vortex in each pair reaches maximum strength. A similar pattern exists as the flow expands to the exit, and while the flow has accelerated through the divergent section of the nozzle, the vortices are reduced in strength somewhat due to the reduction in vortex stretching as the nozzle expands and the lack of lateral divergence.

The movement of the flow is further understood by examination of the surface flow in Figure 4.22. The migration of the upper portion of the flow down and around the sides due to the first bend is observed, as well as the movement of the lower portion of flow upward due to the second bend. The two regions coalesce at the separation line near the second inflection point, where the vortex foci are clear. The reattachment line is seen downstream of the second bend. Lateral divergence of the flow is shown at the sidewalls and between the second inflection point and the throat.

The origins of hot streak phenomena are revealed by examining the development of the total temperature distribution throughout the nozzle, as seen in Figure 4.23. This distribution can be explained through its relation to streamwise vorticity and other complex physics occurring the nozzle, such as flow separation. At the mixing plane the two streams are separated by the liner, with some mixing observed at the upper region of the core section, where back pressure from the upper curvature of the nozzle forces some of the bypass flow into the core region upstream of the mixing plane. This increase in the pressure at the upper mixing plane is shown in Figure 4.19 at $x/L = 0$ and can be inferred from the region of lower Mach flow in Figure 4.18. At the first inflection point the migration of the bypass flow from the upper portion of the nozzle down and around the sides to the lower portion is demonstrated. Also seen is initial mixing of the two streams in the thermally-

(a) Mixing Plane

(b) 1st Inflection

(c) 2nd Inflection

(d) Nearing Throat

(e) Throat

(f) Exit
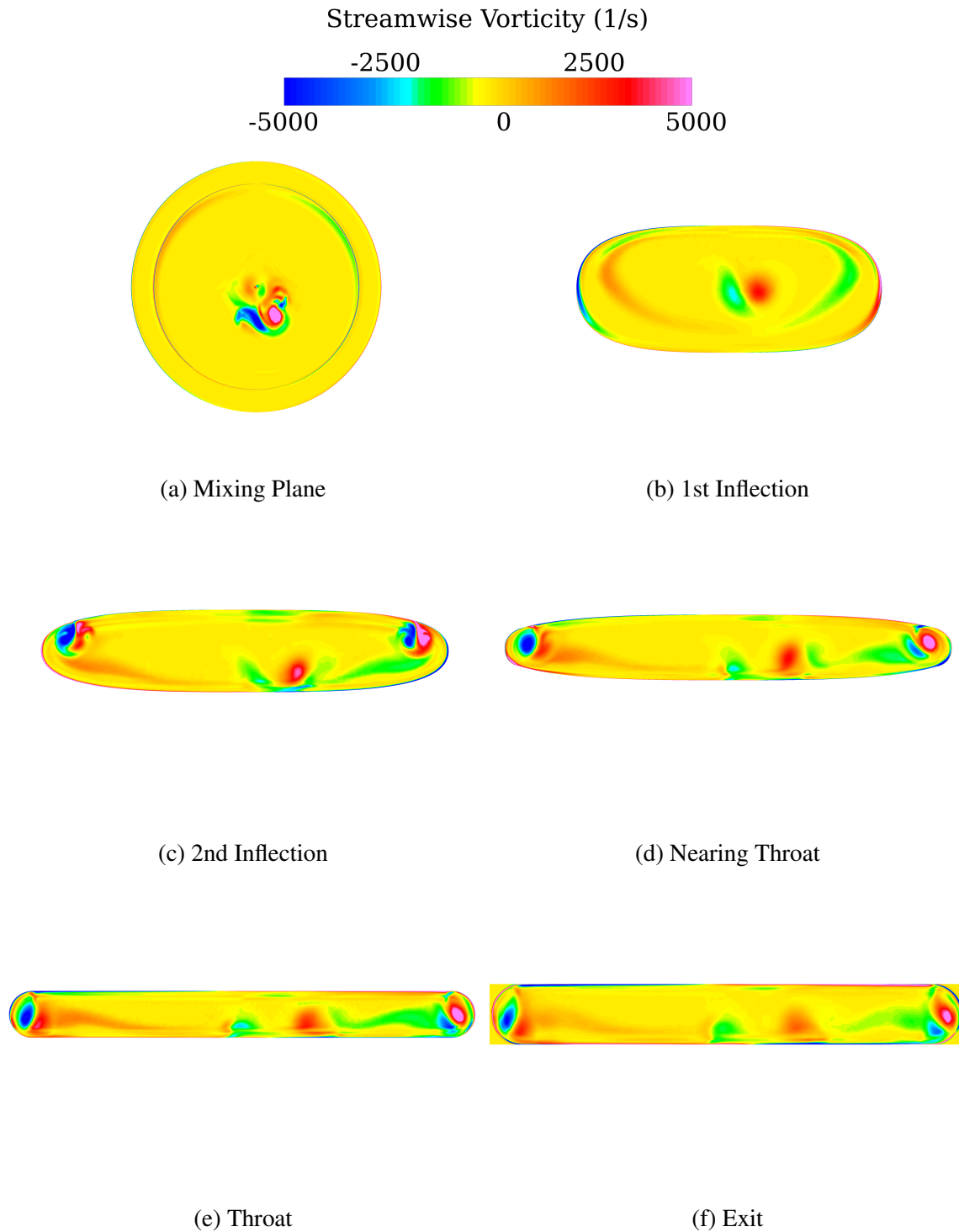
Figure 4.20: Progression of vorticity development, LD2_AR10.
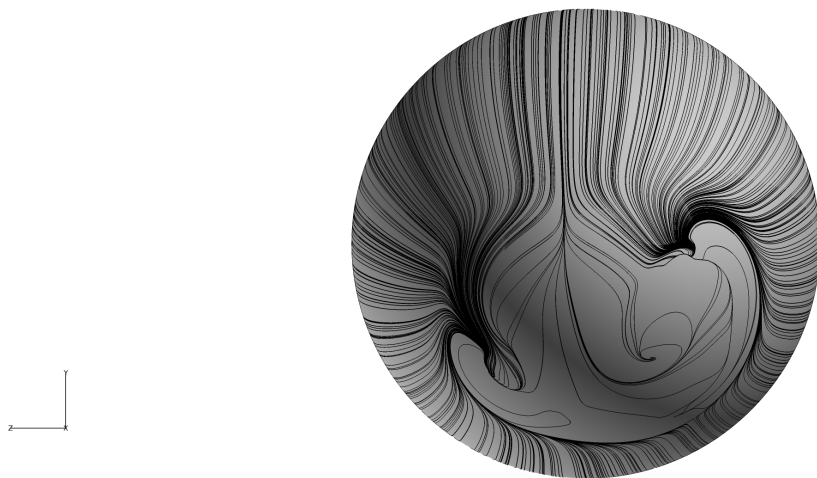
Figure 4.21: Tailcone surface flow, LD2_AR10.
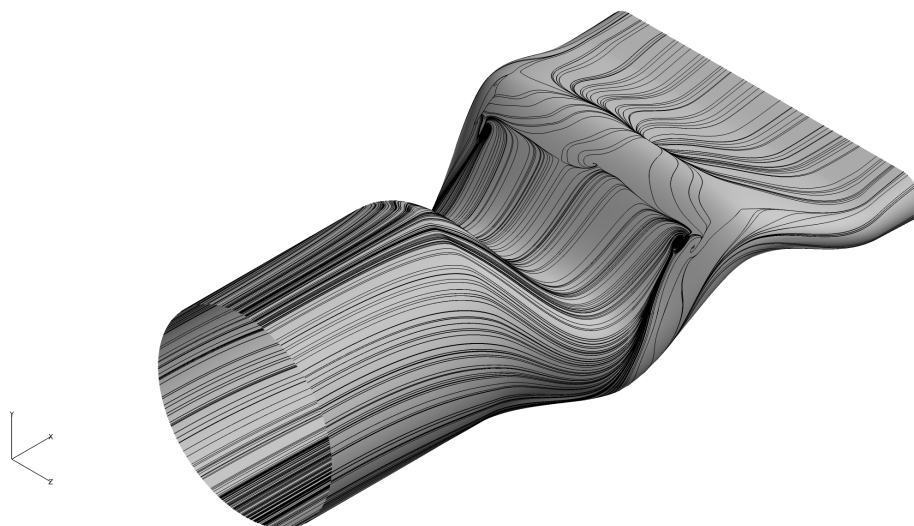
Figure 4.22: Surface flow, LD2_AR10.

stratified shear layer. The distribution is slightly asymmetric as the tailcone vortices in the core have migrated downward due to the upper surface curvature. The downward trajectory of the vortices is seen in the low-Mach region downstream of the tailcone in Figure 4.18. At the second inflection point the relationship between secondary flow features and the temperature distribution is observed. Flow separation at the upper surface results in a flow in the mid-temperature range due to enhanced mixing in the recirculation region. Near the lower surface the strong starboard tailcone vortex entrains cooler bypass flow from the lower surface into the core. At the sidewalls, the core flow is drawn outward by the strong sidewalls vortices. Nearing the throat the previous features are intensified. The upper region is heated downstream of the reattachment point due to the recirculation of cooler flow in the separated region. At the lower region the strong tailcone vortex continues to draw in bypass flow, while hot core flow impinges on the lower surface as the tailcone vortices push hot flow downward—the first indication of a surface hot streak. At the sidewalls the strong vortices have essentially "trapped" a large portion of the cooler bypass flow, and the entrainment of core flow is clearly seen. At the throat a "whale tail" shape has formed, with the core flow heavily influencing the hot upper region, the central vortex continuing to entrain cooler flow into the core, the sidewall vortices continuing to trap bypass flow, and the persistence of a distinct thermal shear layer near the lower surface. The lower surface hot streak widens with the lateral divergence of the nozzle. A similar but expanded distribution is seen at the exit, with slightly more entrainment of hot flow towards the sidewalls.

Total Temperature (K)

(a) Mixing Plane

(b) 1st Inflection

(c) 2nd Inflection

(d) Nearing Throat

(e) Throat

(f) Exit
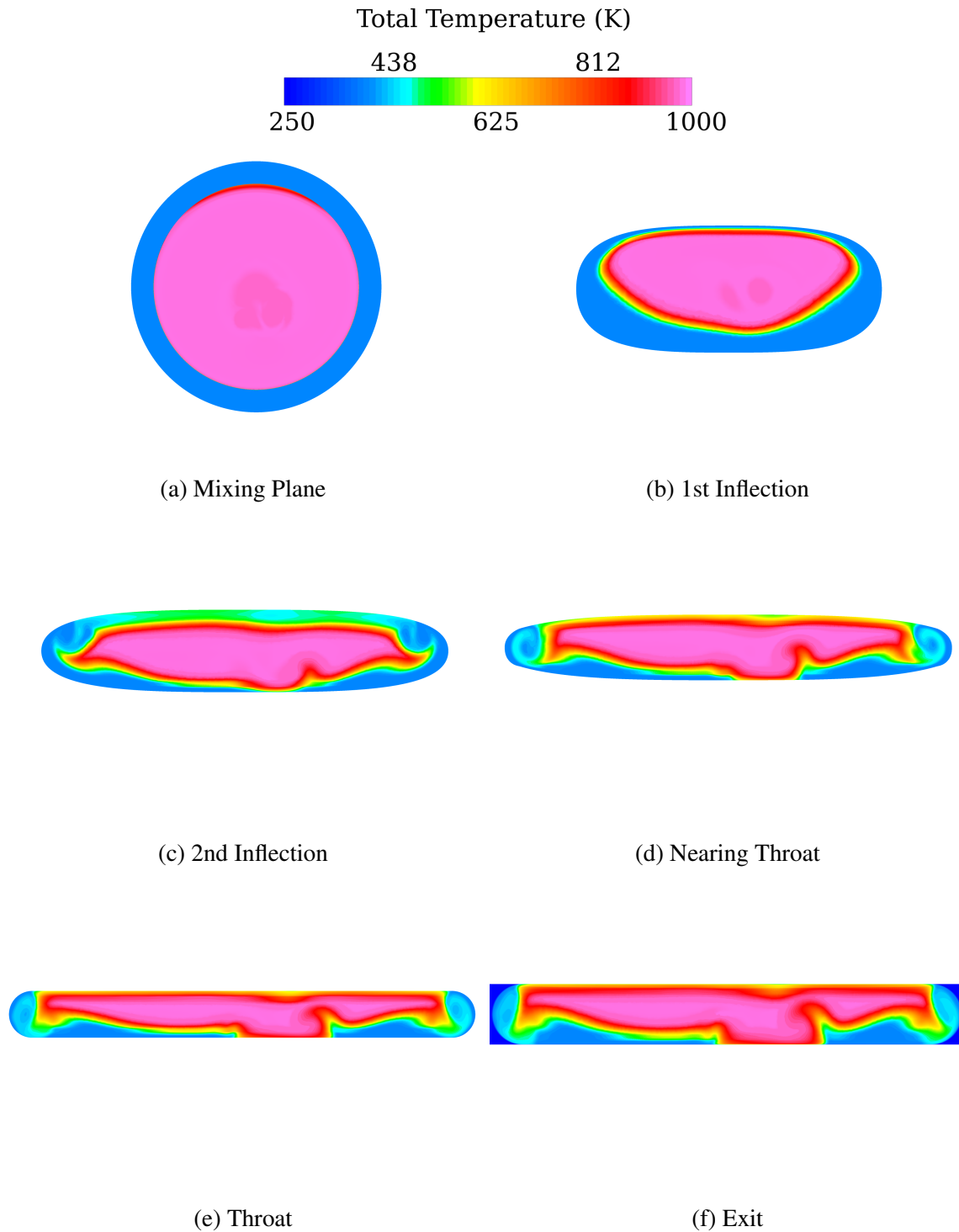
Figure 4.23: Progression of temperature distribution, LD2_AR10.

4.3.2   LD2_AR10, Swirl.

Examination of the LD2_AR10 nozzle with swirl reveals stark differences from the no-swirl solution. The contours of Mach number in Figure 4.24 show a much different tailcone separation behavior. The same areas of flow acceleration are observed but with less separation at the second bend. The throat location is similar. Examination of $P_{st}/P_{st,amb}$ at the centerline upper and lower surface confirms the reduction in flow separation at the upper bend, where the flat region of pressure is not present in Figure 4.25. The lower surface pressures are nearly identical. Like the no-swirl solution, the nozzle is overexpanded at the exit near the lower surface. The dramatic difference in tailcone separation is observed in the surface flow, shown in Figure 4.26. Here the swirling flow has repressed the formation of a pair of counter-rotating vortices, instead driving the flow to a single vortex focus.
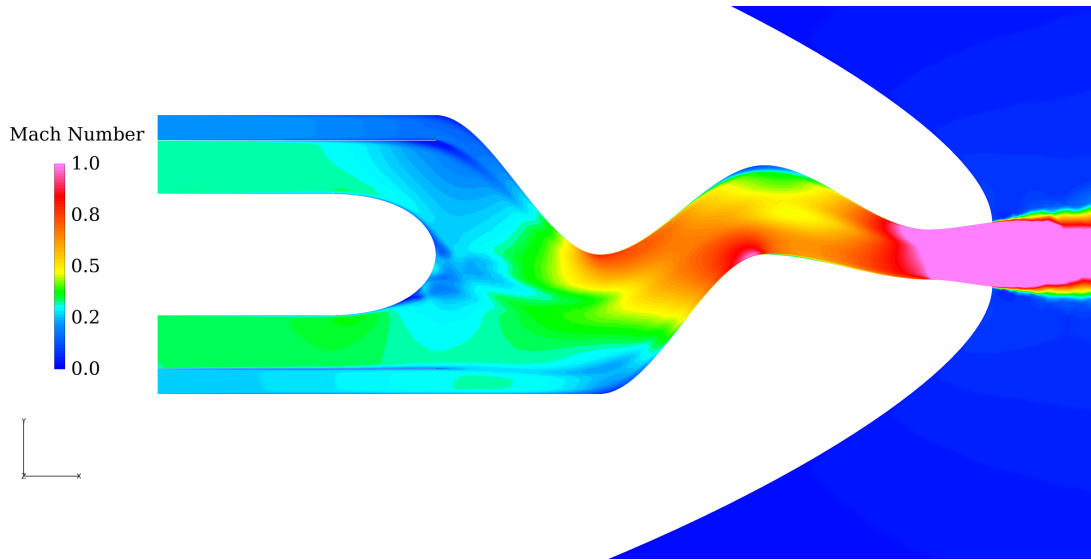
Figure 4.24: Centerline Mach number contours, LD2_AR10 with swirl.

Difference from the no-swirl case are also shown in the development of streamwise vorticity in Figure 4.27. At the mixing plane, a tight spiral of vorticity in the direction of the swirl is observed near the center of the mixing plane. The central vortex is generated due to conservation of angular momentum, which causes the swirl velocity to increase
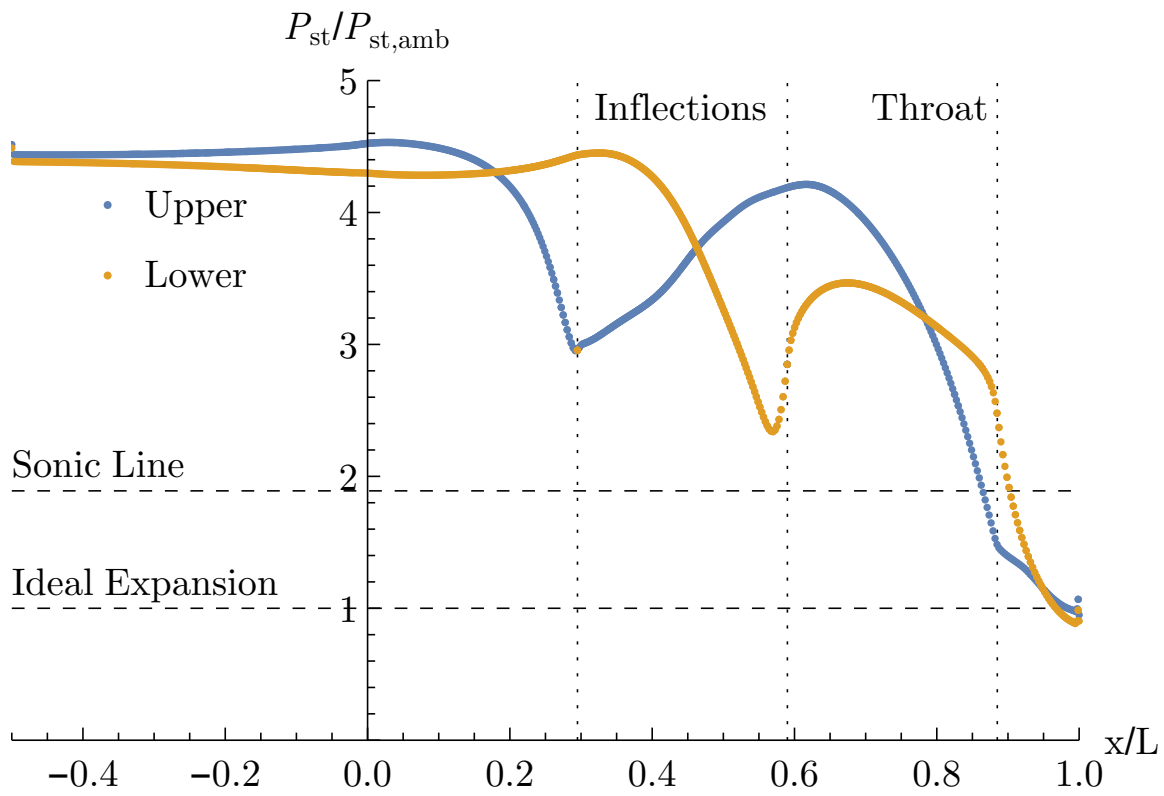
Figure 4.25: Centerline surface $P_{st}/P_{st,amb}$, LD2_AR10 with swirl.
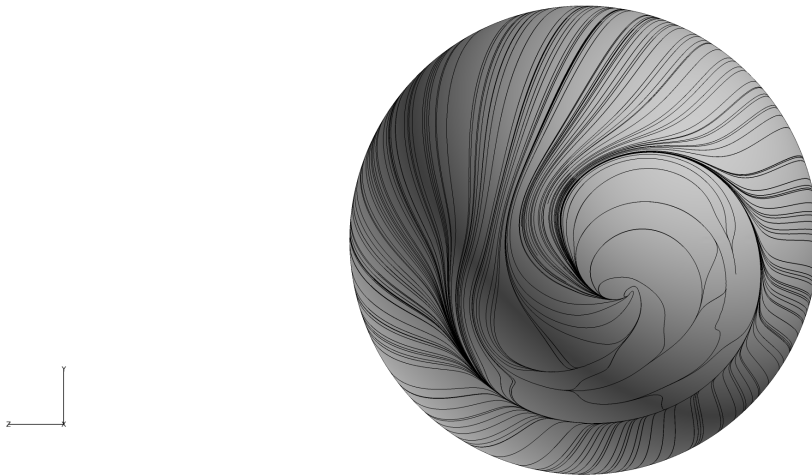
Figure 4.26: Tailcone surface flow, LD2_AR10 with swirl.

as the radius of the centerbody decreases, terminating at the mixing plane. At the first inflection point, a stark difference from the no-swirl solution is seen in the form of a single strong vortex from the tailcone. The same central vortex was seen by Sobota and Marble in their experiments with swirl [50]. The sidewall vorticity due to changes in cross-sectional area is still present, but the positive vorticity from the mixing layer has diminished. The reduction of vorticity from the mixing layer is caused by the competing forces acting on the flow on that side of the nozzle. The swirl velocity is in the opposite direction as the lateral divergence. The opposing directions causes a decrease in the v_z component of the streamwise vorticity in Equation 4.2. On the starboard side, the swirl is in the direction of the lateral divergence, and the line separating flow with positive and negative z components of the velocity vector is shifted from the centerline toward the port side. At the second inflection point, the strong central vortex persists. Similar to the no-swirl case, pairs of counter-rotating vortices have developed at the sidewalls, again due to the change in curvature direction and flow separation. Also present at the upper portion of the nozzle is an additional pair of counter-rotating vortices. The generation of these vortices is due to flow separation near the centerline, as seen in the surface flow depicted in Figure 4.28. Two vortex foci are clearly seen just upstream of the second inflection point; a version of the "owl-face of the first kind" as coined by Perry [10]. Also seen are the strong coalescence of the sidewall flow and foci for the pair of counter-rotating vortices at the sidewalls. Nearing the throat, the central vortex persists, while the sidewall vortices are strengthened due to continued vortex stretching. The swirl causes the starboard vortex pair to move downward compared to the no-swirl case. At the throat, the central vortex remains strong. The upper pair of vortices dissipate somewhat but are still present. At the sidewalls, the strong outer vortex on each side is strengthened due to the final contraction of the nozzle which induces more vortex stretching. At the exit, the patterns of vorticity are similar but weakened due to the expansion of the flow in the vertical directions.

124

Streamwise Vorticity (1/s)

(a) Mixing Plane

(b) 1st Inflection

(c) 2nd Inflection

(d) Nearing Throat

(e) Throat

(f) Exit
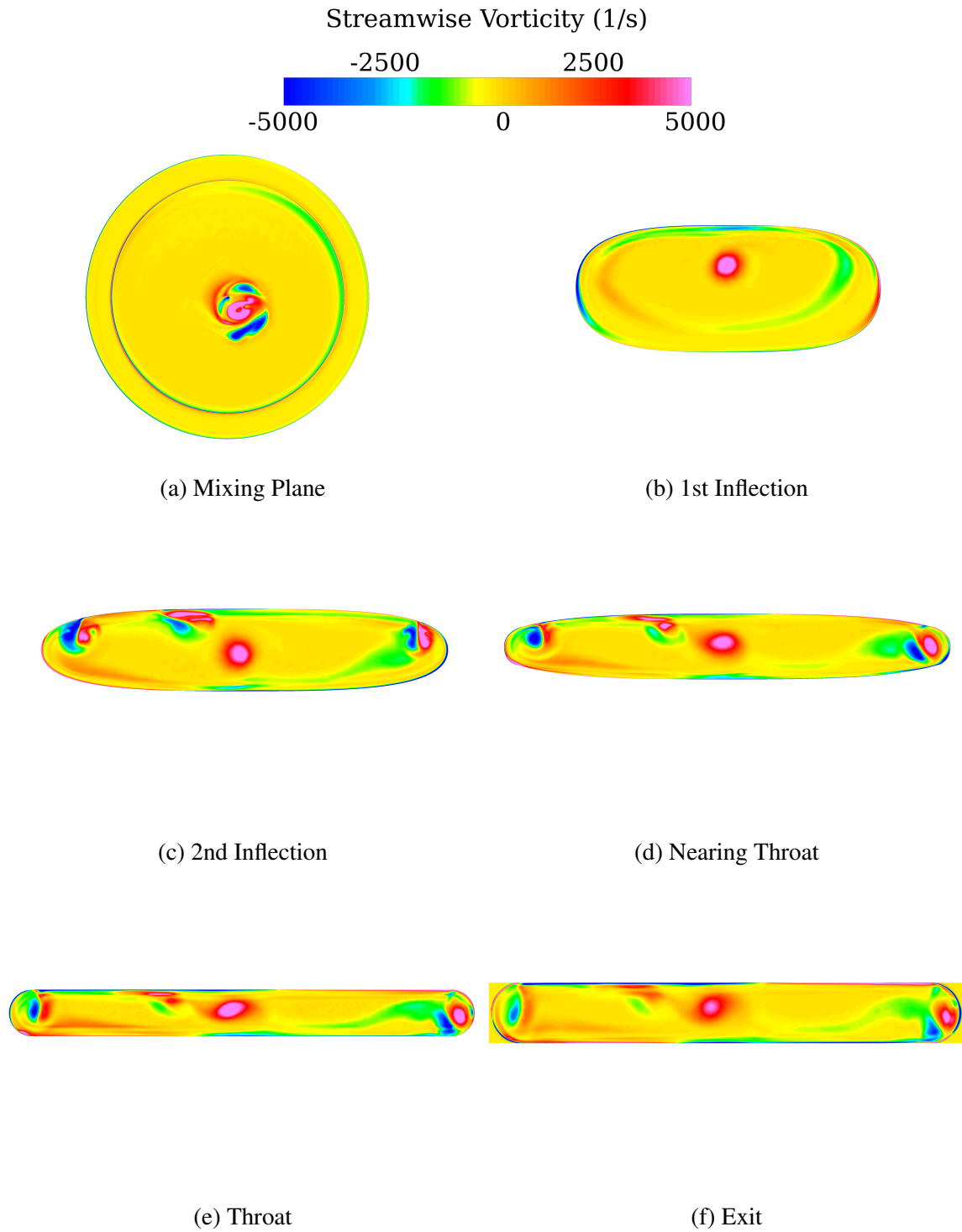
Figure 4.27: Progression of vorticity development, LD2_AR10 with swirl.
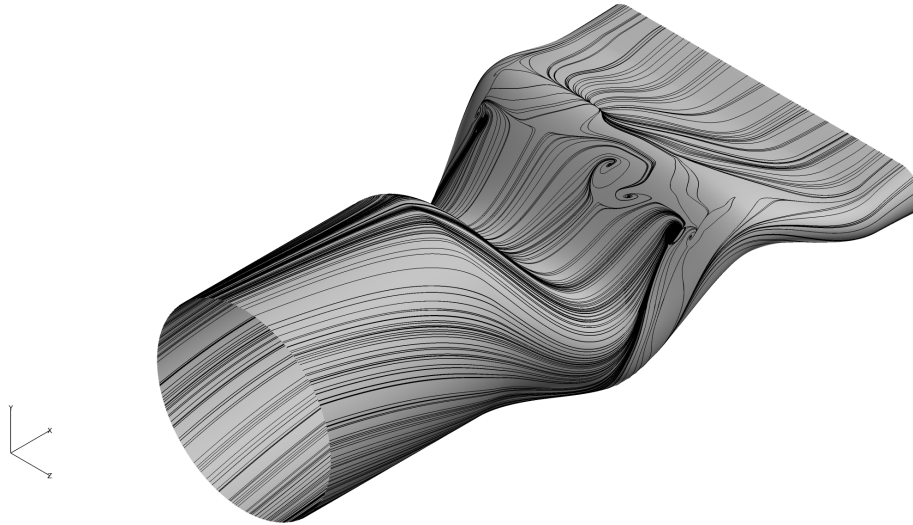
Figure 4.28: Surface flow, LD2_AR10 with swirl.

The development of temperature distribution throughout the nozzle is shown in Figure 4.29. At the mixing plane, the small amount of mixing between the streams at the upper portion of the liner due to backpressure from the streamline curvature is slightly rotated in the direction of the swirl compared to the no-swirl case. At the first inflection point, similar mixing is seen, but again the mixing layer is slightly shifted in the direction of the swirl. At the second inflection point, a very different and asymmetric pattern emerges. The separated region on the port side of the centerline at the upper portion of the nozzle occurs in a region of cooler bypass flow. The resulting counter-rotating vortex pair penetrates the hotter core region. At the sidewalls, the strong vortices begin to draw core flow to the outer edges while holding cooler bypass flow in place. The lower surface is different from the no-swirl case in that the strong central vortex remains in the middle of the core region, preventing additional mixing of this flow with the bypass flow at the bottom of the nozzle. Nearing the throat, the asymmetric pattern is exacerbated, first at the upper region where the vortex pair drives additional mixing in the area, seen by the higher temperature than at the second inflection point. Hot core flow impacts the upper surface, indicating the formation of a

126

hot streak. The appearance of an upper surface hot streak reveals a fundamentally different behavior between the swirl and no-swirl cases—hot streaks are present on the lower surface of the no-swirl solution and on the upper surface of the swirl case. At the sidewalls, the strong vortex pairs entrain core flow in opposite directions of rotation. At the throat, the upper vortex pair continues to mix the flow, while the extent of hot flow impacting the upper surface increases. The central vortex continues to entrain cooler flow from the bottom of the nozzle on the starboard side. The sidewalls exhibit continued mixing and entrainment of hot core flow. At the exit, a very similar temperature distribution is present, only expanded somewhat due to the vertical divergence.

(a) Mixing Plane

(b) 1st Inflection

(c) 2nd Inflection

(d) Nearing Throat

(e) Throat

(f) Exit
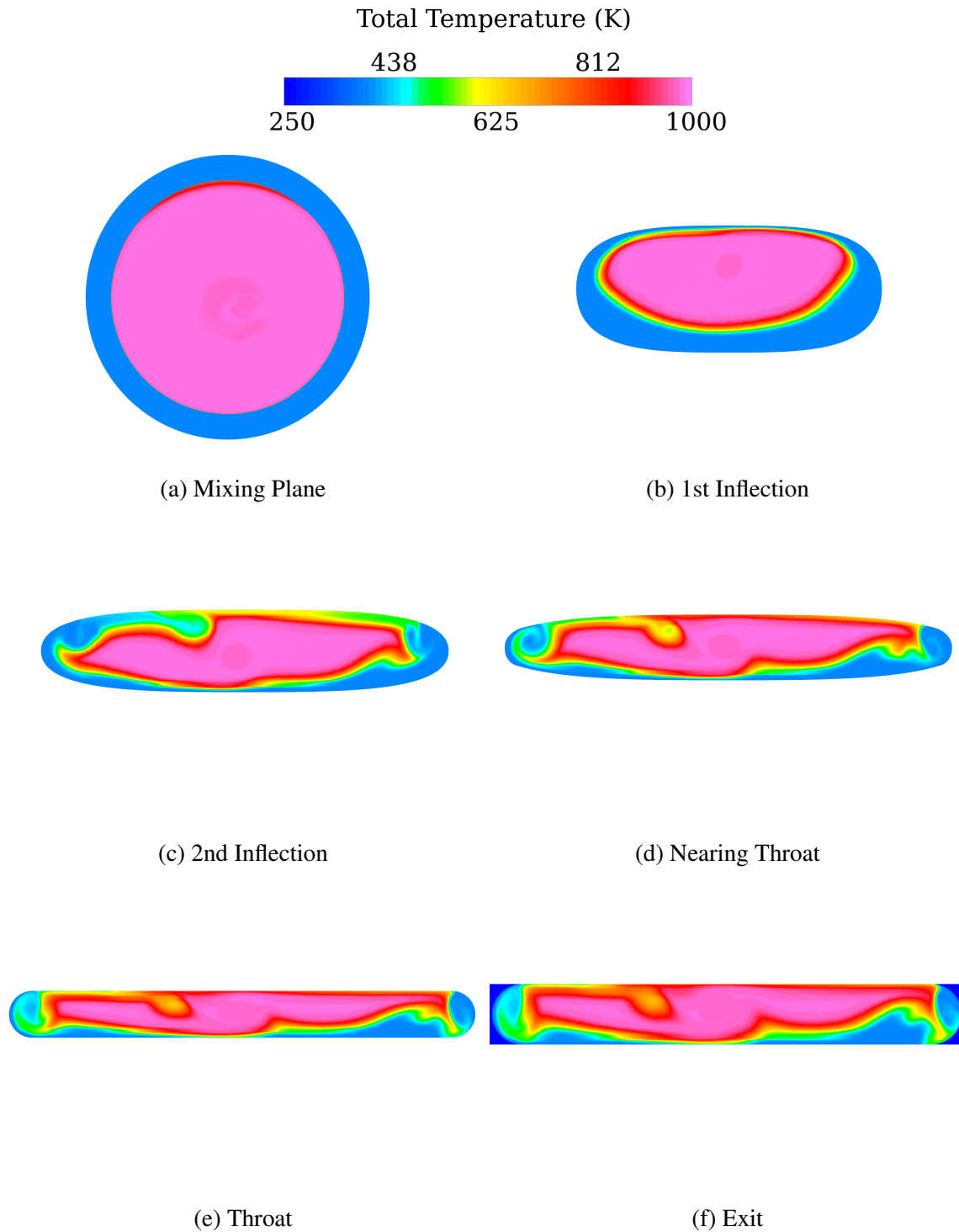
Figure 4.29: Progression of temperature distribution, LD2_AR10 with swirl.

4.3.3 LD3_AR10, No-swirl.

Centerline flow features for the LD3_AR10 nozzle are shown in Figure 4.30. Low-momentum fluid from the tailcone separation propagates downstream similar to the LD2_AR10 nozzle. The fluid does not accelerate around the two bends as much as the shorter nozzle due to the increase in radius of curvature. Also, the increased radius of curvature at the second inflection results in reduced flow separation. The flow reaches sonic velocity near the throat, and because the upper radius of curvature near the throat has increased compared to the shorter nozzle, the sonic line is more vertical. This behavior is further confirmed by examination of the upper and lower surface pressures in Figure 4.31. The lack of a flat pressure line at the second inflection demonstrates the reduction in flow separation. The reduction in flow separation is also confirmed by examination of the surface flow in Figure 4.32, where no separation line is observed as in the LD2_AR10 nozzle. Also, the values of $P_{st}/P_{st,amb}$ at the inflection points are higher than in the shorter nozzle, which implies lower momentum fluid in these regions. The nozzle is nearly ideally expanded at the exit.
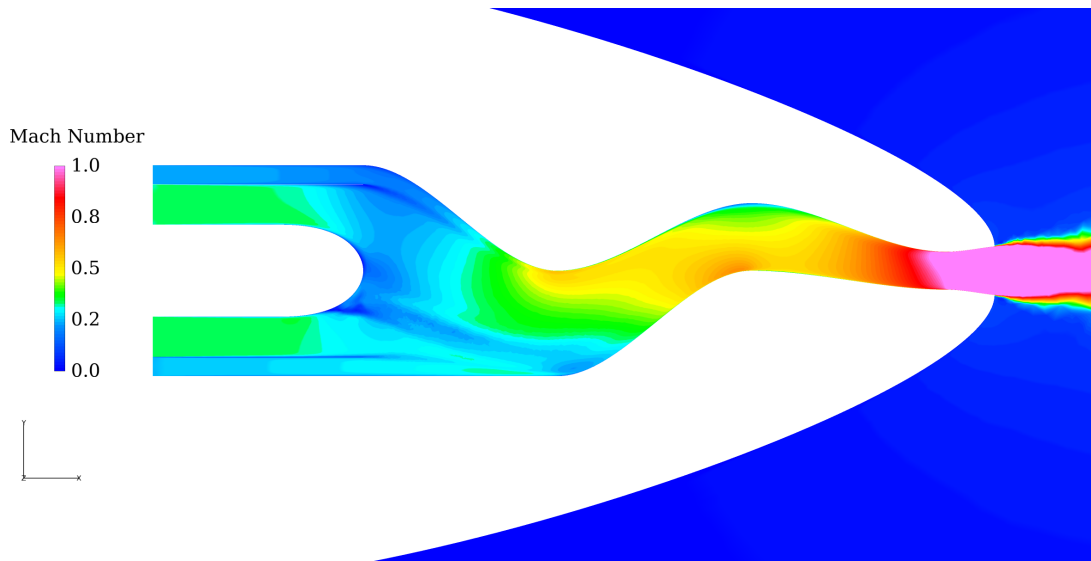
Figure 4.30: Centerline Mach number contours, LD3_AR10.
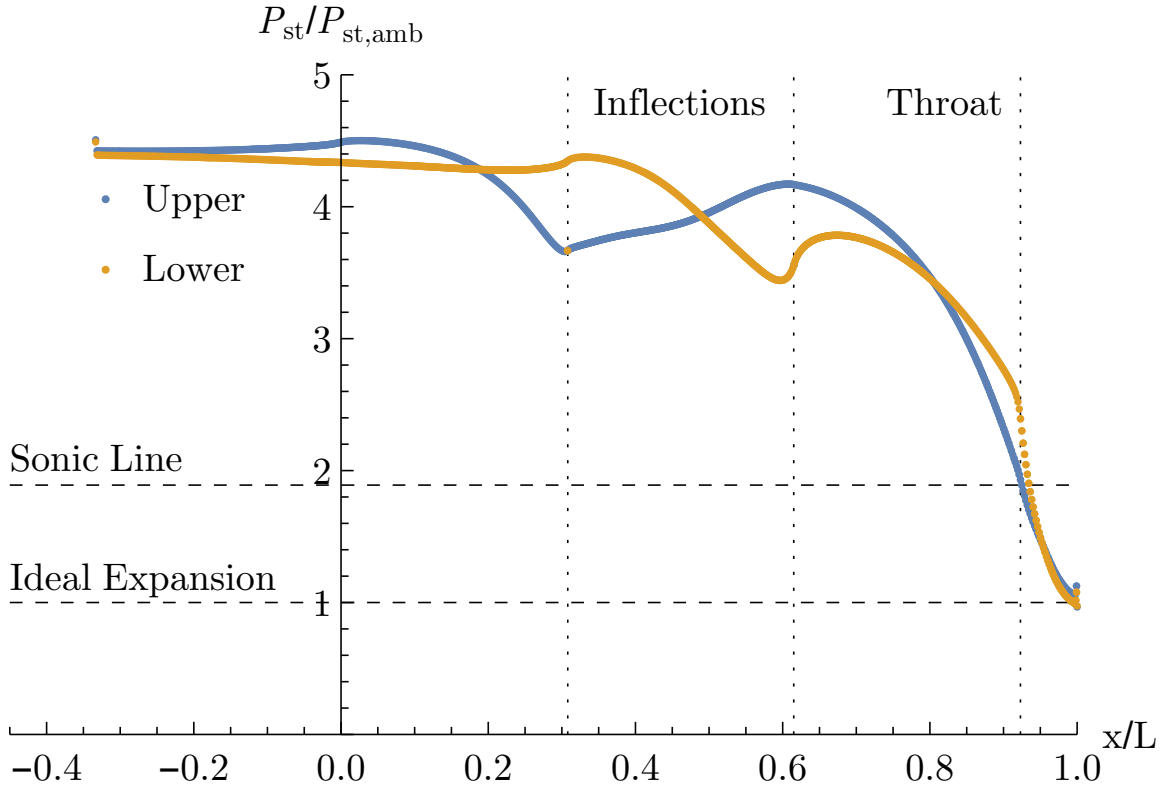
Figure 4.31: Centerline surface $P_{st}/P_{st,amb}$, LD3_AR10.

Examination of the streamwise vorticity at the mixing plane in Figure 4.33 reveals a pair of counter-rotating vortices. Backpressure due to the upper curvature is reduced because the first inflection point is further away from the mixing plane. Thus the influence of backpressure is reduced, as seen by a reduction in the vorticity generated at the inner liner. At the first inflection point, the pair of counter-rotating vortices appear near the lower surface of the nozzle. Compared to the shorter nozzle, the trajectory of the vortex pair is similar but with the added length to the first inflection point, the vortices end up at a lower position. Also, vorticity production at the sidewalls is evident due to the change in streamline curvature and transition in cross-sectional area. Vorticity in the mixing layer is reduced compared to the LD2_AR10 nozzle, again due to more gradual upper curvature reducing the migration of flow. At the second inflection point, the rollup of the sidewall
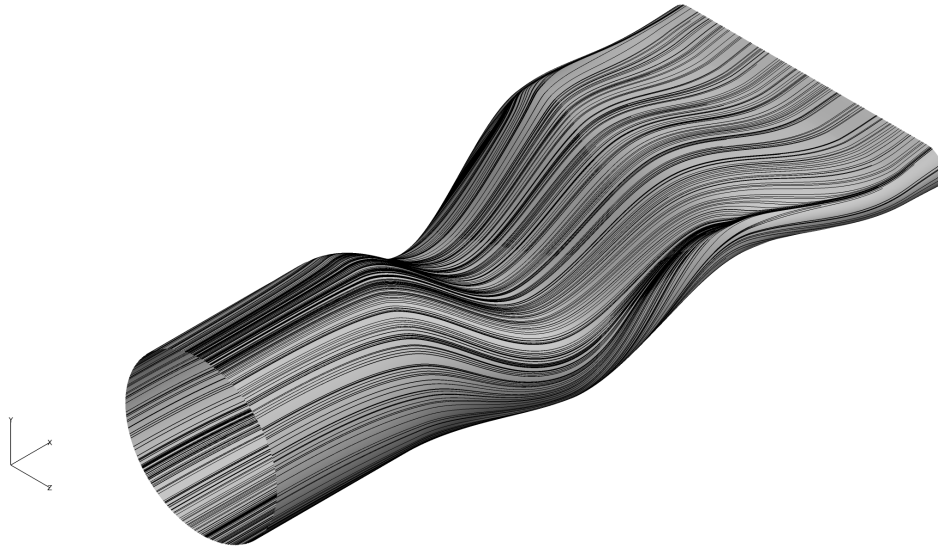
Figure 4.32: Surface flow, LD3_AR10.

vortices is clear. The generation of sidewall vortices is also clearly seen by the coalescence of surface streamlines in Figure 4.32. Compared to the shorter nozzle, the second vortex of the pair is weaker due to the lack of flow separation. The tailcone vortex pair remains well established at the bottom of the nozzle. Nearing the throat, the tailcone vortex pair begins to separate due to continuing lateral divergence. The sidewall vortices are present but again weaker than the shorter nozzle due to more gradual streamline curvature changes. At the throat, the tailcone vortices are established almost symmetrically about the vertical centerline. The sidewall vortices remain but are weakened by the final curvature change. At the exit, a similar pattern is established with continued weakening of vorticity due to the vertical expansion of the flow.

Temperature distribution for the LD3_AR10 nozzle is shown in Figure 4.35. At the mixing plane, the slight mixing that occurs in the shorter nozzle is not present since the region of backpressure is greatly reduced due to the more gradual upper curvature of the first inflection. At the first inflection point, the migration of bypass flow is shown, and the core flow penetrates the cooler flow near the lower surface of the nozzle. This penetration

(a) Mixing Plane

(b) 1st Inflection

(c) 2nd Inflection

(d) Nearing Throat

(e) Throat

(f) Exit
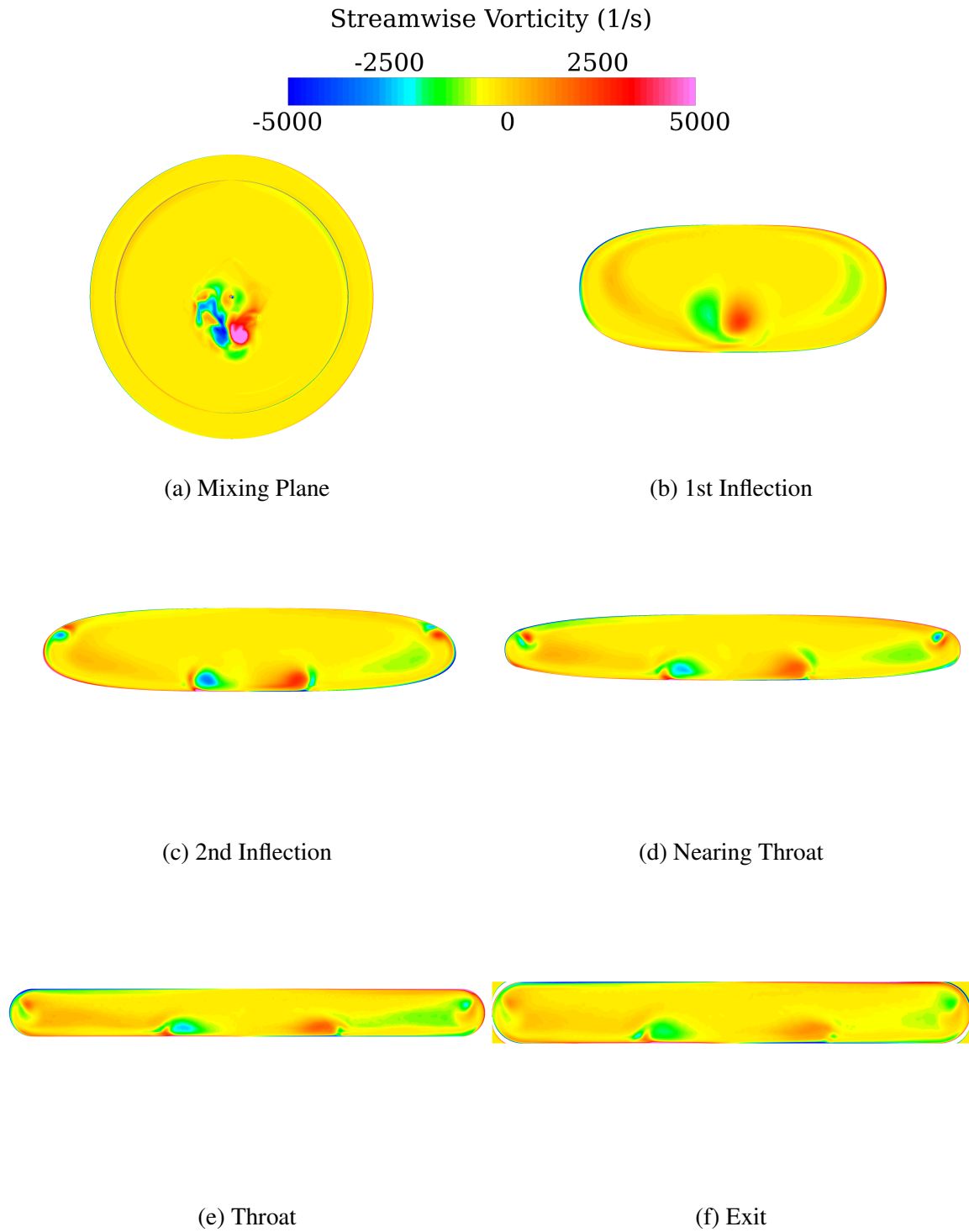
Figure 4.33: Progression of vorticity development, LD3_AR10.
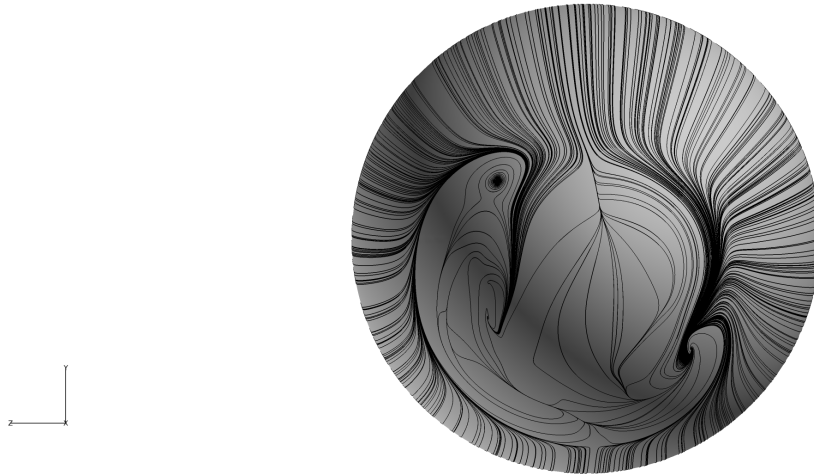
Figure 4.34: Tailcone surface flow, LD3_AR10.

is also seen in the direction of low-momentum separated flow off the tailcone in the Mach contours. At the second inflection, a stark difference between the LD2_AR10 nozzle is evident. The core flow impacts the lower surface—an indication that the surface hot streak forms further upstream. Similar to the shorter nozzle, the central vortex pair entrains bypass flow into the center asymmetrically. The weak sidewall vortices do not entrain core flow as much as the LD2_AR10 nozzle. Nearing the throat, the influence of vorticity on the temperature distribution is greater. At the sidewalls, the vortices entrain some warmer flow to the outside. In the center, the hot core flow continues to impact the lower surface, while the vortices draw cooler flow towards the centerline. At the throat, a similar pattern persists, with more mixing near the center due to the right vortex. At the exit, the pattern has not changed, again only expanded due to vertical divergence. The extent of hot flow impacting the lower surface is much wider compared to the LD2_AR10 nozzle.

Total Temperature (K)

(a) Mixing Plane

(b) 1st Inflection

(c) 2nd Inflection

(d) Nearing Throat

(e) Throat

(f) Exit
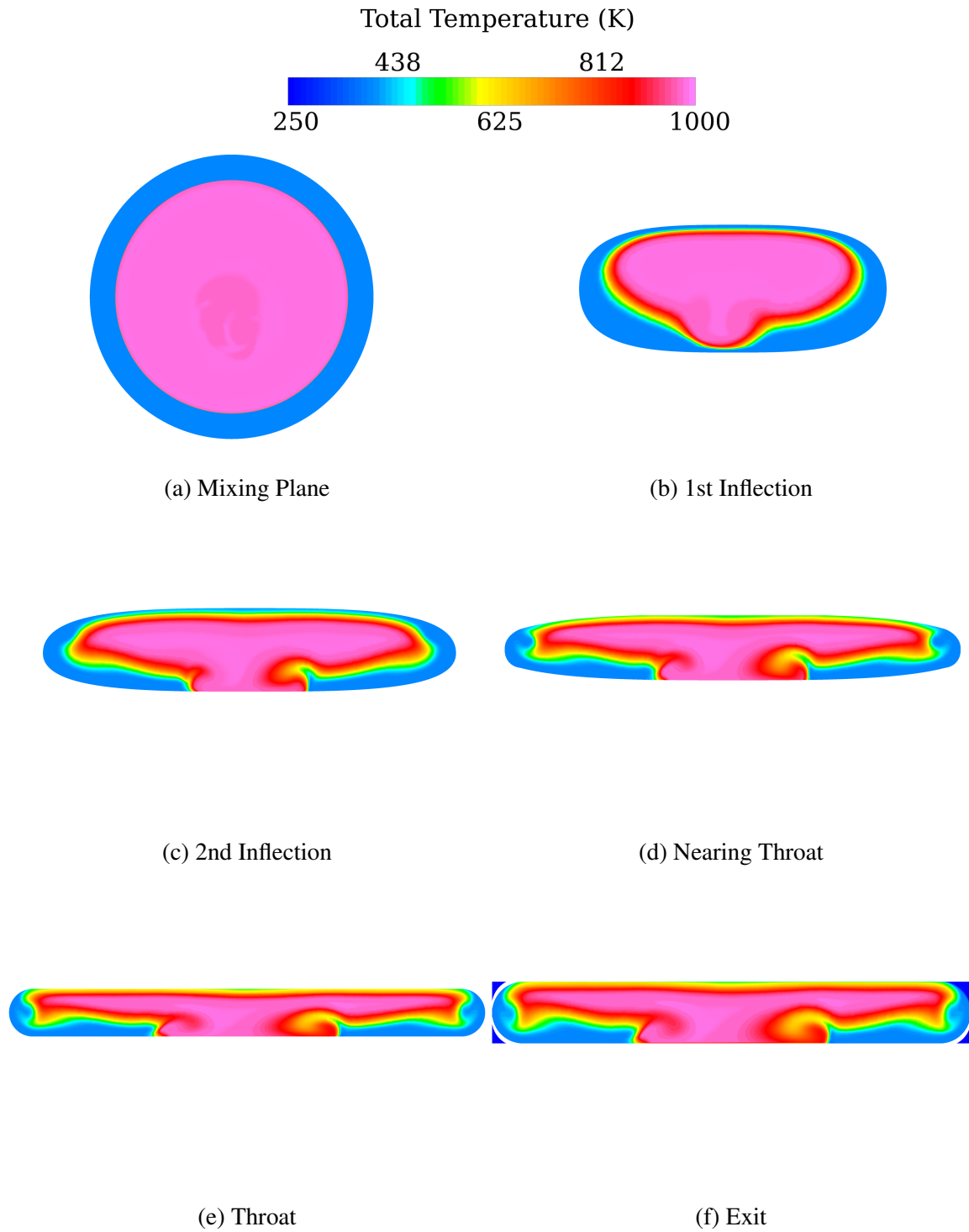
Figure 4.35: Progression of temperature distribution, LD3_AR10.

4.3.4 LD3_AR10, Swirl.

Examination of the LD3_AR10 nozzle with swirl indicates distinct changes from the no-swirl case. Like the LD2_AR10 swirl case, the Mach contours (see Figure 4.36) reveal a different behavior downstream of the tailcone. The separation characteristics are altered from the counter-rotating vortex pair to a single vortex, as shown in Figure 4.37. The low-momentum fluid is also not convected to the lower portion of the first bend like in the no-swirl case. Downstream of the tailcone, the flow behavior at the centerline is similar to the no-swirl case, with the exception of the second upper bend, where the fluid has slightly higher Mach. The location of the throat is nearly identical to the no-swirl case, as seen in the pressure plots in Figure 4.38. Ideal expansion is apparent like the no-swirl solution.
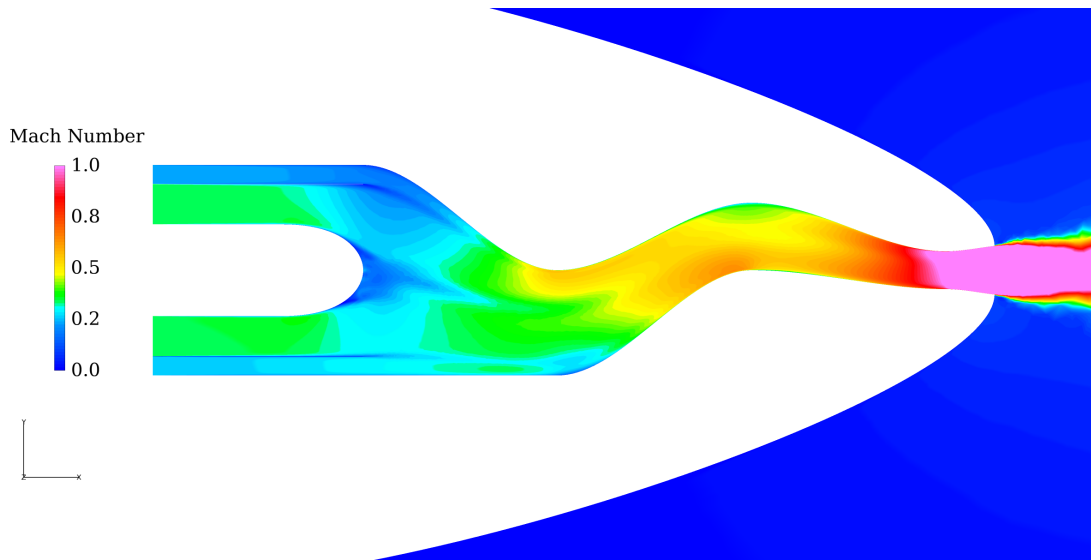
Figure 4.36: Centerline Mach number contours, LD3_AR10 with swirl.

Examination of the streamwise vorticity in Figure 4.39 reveals behavior similar to the LD2_AR10 nozzle. At the mixing plane, the strong central vortex is present. At the first inflection point, the strong central vortex persists, and a majority of the positive vorticity from the mixing plane is eliminated by the swirl. At the sidewalls, the vorticity generation due to the change in curvature is seen. At the second inflection, the sidewalls vortices due

135
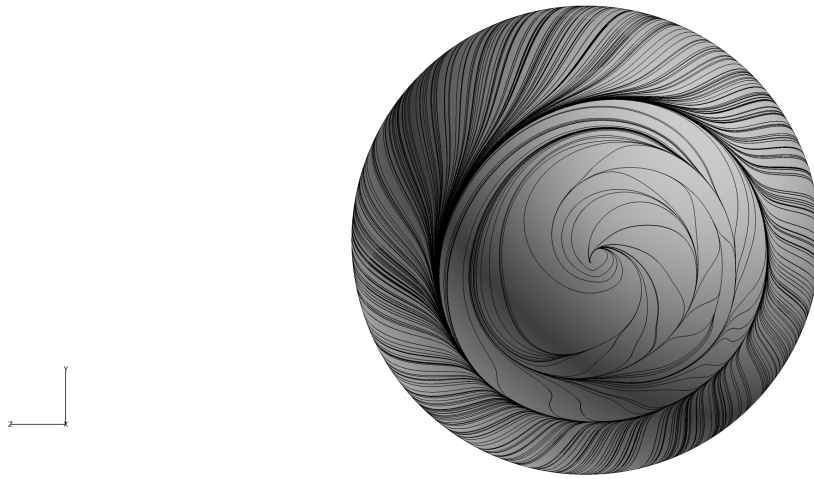
Figure 4.37: Tailcone surface flow, LD3_AR10 with swirl.
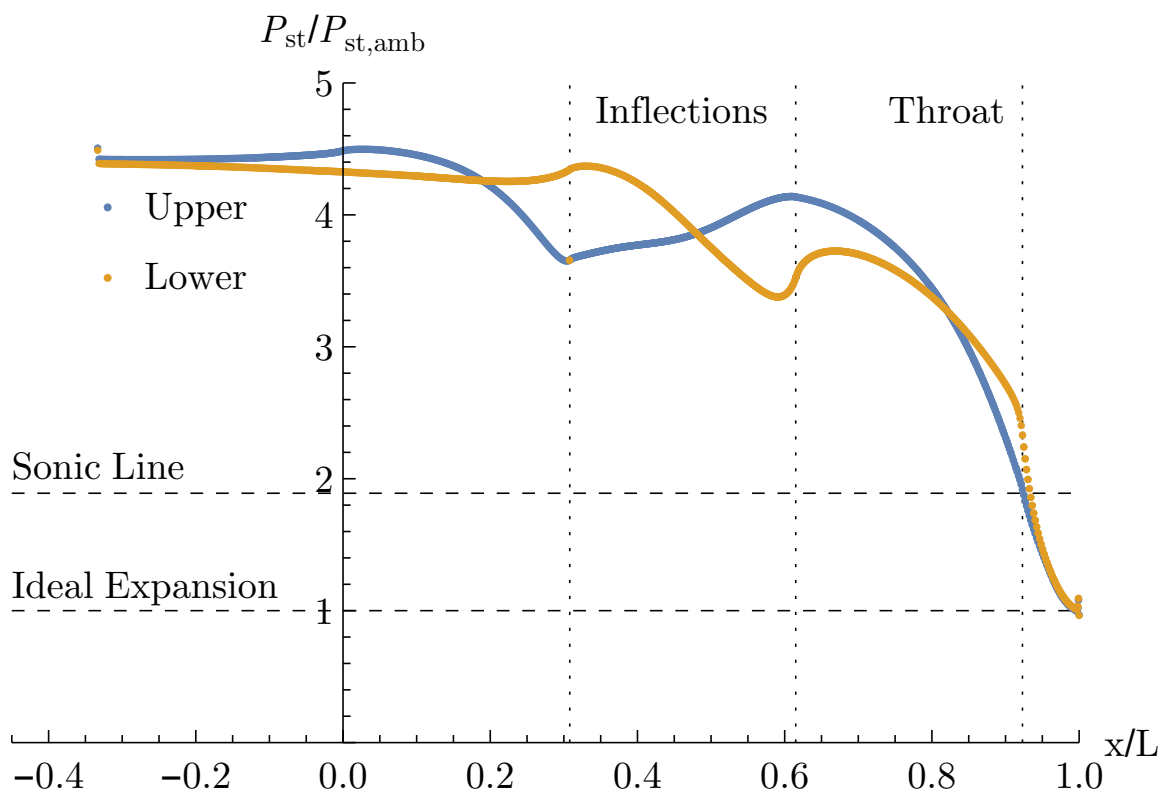
Figure 4.38: Centerline surface $P_{st}/P_{st,amb}$, LD3_AR10 with swirl.

to the change in curvature are similar to the no-swirl case. The lack of a strong second pair suggests the lack of flow separation at the second bend, and like the no-swirl case, this is confirmed by examination of the surface flow in Figure 4.40. The coalescence of surface streamlines demonstrates competing influences from the nozzle curvature and swirl at the upper sidewalls and centerline. The coalescence at the upper surface generates weak vorticity compared to the separation in the LD2_AR10 swirl solution. Nearing the throat, the strong central vortex still heavily influences the flowfield. The sidewall vortices are present at nearly the same strength as the no-swirl case. At the throat, the strong central vortex is present. The sidewall vortices remain and vorticity generation is seen in the boundary layers. At the exit, the flow features are similar though weakened due to the expansion of the flow.

Development of the temperature distribution is shown in Figure 4.41. At the mixing plane, the flow resembles the no-swirl case. At the first inflection point, the swirl affects the distribution in two ways. First, the penetration by core flow into the lower portion of the nozzle due to the counter-rotating vortices seen in the no-swirl case is not present due to the higher initial trajectory of the strong central vortex. Second, the distribution is asymmetric at the upper surface due to the direction of swirl causing a rotation of the bulk core flow. At the second inflection, the coalescing upper port-side flow promotes more mixing of the streams. Unlike the LD2_AR10 swirl case, the sidewall vortices do not have strong influence at the sidewalls. But like the shorter nozzle, the core flow has migrated to the upper surface, indicating the same fundamental difference between the swirl and no-swirl solutions for the LD3_AR10 nozzle. Nearing the throat, the upper port-side mixing behavior continues due to entrainment by the strong central vortex. The sidewall vortices begin to entrain some warmer flow to the sidewalls. More hot flow migrates to the upper surface. At the throat, the motion of the sidewall vortices continues, as does the upper port-side penetration into the core. The hot core flow migrates very near lower surface, thus

137

(a) Mixing Plane

(b) 1st Inflection

(c) 2nd Inflection

(d) Nearing Throat

(e) Throat

(f) Exit
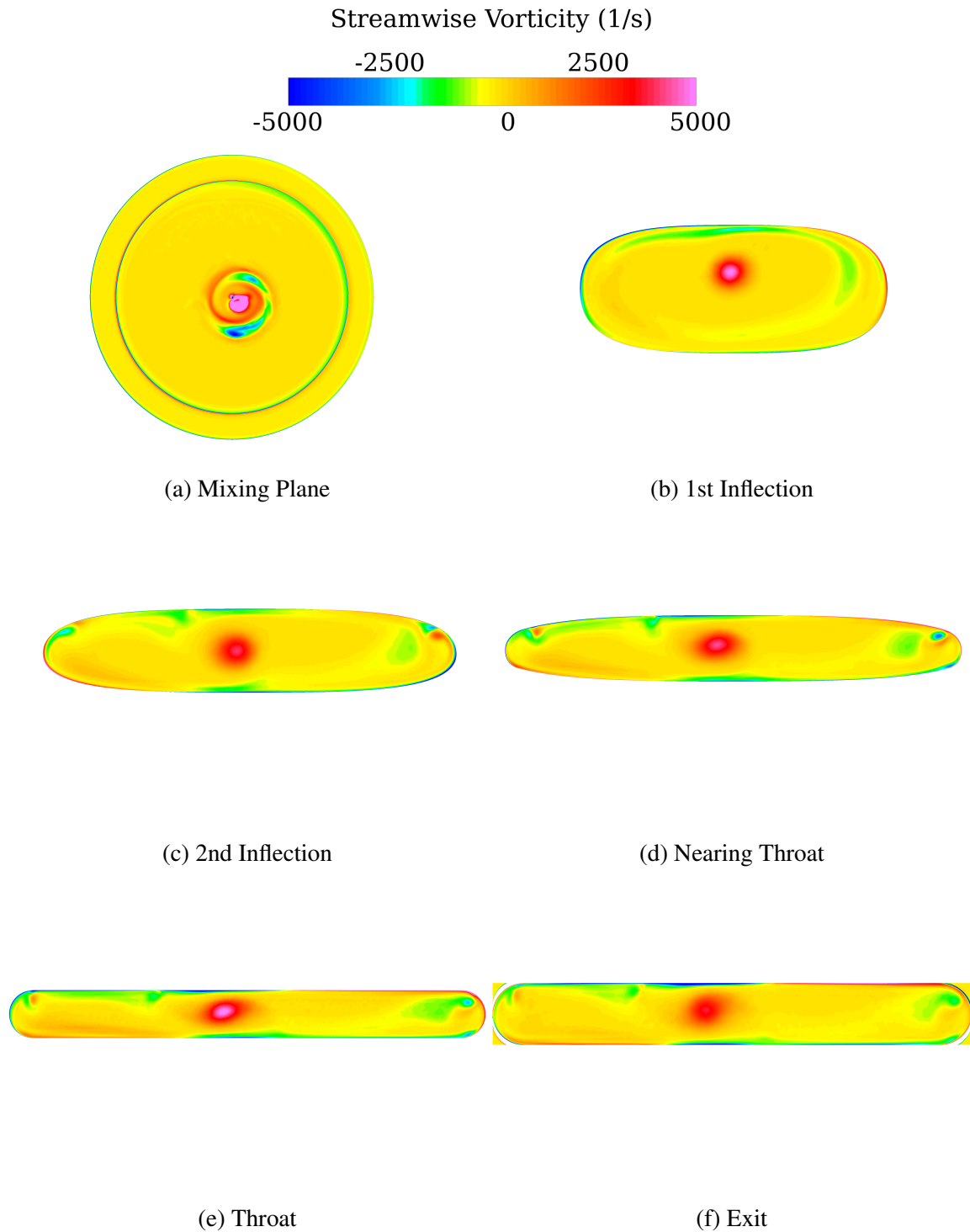
Figure 4.39: Progression of vorticity development, LD3_AR10 with swirl.
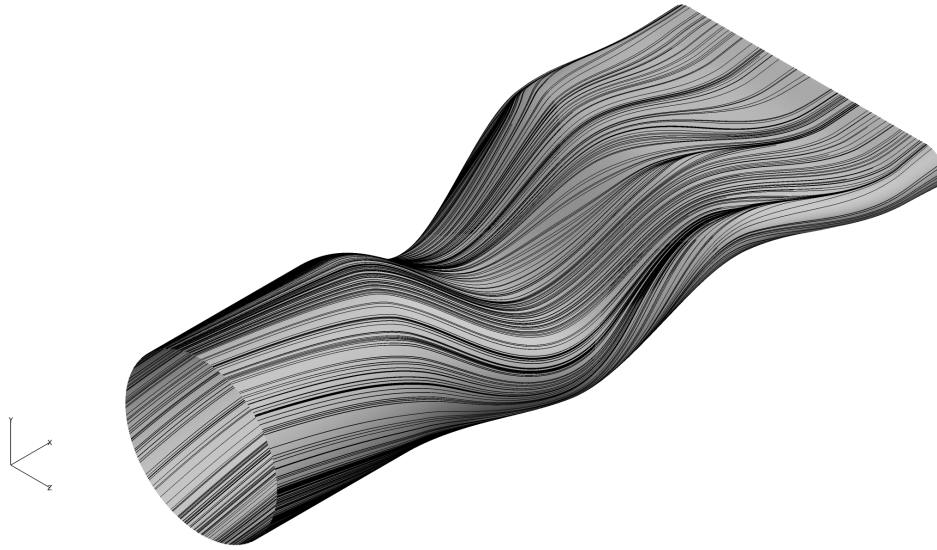
Figure 4.40: Surface flow, LD3_AR10 with swirl.

filling the entire height of the throat. The extent of hot flow impacting the upper surface increases. At the exit, a similar distribution is shown.

(a) Mixing Plane

(b) 1st Inflection

(c) 2nd Inflection

(d) Nearing Throat

(e) Throat

(f) Exit
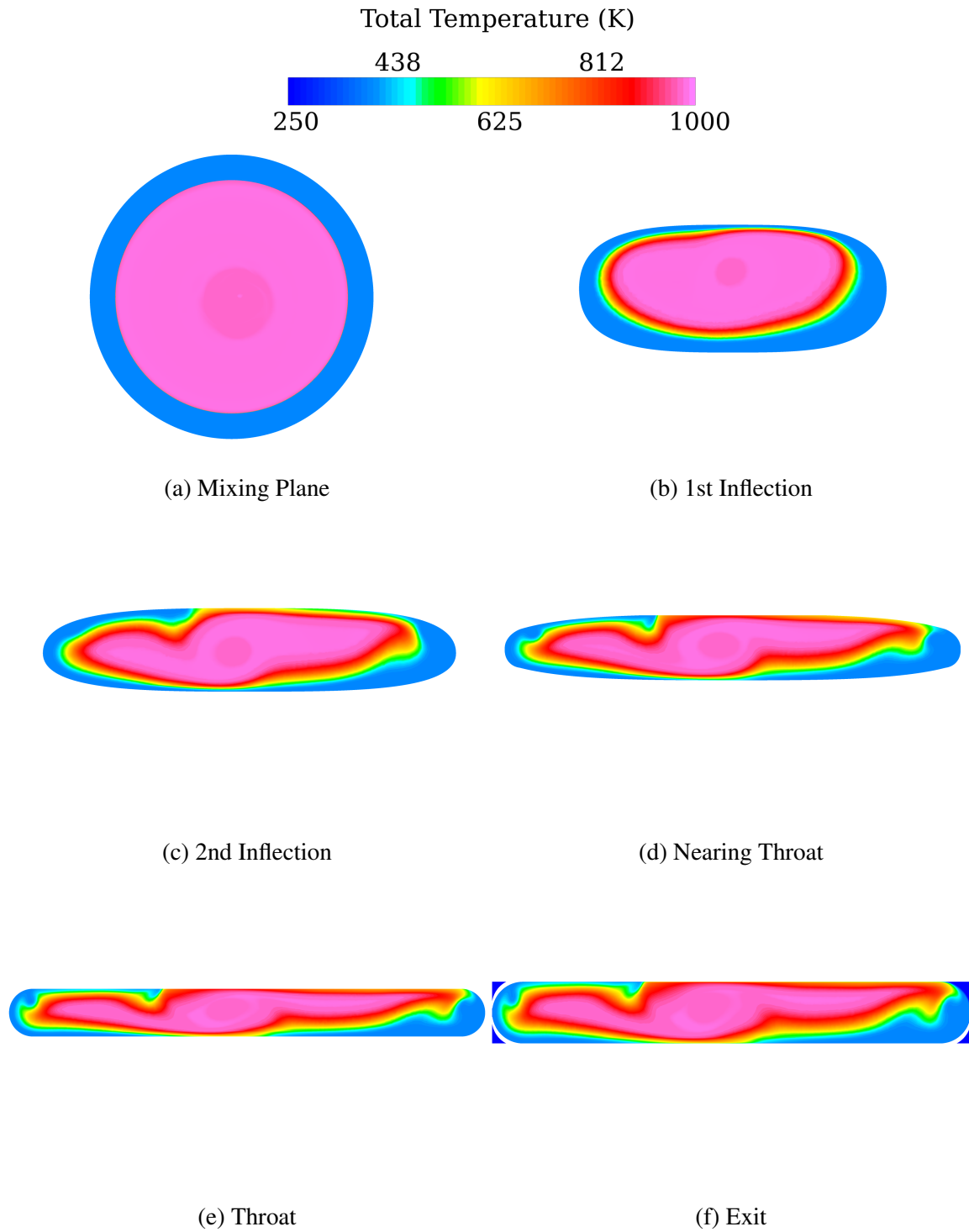
Figure 4.41: Progression of temperature distribution, LD3_AR10 with swirl.

4.3.5   *LD4_AR10, No-swirl.*

Examination of the LD4_AR10 nozzle reveals similar, but more subtle, trends as the LD3_AR10 nozzle. Mach contours in Figure 4.42 show a similar tailcone separation behavior. However, the surface flow on the tailcone in Figure 4.45 shows the vortex foci are highly skewed, with multiple separation points. Such a different pattern has arisen compared to the shorter no-swirl cases due to the reduction in influence from the upper curvature back pressure. The Mach contours show less acceleration of the flow around the bends compared to the shorter nozzles due to the increase in radius of curvature at the inflection points. The nozzle reaches sonic velocity very near the throat, and again because of the reduced turning of this longer nozzle, the sonic line is more vertical. This behavior is confirmed by examination of centerline $P_{st}/P_{st,amb}$ in Figure 4.43. The change in $P_{st}/P_{st,amb}$ on both the upper and lower surfaces is less drastic than the shorter nozzles, and the exit is nearly ideally expanded. The surface flow in Figure 4.44 shows no flow separation and a lower amount of streamline coalescence at the sidewalls due to less streamline curvature as well as lateral divergence that occurs over a longer distance.
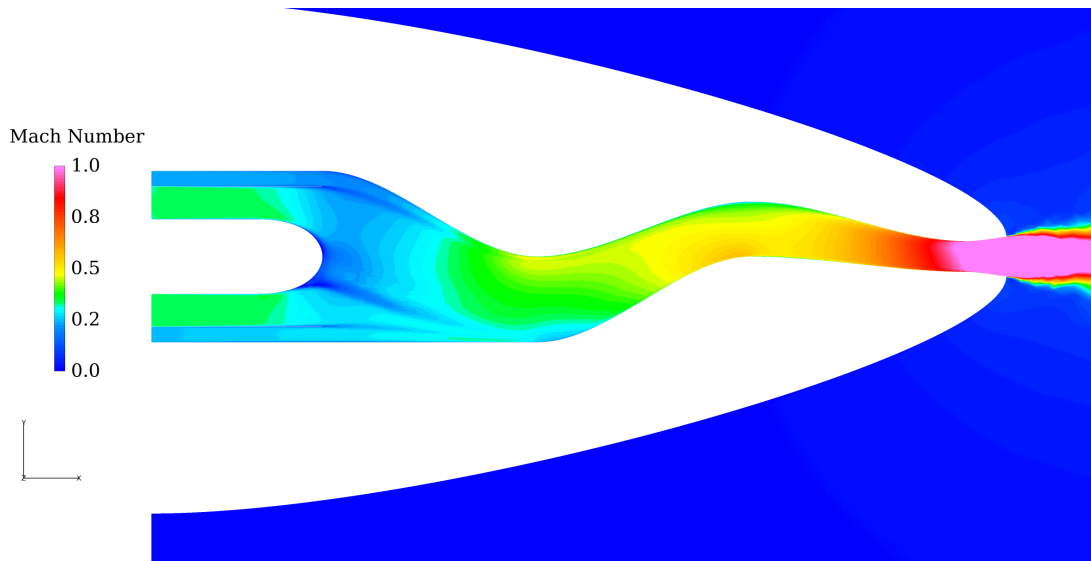
Figure 4.42: Centerline Mach number contours, LD4_AR10.
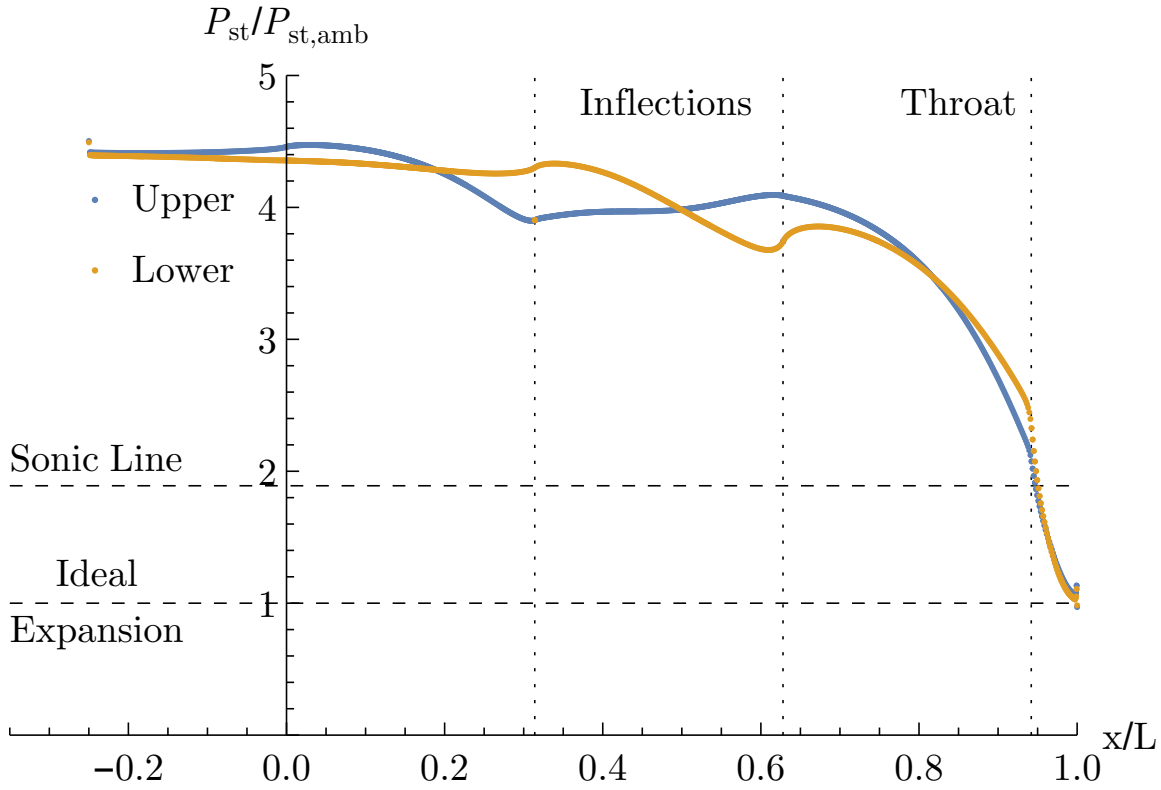
Figure 4.43: Centerline surface $P_{st}/P_{st,amb}$, LD4_AR10.

The development of streamwise vorticity for the LD4_AR10 nozzle is shown in Figure 4.46. At the mixing plane, vorticity generation due to a pair of counter-rotating vortices is observed, which was already seen in Figure 4.45. At the first inflection point, a distribution very similar to the LD3_AR10 nozzle has emerged, with the vorticity comparatively reduced in strength due to the more gradual lateral divergence at the sidewalls and reduced vortex stretching of the center pair as the contraction of the nozzle occurs over a longer distance. Very little vorticity is present downstream of the mixing layer. At the second inflection point, the pattern is again similar but reduced in strength when compared to the LD3_AR10 nozzle. The coalesce of sidewall flow seen in Figure 4.44 contributes to the vortices seen in the upper corners. The central vortex pair persists and resides very near the lower surface. Nearing the throat, weak counter-rotating pairs form in the upper corners,
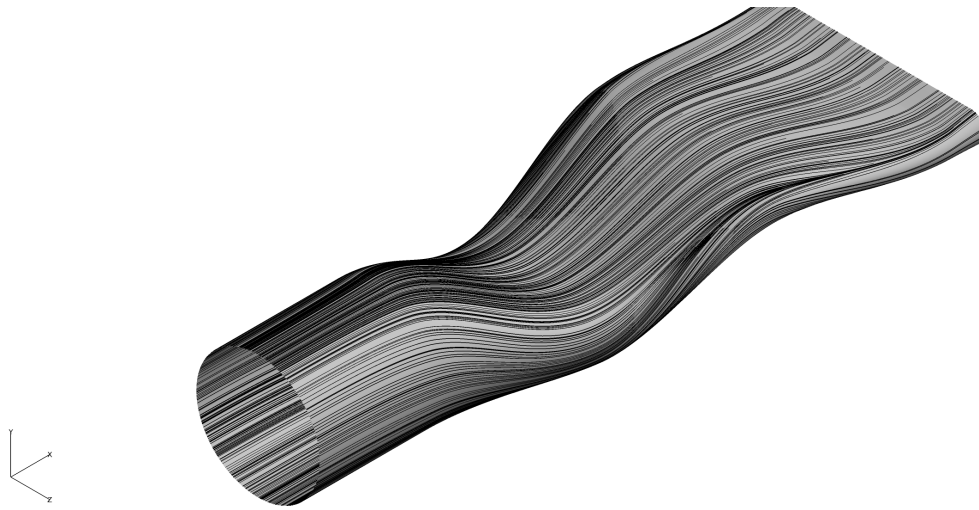
Figure 4.44: Surface flow, LD4_AR10.
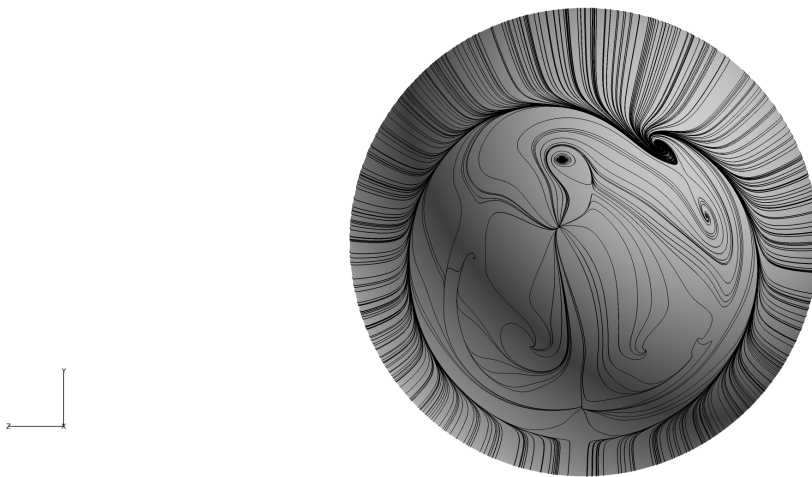
Figure 4.45: Tailcone surface flow, LD4_AR10.

and the central vortex pair moves apart due to the final lateral divergence. At the throat, the vorticity distribution is dissipated, with the corner vortices hardly present and the central vortex pair spread even further. At the exit, the vorticity is further reduced due to the vertical expansion of the flow.

The temperature distribution for the LD4_AR10 nozzle is shown in Figure 4.47. At the mixing plane, virtually no mixing due to back pressure has occurred due to the gradual nature of the first curve. At the first inflection point, the temperature distribution is symmetric, with the influence of the central vortex pair's initial trajectory seen by the dip of the core flow towards the lower surface of the nozzle. At the second inflection point, a symmetric "whale tail" pattern has emerged, with the core flow spreading and mixing outward due to the lateral divergence of the nozzle. The sidewall vortices contribute little to the entrainment of core flow. Like the LD3_AR10 nozzle, the core flow impacts the lower surface, initiating a hot streak. The central vortices entrain bypass flow toward the center. Nearing the throat, the mechanisms for mixing continue, with the weak sidewall vortices entraining some warmer flow to the edges and the central vortices continuing to pull in cooler flow. The hot streak spreads along the lower surface. At the throat, the same pattern exists but is stretched due to the final lateral divergence of the nozzle. At the exit, the temperature distribution remains the same, although expanded due to vertical divergence.

(a) Mixing Plane

(b) 1st Inflection

(c) 2nd Inflection

(d) Nearing Throat

(e) Throat

(f) Exit
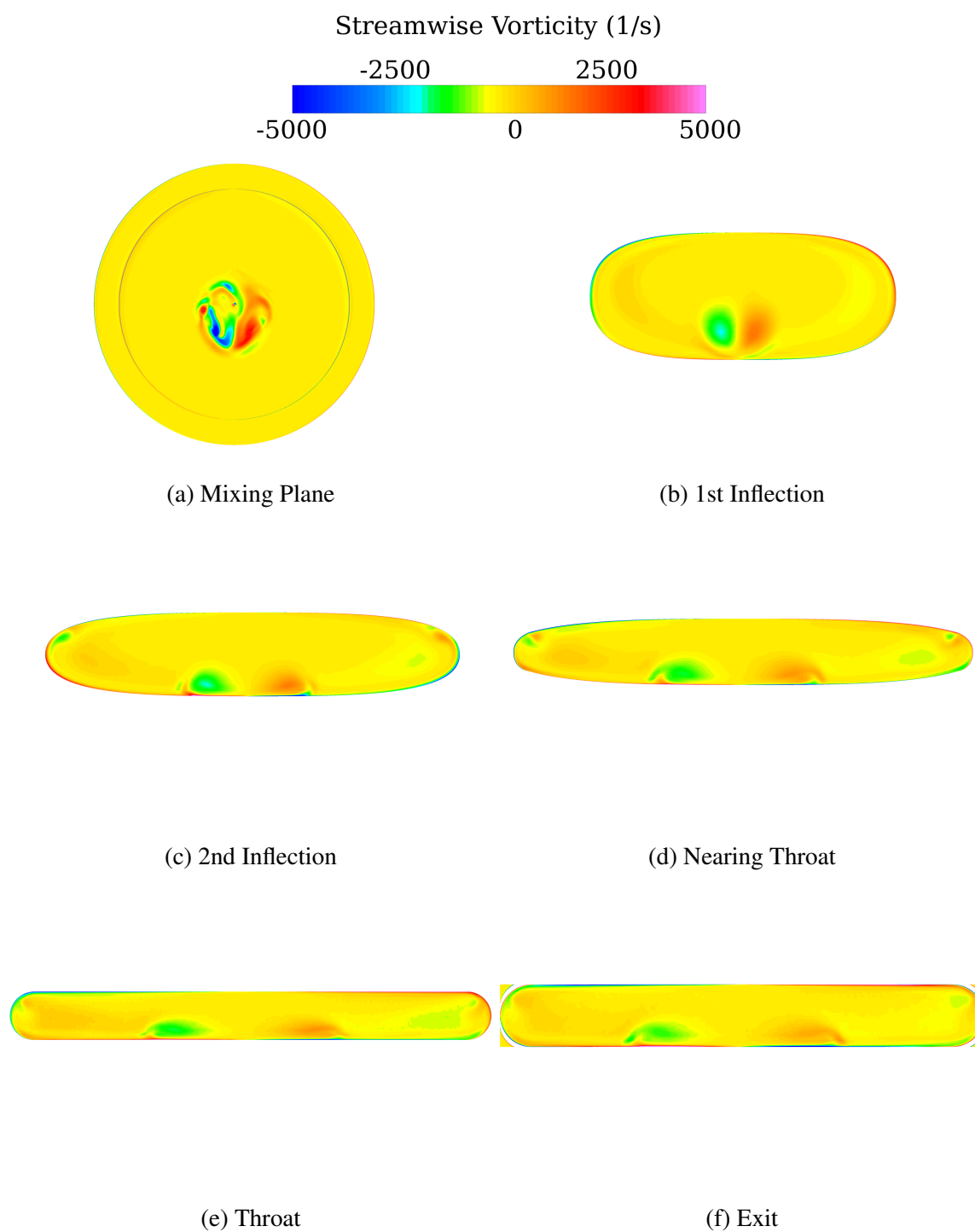
Figure 4.46: Progression of vorticity development, LD4_AR10.

(a) Mixing Plane

(b) 1st Inflection

(c) 2nd Inflection

(d) Nearing Throat

(e) Throat

(f) Exit
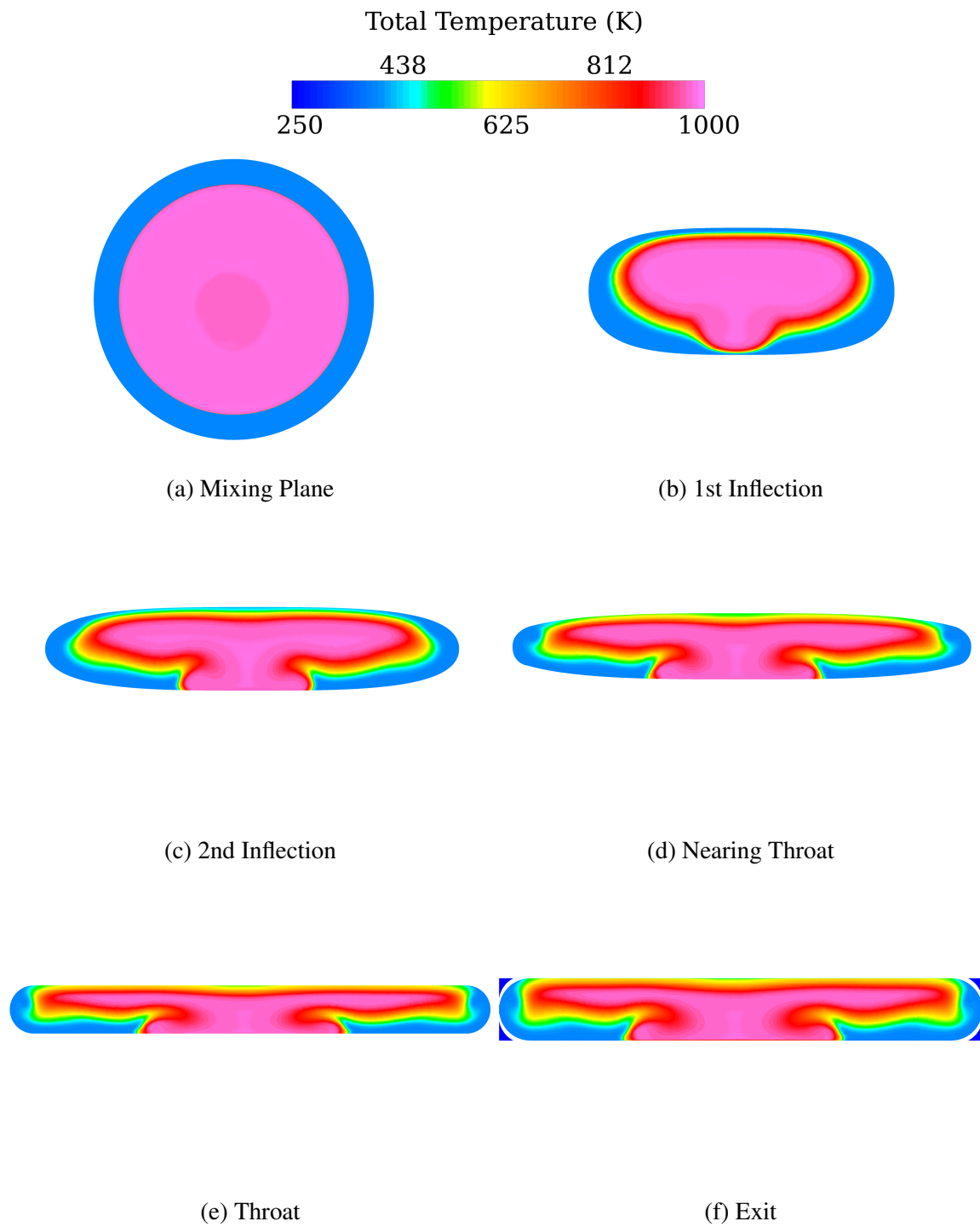
Figure 4.47: Progression of temperature distribution, LD4_AR10.

4.3.6 LD4_AR10, Swirl.

As in the shorter nozzles discussed above, swirl is seen to dramatically change the flow physics of the LD4_AR10 nozzle. Contours of Mach number in Figure 4.48 show a more symmetric separation behavior at the tailcone, but the remainder of the flowfield, including the location of the sonic line, seems to be similar to the no-swirl case. The single vortex separation behavior is confirmed in the tailcone surface flow shown in Figure 4.49. Differences are not as obvious in the plots of $P_{st}/P_{st,amb}$ along the centerline shown in Figure 4.50, where only minor changes from the no-swirl solution are observed.
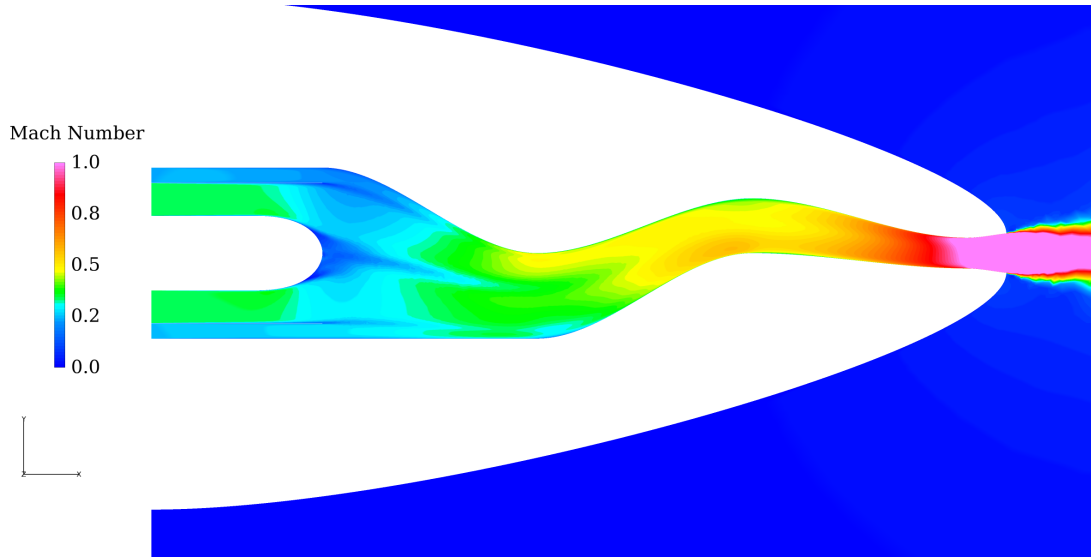
Figure 4.48: Centerline Mach number contours, LD4_AR10 with swirl.

Examination of the streamwise vorticity in Figure 4.51 reveals differences from the no-swirl case and similarities to the LD3_AR10 swirl case. At the mixing plane, the strong central vortex dominates the vorticity field. At the first inflection point, the central vortex persists, and vorticity generation occurs at the sidewalls due to the change in curvature. Only negative vorticity is generated downstream of the mixing layer. At the second inflection point, the sidewall vorticity changes sign to reflect the change in curvature direction, the central vortex remains, and the upper port-side pocket of vorticity is present

147
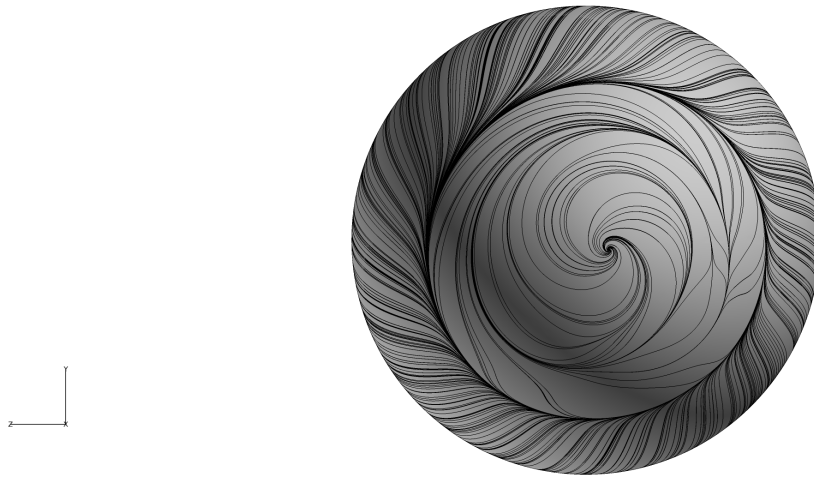
Figure 4.49: Tailcone surface flow, LD4_AR10 with swirl.
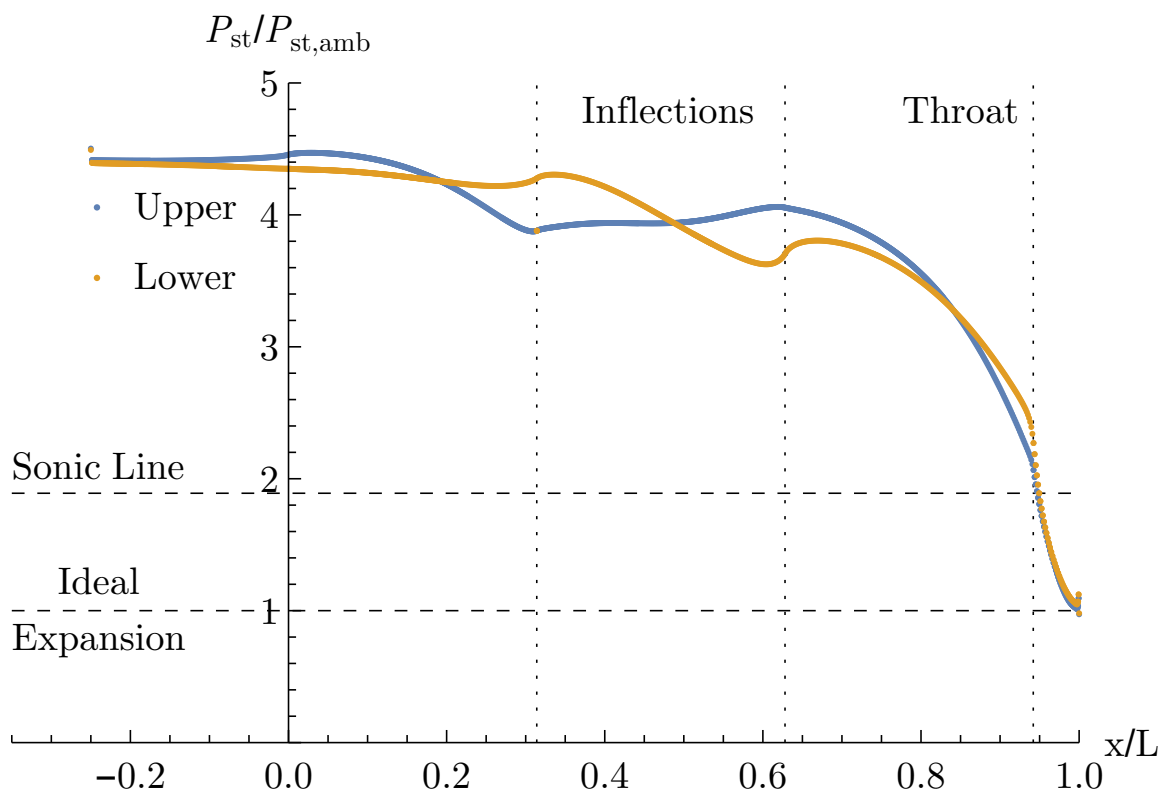
Figure 4.50: Centerline surface $P_{st}/P_{st,amb}$, LD4_AR10 with swirl.

as in the LD3_AR10 case. Similarly, this is attributed to the coalescence of flow due to the combination of streamline curvature and swirl direction, as shown in Figure 4.52. Nearing the throat, the pattern remains similar, with weak vortices at the upper corners. At the throat, the central vortex is strengthened due to the final convergence of the nozzle. At the exit, the pattern is similar to the throat but with some weakening of the vorticity field due to expansion of the flow.

Examination of the temperature distribution in Figure 4.53 shows many differences from the no-swirl case and reflects a very similar pattern to the LD3_AR10 swirl solution. At the mixing plane, as in the no-swirl case, the temperature distribution is symmetric due to the lack of influence from the downstream curvature. At the first inflection point, the influence of the upper port-side flow coalescence begins to be apparent. At the second inflection point, the asymmetric mixing of the two streams is seen by the dip into the core at the upper port-side and the effect of the swirl direction at the sidewalls. The lower momentum flow near the wall on the port side competes against the swirl, allowing more mixing and migration of the core flow, while on the starboard side the outer bypass flow is rotated in the direction of the swirl. The hot flow initiates a hot streak at the upper surface. Nearing the throat, the pattern is similar but stretched by the lateral divergence, with the hot core flow spreading along the upper surface. At the throat, a larger region of bypass flow is contained at the right sidewall, and the hot core flow spans the entire vertical space at the centerline. At the exit, a similar expanded pattern exists.

(a) Mixing Plane

(b) 1st Inflection

(c) 2nd Inflection

(d) Nearing Throat

(e) Throat

(f) Exit
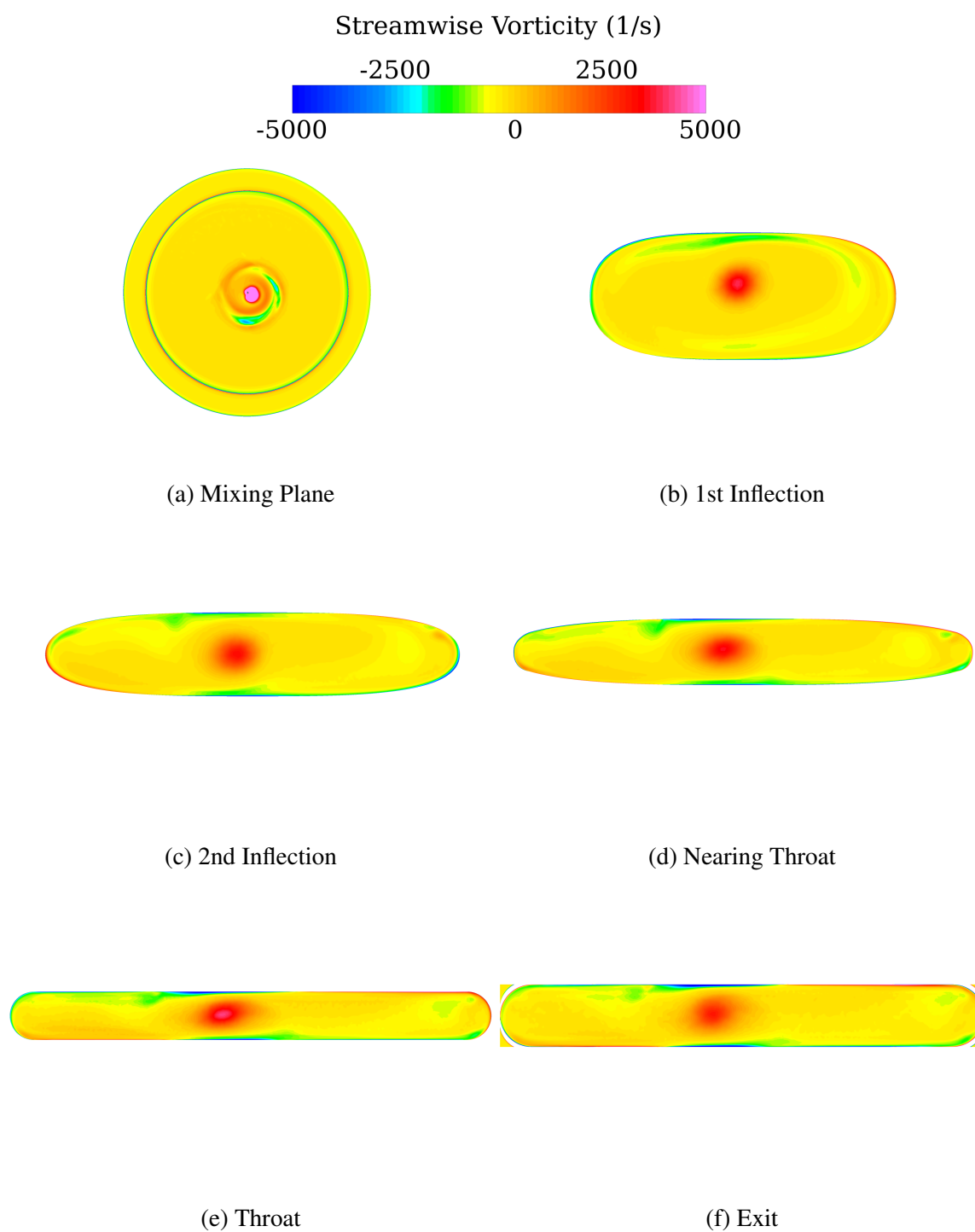
Figure 4.51: Progression of vorticity development, LD4_AR10 with swirl.
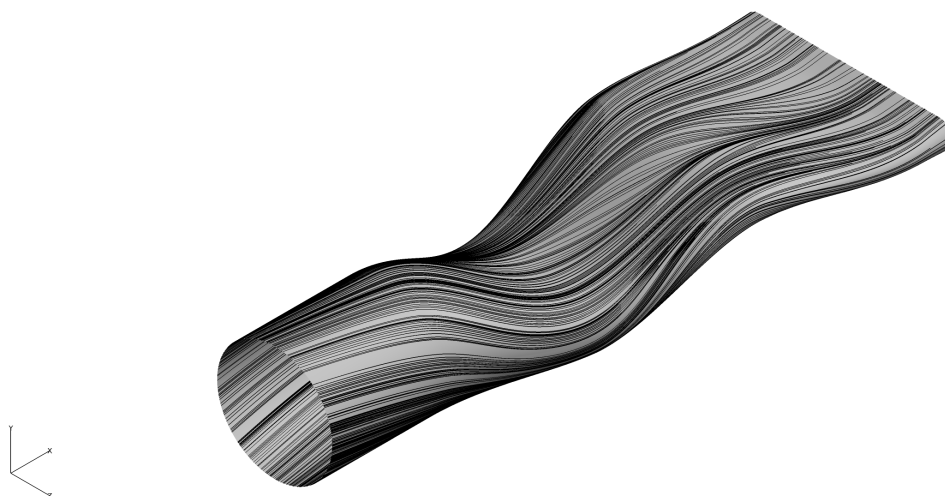
Figure 4.52: Surface flow, LD4_AR10 with swirl.

Total Temperature (K)

(a) Mixing Plane

(b) 1st Inflection

(c) 2nd Inflection

(d) Nearing Throat

(e) Throat

(f) Exit
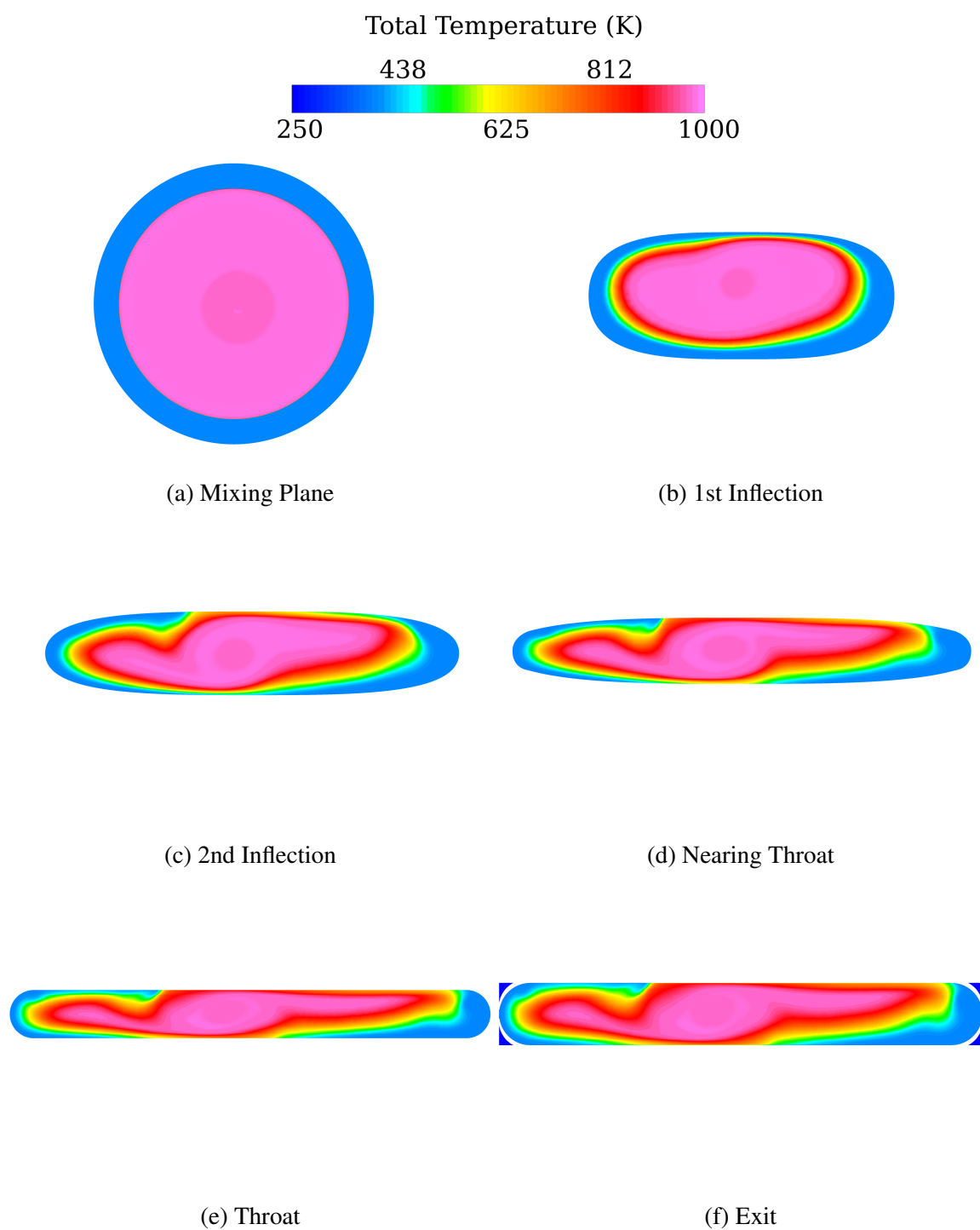
Figure 4.53: Progression of temperature distribution, LD4_AR10 with swirl.

4.3.7 *LD2 AR4, No-swirl.*

Examination of the flow characteristics for the LD2_AR4 nozzle reveals the strong effect of reducing the aspect ratio on a $L/D = 2$ nozzle. The Mach contours in Figure 4.54 shows many differences from the LD2_AR10 solution. As described in Chapter 3, the divergent section of the $AR = 4$ nozzles is relatively longer than the $AR = 10$ nozzles, thus the axial location of the inflection points are closer to the mixing plane. The location of the inflection points results in an increase in the radius of curvature at the inflection points and an increase in the influence from the upper curvature downstream of the mixing plane. Tailcone surface flow in Figure 4.55 shows the same pair of vortex foci, although rotated about the centerline. Like the LD2_AR10 nozzle, there is a region of flow separation at the upper portion of the second bend. But unlike the LD2_AR10 nozzle, a large region of flow separation is present at the lower portion of the second bend. The increased radius curvature at the second inflection point induces flow separation with a reattachment point near the throat. The final distinguishing characteristic of the Mach contours is the location of supersonic flow. The increase in radius of curvature accelerates the flow more than the LD2_AR10 nozzle, and the nozzle becomes choked with supersonic flow outside the separated region upstream of the throat. The choking is due to the nozzle geometry reaching the design A^* upstream of the throat location. Centerline plots of $P_{st}/P_{st,amb}$ at the surface gives additional detail concerning the flow behavior. The rapid acceleration around the first upper bend is seen by the decrease in $P_{st}/P_{st,amb}$ near $x/L = 0.25$, then a region of constant $P_{st}/P_{st,amb}$ is observed around the curve. The upper flow separation is seen as the flat region of $P_{st}/P_{st,amb}$ near $x/L = 0.5$, followed by the rapid decrease in $P_{st}/P_{st,amb}$ past the sonic line at $x/L = 0.7$. Also seen is the large region of overexpansion of the flow at $x/L = 0.75$ (near the reattachment point) to the exit. For the lower $P_{st}/P_{st,amb}$ curve, the major difference from the LD2_AR10 nozzle is the more rapid decrease in pressure ratio past the sonic line from $x/L = 0.5 - 0.6$. The pressure is then rapidly increased as the flow

passes around the lower bend and separates, represented by the flat pressure line, before the flow reduces to subsonic velocity again. The lower surface flow is then accelerated to sonic velocity at the reattachment point. The lower surface centerline flow is overexpanded more so than than the LD2_AR10 nozzle.
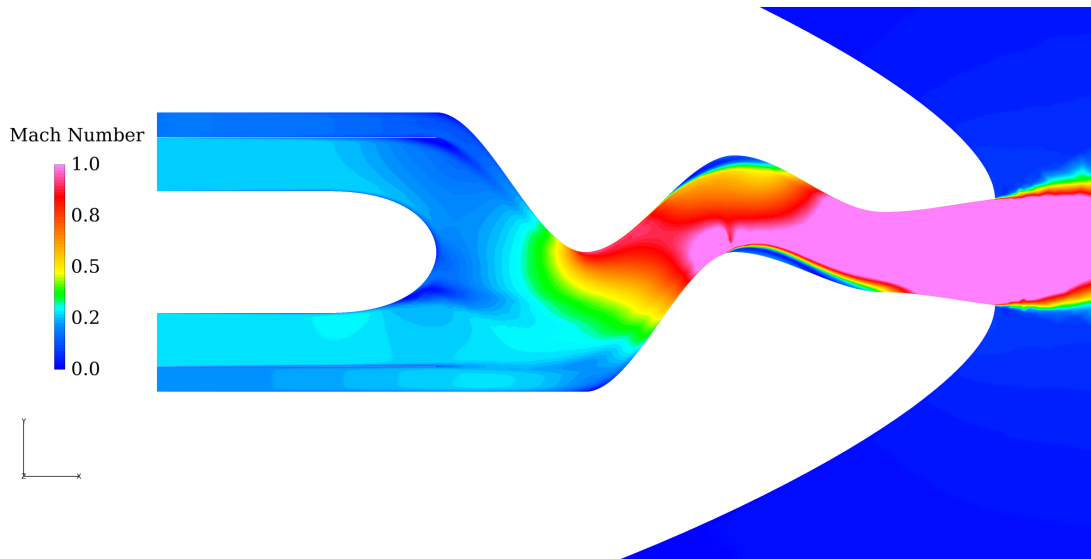
Figure 4.54: Centerline Mach number contours, LD2_AR4.
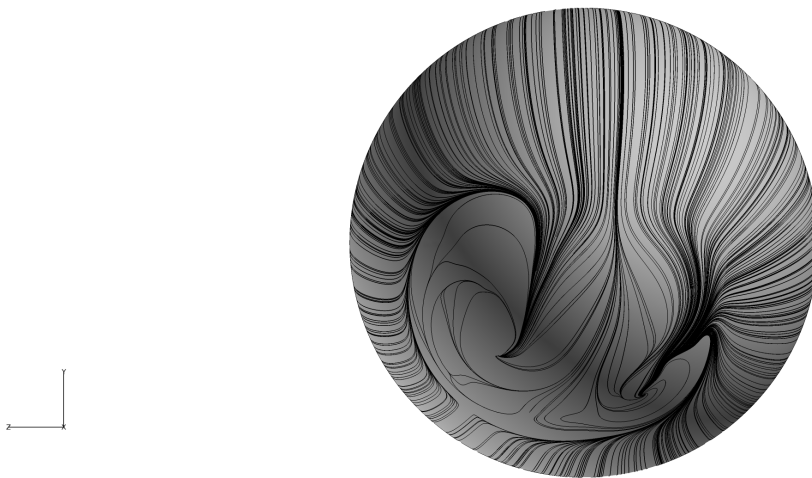
Figure 4.55: Tailcone surface flow, LD2_AR4.
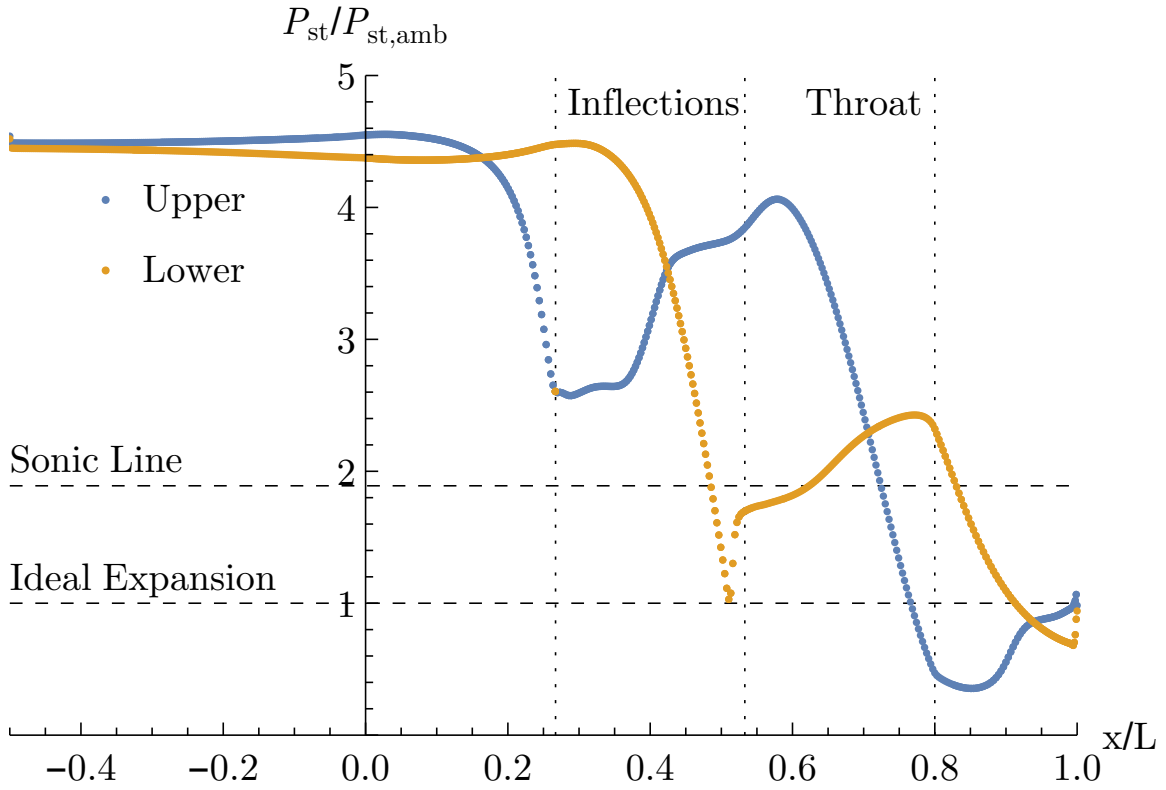
Figure 4.56: Centerline surface $P_{st}/P_{st,amb}$, LD2_AR4.

Examination of the streamwise vorticity in Figure 4.58 also shows a very different behavior from the LD2_AR10 nozzle. At the mixing plane, the counter-rotating vortex pair is clearly observed, with a rotated symmetry plane as seen in Figure 4.55. At the first inflection point, the vorticity generation at the sidewalls and mixing layer due to the change in streamline curvature is similar to the LD2_AR10 nozzle. In the center of the nozzle, the counter-rotating vortex behavior is different not only in the symmetry line but in the strength. Whereas in the LD2_AR10 nozzle the starboard vortex was the stronger of the pair and that strength persisted through the nozzle, in the LD2_AR4 nozzle the port vortex is stronger. At the second inflection point, an interesting streamwise vorticity distribution emerges. As seen in the LD2_AR10 nozzle, pairs of counter-rotating vortices have formed
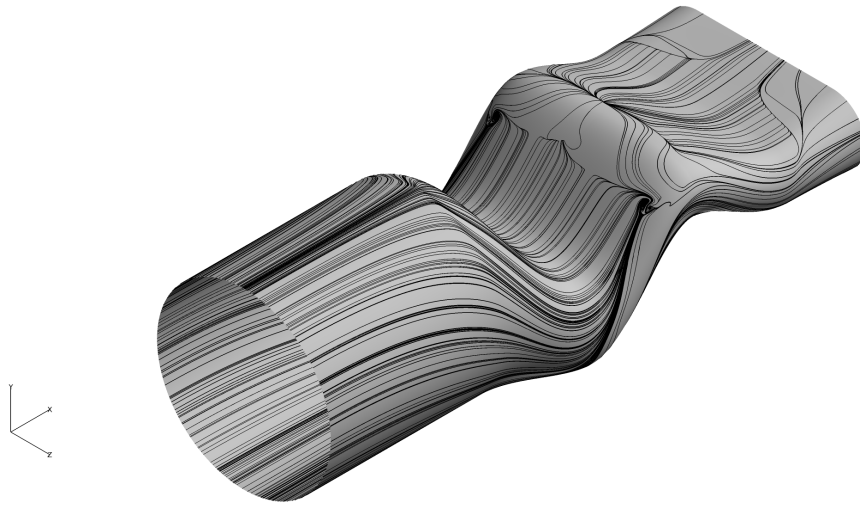
Figure 4.57: Surface flow, LD2_AR4.

at the upper sidewalls. These originate at the separation line shown in the surface flow in Figure 4.57. The vortex foci are clearly seen upstream of the second inflection point. The most interesting feature from this slice is the appearance of several counter-rotating vortex pairs at the separation line. It is unclear whether this is a physical phenomenon or a numeric instability. The instability is similar to Görtler vortices which form in the boundary layer of concave surfaces for high Reynolds number flows [63]. Future examination of other nozzles used in this research at choked conditions (increased $P_{st}/P_{st,amb}$) could be performed to determine if the multiple vortex pairs appear in those solutions as well, indicating a physical phenomenon. Nearing the throat, the strong central vortex persists, as do the strong sidewall pairs. At the lower surface, two regions of vorticity have developed due to the aforementioned separation at the second lower bend, shown in Figure 4.59. At the throat, the central vortex is still present, as are the sidewall vortex pairs. At the lower surface, a complex distribution of streamwise vorticity is established due to the upstream flow separation and the final contraction of the nozzle contributing to vortex stretching. At the exit, the expansion of the nozzle contributes to a decrease in vortex strength for

156

the central, sidewall, and lower vortices. Unlike the LD2_AR10 nozzle, two pockets of vorticity erupt between the throat and exit. Further examination of the upper surface flow reveals additional separation lines on either side of the centerline.

The temperature distribution for the LD2_AR4 nozzle in Figure 4.60 also reveals much about the unique flow physics of this nozzle. The mixing plane shows increased initial mixing of the two streams at the upper portion of the liner when compared to the LD2_AR10 nozzle due to the increased curvature downstream of the plane and thus an increase in the influence of backpressure. At the first inflection point, the movement of the bypass flow around and down to the lower portion of the nozzle is observed. Also, the influence of the asymmetric tailcone vortices is seen from the asymmetric dip in core flow. At the second inflection point, the coalescence of bypass flow by the sidewall vortices is observed, with the entrainment of warmer flow reduced from the LD2_AR10 nozzle since the size and strength of the vortices are reduced because of reduced lateral divergence. Nearing the throat, the sidewall vortices entrain more hot flow toward the outer edges. Compared with the LD2_AR10 nozzle, the tailcone vortices are raised, and this effect contributes to the persistence of the bypass flow on the lower surface. The cooler lower surface is in stark contrast to the LD2_AR10 nozzle where the core flow impacted the lower surface. At the throat, more mixing has occurred near the lower surface, although no core flow has yet to impact the surface. At the sidewalls, the rotation of the vortex pair can be inferred from the temperature distribution, where the bypass flow seems "trapped" by the vortices. At the exit, a stark difference is seen compared to the LD2_AR10 nozzle, where the "whale-tail" shape is not as noticeable, and the lower flow separation delays the migration of the central vortex to the lower surface—in essence preventing the formation of a hot streak.

Streamwise Vorticity (1/s)

(a) Mixing Plane

(b) 1st Inflection

(c) 2nd Inflection

(d) Nearing Throat

(e) Throat

(f) Exit
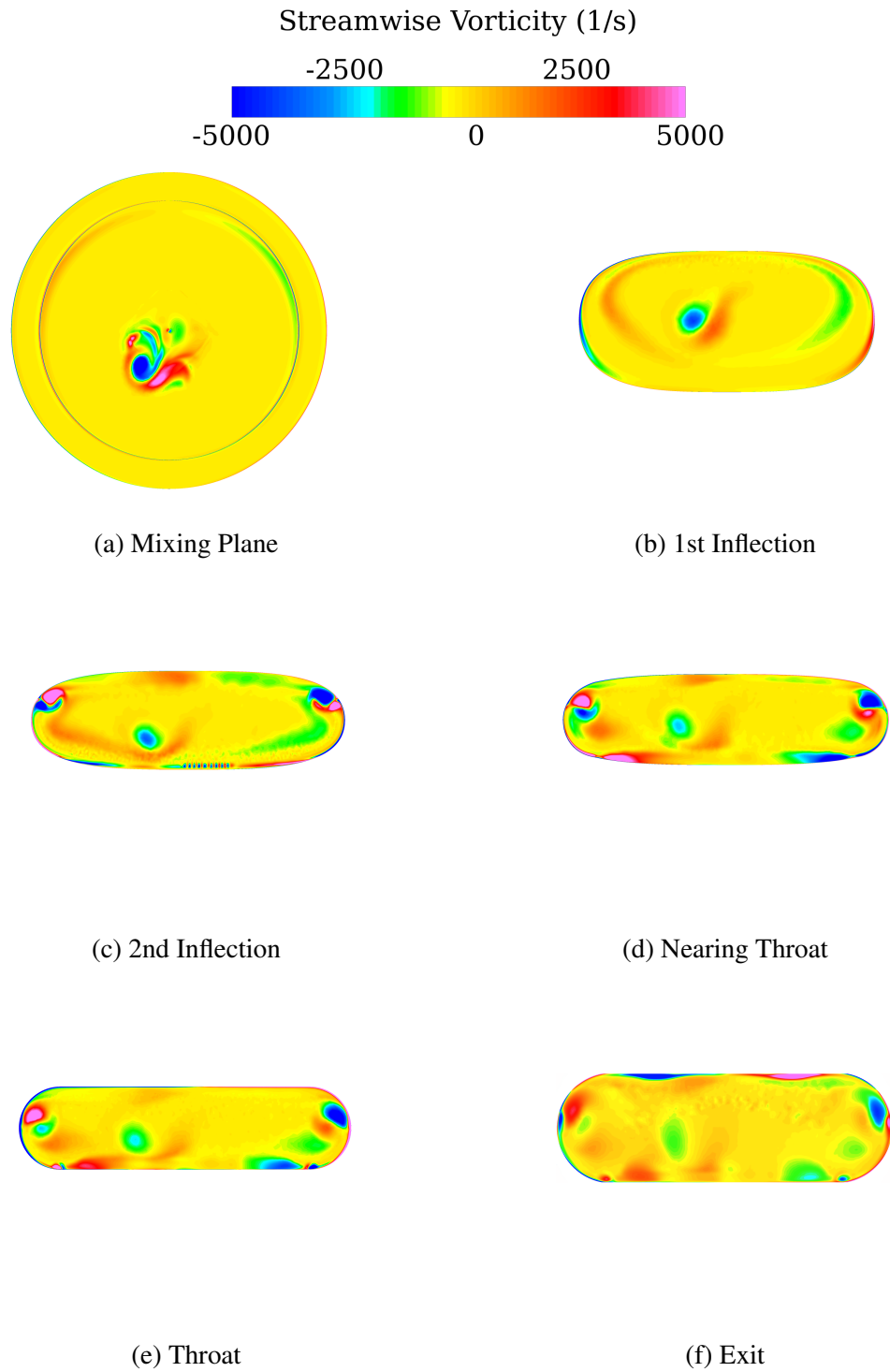
Figure 4.58: Progression of vorticity development, LD2_AR4.
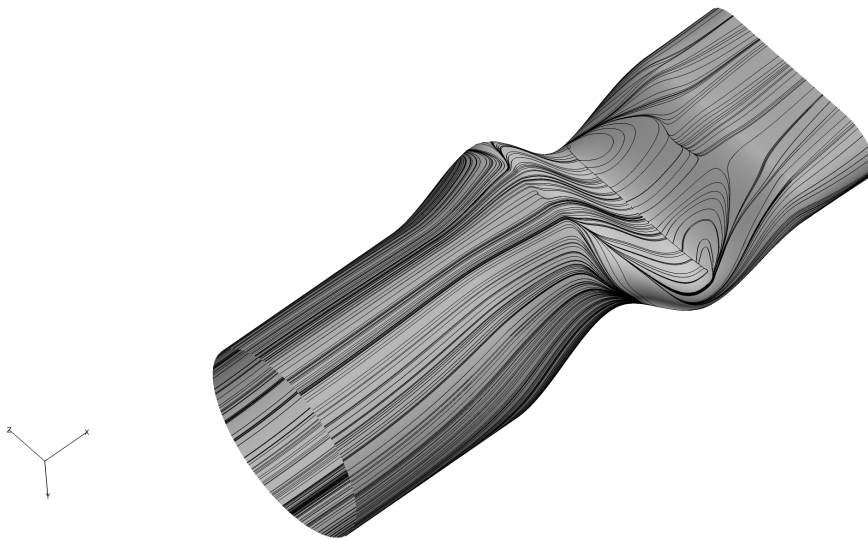
Figure 4.59: Lower surface flow, LD2_AR4.

Total Temperature (K)

(a) Mixing Plane

(b) 1st Inflection

(c) 2nd Inflection

(d) Nearing Throat

(e) Throat

(f) Exit
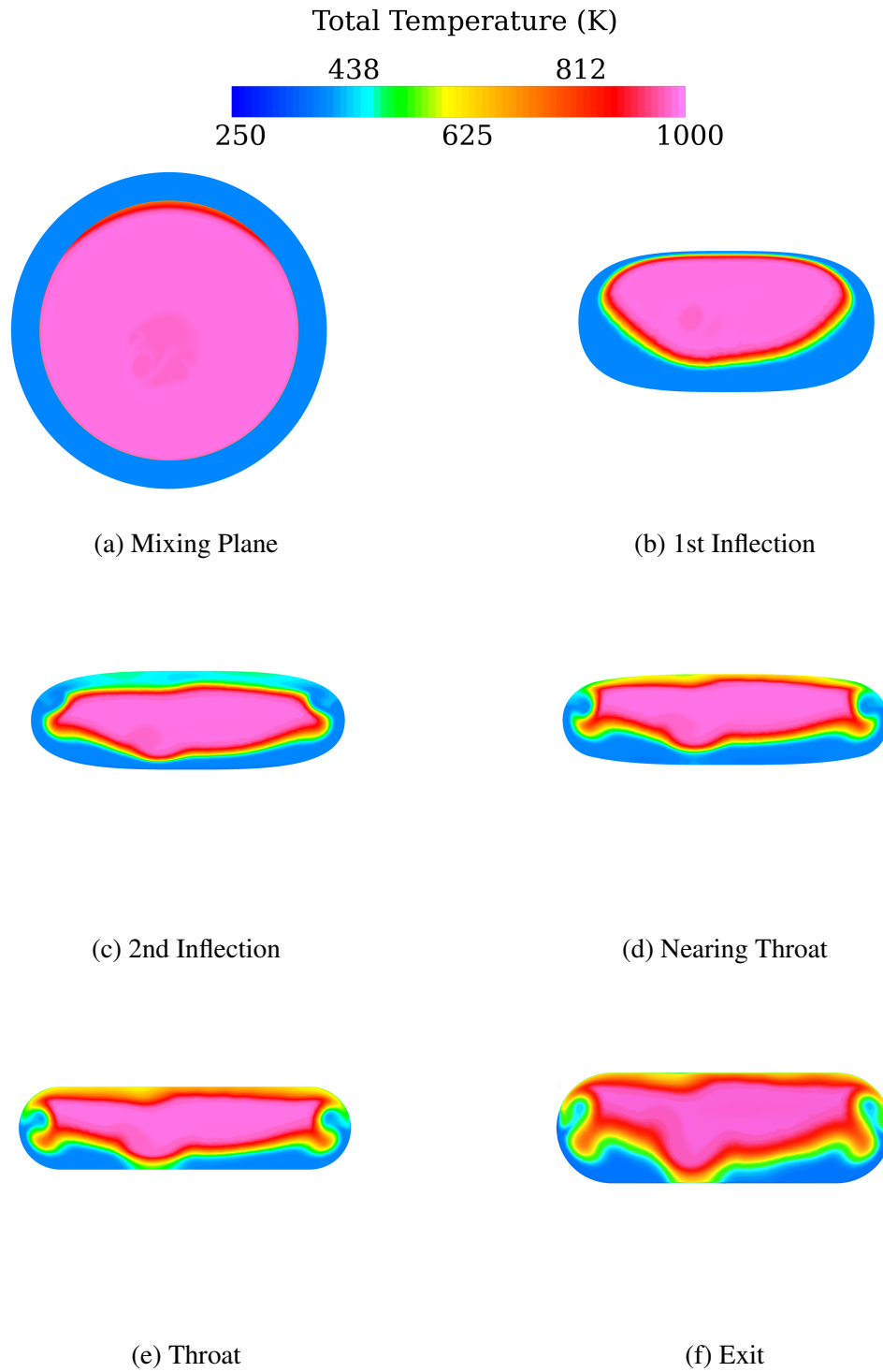
Figure 4.60: Progression of temperature distribution, LD2_AR4.

4.3.8   LD2 AR4, Swirl.

Observations concerning the LD2 AR4 nozzle with swirl begin by examining the centerline Mach contours in Figure 4.61, which show only slight differences from the no-swirl case downstream of the tailcone. As with the LD2 AR10 nozzle, the swirl induces a different separation pattern at the tailcone, which forms a single strong vortex. This behavior is seen in the tailcone surface flow in Figure 4.62. The choking of the flow upstream of the throat and the regions of flow separation at the second bend are similar to the no-swirl case. As such, the plot of upper and lower centerline $P_{st}/P_{st,amb}$ in Figure 4.63 is nearly an exact match of the no-swirl plot.
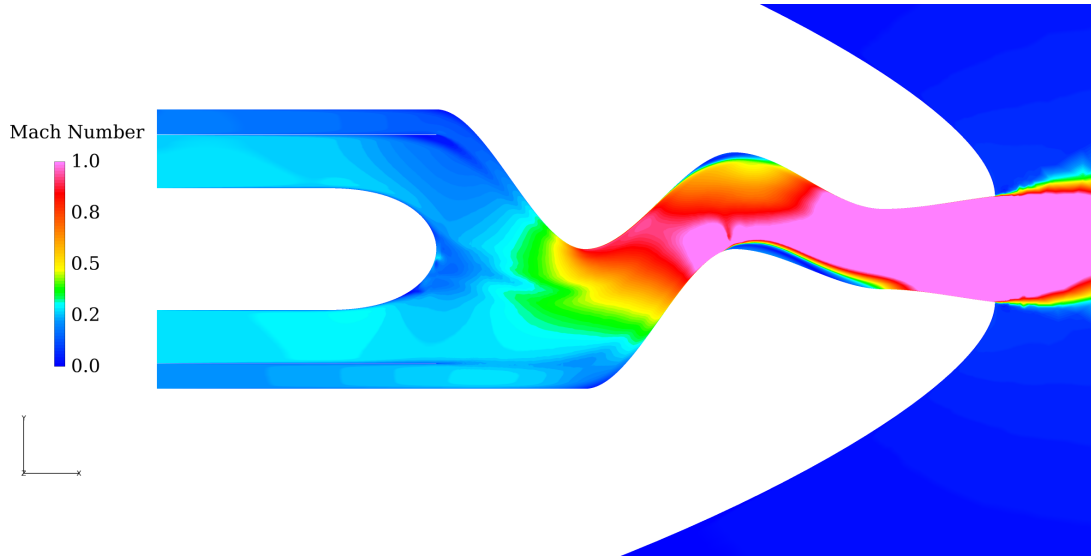
Figure 4.61: Centerline Mach number contours, L2 AR4 with swirl.

Examination of the development of streamwise vorticity in Figure 4.64 reveals the same sort of differences seen in the LD2 AR10 solutions. At the mixing plane, a strong central vortex in the direction of the swirl is observed. At the first inflection point, a similar pattern to the $AR = 10$ swirl case is seen, with a strong central vortex, weak mixing layer vorticity generation, and vorticity generation at the sidewalls due to changes in streamline curvature. At the second inflection point, the strong central vortex persists, and the same

161
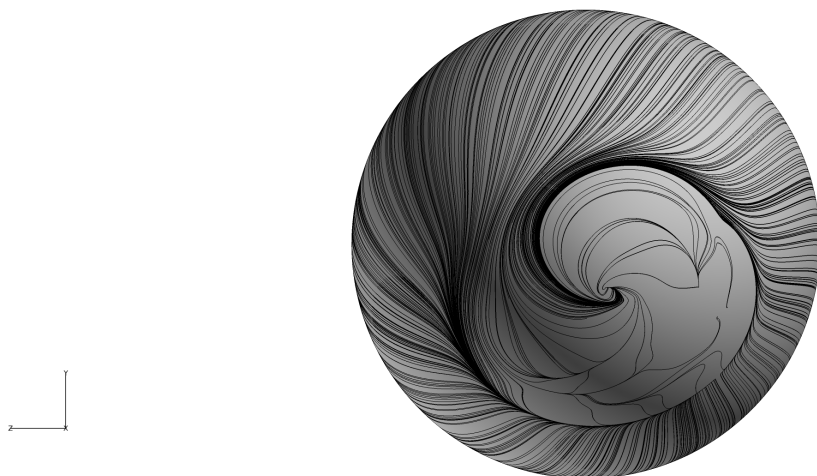
Figure 4.62: Tailcone surface flow, LD2_AR4 with swirl.
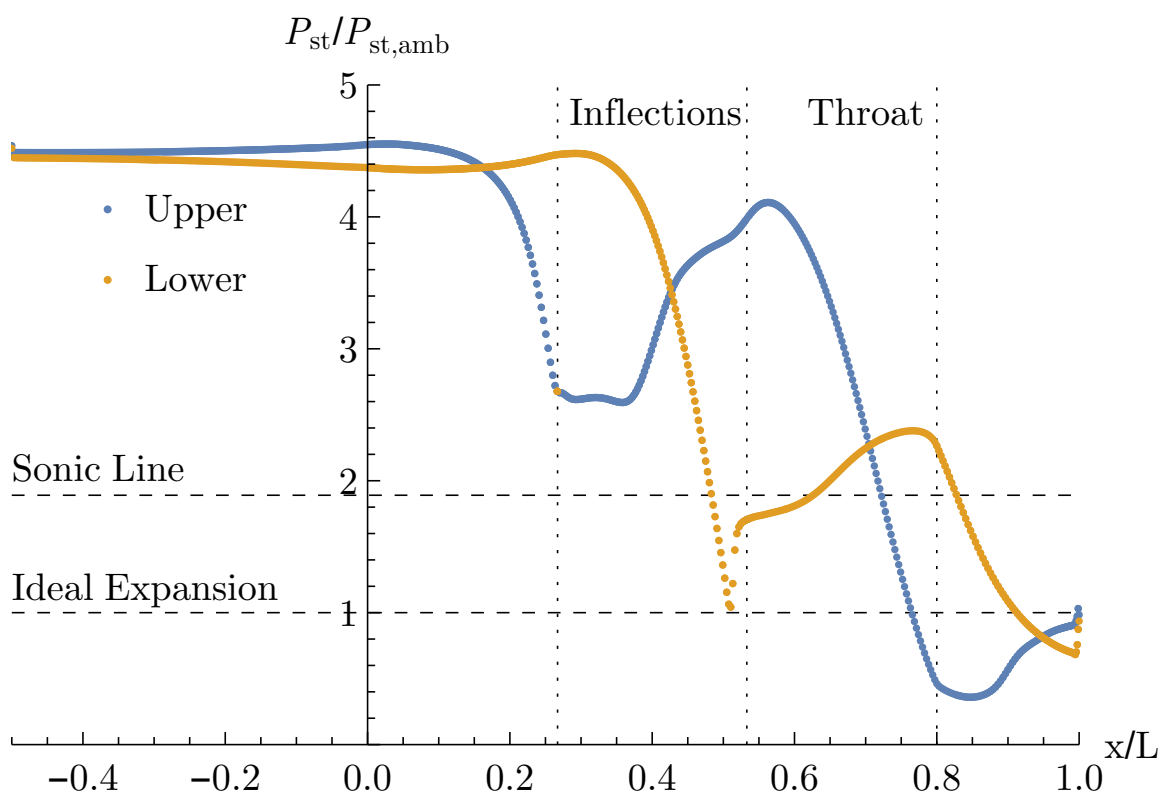
Figure 4.63: Centerline surface $P_{st}/P_{st,amb}$, LD2_AR4 with swirl.

three pairs of counter-rotating vortices are observed as in the LD2_AR10 swirl case. The foci for these pairs of vortices are seen in the upper surface flow at the separation line in Figure 4.65. Nearing the throat, the strong central vortex remains. At the sidewalls, the vortex pairs have rotated around each other due to the downward curvature of the nozzle. Near the upper surface, only the positive vortex remains, with the weaker vortex reduced in strength by the swirl. Near the lower surface, two pockets of vorticity have erupted due to the lower flow separation, as seen in Figure 4.66. At the throat, the pattern continues, with the upper and lower regions of vorticity diminished due the nozzle geometry expanding before the throat. At the exit, the central vortex, port-side vortex pair, and lower vorticity diminishes in strength due to nozzle expansion. The starboard-side pair coalesces at the sidewall. Near the upper surface, regions of vorticity erupt due to flow separation.

The development of temperature distribution through the nozzle is shown in Figure 4.67. At the mixing plane, some interaction between the two streams is seen in the upper portion of the core flow, as in the no-swirl case, due to the back-pressure created by the high degree of upper curvature. At the first inflection point, the movement of the bypass flow downward is similar to the no-swirl case. At the second inflection point, the effect of the counter-rotating vortex pairs is evident. The large regions of bypass flow migrate upward due to the upward curvature of the nozzle and are entrained by vortex pairs. At the upper port-side surface, the vortex pair begins to entrain core flow upward. Nearing the throat, the asymmetric temperature distribution is further observed. The sidewall vortices continue to entrain hot core flow. At the upper surface, the intrusion into the core region by the strong vortex continues, and the hot core flow impacts the upper surface—a distinct difference from the no-swirl solution where no hot streak was observed. Unlike the no-swirl case, the strong central vortex does not seem to play a large role in promoting mixing of the streams. The same holds true at the lower surface, where the pockets of erupted vorticity occur entirely within the bypass flow and thus do not contribute to mixing. At the

(a) Mixing Plane

(b) 1st Inflection

(c) 2nd Inflection

(d) Nearing Throat

(e) Throat

(f) Exit
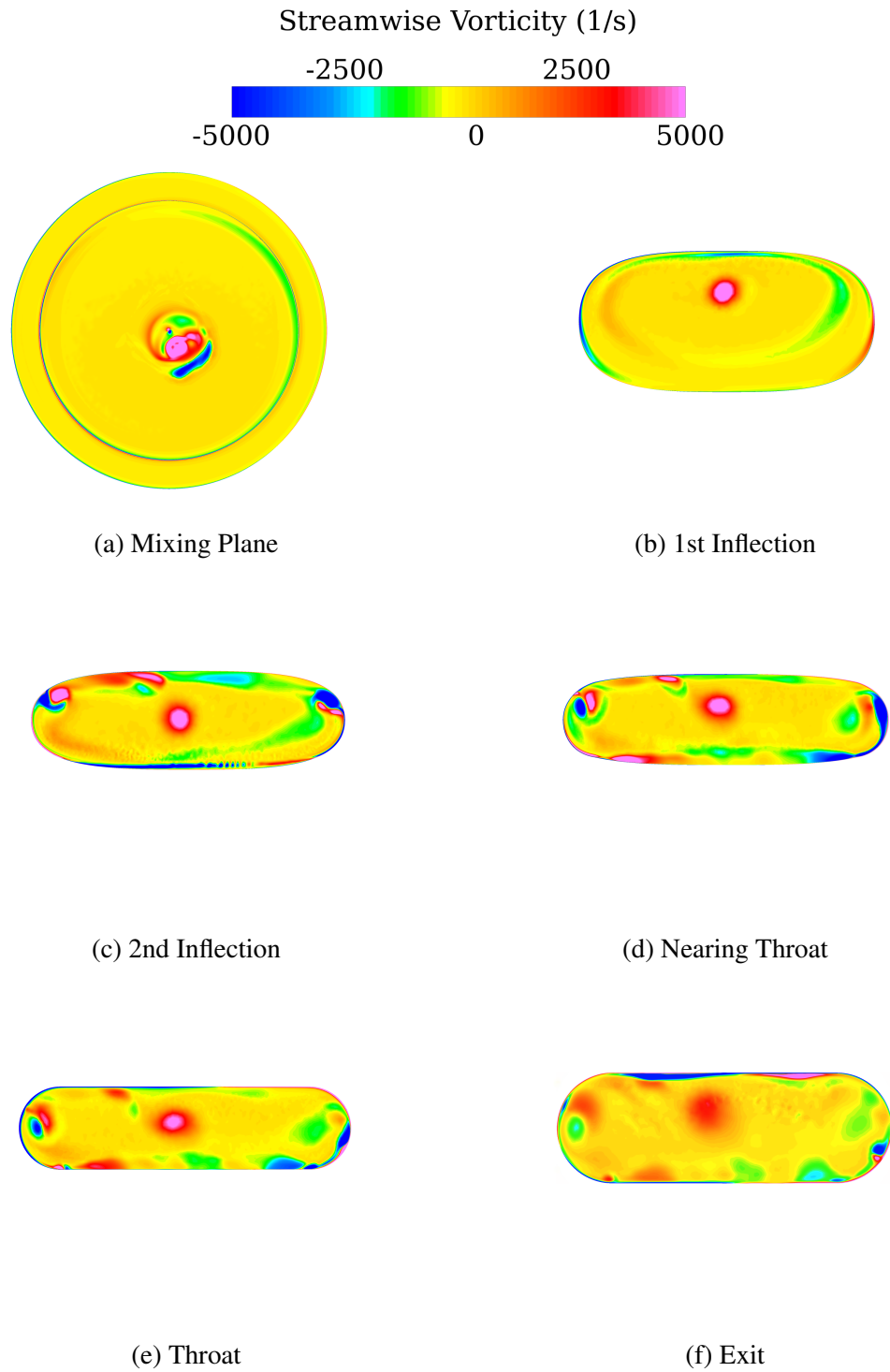
Figure 4.64: Progression of vorticity development, LD2_AR4 with swirl.
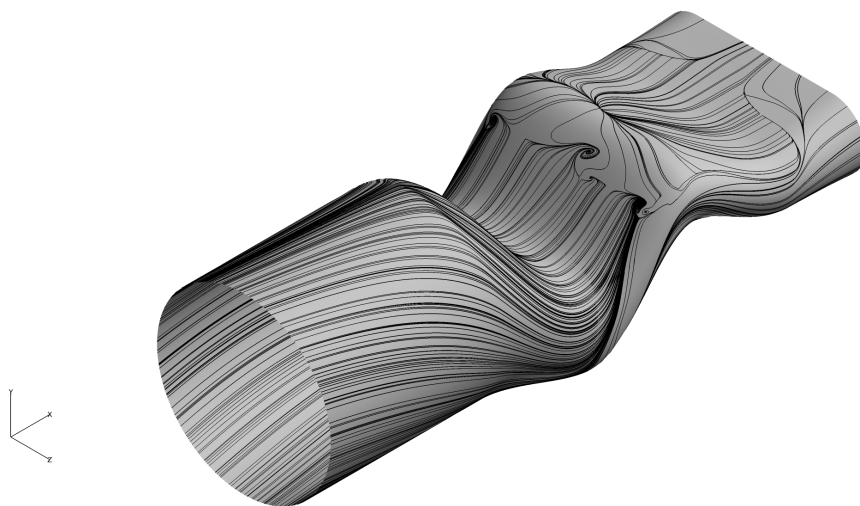
Figure 4.65: Surface flow, LD2_AR4 with swirl.
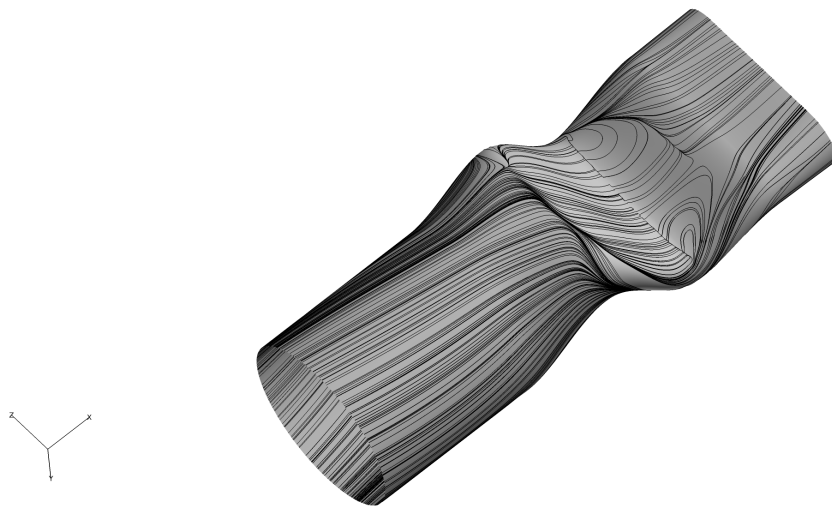
Figure 4.66: Surface flow, LD2_AR4 with swirl, lower surface.

throat, the pattern continues with the final downward curvature of the nozzle contributing to the distribution changes from the previous slice. At the sidewalls, the port-side vortex pair continues the upward entrainment of hot flow, while at the starboard side the entrainment is reduced due to the direction of swirl. At the upper surface, entrainment continues into the core. At the exit, the pattern is similar but stretched due to the nozzle expansion.

Total Temperature (K)

(a) Mixing Plane

(b) 1st Inflection

(c) 2nd Inflection

(d) Nearing Throat

(e) Throat

(f) Exit
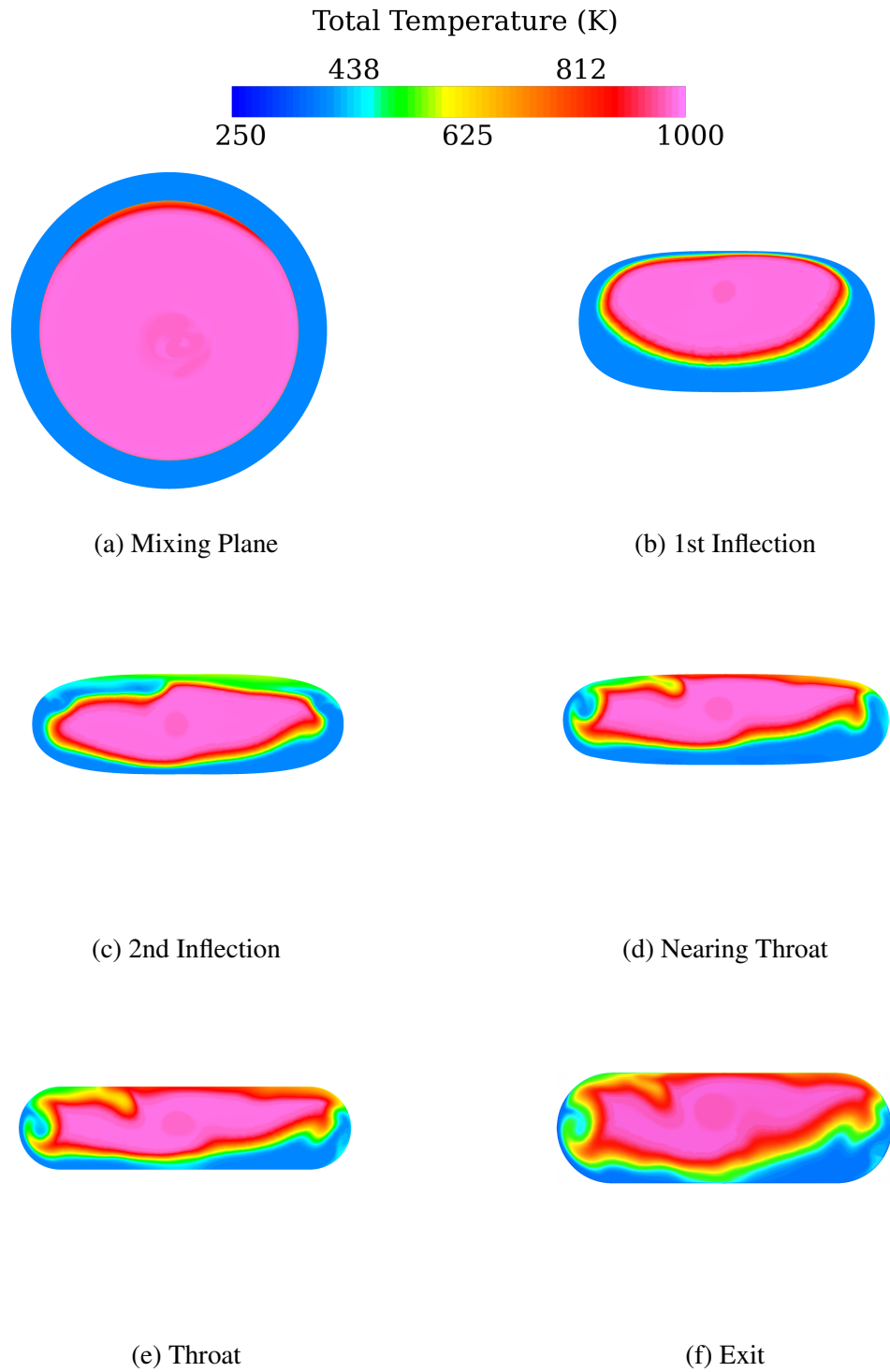
Figure 4.67: Progression of temperature distribution, LD2_AR4 with swirl.

4.3.9   LD3_AR4, No-swirl.

Examination of Mach contours in Figure 4.68 reveals a centerline flow behavior closer to the LD3_AR10 solution than the LD2_AR4 solution. The separation behavior off the tailcone is similar for both $L/D = 3$ nozzles. Due to the increase in radius of curvature compared to the LD3_AR10 nozzle, the flow is accelerated more around the bends, as seen in the higher Mach number between the first and second inflection points and the sonic flow at the second bend. Near the throat, the lower portion of the nozzle reaches sonic velocity near the design throat location. Above the lower surface, the flow reaches sonic velocity upstream of the throat but is not choked far upstream like the LD2_AR4 nozzle. This behavior is confirmed by examination of the centerline surface $P_{st}/P_{st,amb}$ in Figure 4.69, where the upper surface plot gives a lower pressure at the first bend compared with the LD3_AR10 nozzle, and the upper surface crosses the sonic line before the throat. No flow separation is demonstrated in the plot. At the lower surface, a drastic decrease followed by an increase in $P_{st}/P_{st,amb}$ is indicated at the second bend, followed by another sharp decrease in $P_{st}/P_{st,amb}$ near the throat as the flow is accelerated to sonic velocity. The upper surface is more ideally expanded than the lower surface, which is slightly overexpanded. Surface flow results in Figure 4.70 show no flow separation at the upper surface. The coalescence of the flow at the sidewalls from the laterally diverging upper surface flow and flow migrating up the sidewalls from the lower surface is clearly observed. The second bend directs this coalesced flow to the lower sidewalls at the throat.

Contours of streamwise vorticity (Figure 4.71) at the mixing plane show a similar counter-rotating vortex pair as other no-swirl cases. The appearance of the vortex pair is confirmed by examination of the tailcone surface flow (Figure 4.72). At the first inflection point, the vorticity features are similar to the LD3_AR10 nozzle. The flow has migrated down the sidewalls, tailcone vortices are present near the lower surface, and vorticity is generated from the mixing plane. At the second inflection point, the tailcone vortices

168
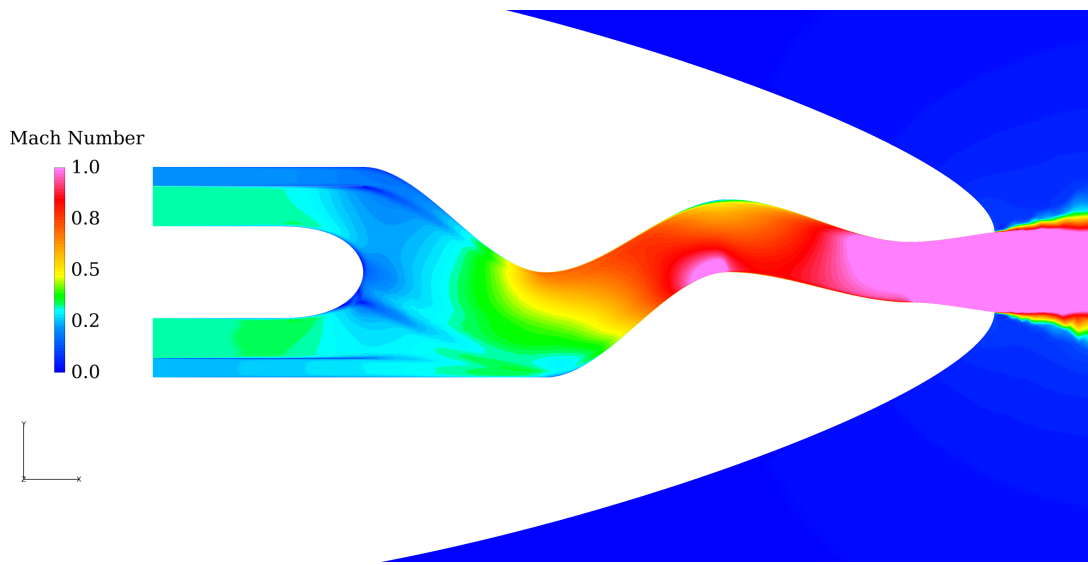
Figure 4.68: Centerline Mach number contours, LD3_AR4.
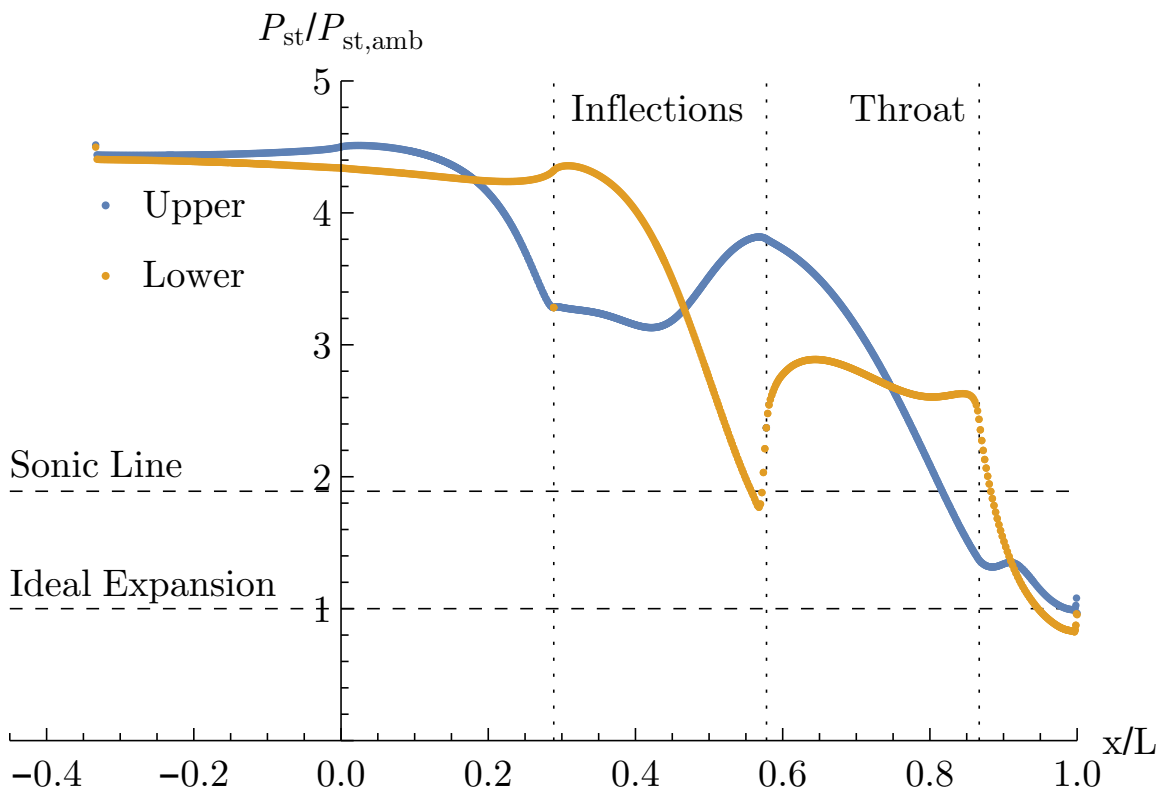
Figure 4.69: Centerline surface $P_{st}/P_{st,amb}$, LD3_AR4.
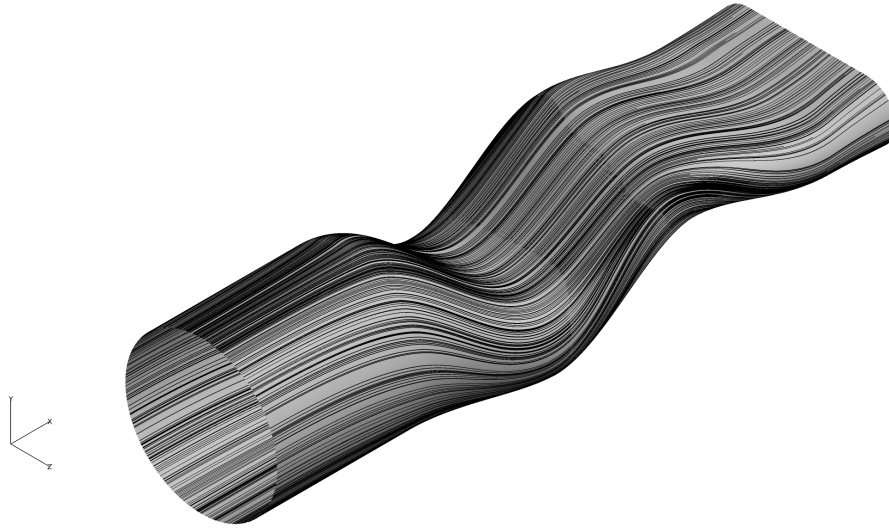
Figure 4.70: Surface flow, LD3_AR4.

are strengthened due to vortex stretching, while pockets of vorticity erupting from the lower surface due to the high degree of turning around the bend. Different than both the LD2_AR4 and LD3_AR10 nozzles, distinct sidewall vortices do not form. Nearing the throat, the tailcone vortices persist, as do the regions of vorticity at the lower surface, while the vorticity from the mixing layer is greatly reduced. At the throat, the small pockets of vorticity are dissipated by the stronger tailcone vortices. No distinct sidewall vortices form, just small regions at the lower corners. At the exit, the tailcone vortices are still present, as well as the smaller regions at the lower corners.

The temperature distribution at the mixing plane in Figure 4.73 is similar to the LD3_AR10 nozzle. At the first inflection, the tailcone vortex trajectory dips into the bypass flow near the lower surface of the nozzle. Migration of the upper bypass flow is observed, although to a lesser extent than the LD3_AR10 nozzle due to the smaller amount of lateral divergence. At the second inflection, the "whale tail" pattern emerges. The tailcone vortices entrain bypass flow into the center of the nozzle, nearly symmetrically. The core flow has extended to the central lower surface, initiating a hot streak. No entrainment of core

(a) Mixing Plane

(b) 1st Inflection

(c) 2nd Inflection

(d) Nearing Throat

(e) Throat

(f) Exit
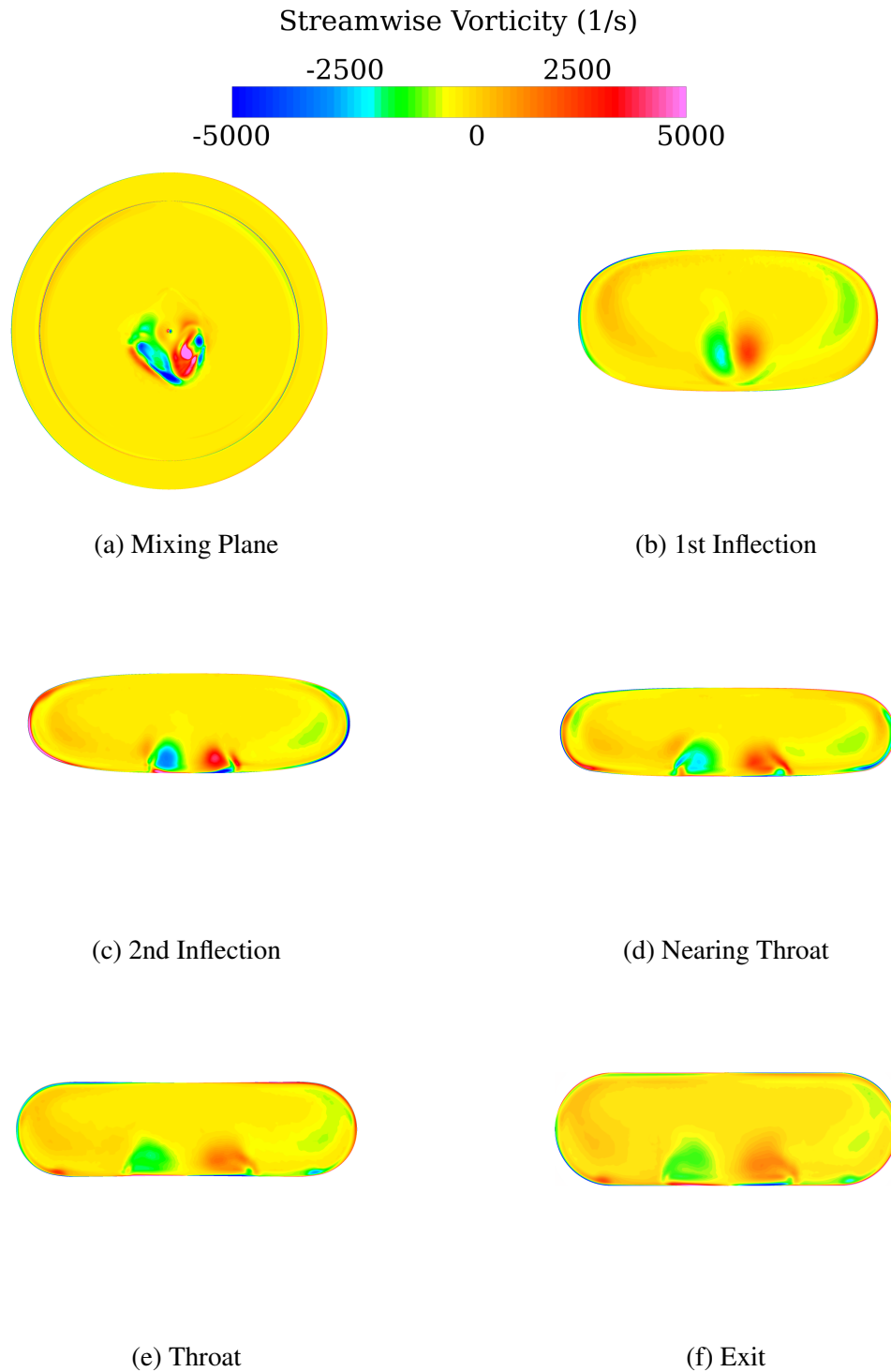
Figure 4.71: Progression of vorticity development, LD3_AR4.
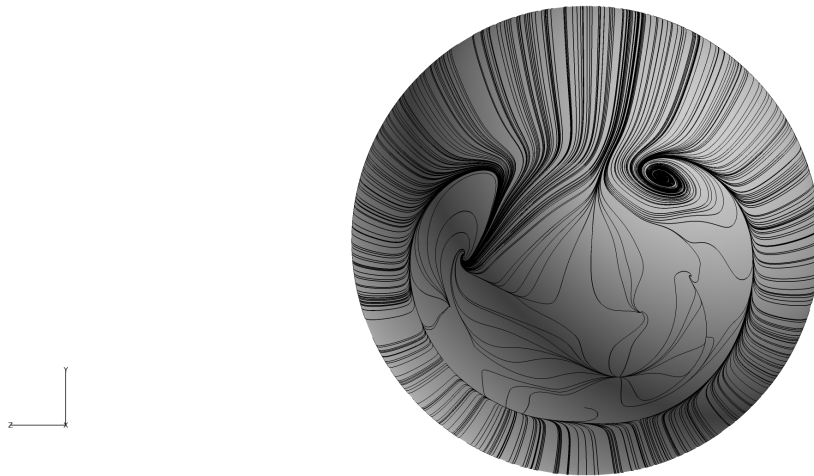
Figure 4.72: Tailcone surface flow, LD3_AR4.

flow to the sidewalls is observed due to the lack of sidewall vortices. Nearing the throat, entrainment by the tailcone vortices continues and the hot core flow at the lower surface spreads laterally. At the throat, the temperature distribution is similar, with more mixing occurring near the lower surface. At the exit, the tailcone vortex entrainment results in an asymmetric distribution, with the bypass flow residing at the outer lower regions of the nozzle.

(a) Mixing Plane

(b) 1st Inflection

(c) 2nd Inflection

(d) Nearing Throat

(e) Throat

(f) Exit
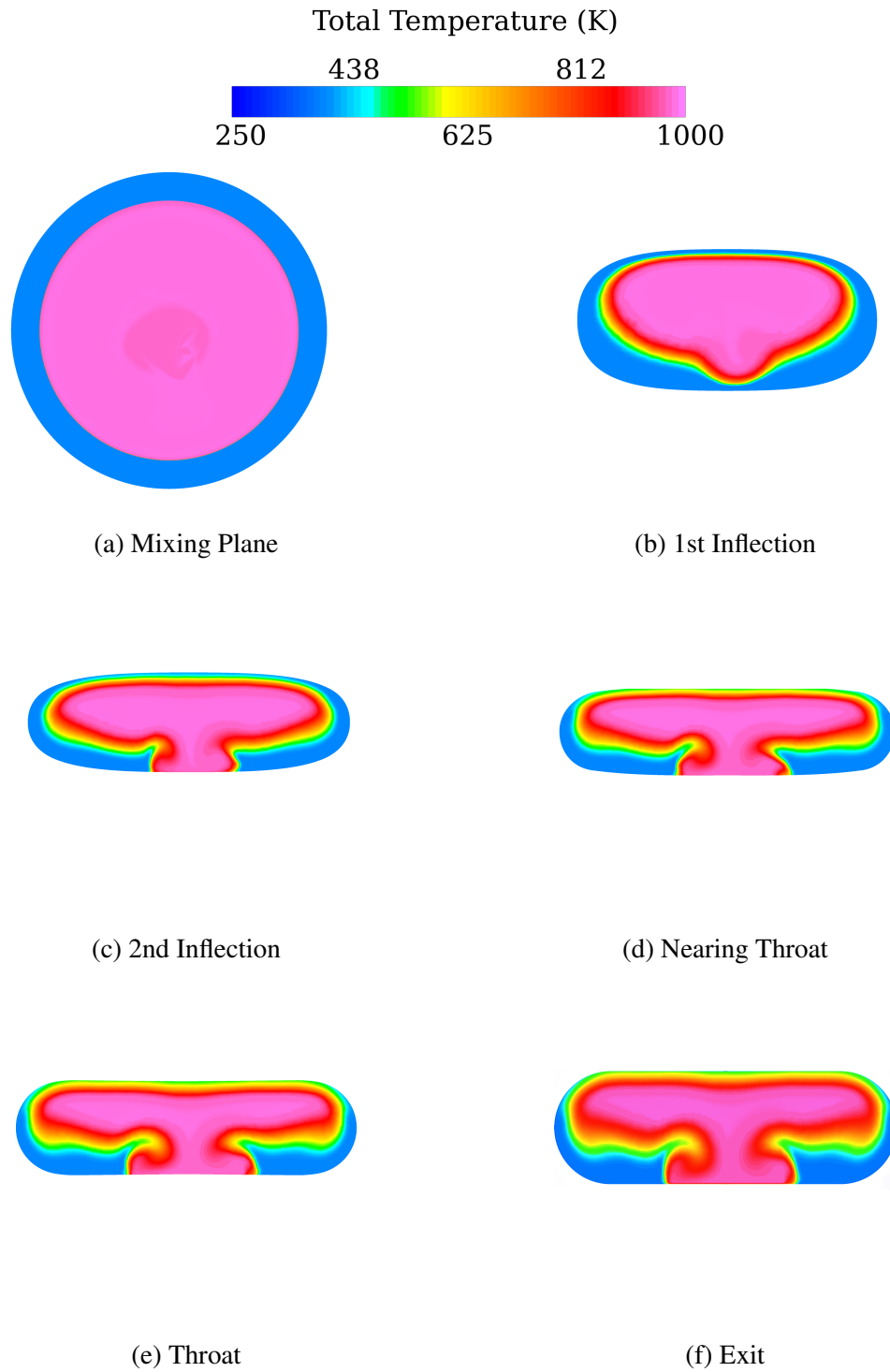
Figure 4.73: Progression of temperature distribution, LD3_AR4.

4.3.10 LD3_AR4, Swirl.

Examination of Mach number at the centerline for the LD3_AR4 nozzle with swirl in Figure 4.74 indicates a different separation behavior off the tailcone but otherwise similar behavior to the no-swirl case. This is confirmed in Figure 4.75, where the swirl induces a single vortex like previous swirl cases. Flow behavior around the bends and at the throat is similar to the no-swirl case, as reflected in the $P_{st}/P_{st,amb}$ plot in Figure 4.76.
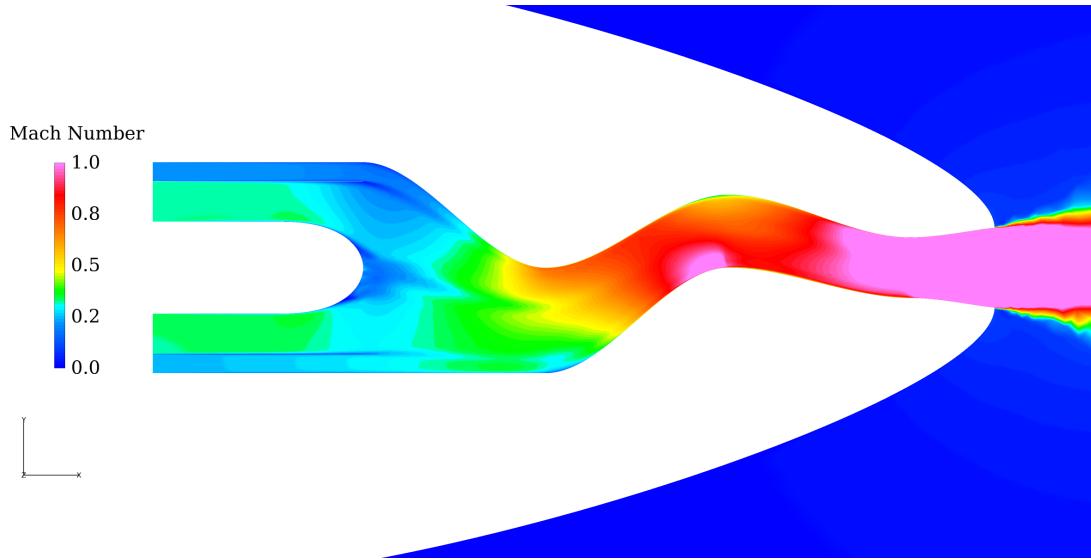
Figure 4.74: Centerline Mach number contours, LD3_AR4 with swirl.

The streamwise vorticity at the mixing plane (Figure 4.77) is almost identical to the LD3_AR10 swirl case. The same is true at the first inflection with the central vortex dominating the vorticity distribution, the movement of the flow at the sidewalls evident, and the positive vorticity of the mixing layer reduced compared to the no-swirl solution due to the swirl direction. At the second inflection point, the central vortex remains strong. Similar to the no-swirl case, no sidewall vortices form. Like previous swirl solutions, a region of negative vorticity has developed in the upper port-side of the nozzle due to the coalescence of flow at the second bend, as seen in Figure 4.78. Nearing the throat, the central vortex persists, and vorticity is stronger at the lower corners. At the throat,

174
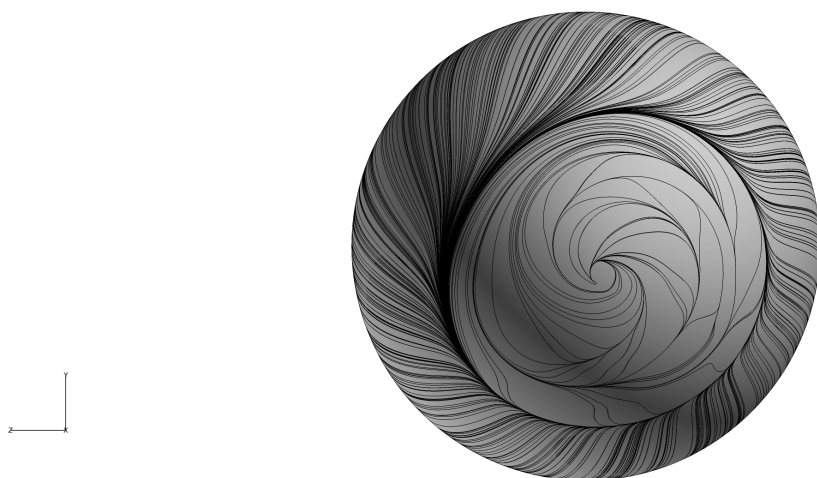
Figure 4.75: Tailcone surface flow, LD3_AR4 with swirl.
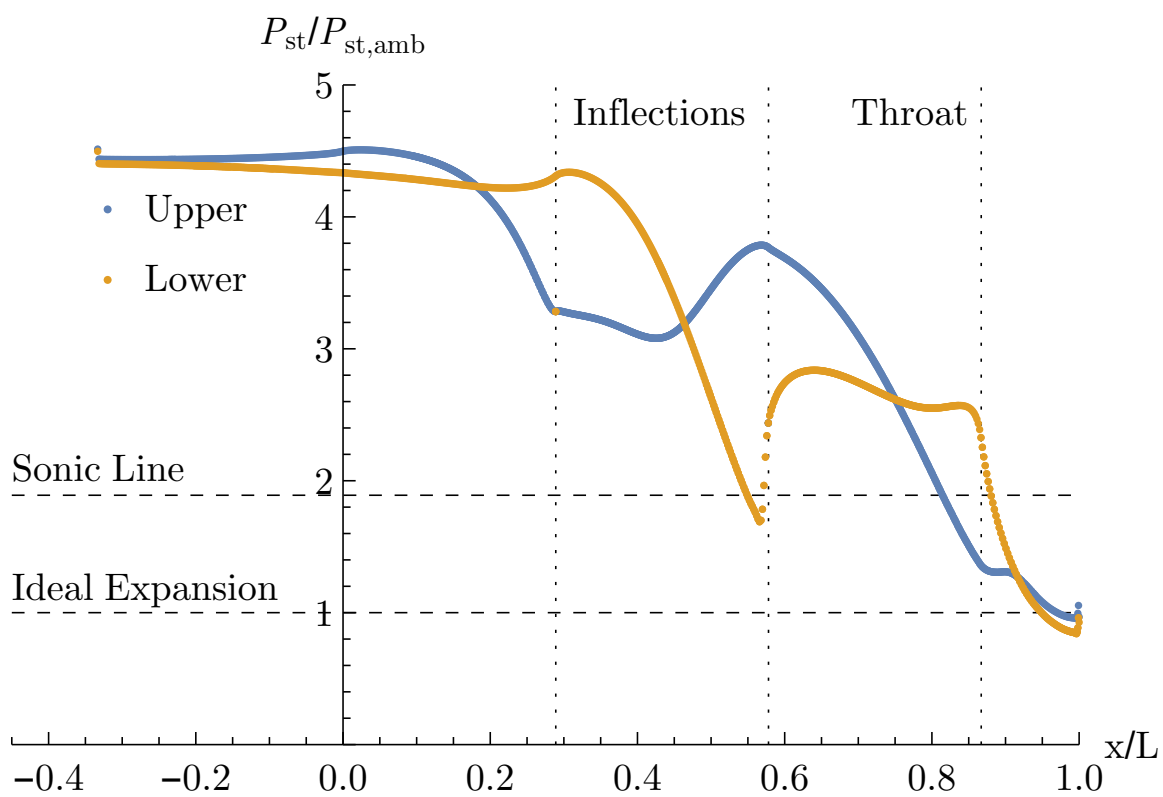
Figure 4.76: Centerline surface $P_{st}/P_{st,amb}$, LD3_AR4 with swirl.

the central vortex is present slightly port of centerline. Small vortices form in the lower corners, which were not present in the no-swirl case. At the exit, the vorticity distribution is weakened due to nozzle expansion.

The temperature distribution in Figure 4.41 reveals a similar pattern as the LD3_AR10 swirl nozzle, though compressed because of the reduced lateral divergence. The distribution differs greatly from the the no-swirl case like previous solutions. The mixing plane is similar to the no-swirl case. At the first inflection point, the swirl causes some asymmetry in the distribution. At the second inflection point, the coalescence of upper port-side flow begins to dip into the core flow, while the movement of the upper bypass flow away from the upper centerline allows the core flow to impinge on the upper surface and initiate a hot streak. Nearing the throat, more hot flow spreads across the upper surface and the distinct barrier created by the upper vorticity is observed. At the throat, the pattern remains similar since the final amount of lateral divergence is small compared to the $AR = 10$ cases, where a larger difference is observed between the two locations. The same holds true at the exit, where the temperature distribution pattern is essentially the same as the throat.

Streamwise Vorticity (1/s)

(a) Mixing Plane

(b) 1st Inflection

(c) 2nd Inflection

(d) Nearing Throat

(e) Throat

(f) Exit
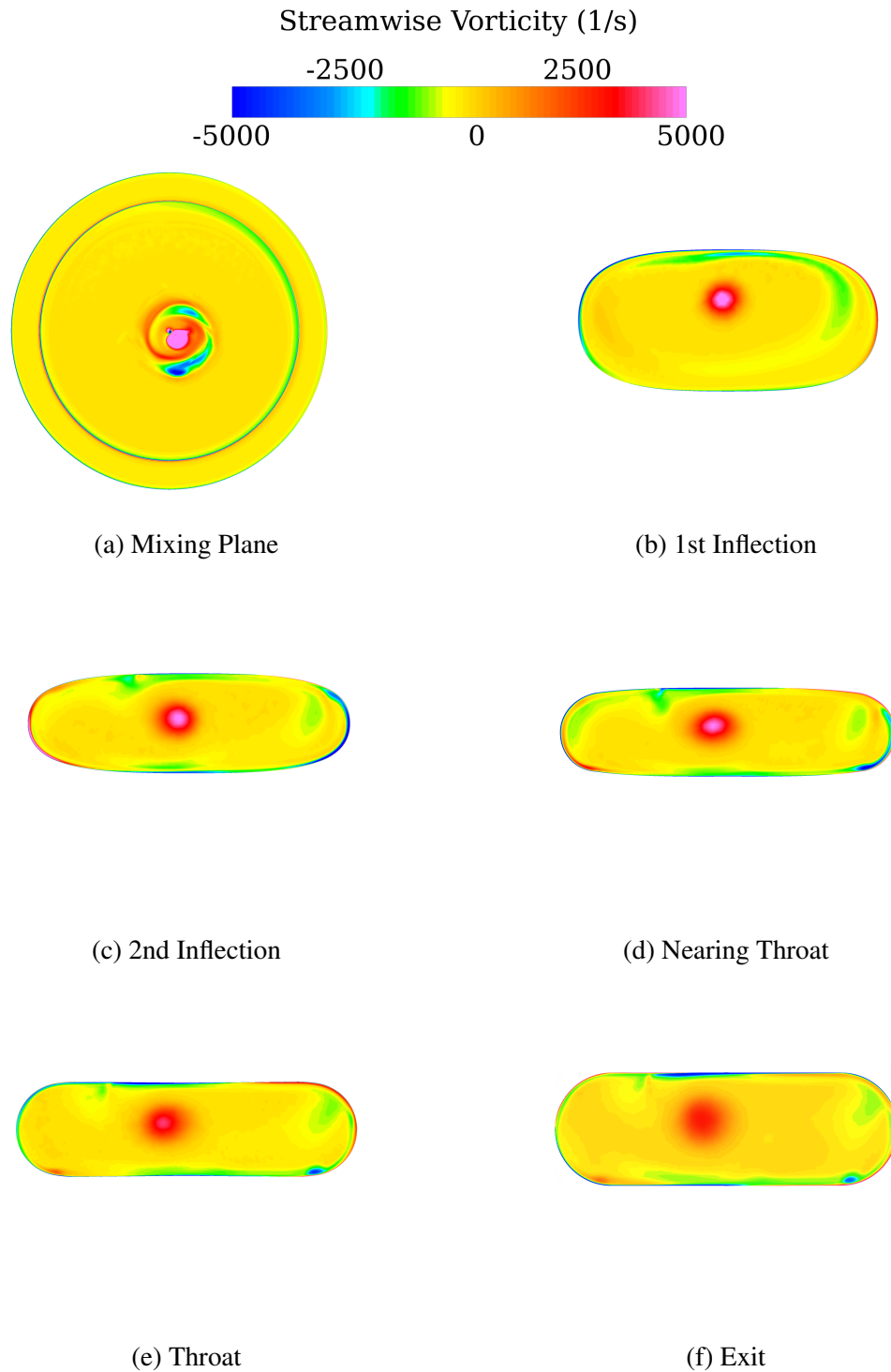
Figure 4.77: Progression of vorticity development, LD3_AR4 with swirl.
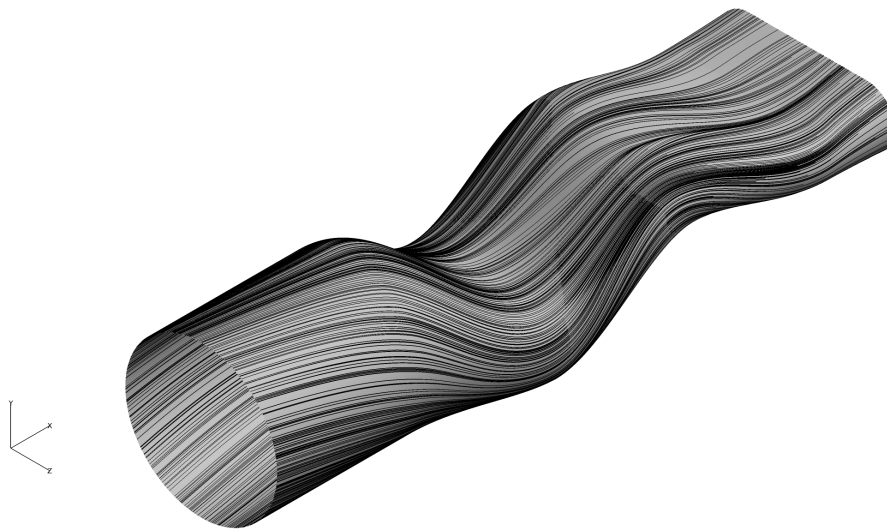
Figure 4.78: Surface flow, LD3_AR4 with swirl.

(a) Mixing Plane

(b) 1st Inflection

(c) 2nd Inflection

(d) Nearing Throat

(e) Throat

(f) Exit
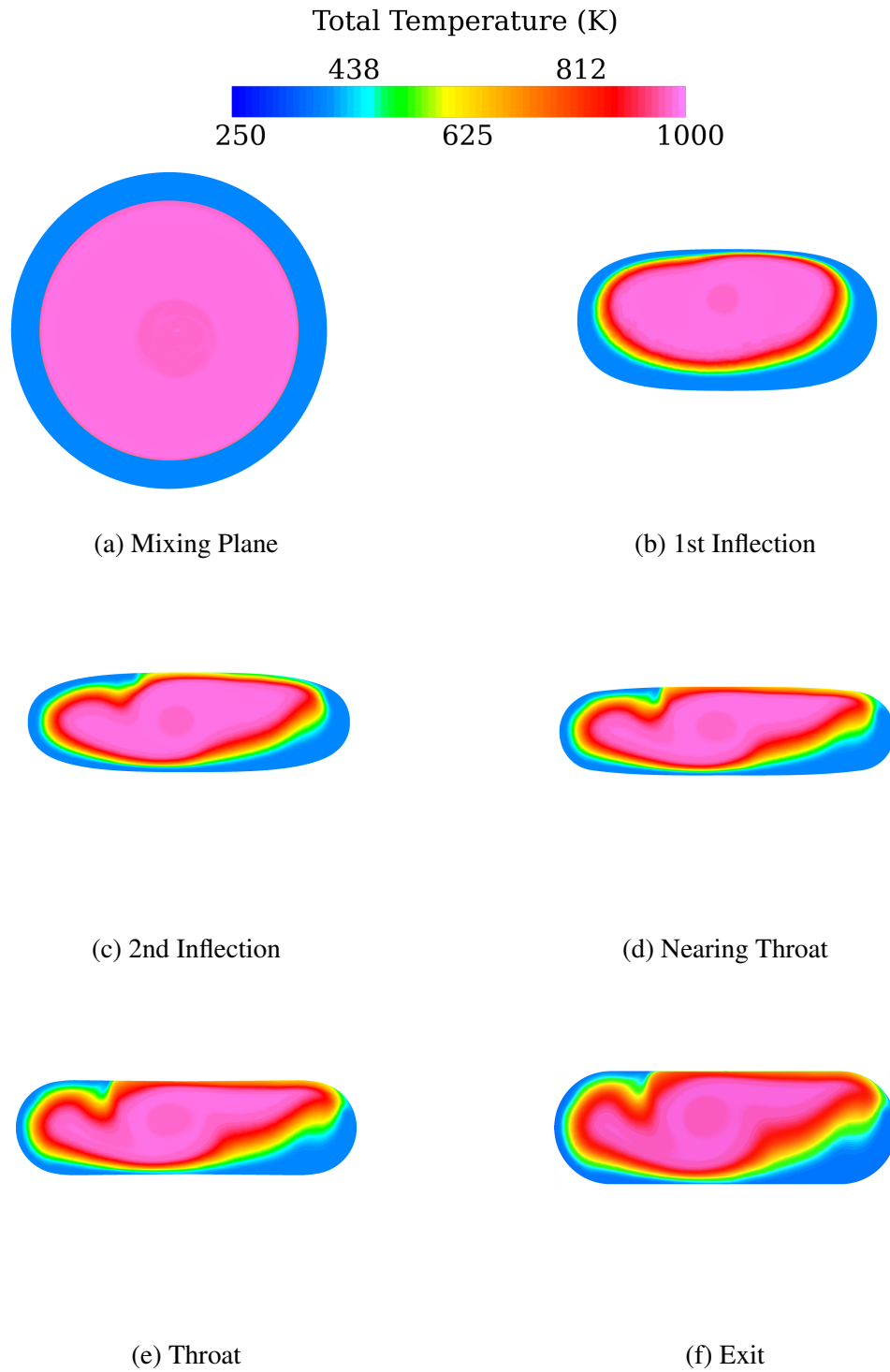
Figure 4.79: Progression of temperature distribution, LD3_AR4 with swirl.

179

4.3.11 LD4_AR4, No-swirl.

Examination of Mach contours for the LD4_AR4 nozzle in Figure 4.80 shows more similarity to the LD4_AR10 nozzle than the shorter LD3_AR4 nozzle. The separation off the tailcone has a similar downward trajectory. Compared to shorter nozzles, the flow acceleration around the bends is lower due to the increase in radius of curvature. As seen in the centerline plots of $P_{st}/P_{st,amb}$ in Figure 4.81, the flow does not reach sonic velocity at the second bend like the LD3_AR4 nozzle. The flow does become sonic upstream of the throat and the upper surface is ideally expanded, while the lower surface is slightly overexpanded. Surface flow results in Figure 4.82 show no flow separation and only slight coalescence of the streamlines at the sidewalls due to the most gradual curvature changes of all nozzles designed for this research.
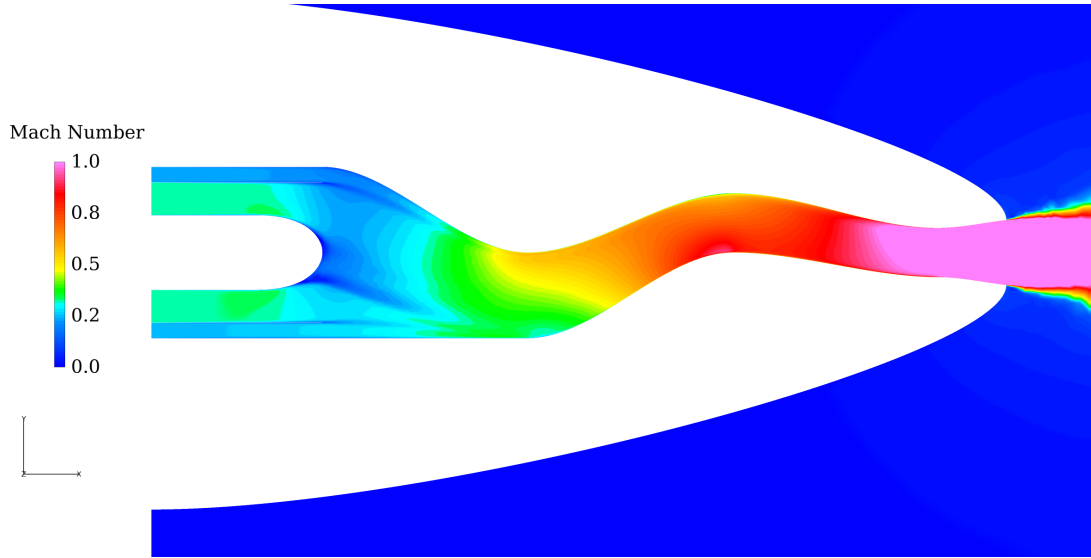
Figure 4.80: Centerline Mach number contours, LD4_AR4.

The contours of vorticity in Figure 4.83 reveal a similar pattern as the LD3_AR4 nozzle, only reduced in strength due to more gradual streamline curvature. The mixing plane shows a similar pair of counter-rotating vortices as with all other nozzles. Examination of the tailcone surface flow in Figure 4.84 shows a separation behavior similar
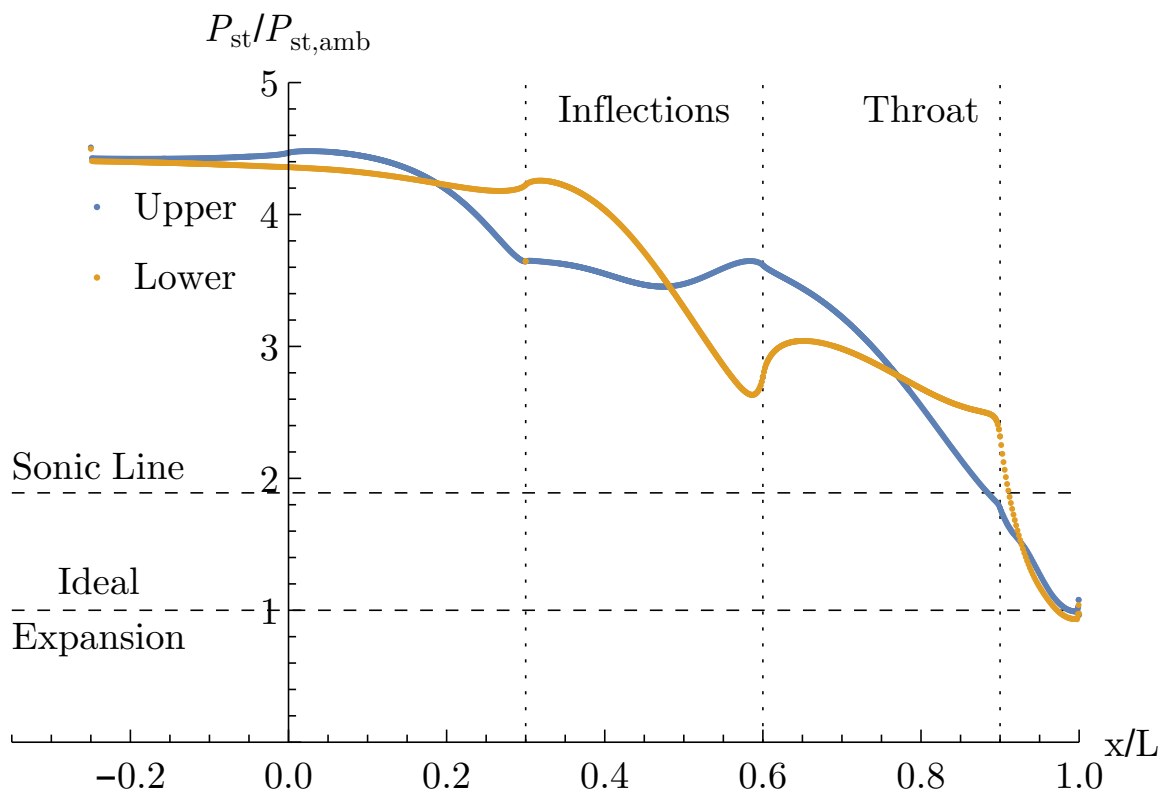
Figure 4.81: Centerline surface $P_{st}/P_{st,amb}$, LD4_AR4.
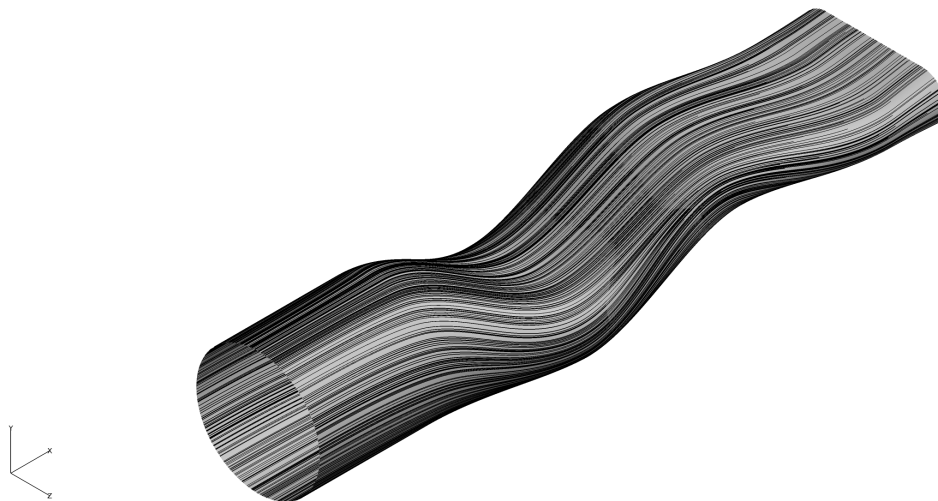
Figure 4.82: Surface flow, LD4_AR4.

to the LD4_AR10 nozzle, again attributed to the low influence of the upper curvature. The vortex foci are seen on the lower half of the tailcone, though not as prominent as shorter nozzles. At the first inflection point, the counter-rotating vortex pair is observed, slightly weaker than shorter nozzles due to a decrease in vortex stretching because of a more gradual curvature. Vorticity generation due to the change in cross-sectional shape is seen at the sidewalls, but like the LD4_AR10 nozzle, almost no streamwise vorticity is generated in the mixing layer. The lack of mixing layer vorticity suggests that the vorticity seen in previous solutions in this region is not due to the mixing layer itself but rather the interaction of the mixing layer with more drastic geometry changes. At the second inflection point, the vortex pair persists at the bottom of the nozzle, and the flow at the sidewalls and bottom surface have changed sign due to the change in streamline curvature direction. Nearing the throat, the vortex pair persists and small regions of vorticity appear below the tailcone vortex like the LD3_AR4 nozzle. At the throat, the vortex pair weakens due to the nozzle reaching minimal area (sonic velocity) upstream of the designed throat. At the exit, the vortex pair has weakened further due to the expansion of the flow.

Like vorticity, temperature distribution in Figure 4.85 is similar to the LD3_AR4 nozzle. The mixing plane reveals no new features. At the first inflection point, the counter-rotating vortices dip into core flow as seen in other nozzles, although the distance to the lower surface is smaller when compared to the shorter nozzles due to the lower trajectory seen in the Mach contours. At the second inflection, the distribution is similar to the LD3_AR4 case, including the initiation of a hot streak along the lower surface. Nearing the throat, the distribution persists, with more mixing occurring at the top of the nozzle demonstrated by an increase in temperature. The vortex pair continues to entrain cooler flow toward the center of the nozzle. The lateral extent of the hot streak increases. The throat and exit planes continue these trends.
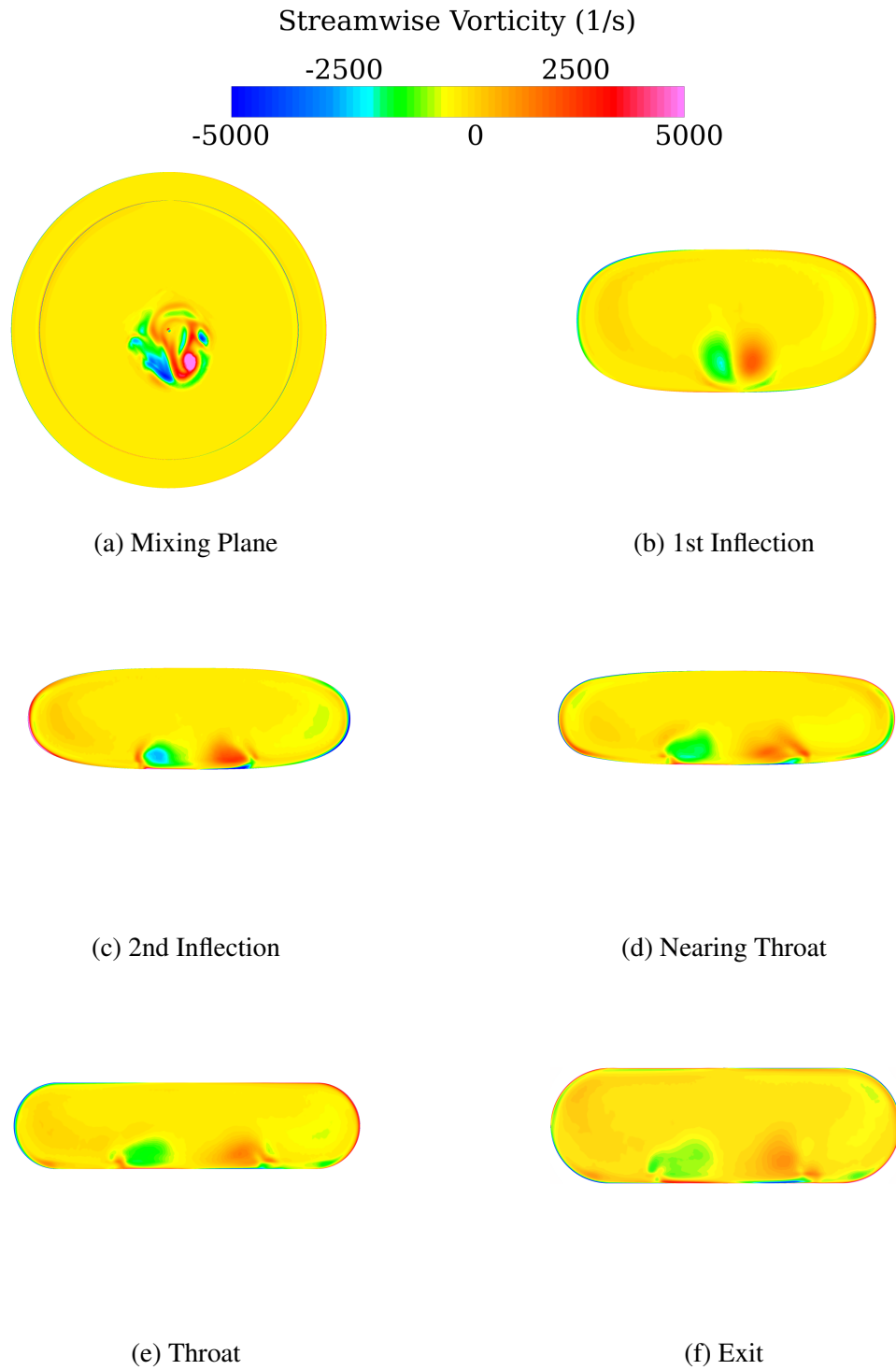
(a) Mixing Plane

(b) 1st Inflection

(c) 2nd Inflection

(d) Nearing Throat

(e) Throat

(f) Exit

Figure 4.83: Progression of vorticity development, LD4_AR4.
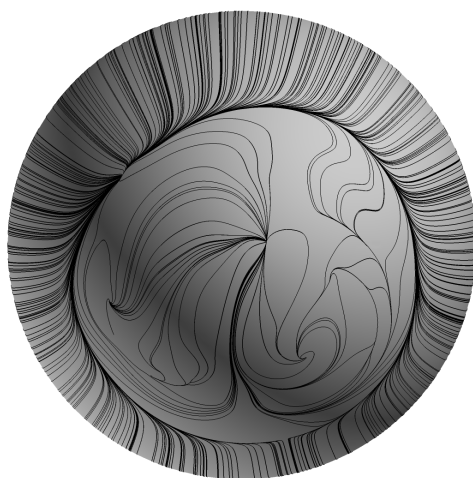
Figure 4.84: Tailcone surface flow, LD4_AR4.

(a) Mixing Plane

(b) 1st Inflection

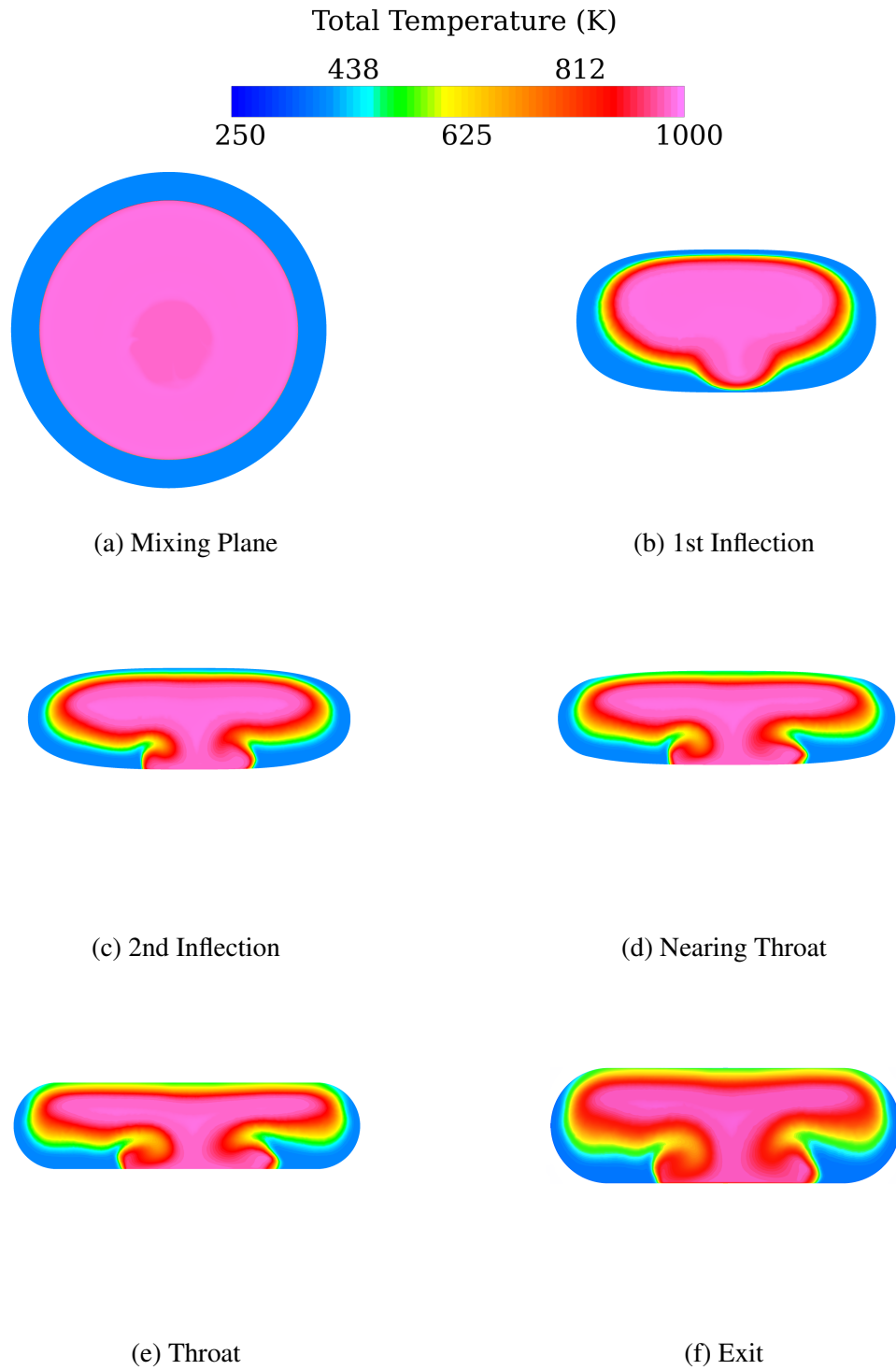(c) 2nd Inflection

(d) Nearing Throat

(e) Throat

(f) Exit

Figure 4.85: Progression of temperature distribution, LD4_AR4.

4.3.12   LD4_AR4, Swirl.

Mach contours are very similar to the no-swirl save for the tailcone separation. The central vortex off the tailcone is shown Figure 4.87 like previous swirl cases. The centerline plots of $P_{st}/P_{st,amb}$ shown in Figure 4.88 are also very similar to the no-swirl case.
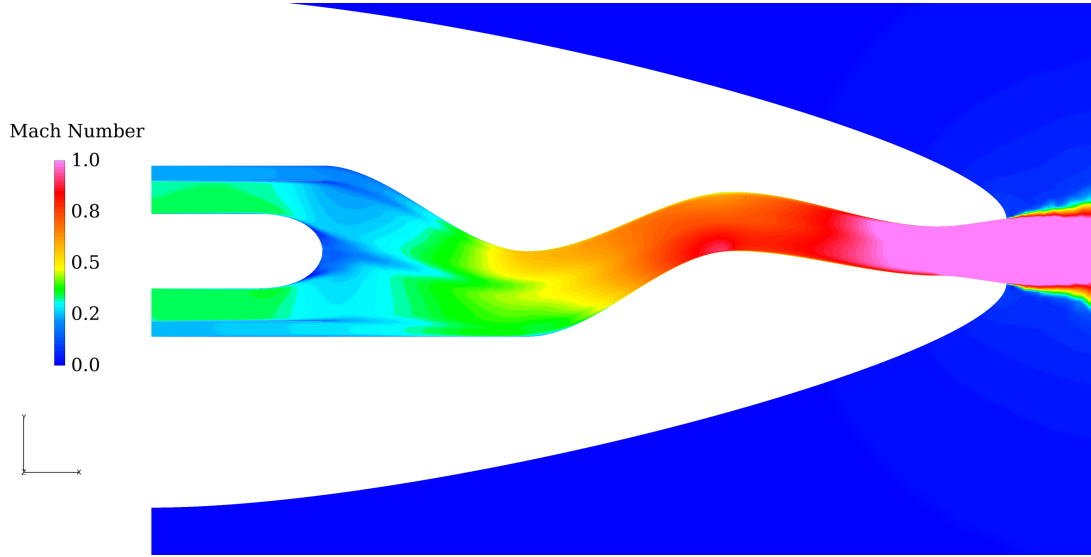
Figure 4.86: Centerline Mach number contours, LD4_AR4 with swirl.
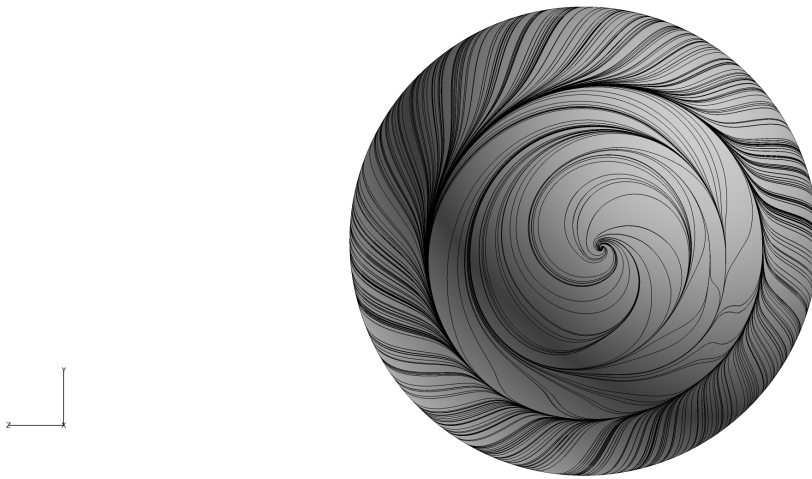
Figure 4.87: Tailcone surface flow, LD4_AR4 with swirl.
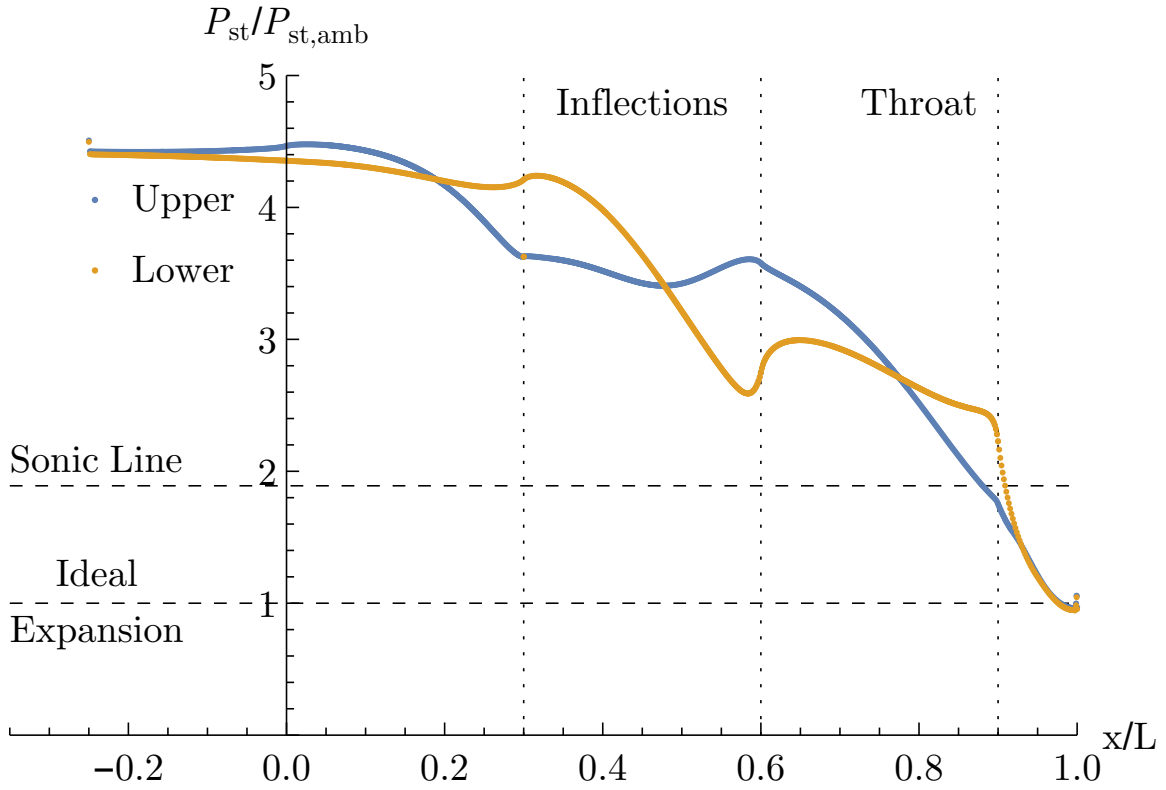
Figure 4.88: Centerline surface $P_{st}/P_{st,amb}$, LD4_AR4 with swirl.

The streamwise vorticity distribution in Figure 4.89, like the no-swirl case, has more in common with the shorter LD3_AR4 nozzle than the LD4_AR10 case. The mixing plane again reveals the strong single vortex from the tailcone separation. At the first inflection point, the strong central vortex dominates the streamwise vorticity. Vorticity generation at the upper mixing layer is observed due to the swirling flow. At the second inflection point, the central vortex persists and the coalescence of the flow at the upper port-side of the nozzle in Figure 4.90 induces a region of negative vorticity. Nearing the throat, all regions of vorticity generation remain. At the lower corners, vorticity is increased due to the downward curvature of the nozzle. At the throat, a similar pattern continues, with the central vortex losing some strength due to the lack of strong vortex stretching. At the exit,

the central vortex strength is further reduced, and the vorticity at the sidewalls is consistent with the expansion of the flow through the divergent section.

The temperature distribution in Figure 4.85 is very similar to the LD3_AR4 nozzle. The mixing plane and first inflection planes are nearly identical to the shorter nozzle. The second inflection point reveals the initiation of a hot streak at the upper surface and the influence of upper surface flow coalescence. Nearing the throat, this behavior is amplified, with more penetration into the core by the cooler flow in the upper vortex and the hot flow spreading across the upper surface. At the throat, the extent of the hot flow impinging on the upper surface increases, with more mixing occurring on the port side. At the starboard side, as seen in other nozzles, the competition between the swirl direction and the direction of lateral divergence prevents mixing as the lower corner remains filled with bypass flow. At the exit, more mixing has occurring at the port side, while the hot flow spreads further across the upper surface.

Streamwise Vorticity (1/s)

(a) Mixing Plane

(b) 1st Inflection

(c) 2nd Inflection

(d) Nearing Throat

(e) Throat

(f) Exit
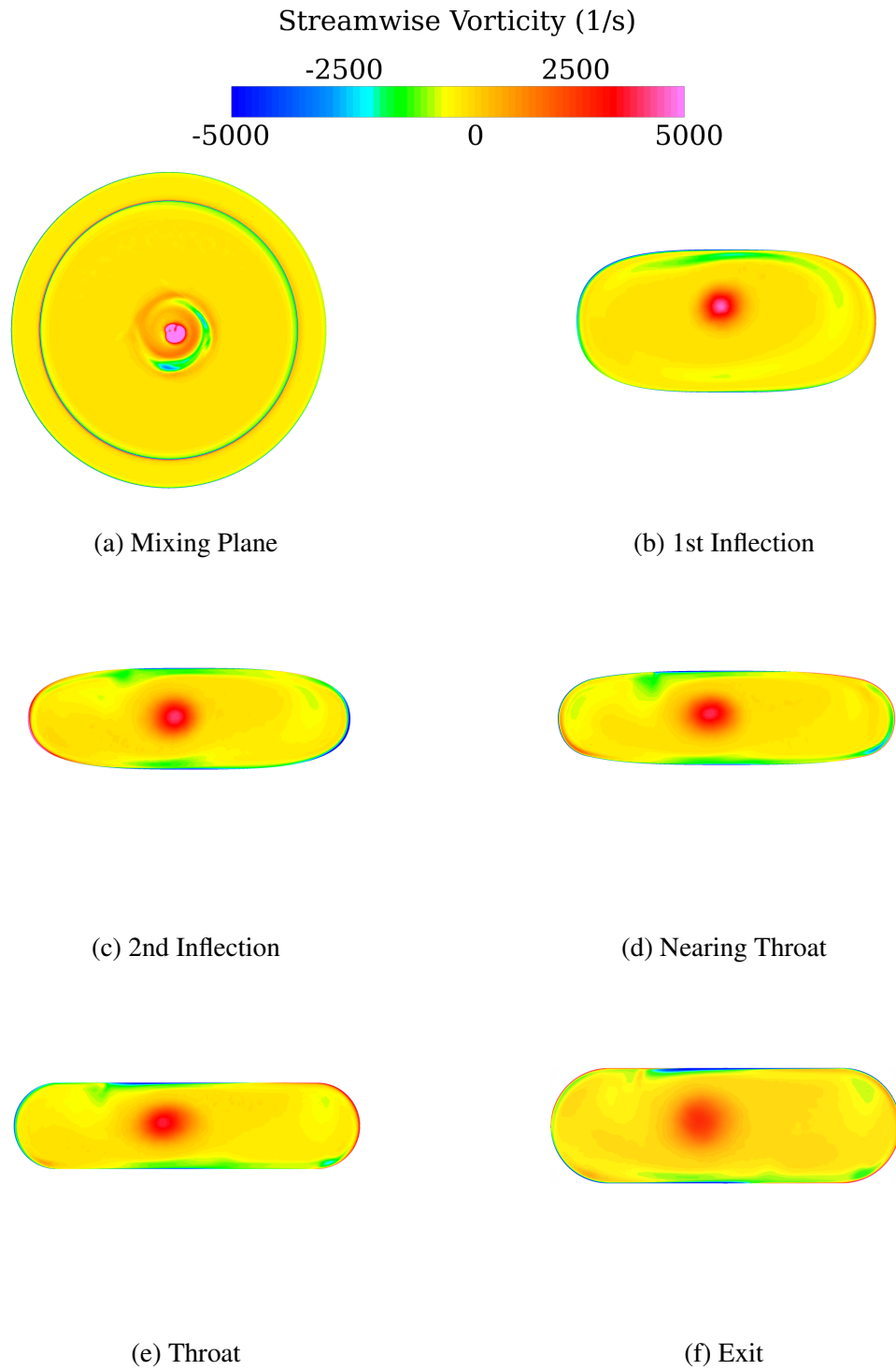
Figure 4.89: Progression of vorticity development, LD4_AR4 with swirl.
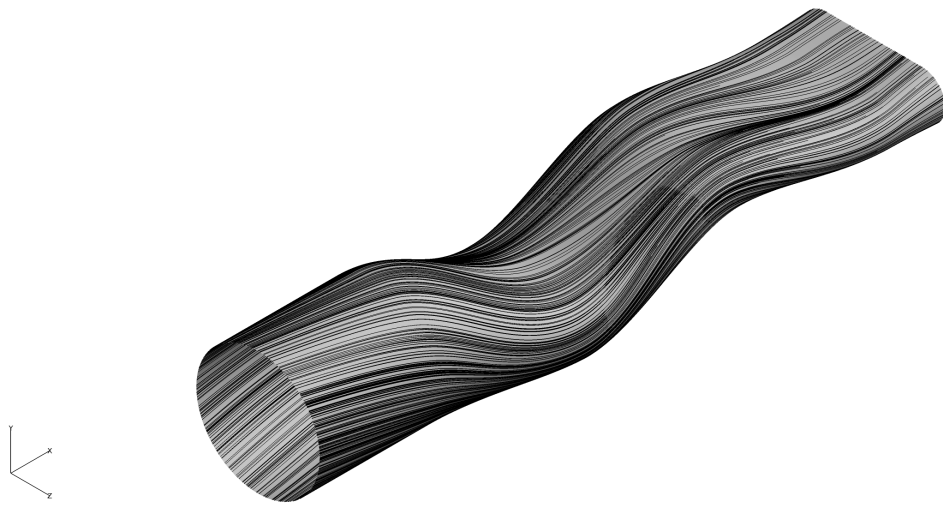
Figure 4.90: Surface flow, LD4_AR4 with swirl.

(a) Mixing Plane

(b) 1st Inflection

(c) 2nd Inflection

(d) Nearing Throat

(e) Throat

(f) Exit
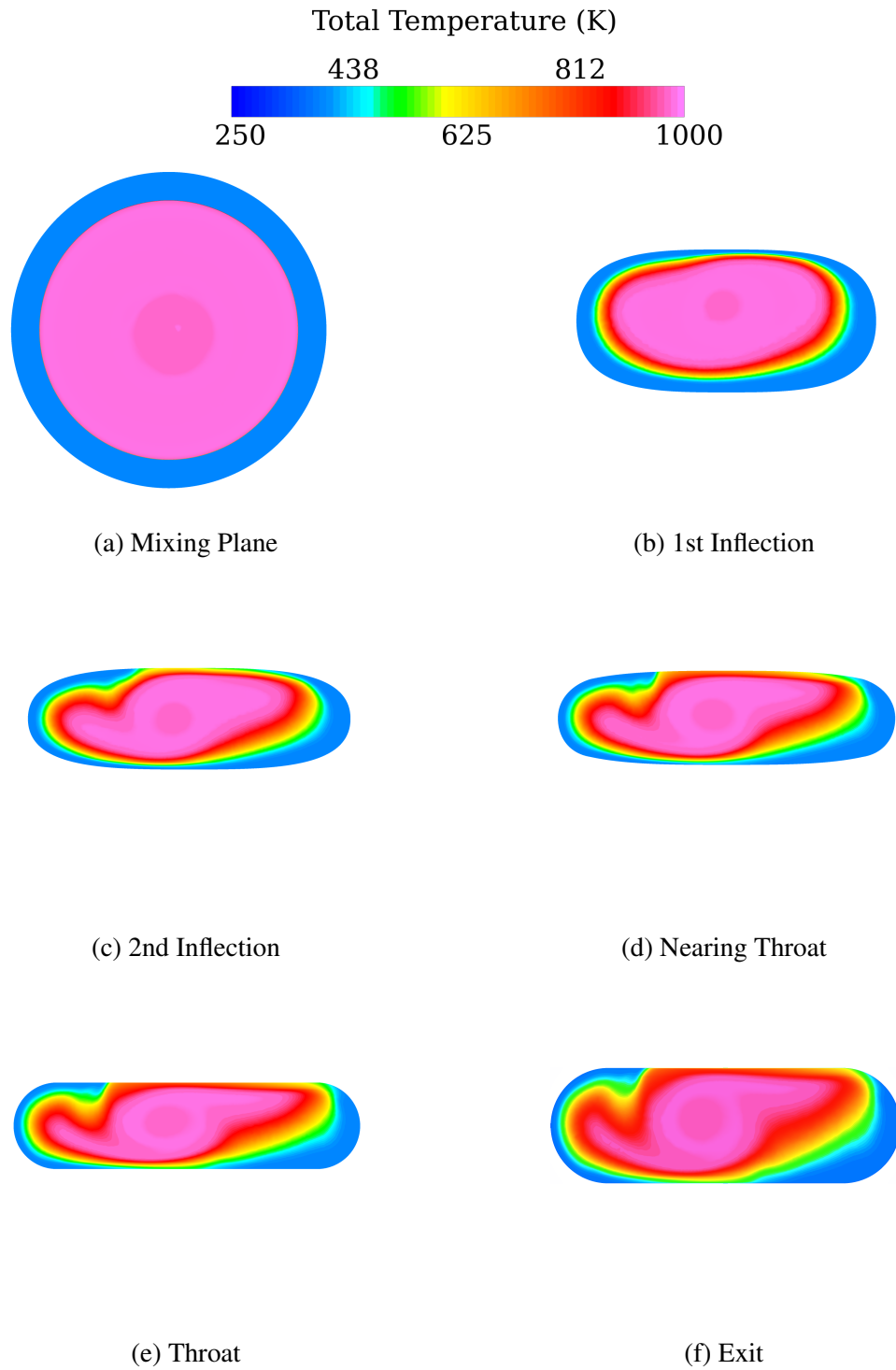
Figure 4.91: Progression of temperature distribution, LD4_AR4 with swirl.

4.4 RSM Demonstration Cases

Section 3.5 notes one of the primary reasons in choosing Fluent for this research is the RSM turbulence model capability, which has been shown to improve results in serpentine flows due to more accurate calculation of the Reynolds stresses. Throughout the course of this research many attempts were made at applying the RSM turbulence model. Unfortunately, a stable second-order solution was not obtainable. The highest fidelity achieved were solutions where all terms are second-order except the turbulent quantities (Reynolds stresses and ω). The lack of a fully second-order RSM solution is the reason the preceding solutions were all accomplished using the K-ω SST model; first-order accurate solutions are unacceptable for academic or practical consideration [48]. The solution instability arose in the supersonic portion of the nozzle between the throat and exit and just downstream of the exit near the OML surface. Discussions with the code developer (ANSYS) revealed a similar issue faced by their researchers in preparation for the second PAW involving a subsonic serpentine duct with turning vane. The issue is currently being investigated by ANSYS. The following results compare the RSM solutions for the LD3_AR4 and LD3_AR10 nozzles with the corresponding K-ω SST no-swirl cases. The demonstration cases presented in this section are narrower in scope than the preceding section for the purpose of showing a difference between the two methods utilizing select but representative nozzle designs. In both cases the computational domain and code settings are identical except for the change in turbulence model.

4.4.1 LD3_AR4.

Figure 4.92 shows little difference in surface $P_{st}/P_{st,amb}$ between the K-ω SST and RSM solutions for the LD3_AR4 nozzle. The same is true of the surface flow in Figure 4.93 and Mach contours in Figure 4.94. There is a distinct difference in the tailcone surface flows in Figure 4.95, where the asymmetry in the RSM shifts to the opposite side as the

192

K-ω SST solution. Stronger vortex foci are displayed in the RSM case due to the increased ability to capture anisotropic Reynolds stresses around curved surfaces.
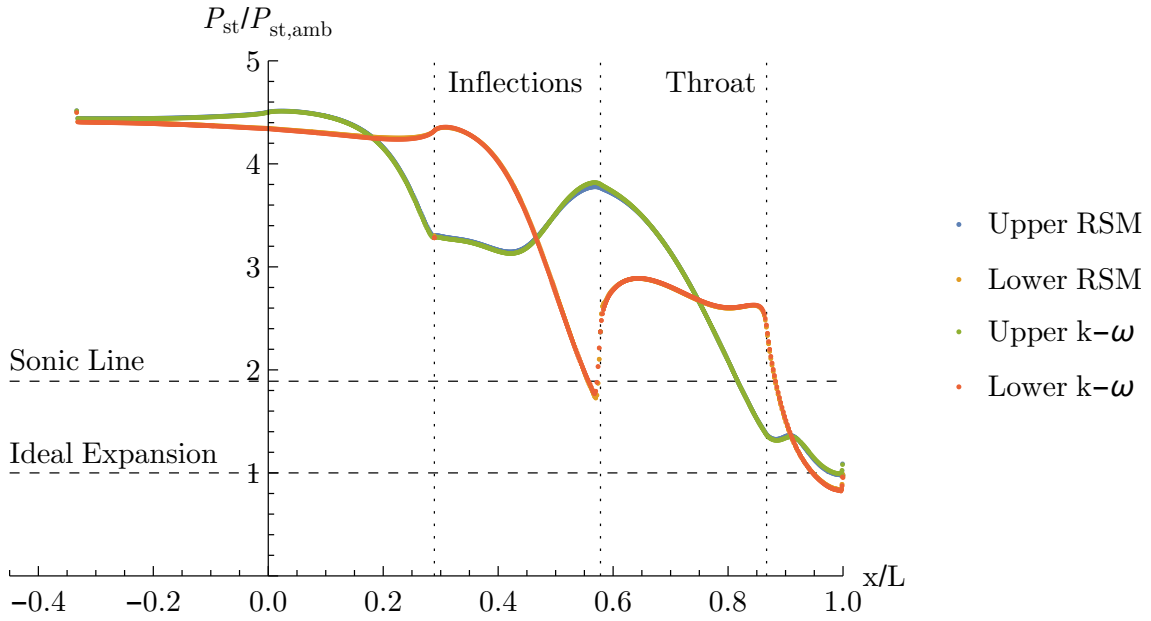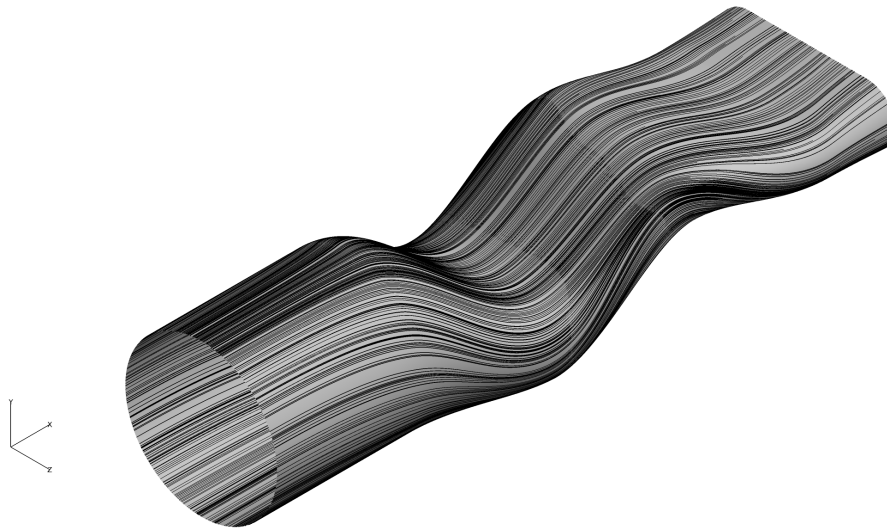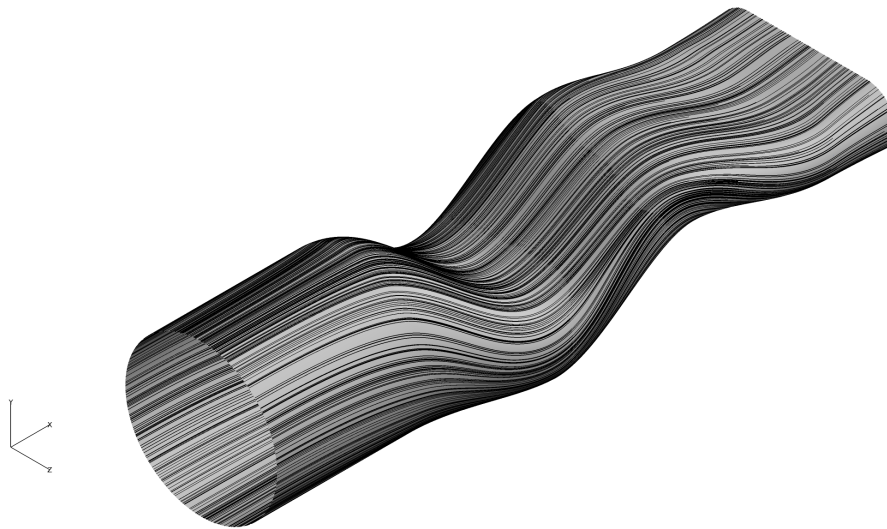

Figure 4.92: Centerline surface $P_{st}/P_{st,amb}$, LD3_AR4, K-ω SST vs. RSM.
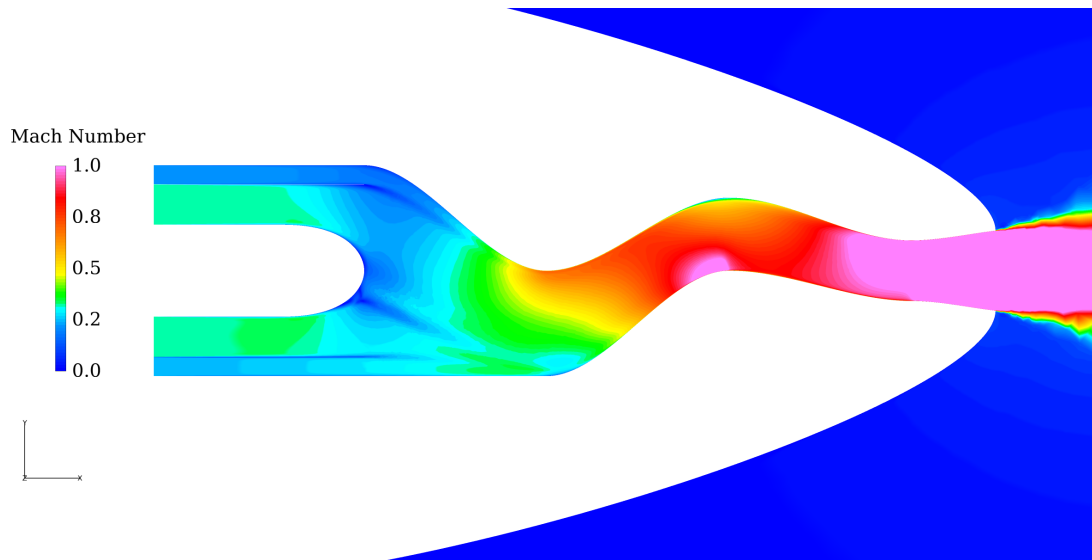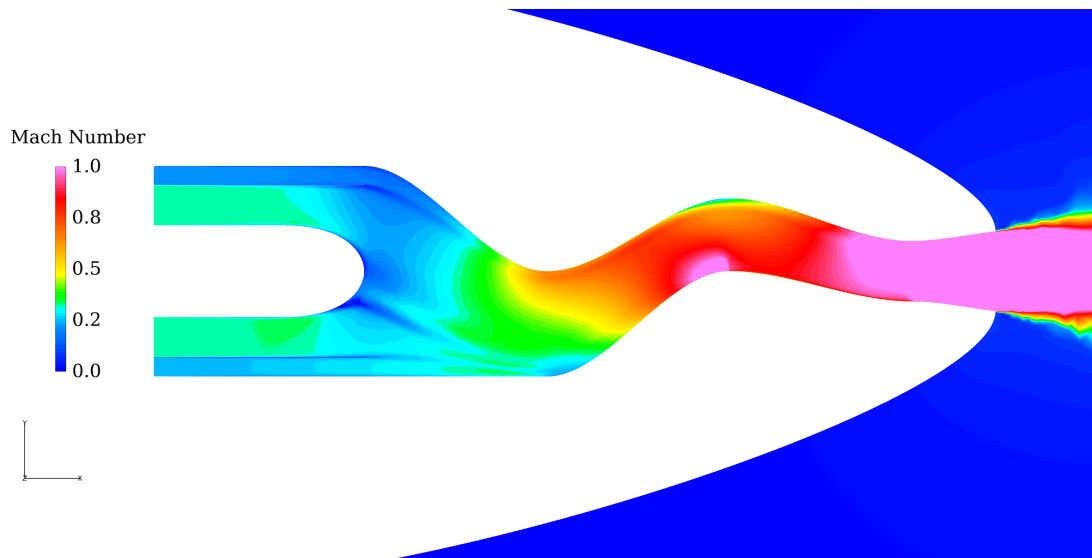
(a) K-ω SST.

(b) RSM.

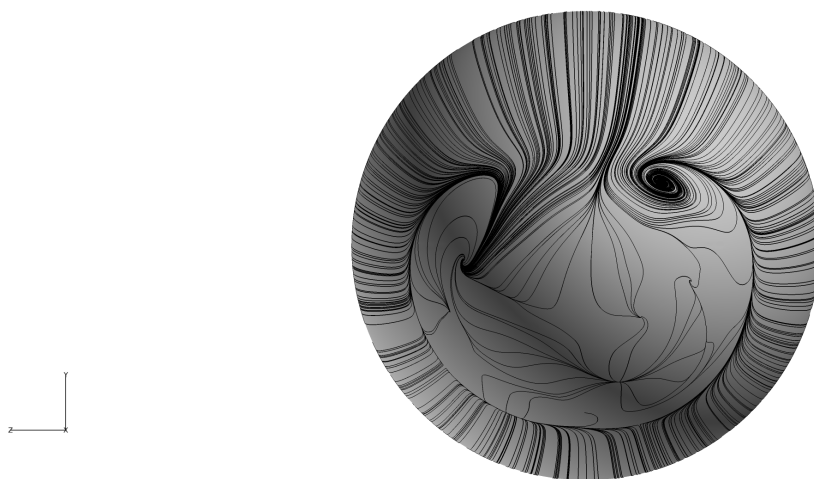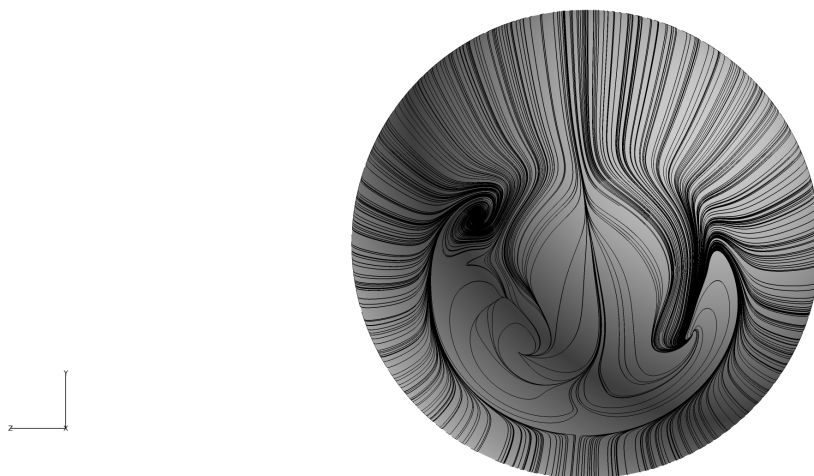Figure 4.93: Surface flow, LD3_AR4, K-ω SST vs. RSM.

(a) K-ω SST.

(b) RSM.

Figure 4.94: Centerline Mach number contours, LD3_AR4, K-ω SST vs. RSM.

(a) K-ω SST.

(b) RSM.

Figure 4.95: Tailcone surface flow, LD3_AR4, K-ω SST vs. RSM.

Differences in the two solutions is also seen in the streamwise vorticity profiles shown in Figure 4.96. The mixing plane clearly displays the change in symmetry at the tailcone. At the first inflection point, the same vorticity pattern is present for both solutions, but the RSM case exhibits higher levels of vorticity for the central counter-rotating vortex pair. A higher level of vorticity is expected due to the increased modeling fidelity of swirling flow. The same is true at the second inflection point, where the central vortex pair is tighter and stronger, with more vorticity at the mixing layer. At the exit, the RSM vorticity distribution is somewhat stronger than the K-ω SST case but is similarly dissipated due to nozzle expansion.

Further differences in the two solutions is seen in the total temperature profiles in Figure 4.97. The mixing planes are similar, but the RSM solution is more symmetric at the first inflection point. Both solutions also display similar levels of mixing, even with different orders of accuracy. At the second inflection point, the differences become more apparent. The RSM case remains more symmetric and more mixing is observed at the central counter-rotating pair. This behavior matches the vorticity distribution, where the increase in vorticity contributes to more mixing in that region. This trend continues to the exit, with more mixing at the lower center for the RSM case. The upper surface also experiences a greater degree of mixing, which contributes to an increase in temperature near the upper surface.
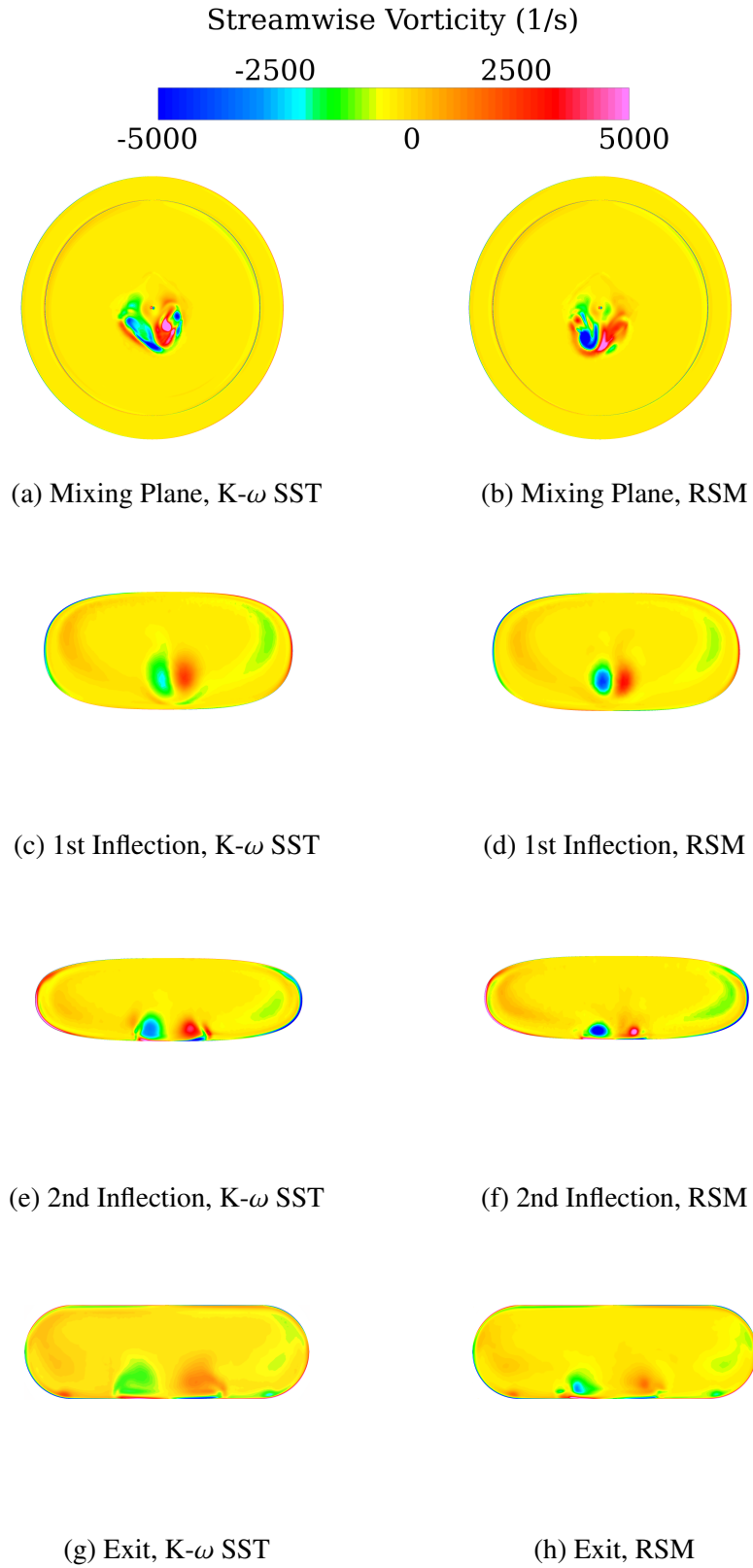
Streamwise Vorticity (1/s)

(a) Mixing Plane, K-ω SST

(b) Mixing Plane, RSM

(c) 1st Inflection, K-ω SST

(d) 1st Inflection, RSM

(e) 2nd Inflection, K-ω SST

(f) 2nd Inflection, RSM

(g) Exit, K-ω SST

(h) Exit, RSM

Figure 4.96: Progression of vorticity distribution, LD3_AR4, K-ω SST vs. RSM.

(a) Mixing Plane, K-ω SST   (b) Mixing Plane, RSM

(c) 1st Inflection, K-ω SST   (d) 1st Inflection, RSM

(e) 2nd Inflection, K-ω SST   (f) 2nd Inflection, RSM

(g) Exit, K-ω SST   (h) Exit, RSM
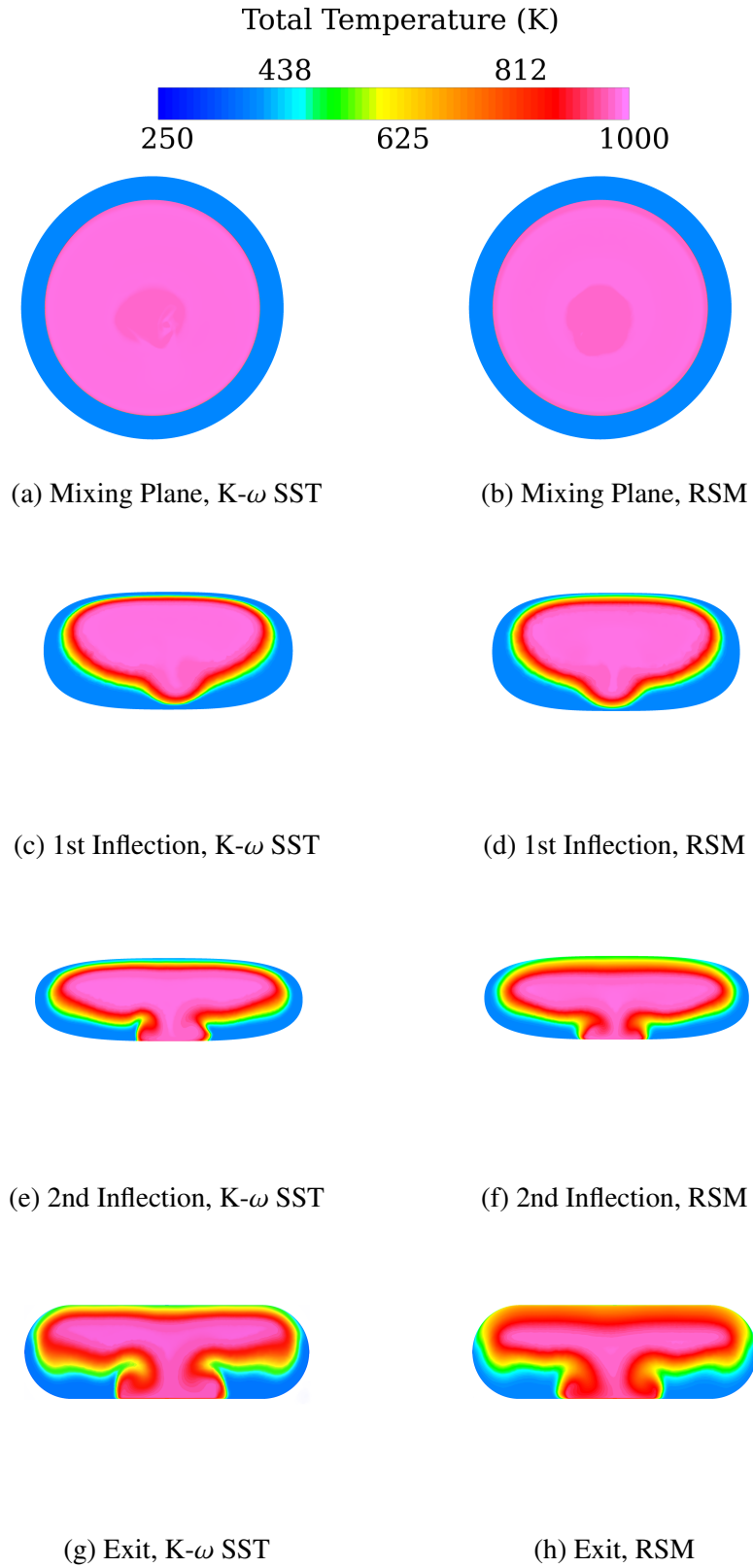
Figure 4.97: Progression of temperature distribution, LD3_AR4, K-ω SST vs. RSM.

4.4.2 LD3_AR10.

For the LD3_AR10 nozzle, Figure 4.98 again shows little difference in surface $P_{st}/P_{st,amb}$ between the K-ω SST and RSM solutions. Differences are seen downstream of the tailcone in the Mach profiles shown in Figure 4.99, with the low momentum fluid in the RSM case forming a more compact separated region. No differences are seen in the surface flow in Figure 4.100, but like the LD3_AR4 nozzle, the tailcone surface flow changes. Figure 4.101 displays more swirling flow on the starboard side around the vortex foci.
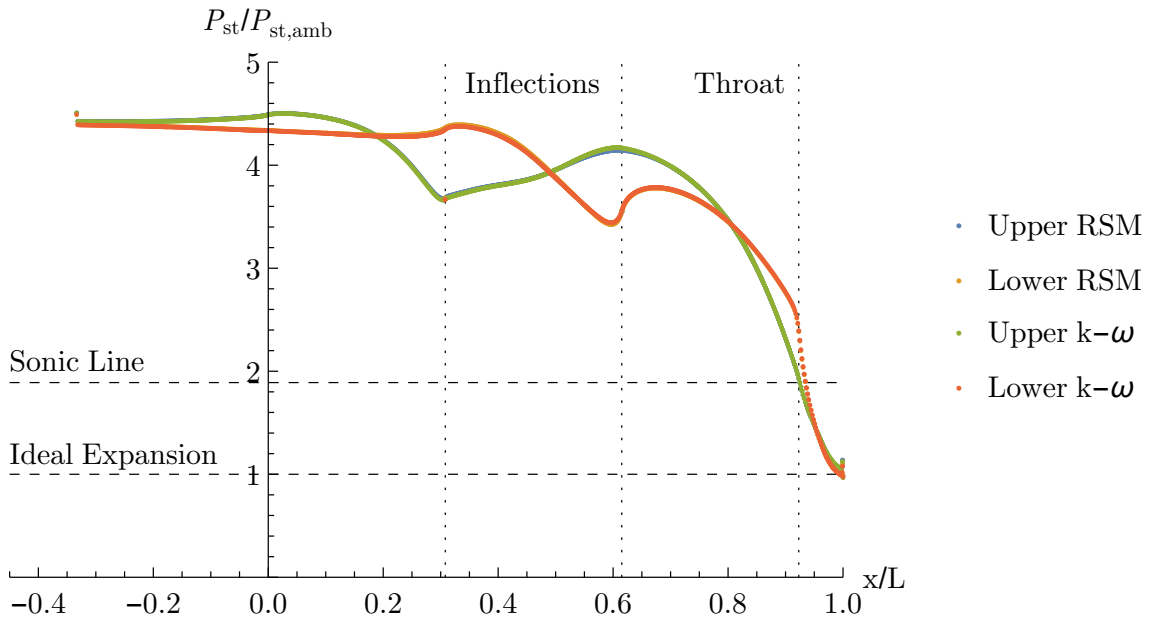
Figure 4.98: Centerline surface $P_{st}/P_{st,amb}$, LD3_AR10, K-ω SST vs. RSM.

All the same relative behavior of the streamwise vorticity and temperature distributions occur for the LD3_AR10 as with the LD3_AR4 nozzle—a general increase in the streamwise vorticity is observed, along with the corresponding increase in mixing of the two streams, especially at the central vortex pair. Comparisons with the K-ω SST solution are shown in Figures 4.102 and 4.103.
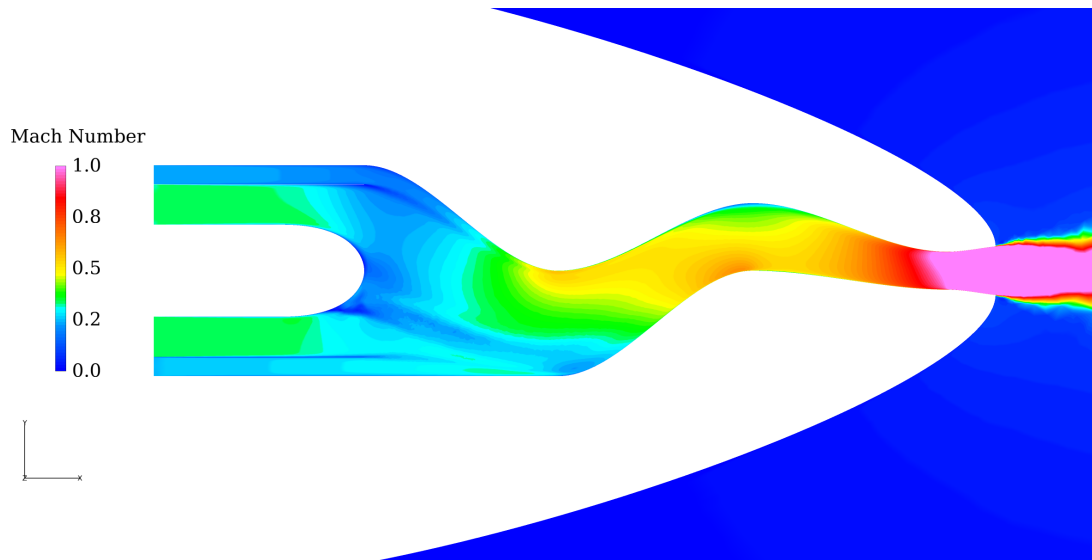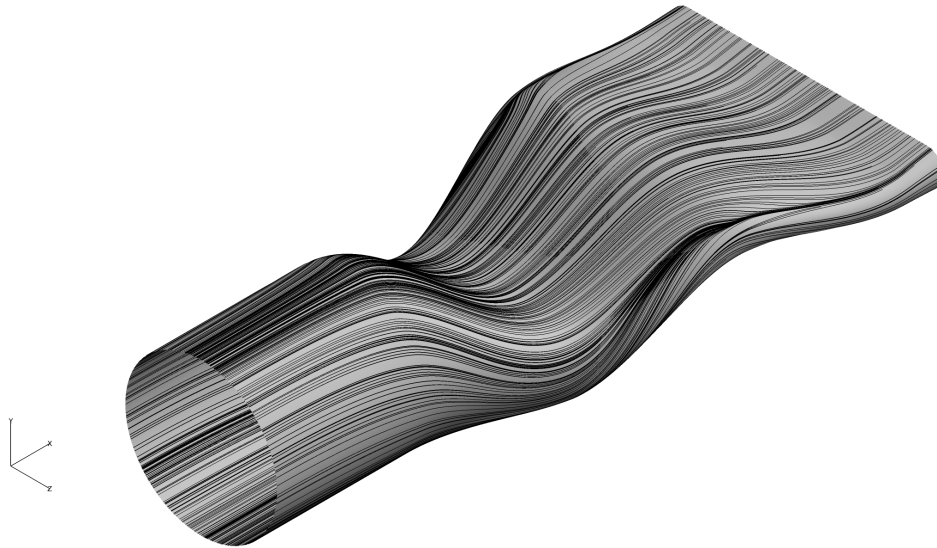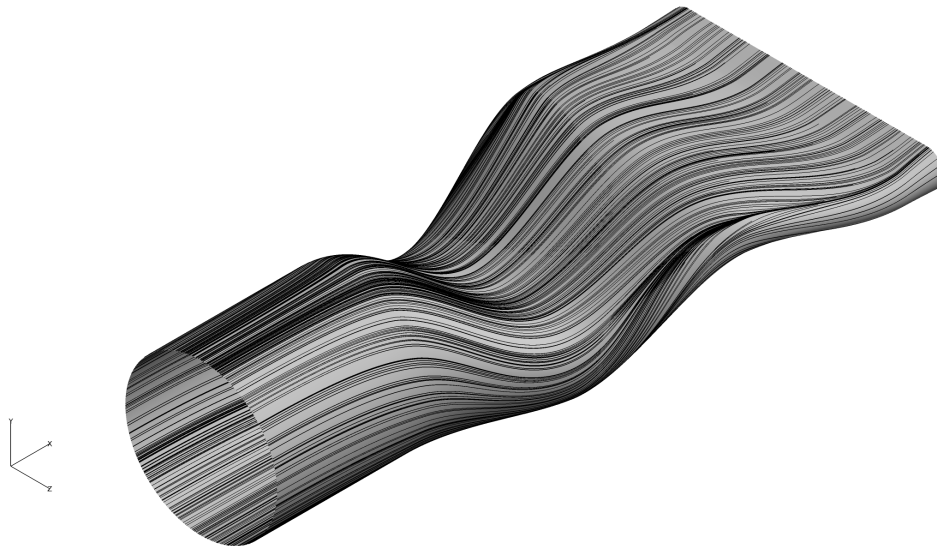
(a) K-ω SST.
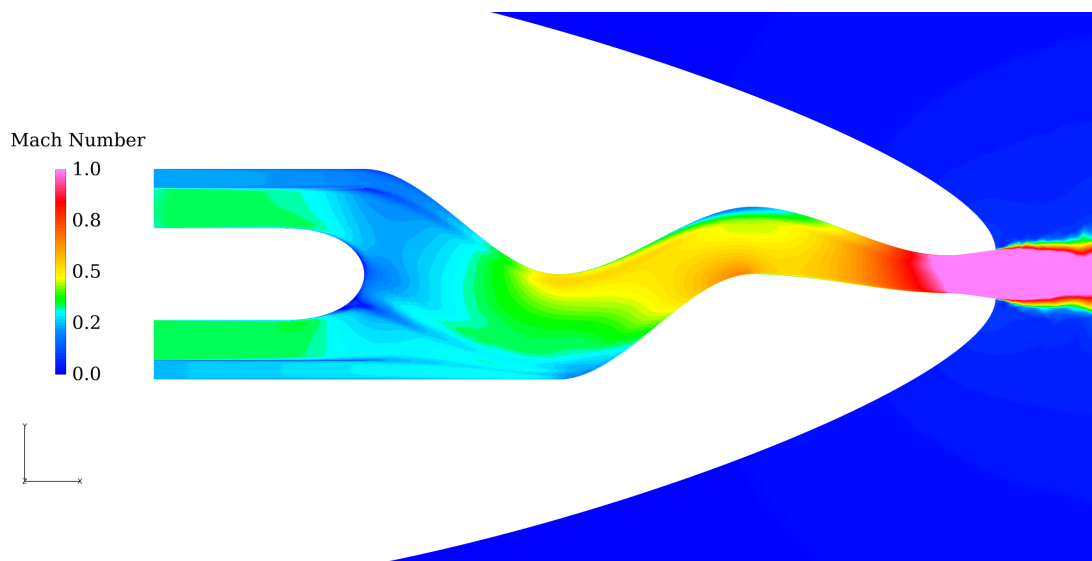
(b) RSM.

Figure 4.99: Centerline Mach number contours, LD3_AR10, K-ω SST vs. RSM.
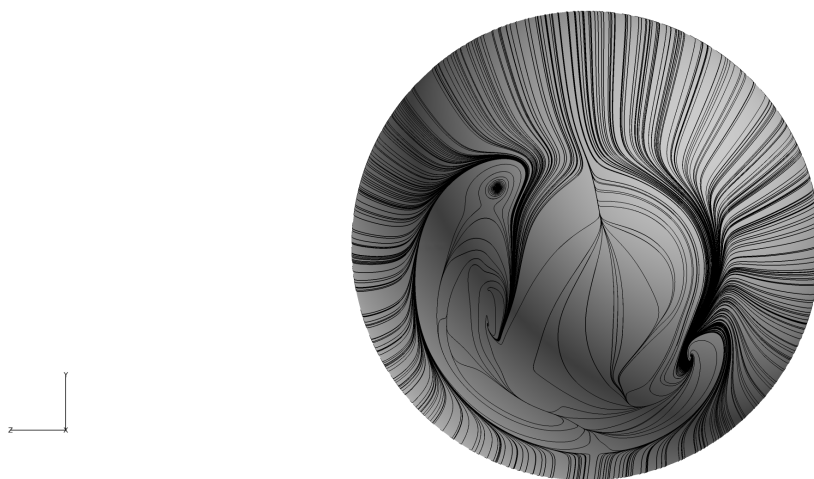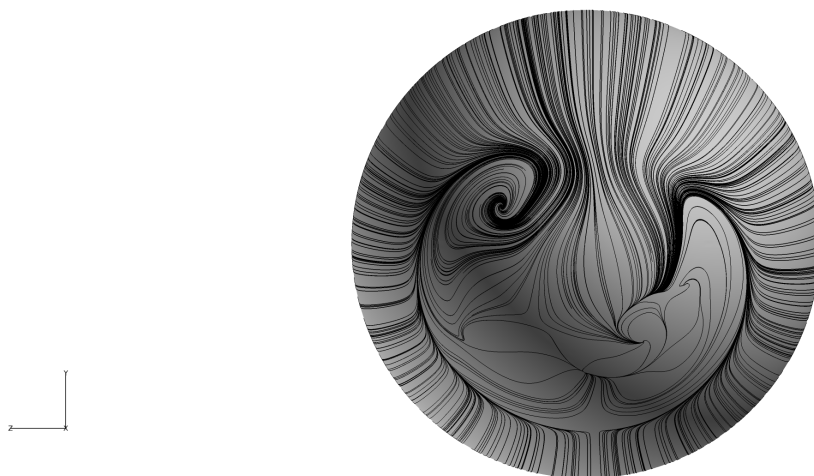
(a) K-ω SST.

(b) RSM.

Figure 4.100: Surface flow, LD3_AR10, K-ω SST vs. RSM.

202

(a) K-ω SST.

(b) RSM.

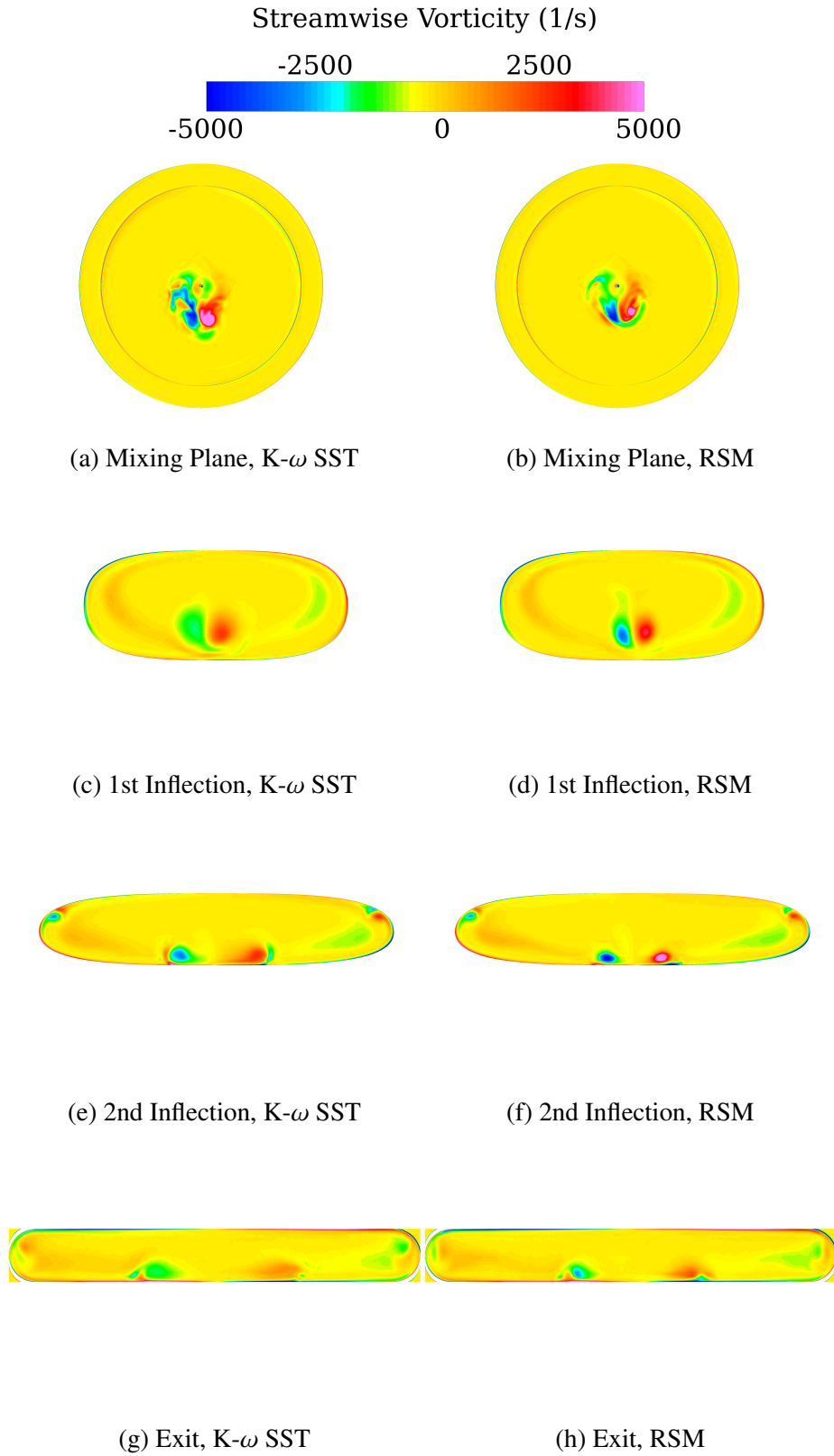Figure 4.101: Tailcone surface flow, LD3_AR10, K-ω SST vs. RSM.

(a) Mixing Plane, K-ω SST

(b) Mixing Plane, RSM

(c) 1st Inflection, K-ω SST

(d) 1st Inflection, RSM

(e) 2nd Inflection, K-ω SST

(f) 2nd Inflection, RSM

(g) Exit, K-ω SST

(h) Exit, RSM

Figure 4.102: Progression of vorticity distribution, LD3_AR10, K-ω SST vs. RSM.

Total Temperature (K)

(a) Mixing Plane, K-ω SST   (b) Mixing Plane, RSM

(c) 1st Inflection, K-ω SST   (d) 1st Inflection, RSM

(e) 2nd Inflection, K-ω SST   (f) 2nd Inflection, RSM

(g) Exit, K-ω SST   (h) Exit, RSM
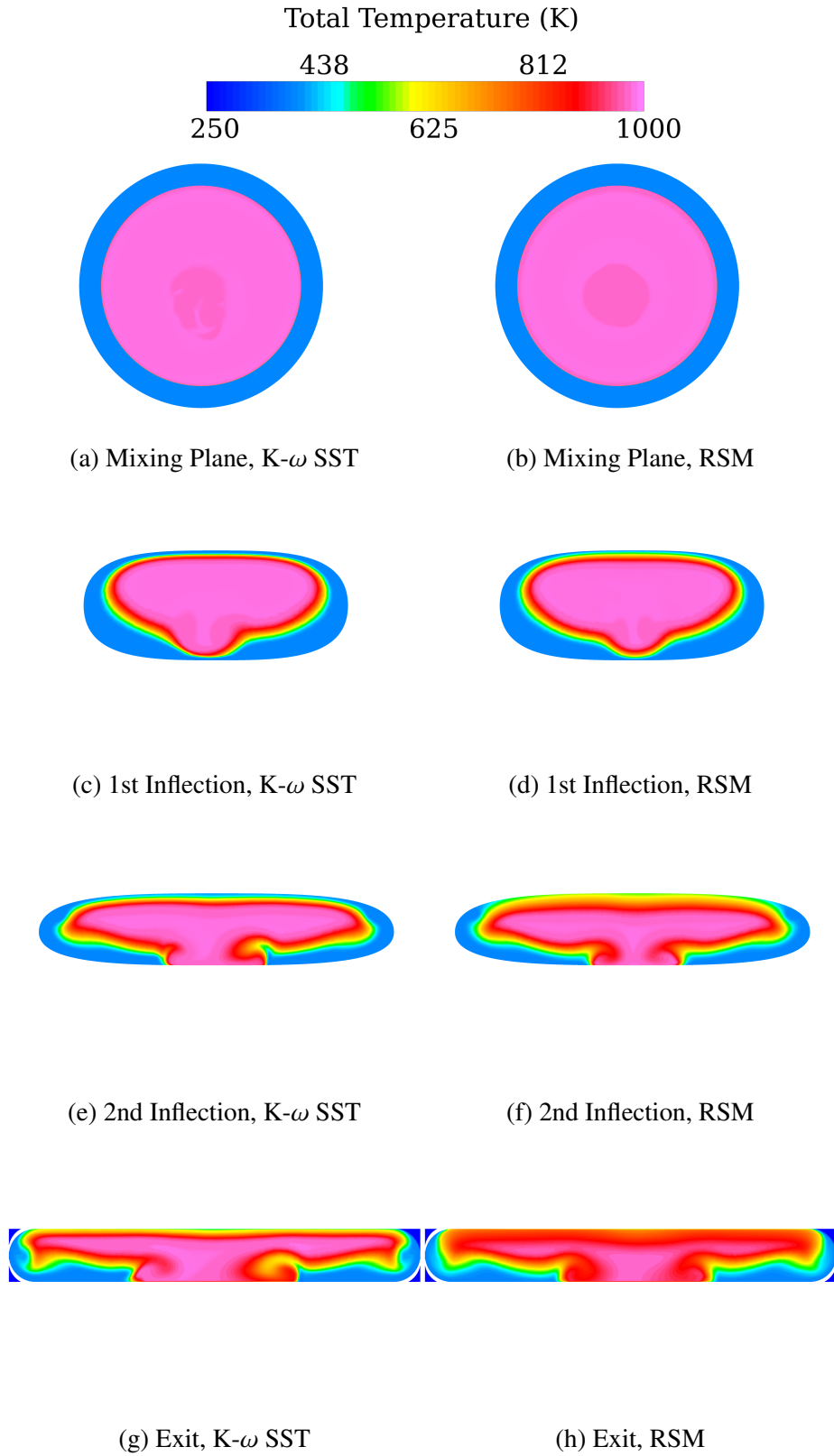
Figure 4.103: Progression of temperature distribution, LD3_AR10, K-ω vs. RSM.

4.5 Characterization Parameters

As discussed in Section 3.6, this research characterizes hot streak phenomena by examining the size, magnitude, and location of hot flow at the exit plane, temperature distortion at the exit plane, and nozzle performance for each geometry and swirl condition. The examination of these parameters reveals the effect of changing nozzle geometry on the temperature distribution at the nozzle exit. Certain characterization parameters are plotted against the modified Dean number discussed in Section 3.6.3. Table 4.4 lists the nozzles in ascending order of De_S. Important observations about Table 4.4 include the independence of the the order on any one parameter, viz., the nozzles are not grouped solely by L/D or AR. Also, the ascending order of De_S does not follow the ascending order of S, indicating the importance of including information about the flow dynamics in the calculation of De_S.

Table 4.4: Nozzles Listed in Ascending Order of Modified Dean Number

Nozzle	No-swirl $Re_{D_{h,8}}$	Swirl $Re_{D_{h,8}}$	S	No-swirl De_S	Swirl De_S
LD4_AR10	3.55×10^6	3.54×10^6	0.561	1.99×10^6	1.98×10^6
LD3_AR10	3.57×10^6	3.56×10^6	0.761	2.72×10^6	2.71×10^6
LD4_AR4	5.13×10^6	5.12×10^6	0.703	3.61×10^6	3.60×10^6
LD2_AR10	3.59×10^6	3.58×10^6	1.185	4.25×10^6	4.23×10^6
LD3_AR4	5.21×10^6	5.21×10^6	0.971	5.06×10^6	5.06×10^6
LD2_AR4	5.20×10^6	5.18×10^6	1.632	8.49×10^6	8.45×10^6

4.5.1 Size, Magnitude, Location.

Hot flow size is plotted against De_S for the no-swirl and swirl cases in Figure 4.104. As stated in Chapter 3, the utility of De_S is the ability to quantify the speed and turning of nozzle flow in one parameter. Low De_S can indicate a lower velocity flow (lower Reynolds

number) which is turned less (lower serpentinity) and therefore contains a lower level of streamwise vorticity and mixing, as observed in previous sections. Conversely, high De_S can indicate a faster flow (higher Reynolds number) which is turned more (higher serpentinity), potentially causing flow separation and/or choked flow, as in the LD2_AR4 nozzle. Also, a slower but higher-turning flow can be equated to a faster, lower-turning flow. Figure 4.104 displays several interesting features. First, swirl increases hot flow size by an average of 3%. Since size is an indicator for the amount of mixing between the two streams, larger size equates to less mixing. The added coherence due to swirl seems to reduce mixing, especially at the center of the nozzle where one vortex is present instead of two. The reduction in mixing is also due to the swirl effectively reducing fluid migration and vorticity generation on the starboard side. However, using GCI=4.45% for hot flow size as a measure of the uncertainty in the computations (see Section 4.2), the increase due to swirl is not statistically significant. The general trend seems to be non-linear, with maximum size occurring in the mid-Dean number range. For the sake of identifying some general trends, the data below has been fitted to quadratic trend lines in order to facilitate a discussion of the results. The curves fit through both sets of points result in low values for the goodness-of-fit test, with R^2 values of 0.3 for the no-swirl case and 0.6 for the swirl case. A goodness-of-fit value of 0.8 or above is considered a good curve fit for engineering purposes, meaning the size data does not trend quadratically. The LD4_AR4 nozzle causes the low R^2 values because a single outlier has a large affect on a small amount of data points. All values are within 11% of each other for the no-swirl cases and 8% for the swirl cases.

Hot flow magnitude is plotted against De_S for the no-swirl and swirl cases in Figure 4.105 and displays a different trend than hot flow size. Here, a general upward trend with De_S is apparent. In both data sets, the lowest De_S nozzle corresponds to the lowest magnitude and vice versa. Similar to size, swirl increases magnitude by an average of 4%.
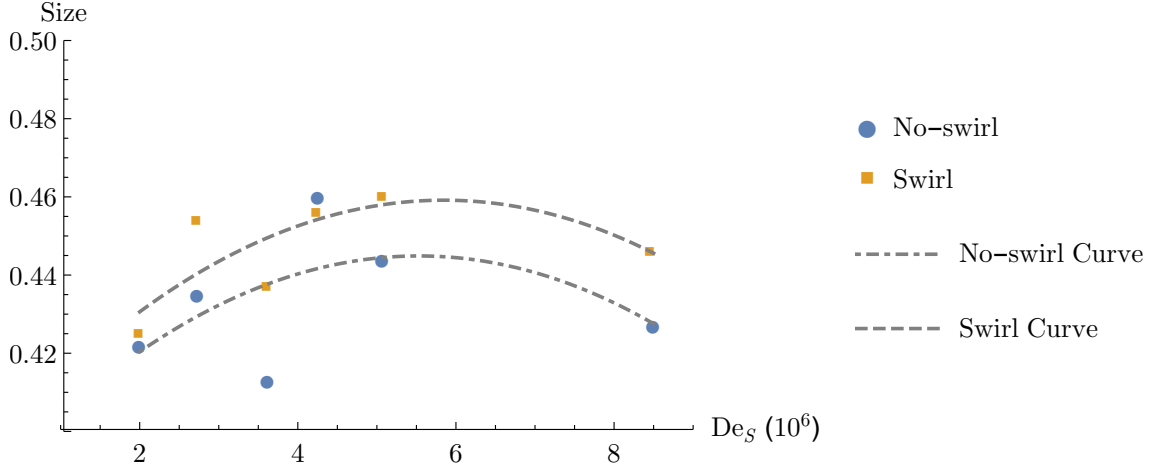
Figure 4.104: Hot Flow Size Versus Modified Dean Number.

Using GCI=1.60% for $TAVHOT$ as a measure of the uncertainty for hot flow magnitude (see Section 4.2), the increase due to swirl is statistically significant. Magnitude is also an indication of mixing, with higher magnitude corresponding to decrease mixing. The hot flow in lower De_S flow has a lower magnitude because the slower, gentler curving flow allows for more convection of the cooler flow into the core, effectively reducing the area of hot flow. The tight vortical structures in high De_S nozzles, which effectively reduce the hot flow size, actually increase the hot flow magnitude. The strong vortices contribute to localized entrainment of the bypass flow, as seen in previous sections, but the central core remains essentially isolated from the bypass flow, thus the increased magnitude. A quadratic curve fit through both data sets result in much higher R^2 values for magnitude; both are 0.89, indicating a strong nonlinear relationship between De_S and hot flow magnitude. All values are within 19% of each other for the no-swirl case and 14% for the swirl cases.

Hot flow centroid location is shown in Figure 4.106 for the no-swirl and swirl cases. Several groupings emerge from this plot based on nozzle geometry and not necessarily De_S. First for the no-swirl cases, the lateral component of the centroid remains fairly centrally
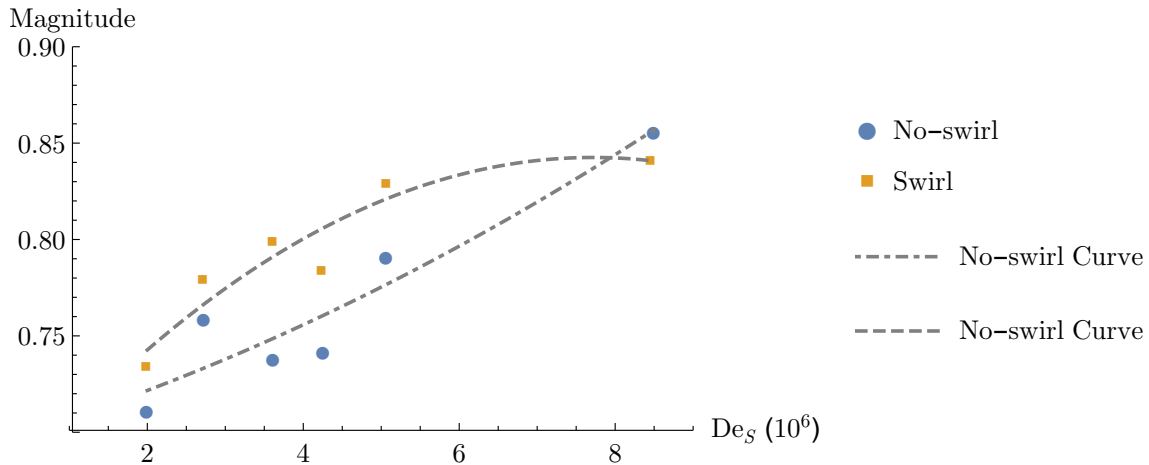
Figure 4.105: Hot Flow Magnitude Versus Modified Dean Number.

location (within 5% of the centerline), with higher serpentinity nozzles closer to the lateral centerline. Departure from the lateral centerline is an indication of asymmetry, as seen in previous sections. The low serpentinity seems to allow the sources of lateral asymmetry, namely the flow separation off the tailcone, to be exacerbated at the nozzle exit. The lower degree of turning reduces the centrifugal forces acting on the central vortices and allows the initial trajectory to persists to the exit. The source of asymmetry is seen in the lower portions of the "whale tail" in Figures 4.35, 4.47, and 4.85. Surprisingly, while the higher serpentinity nozzles appear very asymmetric in Figures 4.23, 4.60, and 4.73, the lateral centroid is actually near the centerline due to a canceling effect of hot regions of flow on either side of the centerline. The no-swirl vertical component of the centroid decreases with nozzle length. As the nozzle is shortened, the higher degree of vertical displacement of the flow within the nozzle causes the hot flow region to be lifted to the upper portion of the nozzle exit, whereas the longer nozzles allow the hot flow to remain more toward the center.

The swirl cases present two distinct groupings of three nozzles—ones that have a positive lateral centroid and ones that have a negative lateral centroid. The groupings are

209

dependent on De_S. The three lowest De_S nozzle have positive lateral components. The lower De_S nozzles all display a similar exit pattern in Figures 4.79, 4.91, and 4.53, where the strong central vortex causes the core flow to shift toward the direction of the swirl and thus toward starboard (positive lateral component). There is also more mixing with the bypass flow in the lower port side, where migration of the core flow outward is reduced as it competes with the swirl direction. As seen in Figures 4.67, 4.29, and 4.41, the higher De_S nozzles have a very different pattern. In these cases, the large disparity between the sidewall behavior, as well as the larger influence of the upper starboard side vortex contributes to a negative lateral component of the centroid. Conversely, the vertical component of the centroid trends positively with De_S. This points to the seemingly stark split between the two groups in terms of exit temperature pattern, whereas the no-swirl cases all feature the same basic "whale-tail" pattern and points to the utility of De_S for investigating complex flows.
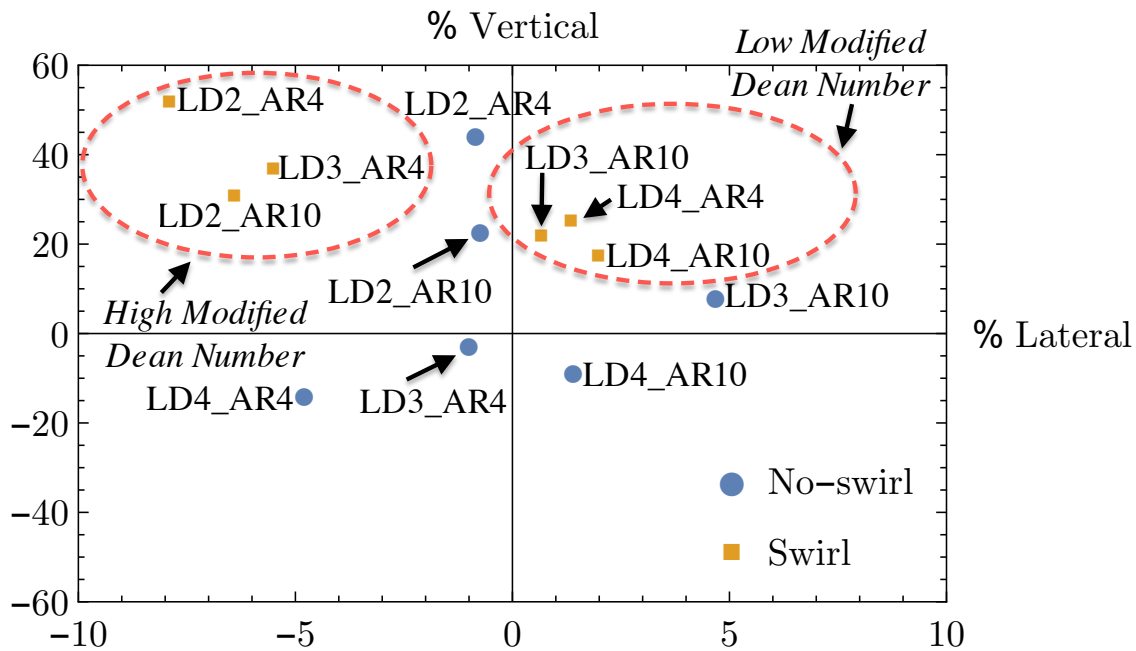
Figure 4.106: Hot Flow Temperature-weighted Centroid Locations.

4.5.2 Temperature Distortion.

Circumferential distortion intensity per ring for each no-swirl case is shown in Figure 4.107. Every nozzle exhibits the same trend of increasing CDI with increasing ring location. This pattern shows that near the centerline the temperature is more circumferentially uniform and decreases in uniformity (increasing distortion) toward the outer edge. There is little connection with $De_\mathcal{S}$ or $\mathcal{S}$, with mid-Dean number and serpentinity nozzles LD2_AR10 and LD3_AR4 bounding the data at Ring 1 and 5. Interestingly, all nozzles flip order from Ring 1 to 5, with the nozzles having the lowest CDI at their cores have the highest CDI at their edges.

Circumferential Distortion
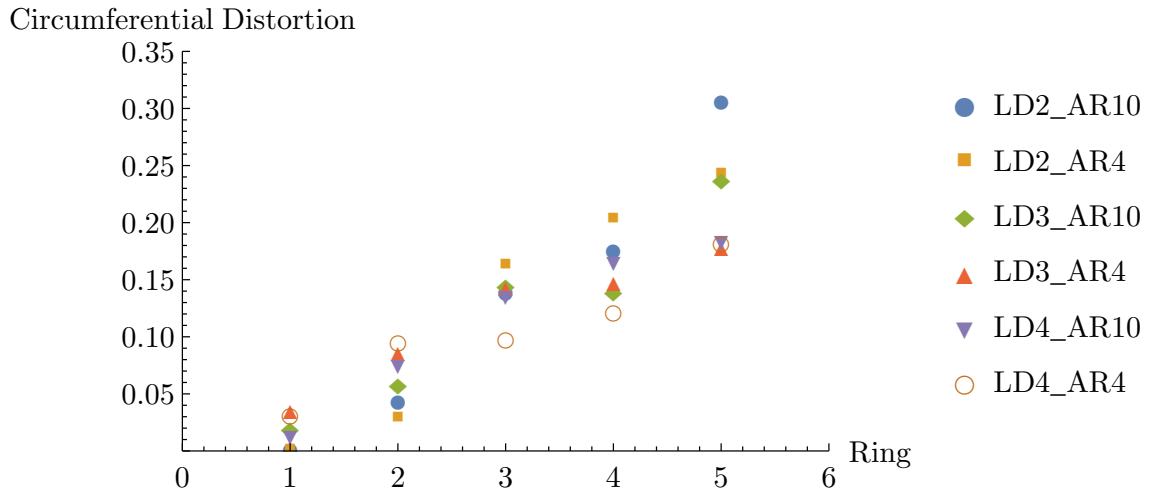
Figure 4.107: Circumferential Distortion Intensity, No-swirl Cases.

Circumferential distortion intensity per ring for each swirl case is shown in Figure 4.108. A different trend emerges at the outer rings. Distortion increases like the no-swirl cases until the outermost ring is reached, where the distortion at Ring 5 is lower than Ring 4. Again, no distinct relationship to $De_\mathcal{S}$ or $\mathcal{S}$ is observed nor is the switching trend seen as in the no-swirl cases. The effect of swirl on CDI for each nozzle is shown in Figures 4.109 and 4.110. In most cases, swirl tends to reduce CDI near the center, where the single strong vortex allows for a more uniform temperature distribution than the counter-rotating

pair. The average CDI per ring, the maximum difference between any two nozzles per ring, and the change due to swirl per ring are given in Table 4.5. Using GCI=2.55% for $TFAV$ as a measure of the uncertainty for CDI (see Section 4.2), changing nozzle geometry has a statistically significant effect on CDI for each ring. The change in CDI due to swirl is also statistically significant except for Ring 3.
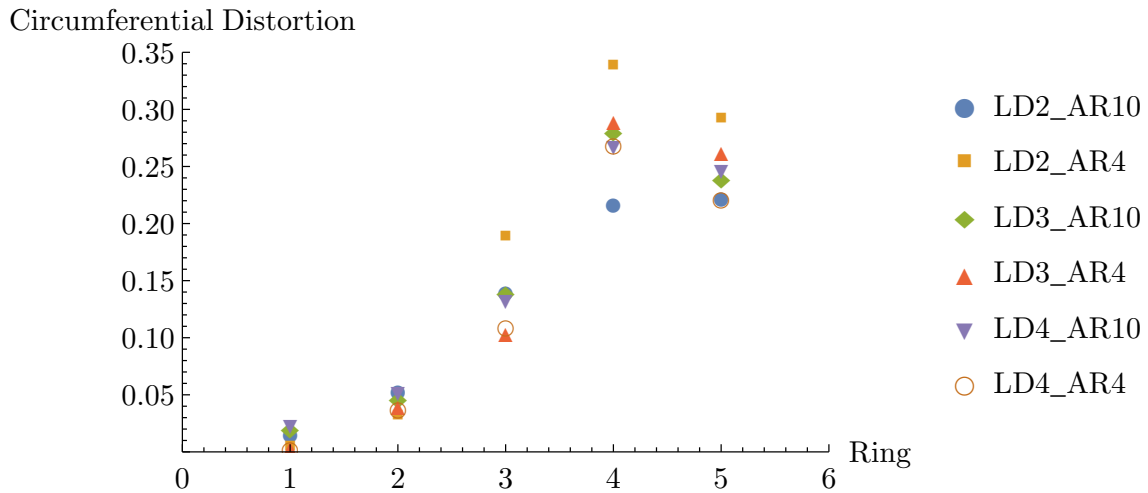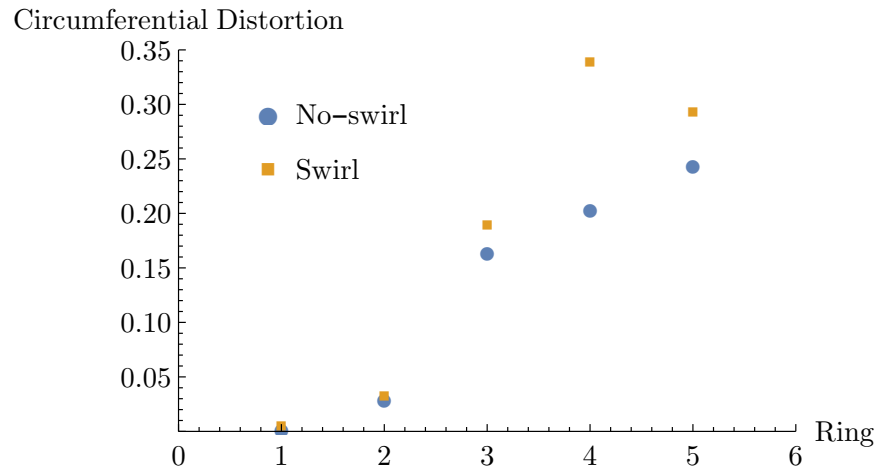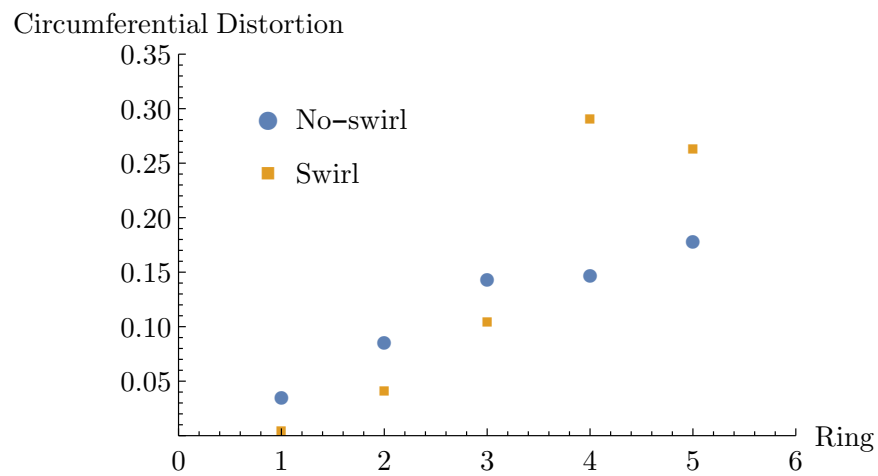

Figure 4.108: Circumferential Distortion Intensity, Swirl Cases.

Table 4.5: CDI Results Per Ring

Ring	No-Swirl Average	No-Swirl Max Difference	Swirl Average	Swirl Max Difference	Change Due to Swirl
1	0.017	92.1%	0.012	84.0%	-30.4%
2	0.065	59.7%	0.044	29.5%	-32.4%
3	0.138	30.6%	0.136	35.2%	-1.4%
4	0.159	31.0%	0.277	27.0%	+74.1%
5	0.222	32.2%	0.248	17.7%	+11.5%

Circumferential Distortion

(a) *L/D* = 2

Circumferential Distortion

(b) *L/D* = 3

Circumferential Distortion
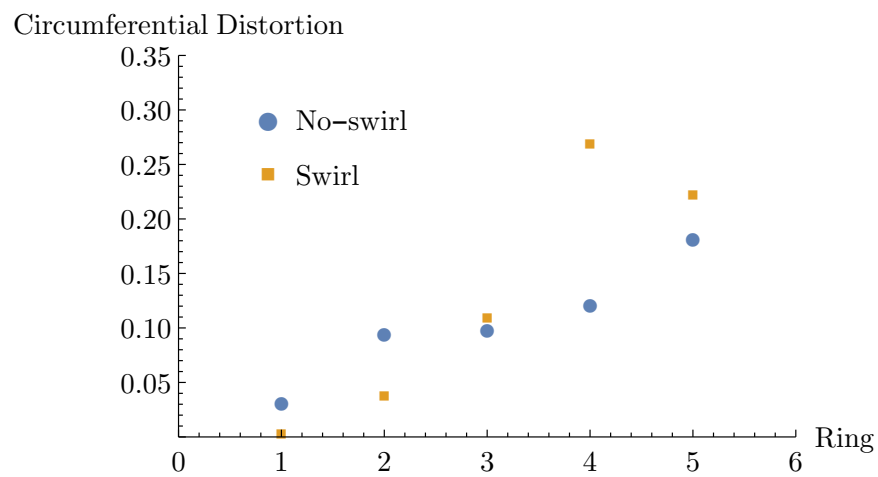
(c) *L/D* = 4

Figure 4.109: No-swirl/Swirl CDI Comparisons, *AR* = 4.

213

Circumferential Distortion

(a) *L/D = 2*

Circumferential Distortion

(b) *L/D = 3*

Circumferential Distortion
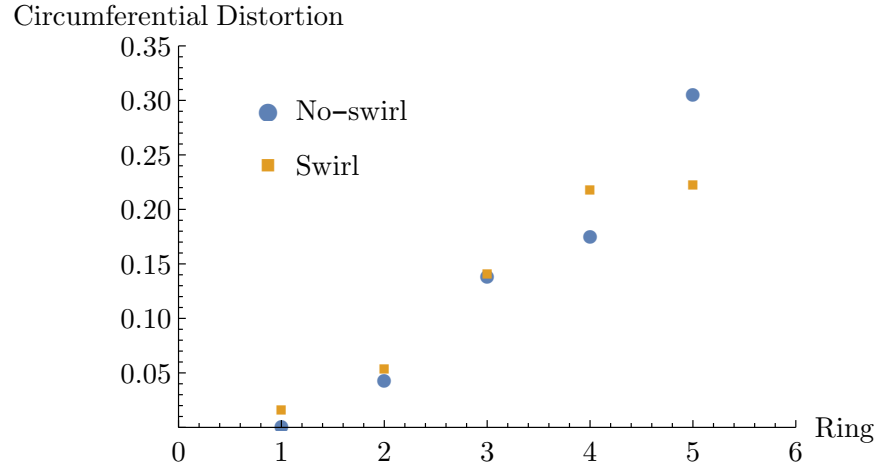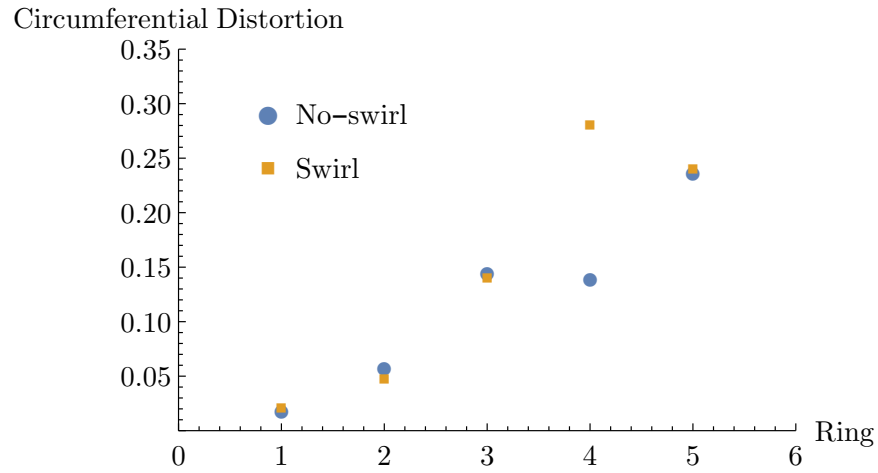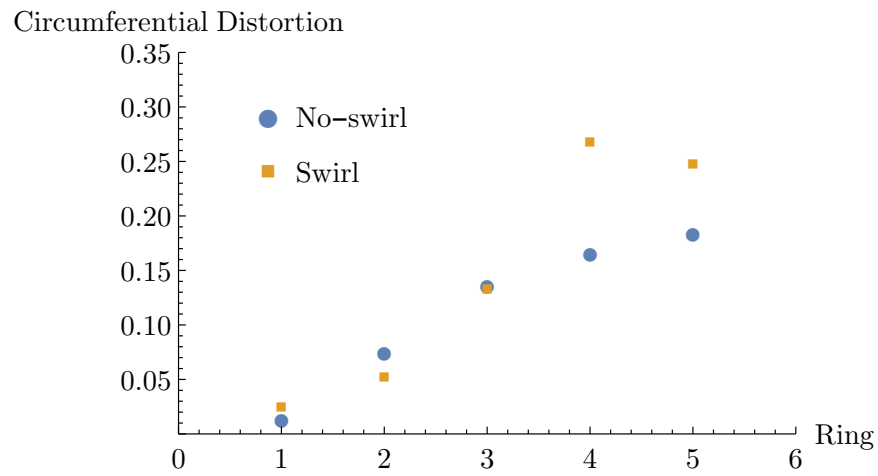
(c) *L/D = 10*

Figure 4.110: No-swirl/Swirl CDI Comparisons, *AR = 10.*

Circumferential distortion coefficient for the no-swirl and swirl cases versus De_S is shown in Figure 4.111. The general trend of swirl increasing circumferential distortion is evident as in the plots of per-ring CDI. The exception is the LD2_AR10 nozzle. The largest increase in CDC (29%) due to swirl occurs for the nozzle with the largest De_S (LD2_AR4). Swirl increases CDC by an average of 19%, which is statistically significant using the same value of uncertainty as with CDI. All values are within 15% of each other for the no-swirl case and 19% for the swirl cases. The quadratic curve fit for each data set is very different, with the no-swirl case containing several jumps in the data, resulting in $R^2 = 0.25$. The swirl data is much more quadratic, with $R^2 = 0.90$. The CDC for the no-swirl cases seem to correlate with L for each AR. Figure 4.112 shows this behavior, in which the $AR = 10$ nozzles have a higher CDC than the $AR = 4$ nozzles. This relationship is due to the higher lateral stretching of the flow for the higher AR nozzles causing a larger disparity in the temperature distribution for a given ring. An increase in CDC as the nozzles get shorter is due to the lateral divergence occurring in a short length, causing more disparity in temperature per ring due to a decrease in mixing. The relationship between CDC and AR for the swirl cases is inclusive, with the nonlinear behavior better described in terms of De_S, as shown by the high R^2 value of the quadratic curve fit.

Radial distortion intensity per ring for each no-swirl case in shown in Figure 4.113. Every nozzle exhibits the same trend—the ring average temperature is above the rake average temperature nearer the center, reaching the average between Rings 3 and 4, and decreases below the average rake temperature nearer the outer edge. This is indicative of the similarity in the basic temperature distribution pattern (the "whale-tail"). Like CDI, no connection with De_S or S is evident.

Radial distortion intensity per ring for each swirl case in shown in Figure 4.114. The same trend occurs as for the no-swirl cases, with again one nozzle displaying slightly higher levels of distortion than the rest, although for these cases the largest De_S nozzle is the
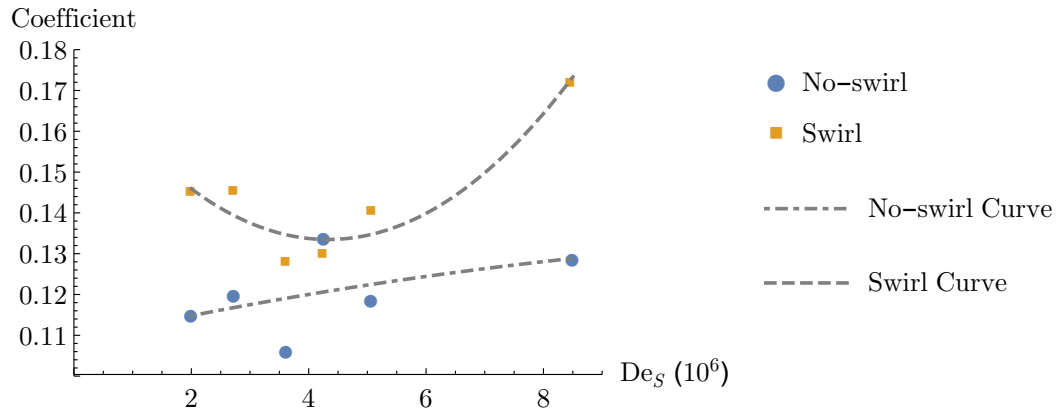
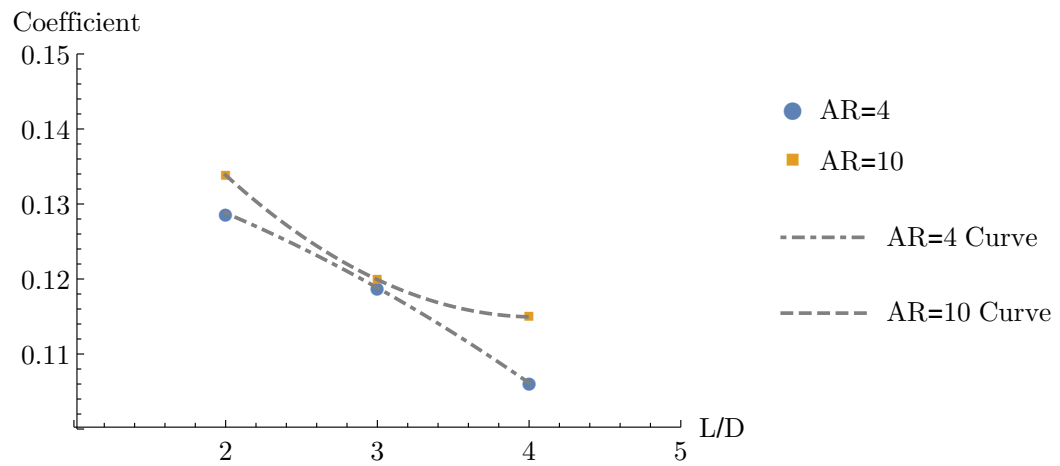Figure 4.111: Circumferential Distortion Coefficient.

Figure 4.112: Circumferential Distortion Coefficient, No-Swirl Cases Versus Length.
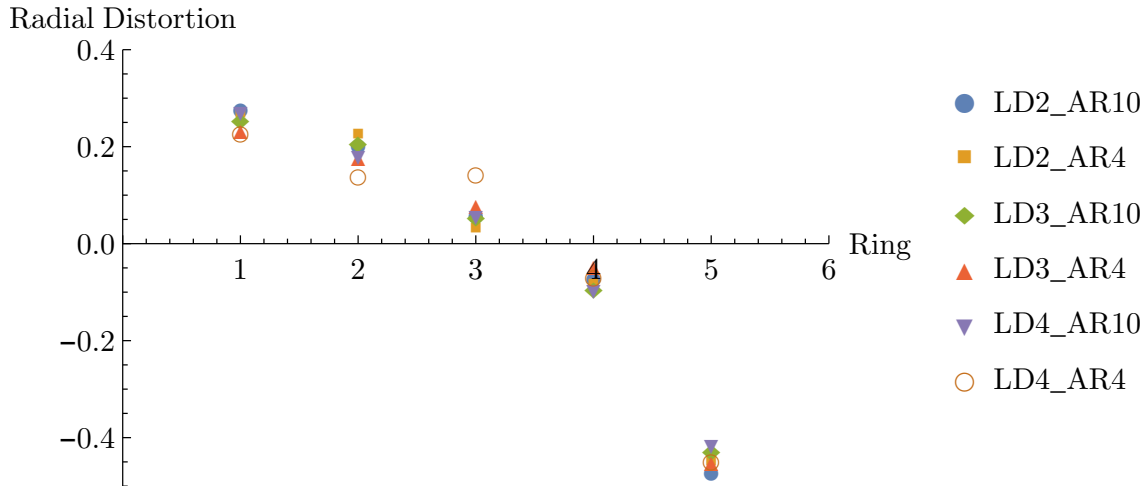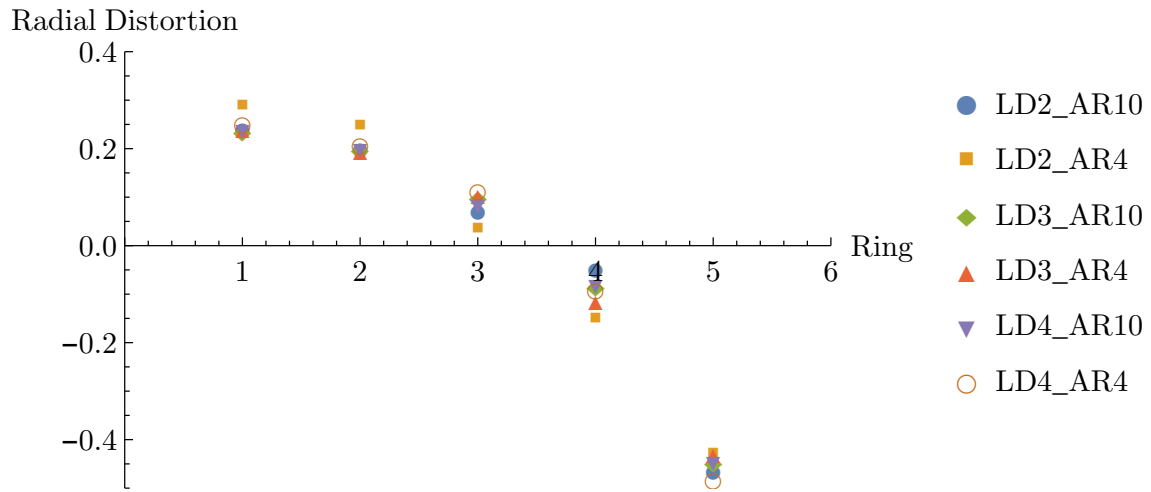
Figure 4.113: Radial Distortion Intensity, No-Swirl Cases.

outlier. The effect of swirl on each nozzle is shown in Figures 4.115 and 4.116. Swirl increases distortion expect for Ring 1, where the strong central vortex promotes a more uniform circumferential temperature distribution. The average RDI per ring, the maximum difference between any two nozzles per ring, and the change due to swirl per ring are given in Table 4.6. Using GCI=2.55% for $TFAV$ as a measure of the uncertainty for RDI (see Section 4.2), changing nozzle geometry has a statistically significant effect on RDI for each ring. The change in RDI due to swirl is also statistically significant except for Ring 5.

Table 4.6: RDI Results Per Ring

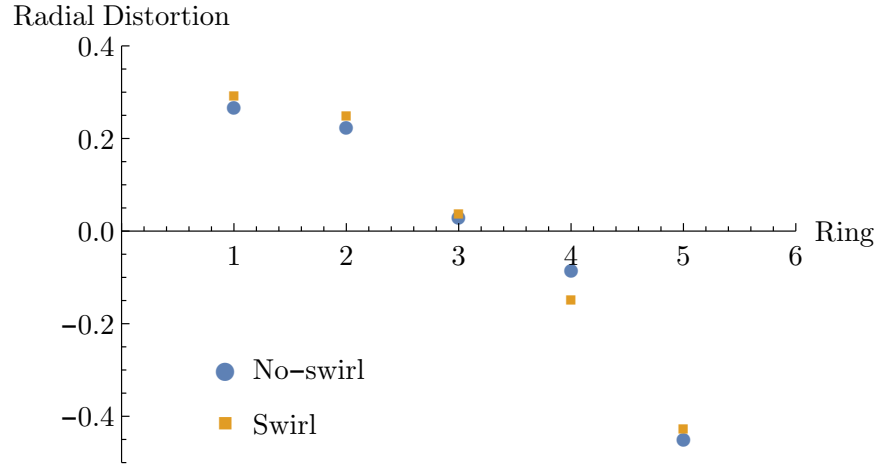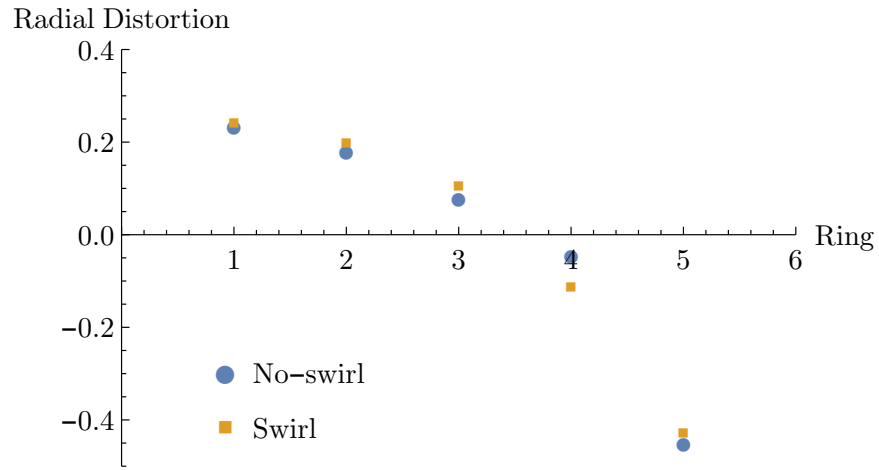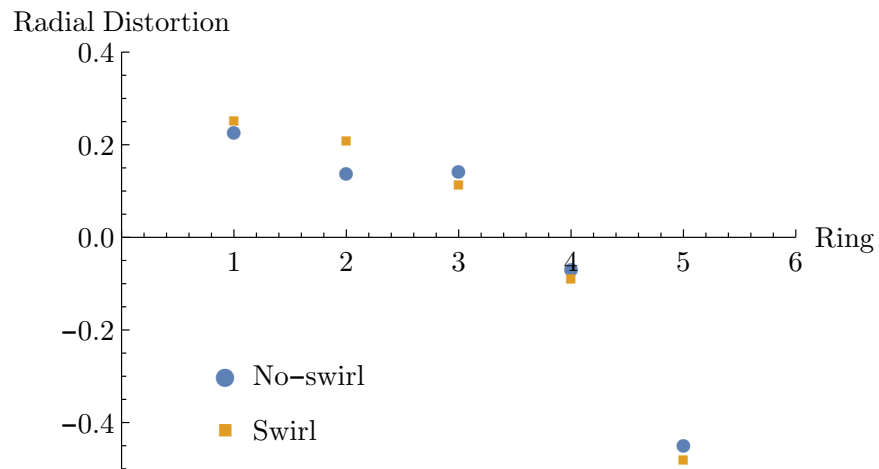| Ring	No-Swirl Average	No-Swirl Max Difference	Swirl Average	Swirl Max Difference	Change Due to Swirl
1	0.257	12.3%	0.250	13.7%	-2.78%
2	0.190	29.2%	0.209	14.9%	+9.86%
3	0.071	69.0%	0.085	57.2%	+19.1%
4	-0.076	54.6%	-0.094	83.5%	+24.8%
5	-0.443	8.66%	-0.449	8.1%	+1.47%

Figure 4.114: Radial Distortion Intensity, Swirl Cases.
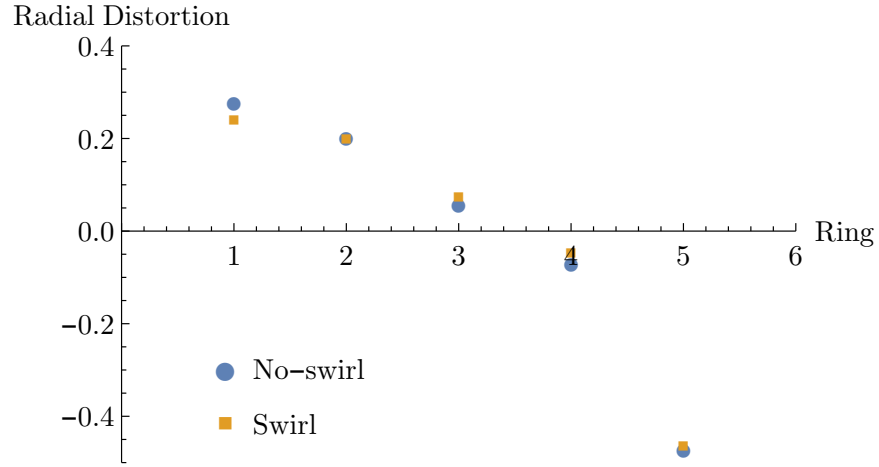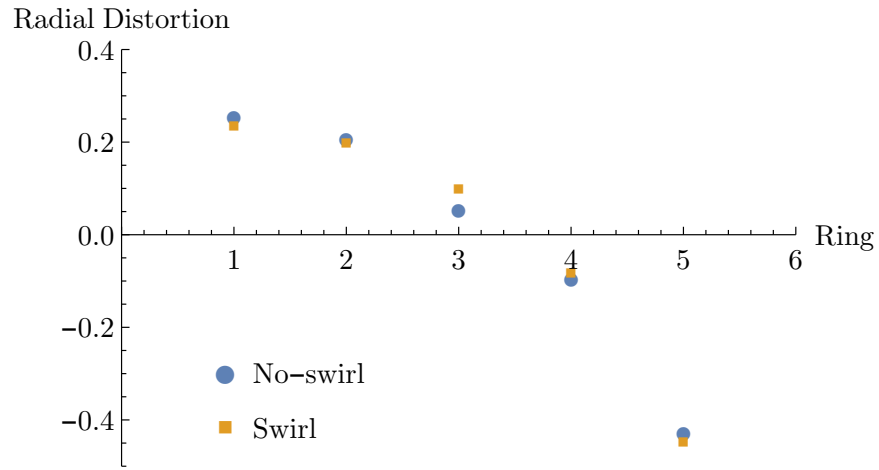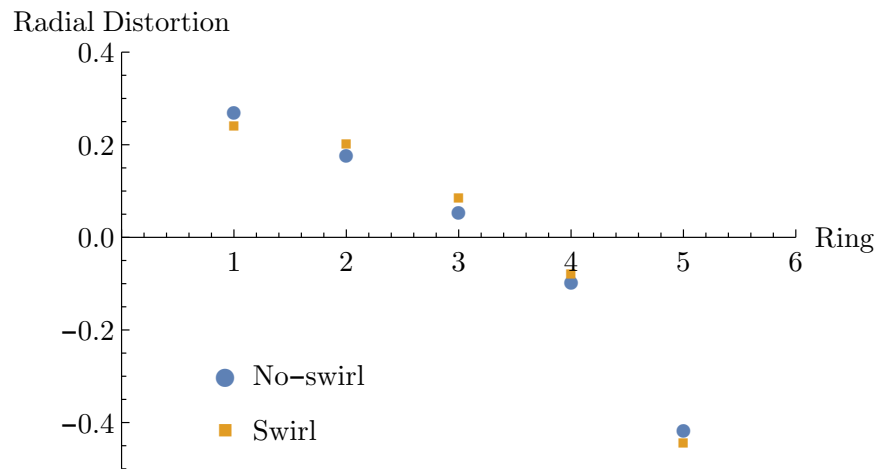
(a) $L/D = 2$

(b) $L/D = 3$

(c) $L/D = 4$

Figure 4.115: No-swirl/Swirl RDI Comparisons, $AR = 4$.

(a) *L/D = 2*

(b) *L/D = 3*

(c) *L/D = 10*

Figure 4.116: No-swirl/Swirl RDI Comparisons, *AR = 10*.

4.5.3 Performance.

Discharge coefficient versus De_S for the no-swirl and swirl cases is shown in Figure 4.117. Swirl has virtually no effect on C_d, with the largest difference for any case being 0.2%. The data exhibits a strong relationship to the quadratic curve fit, with R^2 values of 0.995 for each data set. The difference between the first five nozzles is less than 3%, with an average difference of only 0.05%, which suggests changes in nozzle geometry has minimal effect on C_d. The lowest C_d is the nozzle with the highest De_S, the LD2_AR4 case. This nozzle is choked upstream of the design throat and therefore has a lower mass flow than the other nozzles, which is reflected in the low discharge coefficient since the computed mass flow is much lower than the ideal designed mass flow. A direct relationship between C_d and L/D and AR is seen in Figure 4.118. Surprisingly, an increase in AR slightly increases C_d. As seen in the plots of Mach contours and $P_{st}/P_{st,amb}$, the $AR = 4$ nozzles reached sonic conditions slightly upstream compared to the $AR = 10$. The upstream location of the throat sets the area through which flow can pass, effectively choking the $AR = 4$ nozzle more so than the $AR = 10$ nozzles and reducing the ratio of actual-to-ideal mass flow. Also, C_d increases with L/D due to an increase in losses in the shorter nozzles as the stronger vortical structures and flow separation reduce the amount of axial flow. Swirl slightly reduces flow performance due to an increase in angularity losses.

Thrust coefficient versus De_S for the no-swirl and swirl cases are shown in Figure 4.119. Like C_d, a downward trend is displayed, with a strong relationship to the quadratic curve fit where $R^2 = 0.96$ for each case. Also like C_d, when the data is plotted against L/D in Figures 4.120, the effect of nozzle geometry becomes clearer—an increase in nozzle length tends to increase the thrust performance as losses due to curvature are reduced. Also, the $AR = 10$ nozzles tend to have higher thrust performance than the $AR = 4$ nozzles, and swirl slightly reduces thrust performance for all the same reasons as for C_d. However, the largest difference due to swirl for any nozzle is again only 0.2%, and the largest difference
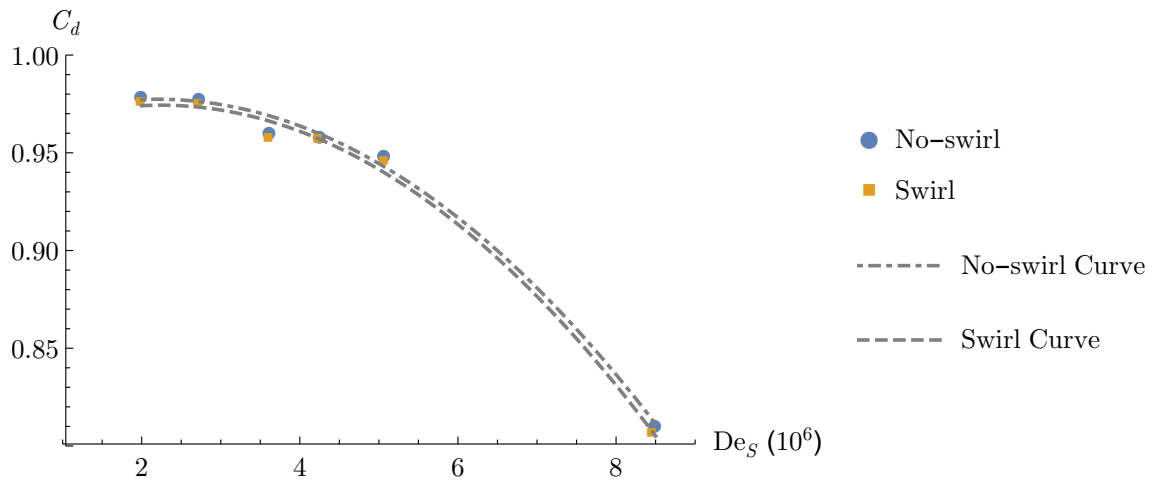
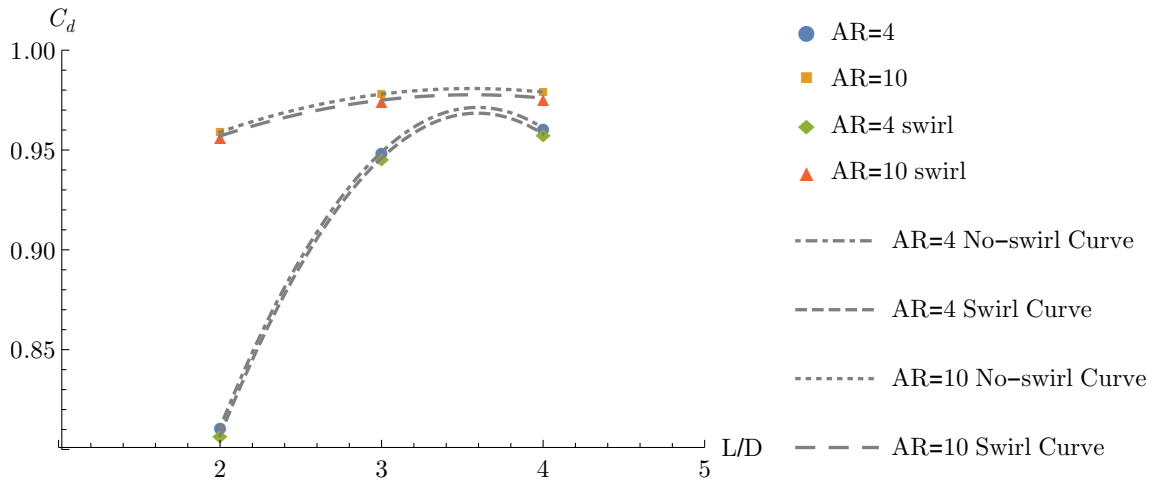Figure 4.117: Discharge Coefficient vs. Modified Dean Number

Figure 4.118: Discharge Coefficient vs. L/D.

between any of the first five nozzles is only 0.5%. Therefore, excluding the LD2_AR4 nozzle, changes in nozzle geometry and swirl have virtually no effect on C_{F_g}. Dimensional gross thrust is plotted in Figures 4.121 and 4.122, with the same trends reproduced since all nozzles are dimensionalized by the same ideal values.
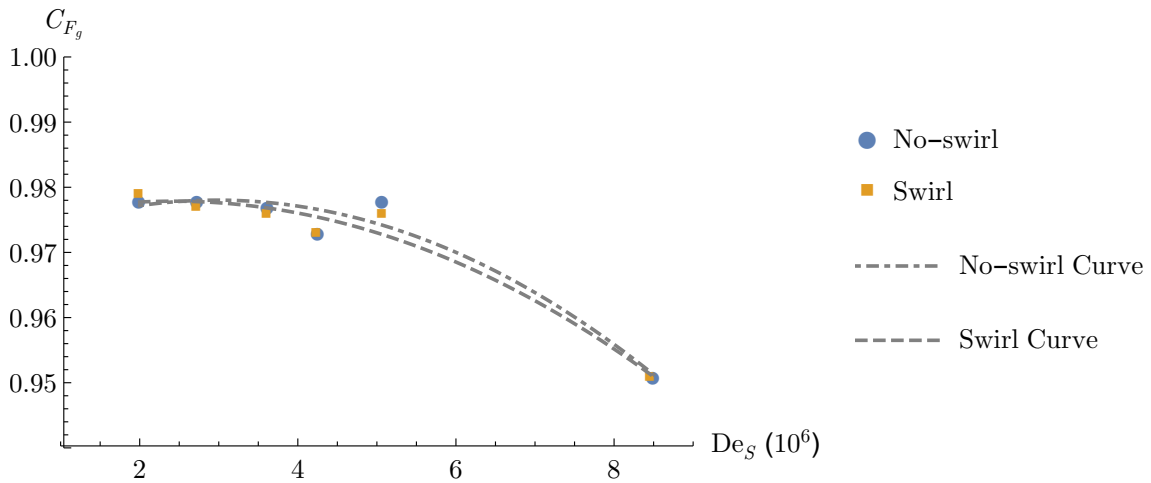

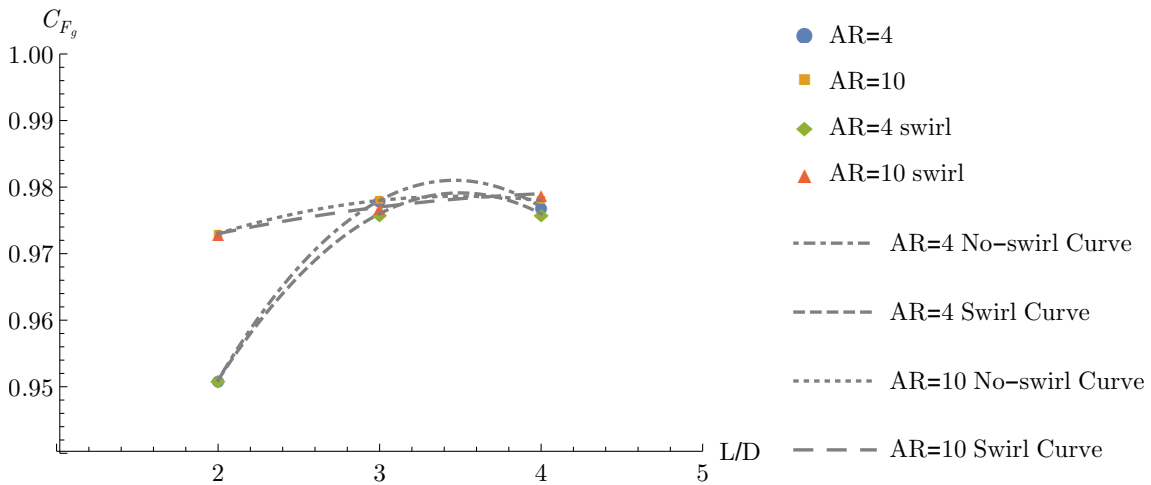Figure 4.119: Thrust Coefficient vs. Modified Dean Number.
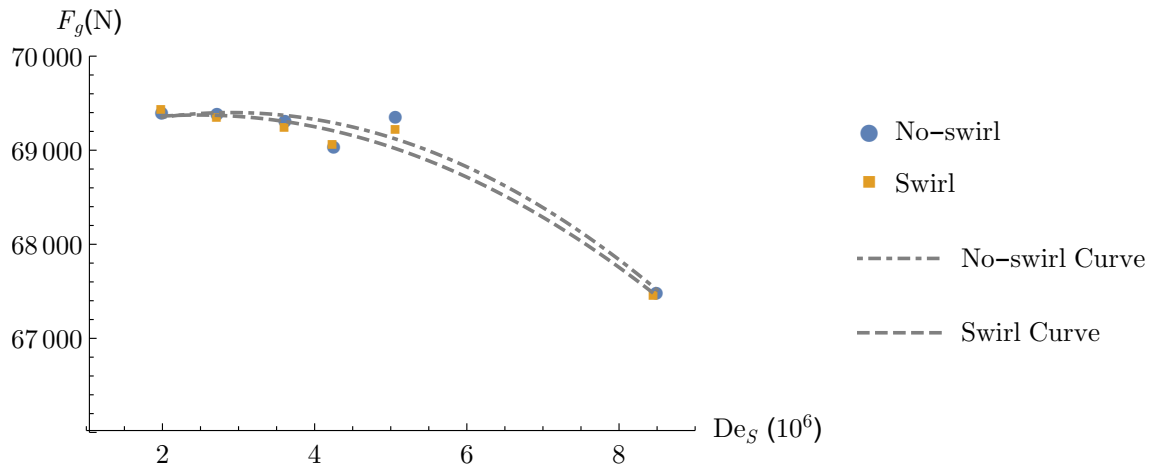

Figure 4.120: Thrust Coefficient vs. L/D.
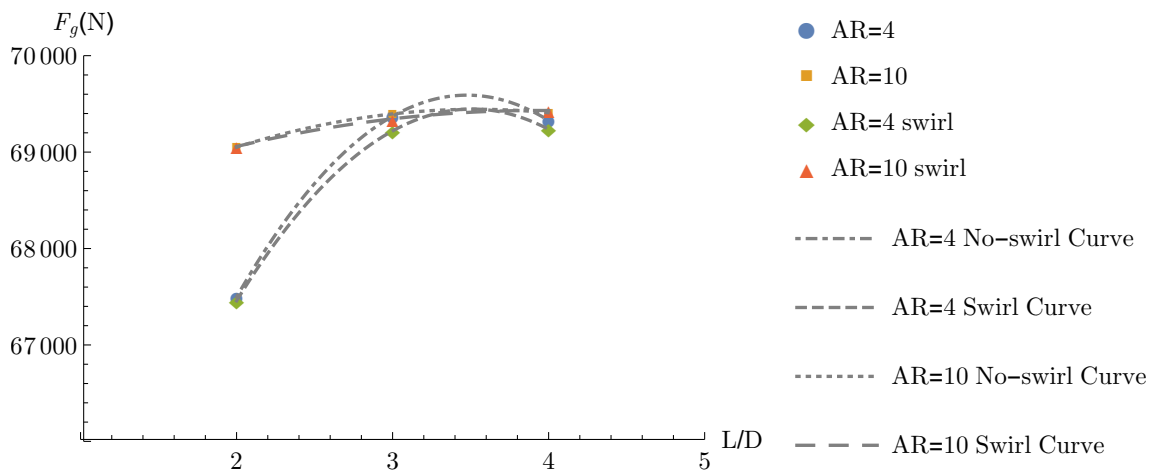
Figure 4.121: Gross Thrust vs. Modified Dean Number.

Figure 4.122: Gross Thrust vs. L/D.

4.6 Comparison to Straight Nozzle Solutions

One aspect of nozzle flow that needs consideration is dwell time, which increases with nozzle length and therefore represents an increased opportunity for mixing. In steady state computations such as those in this research, dwell time can be thought of as the amount of "contact area" of the two streams—longer nozzles equate to more contact area between the two streams. The preceding analysis used De_S as a method to compare nozzles of different geometry. The modified Dean number accounts for changes in nozzle length, and by extension dwell time, using the serpentinity parameter. As shown in Table 4.4, longer nozzles have lower serpentinity due to a decrease in global radius curvature. This method provides valuable characterization information for the integrated parameters size, magnitude, and all the performance parameters. An alternate method that provides further information is to compare those parameters for each nozzle with the corresponding straight nozzle solution of the same length. This section describes the results using the straight nozzle comparisons for no-swirl and swirl solutions.

4.6.1 Straight Nozzle Solutions.

Three axi-symmetric nozzles are designed using the methodology described in Section 3.2. The nozzle use the same L/D, A^*, and A_9 as the serpentine nozzles. The entrance section, including the liner and tailcone, are identical to the serpentine nozzles. Bézier curves are used along the length of the nozzle to create a constantly-converging duct to the throat and a constantly diverging exit section. Similar methodology is used for the OML as well. Identical surface grid spacing to the serpentine nozzles is used throughout. The same solution methods as used with the serpentine nozzles are applied to the straight nozzles to achieve second-order K-ω SST solutions for no-swirl and swirl cases.

Figure 4.123 shows centerline Mach contours for the straight nozzles. All nozzles exhibit more symmetric behavior in the region downstream of the tailcone separation due to the lack of influence from any nozzle curvature. The throat of all nozzles is vertical, again

due to no nozzle curvature. Figures 4.124 and 4.125 show the centerline $P_{st}/P_{st,amb}$ on the upper and lower surfaces. As expected, the upper and lower surfaces are identical due to the nozzles being axi-symmetric. All nozzles are underexpanded and achieve minimum $P_{st}/P_{st,amb}$ upstream of the exit. Underexpansion is caused by pressure increases within the nozzle due to the massive flow separation downstream of the tailcone. Since the nozzle is designed using ideal quasi-one-dimensional isentropic relations (like the serpentine nozzles), which do not take actual flow physics like separation into account, the solution does not achieve ideal expansion. Interestingly, the flow acceleration around the bends in the serpentine nozzles seems to allow those nozzles to expand closer to ideal conditions than the straight nozzles.

Tailcone surface flow for each nozzle is shown in Figure 4.126. The no-swirl solutions are all similar to the LD4_AR4 nozzle, which displayed no distinct vortex foci due to the low influence of nozzle curvature. The swirl solutions are also similar to the serpentine nozzles, with a single strong vortex at the center of the tailcone. Contours of streamwise vorticity at the exit for each nozzle are shown in Figure 4.127. Virtually no vorticity is present at the exit plane for the no-swirl cases, although some asymmetric is evident in the shorter nozzles. The swirl cases all display a strong positive region of vorticity at the exit center due to the single tailcone vortex. The strength of the vorticity diminishes with length, as would be expected. Figure 4.128 shows the exit total temperature distribution for each nozzle. There is little difference in the no-swirl and swirl cases. The hot central core gets smaller as length increases due to the increased mixing of the flow with increased dwell time. This behavior confirms the need to examine the integrated characterization parameters of the serpentine nozzles in terms of their relationship to the straight nozzle solutions.

Figures 4.129 and 4.130 show the characterization parameters size and magnitude and performance parameters C_d and C_{F_g} for the straight nozzle solutions. All plots display a

similar, and expected, trend of decreasing value with increasing length for both no-swirl and swirl solutions. Size and magnitude decrease as length increases because of increased dwell time allowing for more mixing of the two streams. More mixing equates to a decrease in hot flow size and magnitude. The difference between $L/D = 2$ and 4 for size and magnitude is 7.6% and 14.1%, respectively. Performance decreases with an increase in length due to an increase in viscous losses. However, the difference between the $L/D = 2$ and 4 is less than 0.5% for all performance parameters, indicating that viscous losses have only a minor effect on performance. Swirl also only has a minor effect on the parameters; it actually increases thrust performance due to the strong central vortex reducing losses compared to the counter-rotating pair. Swirl decreases discharge performance due to angularity losses, but only by 1%.
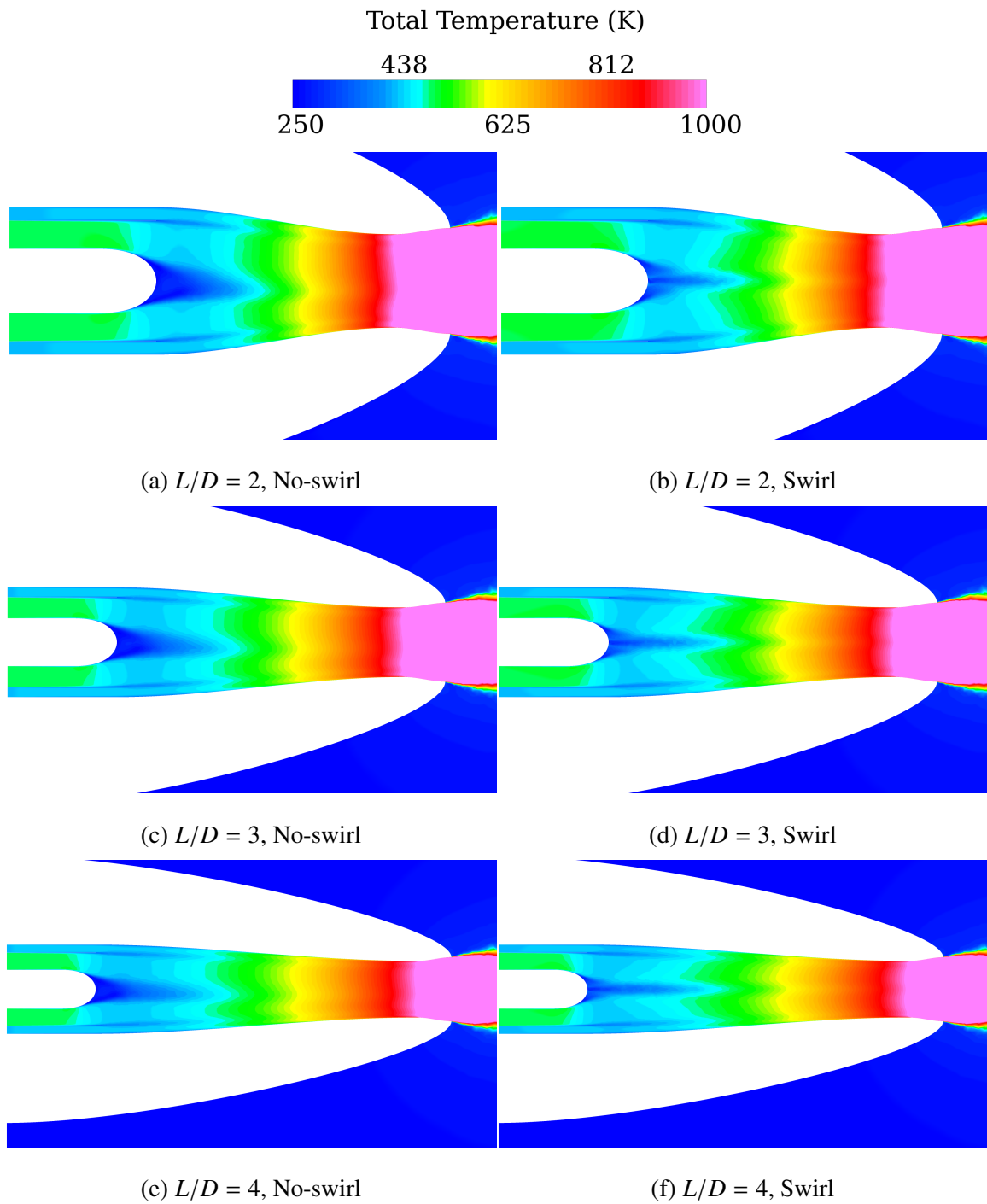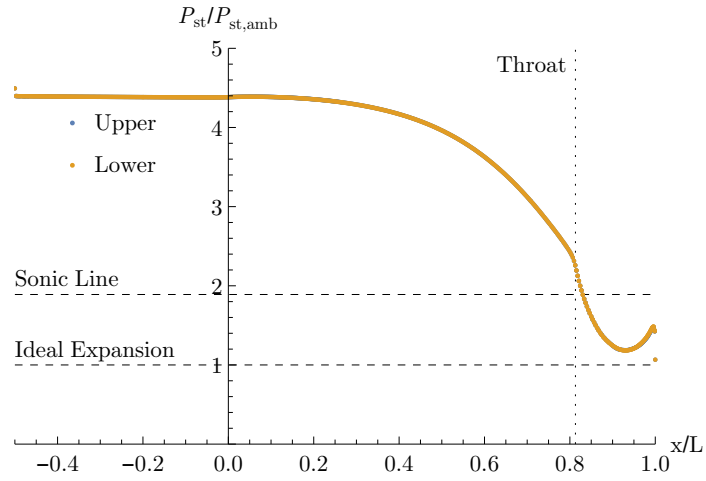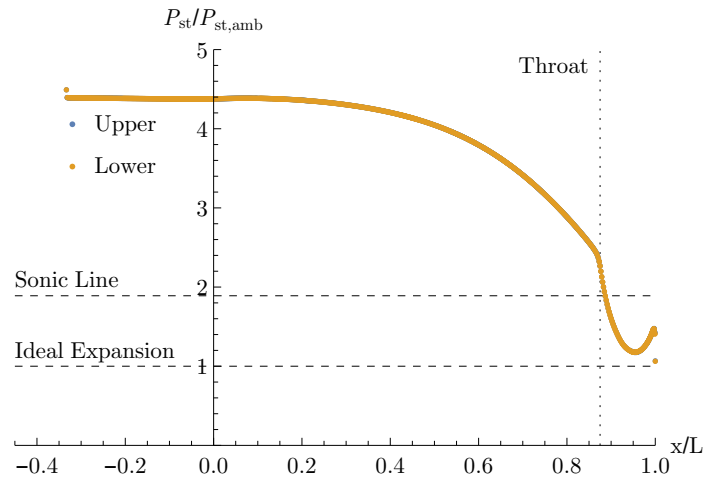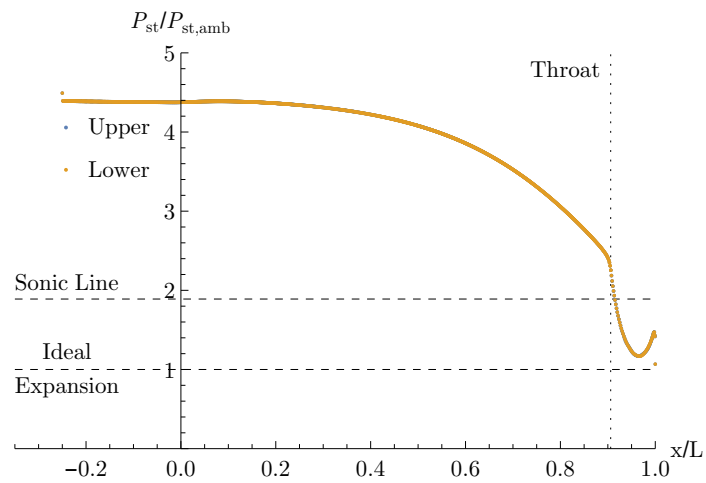
(a) $L/D = 2$, No-swirl

(b) $L/D = 2$, Swirl

(c) $L/D = 3$, No-swirl

(d) $L/D = 3$, Swirl

(e) $L/D = 4$, No-swirl

(f) $L/D = 4$, Swirl

Figure 4.123: Straight nozzle Mach contours.

228

(a) $L/D = 2$

(b) $L/D = 3$

(c) $L/D = 4$

Figure 4.124: Straight nozzle centerline $P_{st}/P_{st,amb}$, No-Swirl.

229

(a) $L/D = 2$
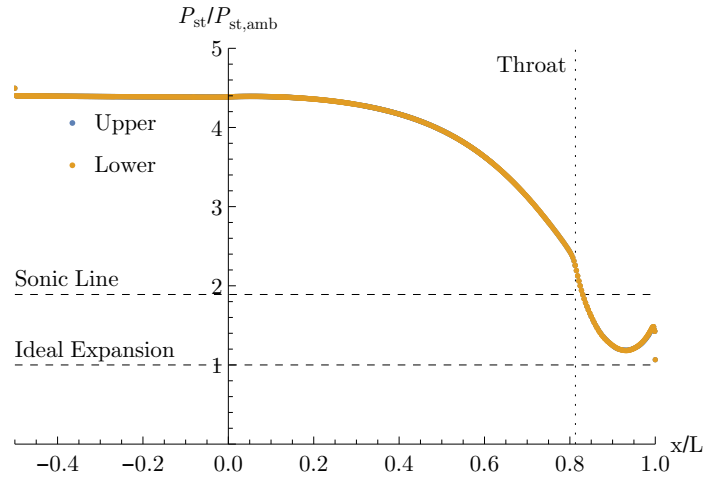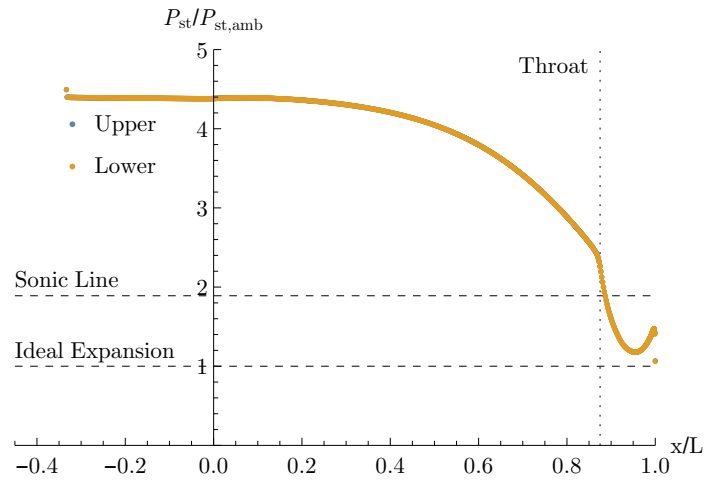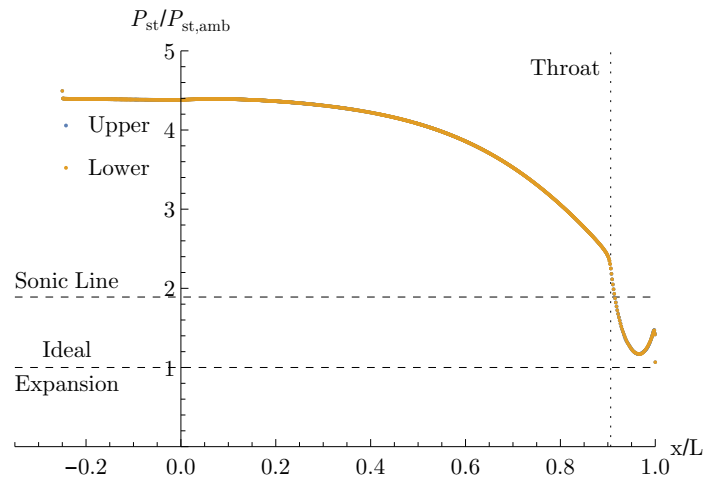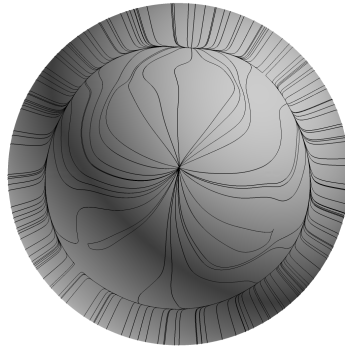

(b) $L/D = 3$

(c) $L/D = 4$

Figure 4.125: Straight nozzle centerline $P_{st}/P_{st,amb}$, Swirl.

(a) $L/D = 2$, No-swirl

(b) $L/D = 2$, Swirl
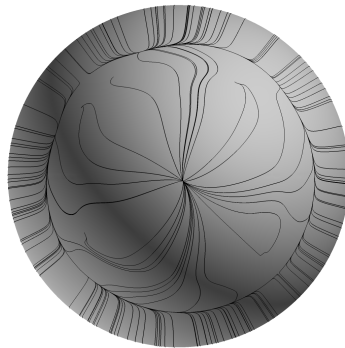
(c) $L/D = 3$, No-swirl

(d) $L/D = 3$, Swirl

(e) $L/D = 4$, No-swirl

(f) $L/D = 4$, Swirl

Figure 4.126: Straight nozzle tailcone surface flow.

Streamwise Vorticity (1/s)

(a) *L/D* = 2, No-swirl

(b) *L/D* = 2, Swirl

(c) *L/D* = 3, No-swirl

(d) *L/D* = 3, Swirl

(e) *L/D* = 4, No-swirl

(f) *L/D* = 4, Swirl

Figure 4.127: Straight nozzle exit streamwise vorticity distribution.

Total Temperature (K)

(a) $L/D = 2$, No-swirl (b) $L/D = 2$, Swirl

(c) $L/D = 3$, No-swirl (d) $L/D = 3$, Swirl

(e) $L/D = 4$, No-swirl (f) $L/D = 4$, Swirl

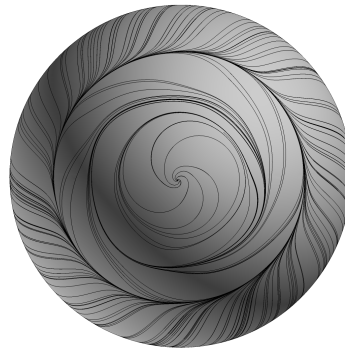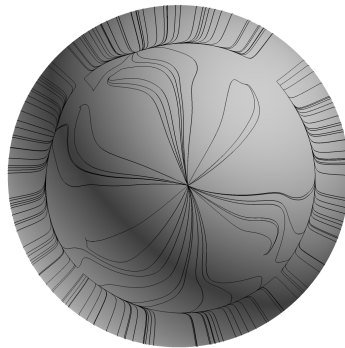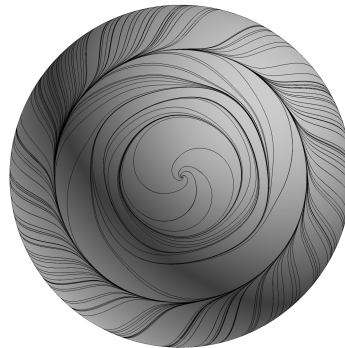Figure 4.128: Straight nozzle exit total temperature distribution.
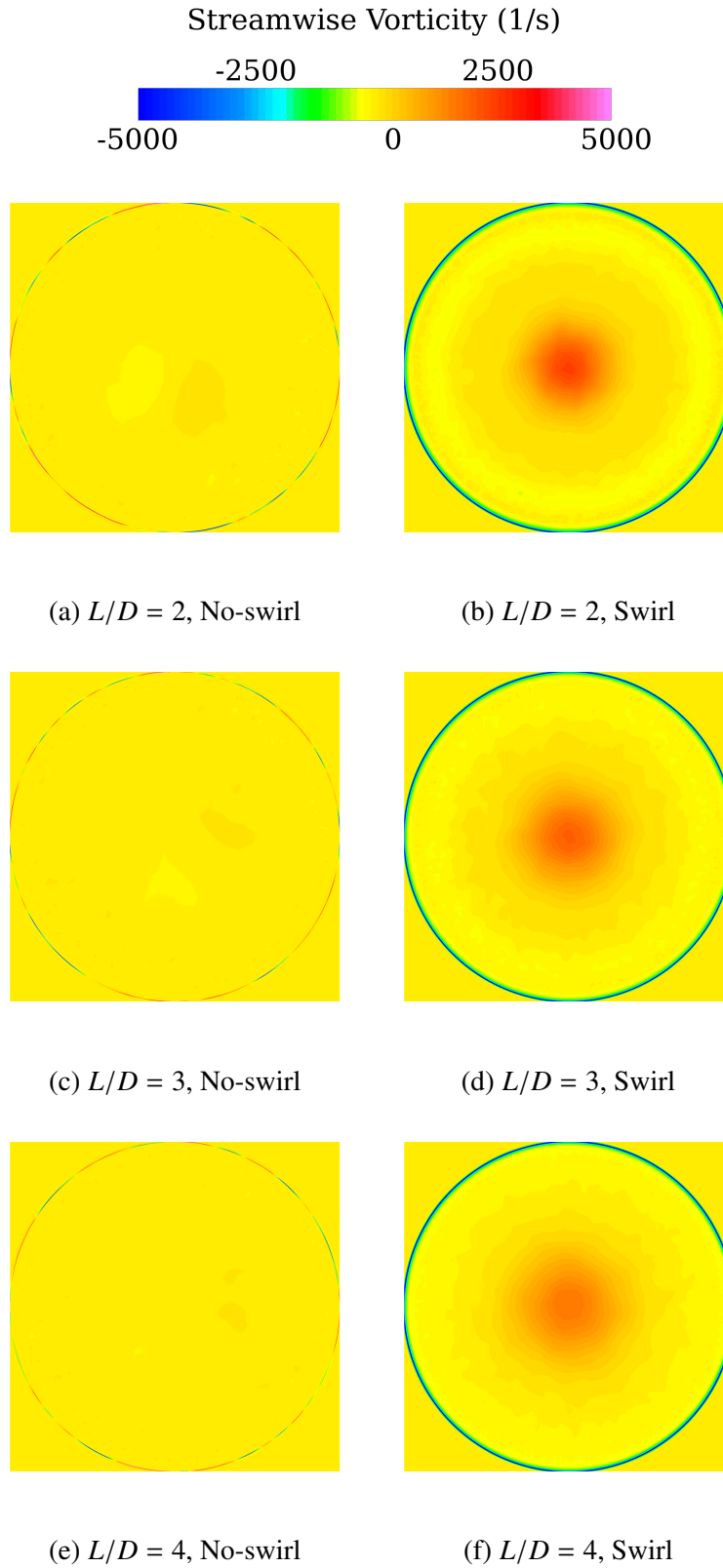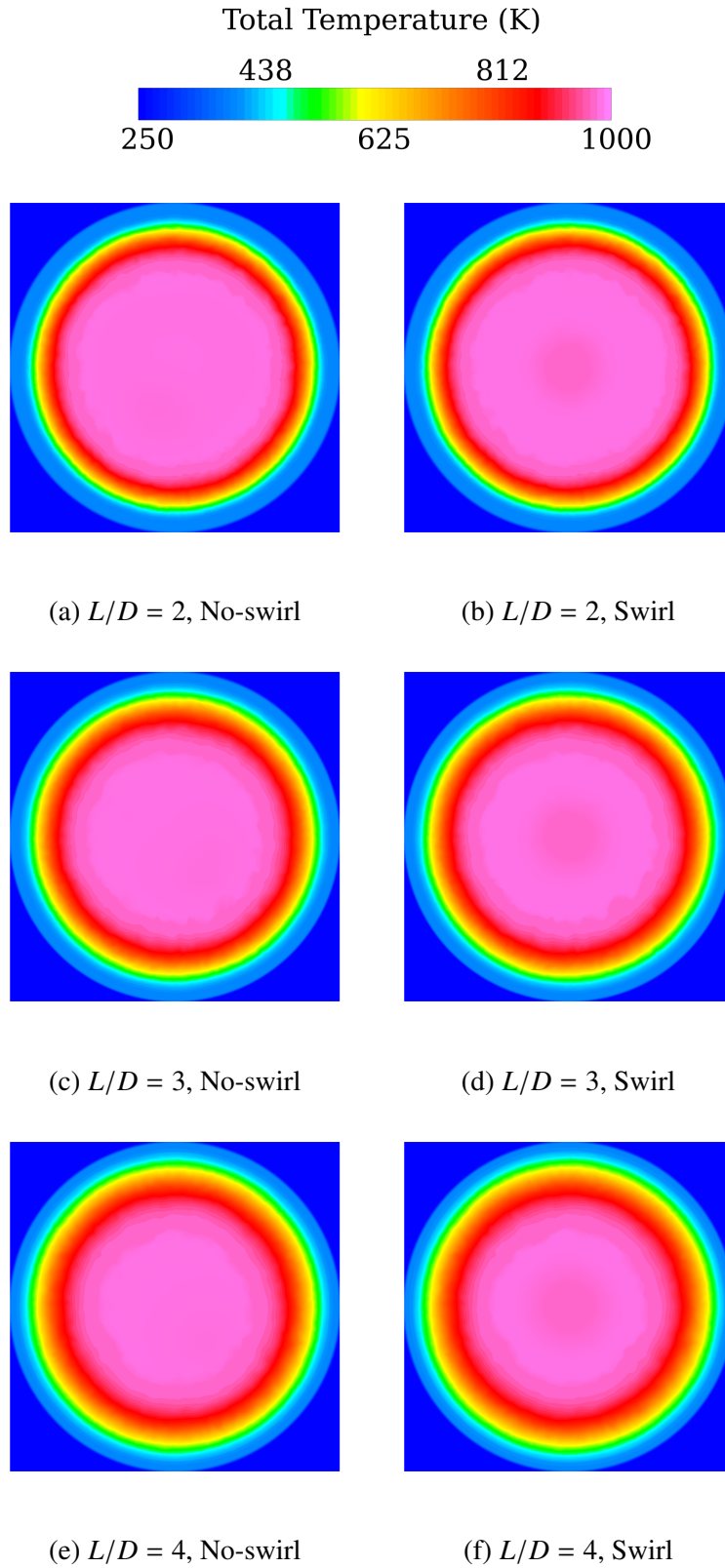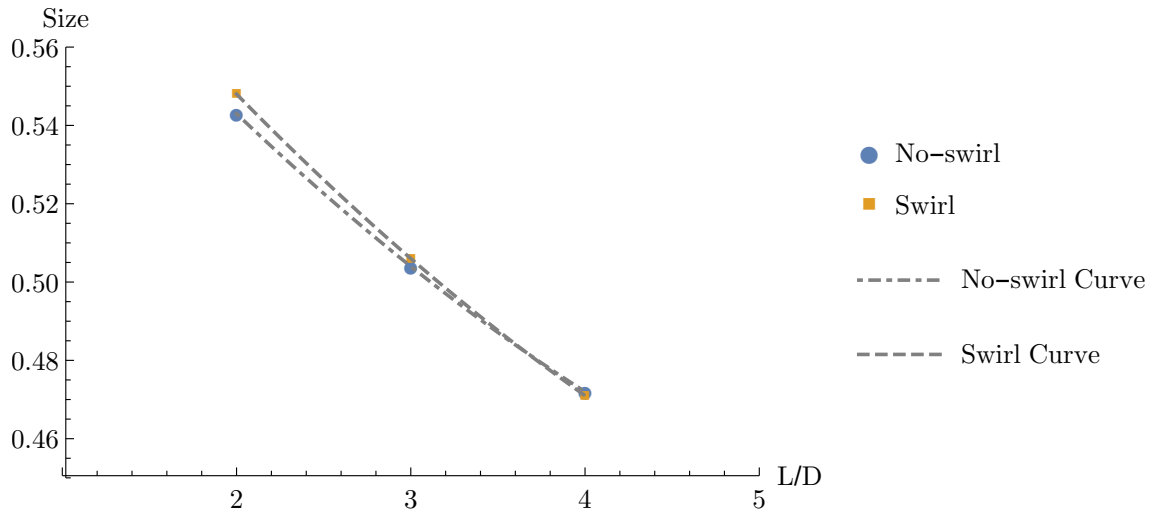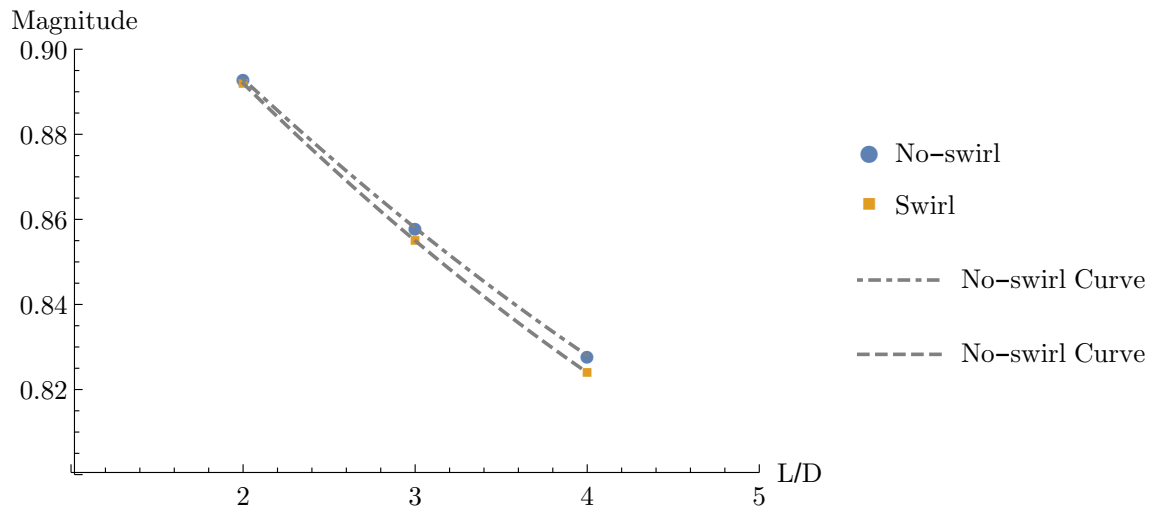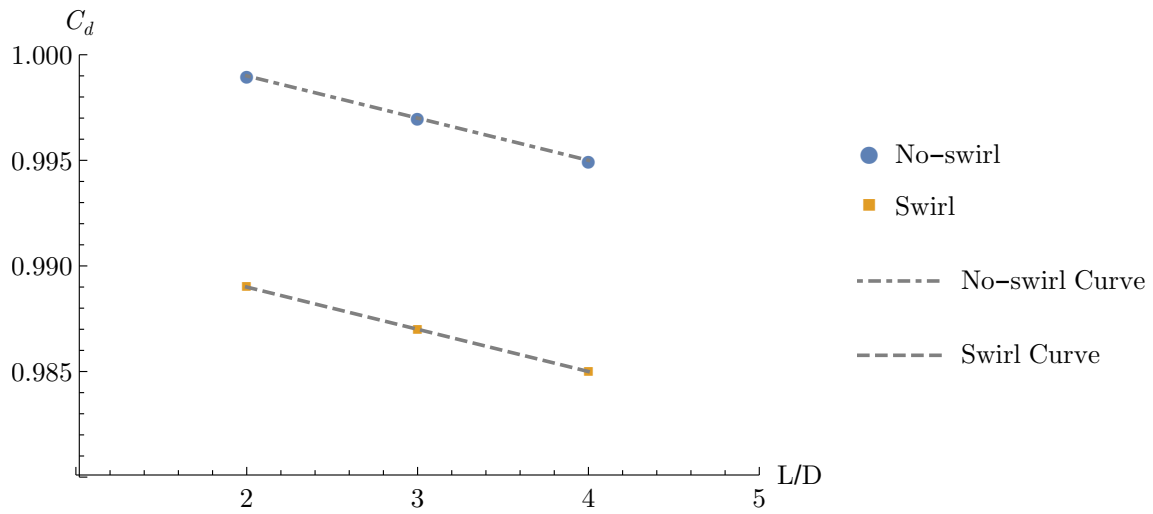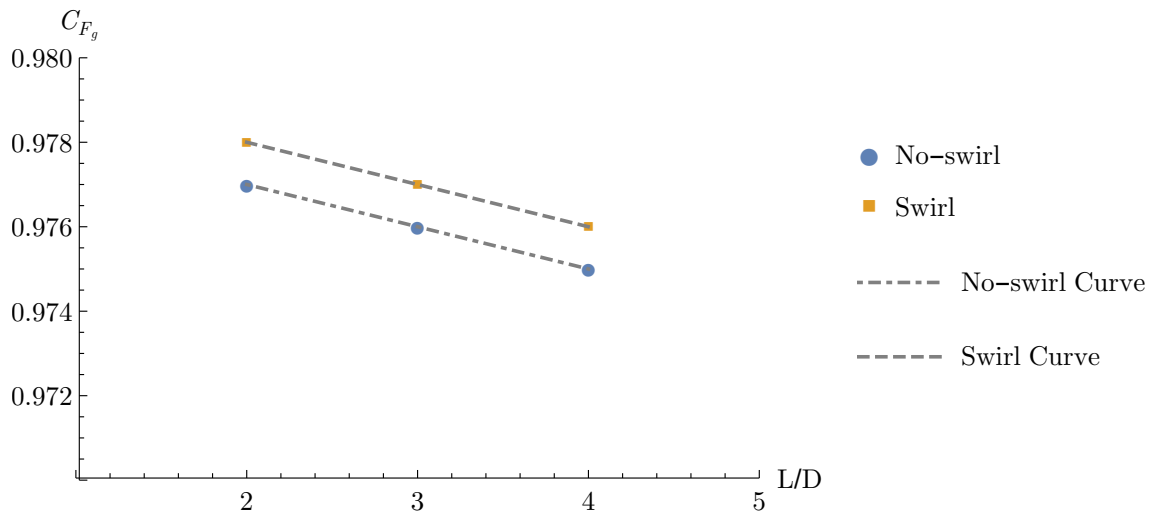
(a) Hot flow size.

(b) Hot flow magnitude.

Figure 4.129: Straight nozzle characterization parameters.

(a) Discharge coefficient.

(b) Thrust coefficient.

Figure 4.130: Straight nozzle performance parameters.

4.6.2 Serpentine Nozzles Comparison with Straight Nozzles.

The relationship between serpentine and straight nozzles of the same length is discussed next. Each characterization and performance value for the serpentine nozzles is normalized by the straight nozzle value of corresponding length. As such, normalized values give an indication of the effect of nozzle curvature on a particular parameter. The closer a normalized value is to unity, the less that parameter is affected by changes in nozzle geometry. Figure 4.131 shows the normalized values for hot flow size for each AR as a function of L/D. All nozzle have a normalized value less than unity, indicating the serpentine hot flow size is smaller than the straight nozzle value. This result equates to the serpentine nozzles promoting more mixing than the straight nozzles due to the curvature-induced vorticity, as would be expected. For each plot, normalized hot flow size increases with L/D, indicating the shorter nozzles promote more mixing, primarily due to stronger vortical structure as previously discussed. This result provides valuable insight into the relationship between the temperature distribution and the flow physics in the nozzles, as a direct comparison between serpentine hot flow size shows the shorter nozzles have higher values. The comparison would lead to the belief that somehow shorter nozzles (and an increase in vorticity strength) promote *less* mixing, but the normalized values reveal the expected behavior. For most nozzles, the swirl cases are closer to their respective straight nozzle solutions than the no-swirl cases. Thus swirl reduces the effect geometry has on mixing. As discussed in previous sections, the vorticity reduction is due primarily to the single vortex versus the counter-rotating pair, which tend to entrain more bypass flow into the center of the nozzle. Another factor is the competition between the swirl direction and lateral divergence of the flow on the lower starboard side, where bypass flow tends to pool. The conclusion is that shorter nozzles are more affected by changes in geometry than longer nozzles, with swirl reducing the effect of geometry changes.
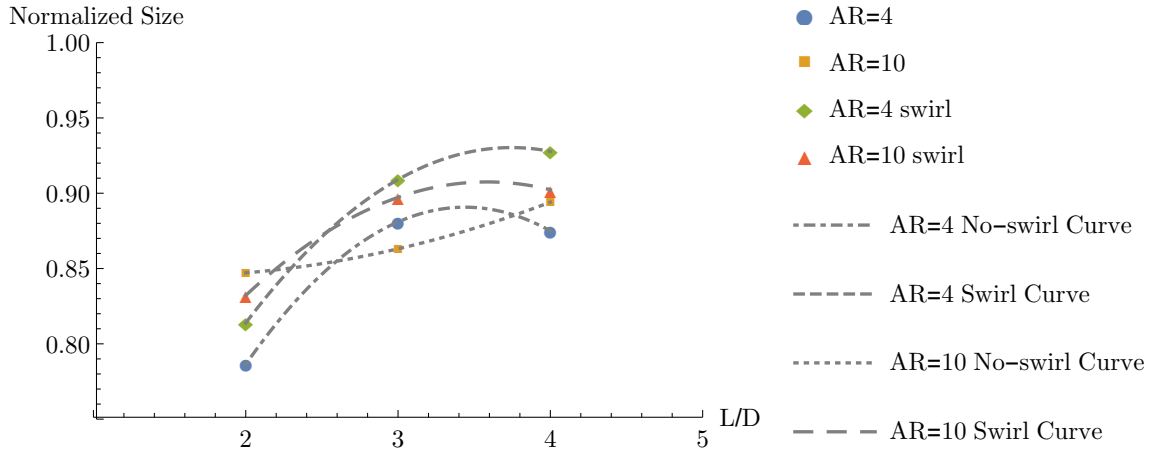
Figure 4.131: Normalized hot flow size.

Normalized values of hot flow magnitude are shown in Figure 4.132. Since all values are below unity the same conclusion that changing nozzle curvature increases overall mixing is drawn similar to hot flow size. However, several differences from normalized hot flow size are apparent. First, like other parameters discussed in previous sections, the LD2_AR4 nozzle is an outlier. The choked and separated flow in this nozzle prevents mixing and causes a high magnitude value that is closer to the straight nozzle magnitude than longer nozzles. For the remaining nozzles, the trend is different from normalized hot flow size. The $L/D = 3$ nozzles display the highest values, meaning these nozzles promote the least amount of mixing in terms of spreading the hot core flow. This complex behavior must be explained using both the shorter and longer nozzles. The $L/D = 2$ nozzles compare similarly as with hot flow size, with the flow separation increasing overall vorticity strength, promoting more mixing, and decreasing normalized magnitude. But the increase in L/D from 3 to 4 also *increases* mixing, at least in terms of "spreading out" the hot core flow. This spreading of the flow is seen in the temperature distributions at the exit for each nozzle and results in more mixing near the upper and lower surface of the $L/D = 4$ nozzle than for $L/D = 3$, even though less mixing is occurring at the sidewalls due to lower levels of

237

vorticity. This phenomenon results in slightly lower normalized magnitude, with the largest difference between any two $L/D = 3$ and 4 nozzles being 3.5%. Like normalized size, swirl has the affect of reducing the effect of geometry changes and thus increases normalized hot flow magnitude. For both no-swirl and swirl cases, an increase in AR from 4 to 10 reduces the normalized magnitude, meaning the higher aspect ratio nozzles are more affected by lateral divergence than the lower AR nozzles.
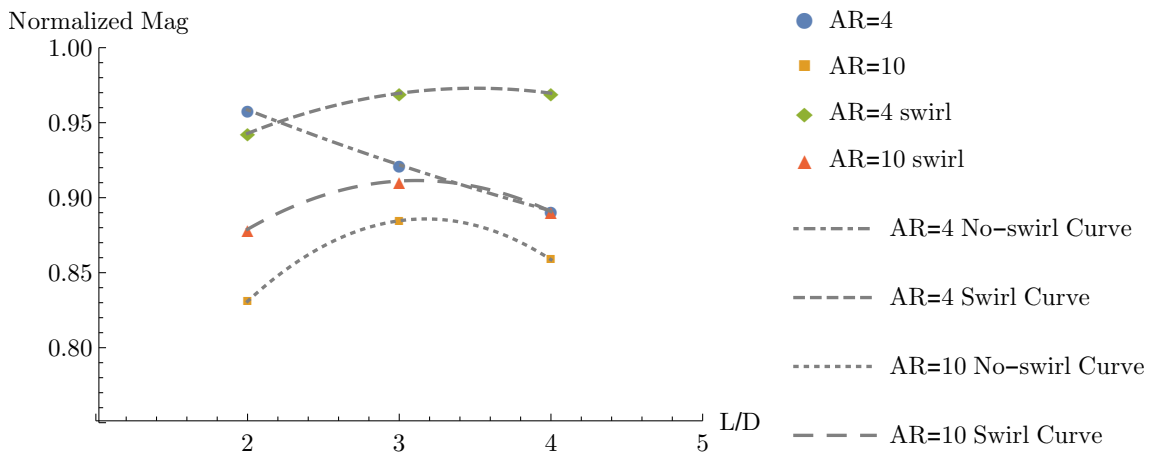
Figure 4.132: Normalized hot flow magnitude.

Normalized performance parameters in Figure 4.133 show only minor differences from their non-normalized counterparts in Figures 4.118, 4.120, and 4.122. For C_d, the serpentine solution is closer to the straight nozzle as length is increased and losses due to flow separation are reduced. Like size and magnitude, swirl reduces the effect of geometry causing the normalized swirl values to be closer to their respective straight nozzle solution, but the differences between the swirl and no-swirl cases is very small. Thrust coefficient and gross thrust follow similar patterns, with an increase in length reducing the effect of geometry. The $L/D = 3$ and 4 nozzles actually have a normalized C_d and F_g greater than 1, which results in the serpentine nozzles performing equal to or *better* than the straight nozzle. Re-examination of the centerline $P_{st}/P_{st,amb}$ for each case shows how this can be

the case. The straight nozzles are all underexpanded, meaning the nozzle does not perform the appropriate amount of work to fully accelerate the flow to the designed value. Thus the straight nozzles fall short of producing the maximum amount of thrust. The longer serpentine nozzles are more ideally expanded and thus have higher values of C_d and F_g.
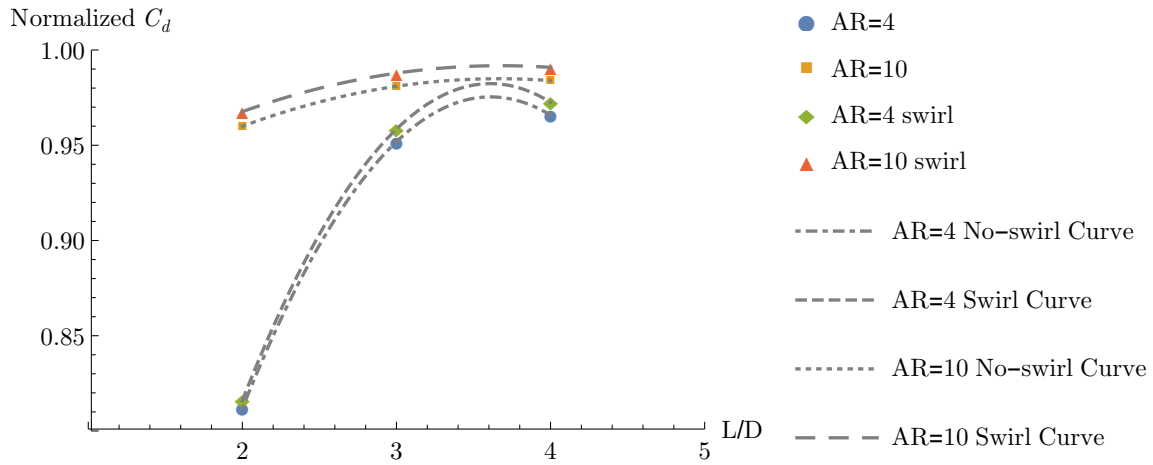
(a) Discharge Coefficient
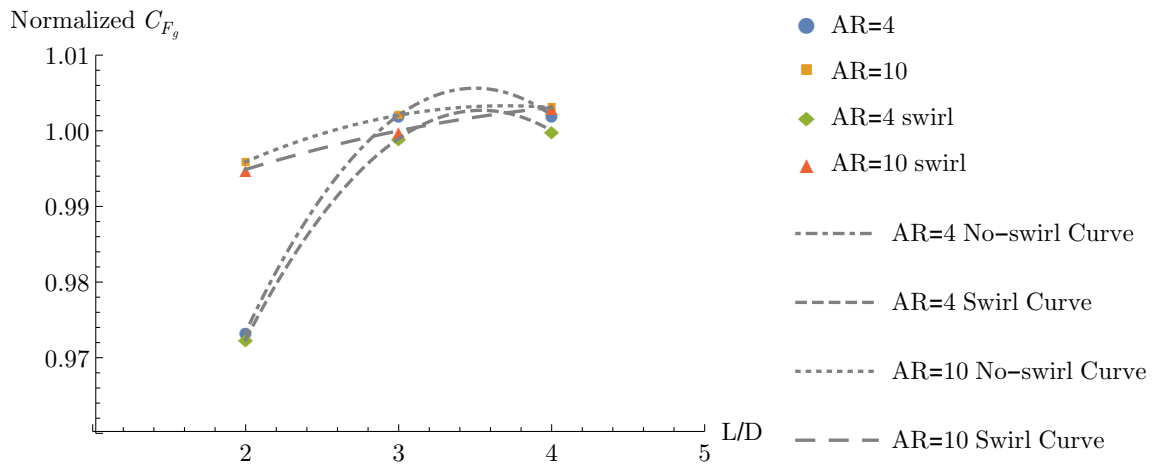
(b) Thrust Coefficient
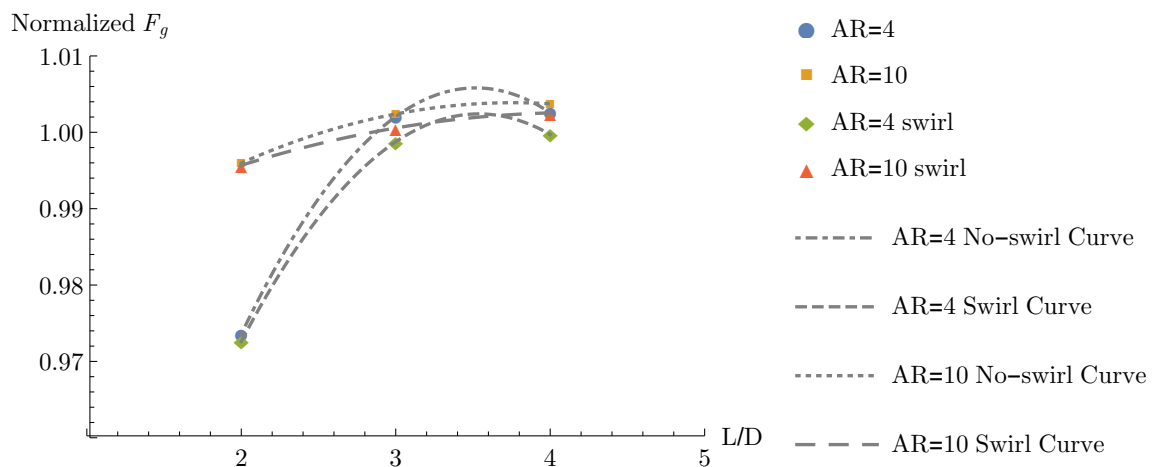
(c) Gross Thrust

Figure 4.133: Normalized performance parameters.

240

4.7 Surface Temperature and Hot Streaks

Finally, examination of the nozzle static surface temperature at the exit reveals changes in hot streak phenomena with changes in nozzle geometry and swirl. A connection is made between the surface flow and the exit surface temperature distribution. Figures 4.134(a) and (b) show the upper and lower surface temperature with imposed surface flow for the LD2_AR10 nozzle. On the upper surface, a distinct connection between the flow separation and flow temperature is seen at the second bend. There is also a relationship between hotter flow impacting the surface at the reattachment line, and the asymmetry due to the counter-rotating vortex pair from the tailcone. On the lower surface, a hot streak is observed starboard of the centerline. The hot core flow is seen to push the surface flow outward as it impacts the surface. Figure 4.134(c) shows a plot of surface temperature at the exit plane as a function of the position along the normalized width of the exit (z/w_9). The pattern observed in the surface flow is shown in the plot. The upper surface plot shows the relatively uniform increase in temperature from the outer edges, with a slight dip starboard of centerline. The lower surface plot shows the distinct increase in surface temperature due to the hot streak.

Figures 4.135(a) and (b) show the upper and lower surface temperature with imposed surface flow for the LD2_AR10 swirl case. A drastically different surface temperature distribution is observed compared to the no-swirl case. The hot flow is now exclusively at the upper surface, with a distinct separation between hot core flow and cooler mixed flow due to the upper surface separation and resulting vortex. The lower surface is quite cool, with only a small increase in temperature near the centerline. Figure 4.135(c) reflects this behavior at the exit, with the lateral extent of the upper surface hot streak greater than the lower surface no-swirl streak. Thus an important behavior is revealed where swirling flow flips the appearance of hot streaks from the lower to the upper surface and in essence shields the lower surface from hot flow.
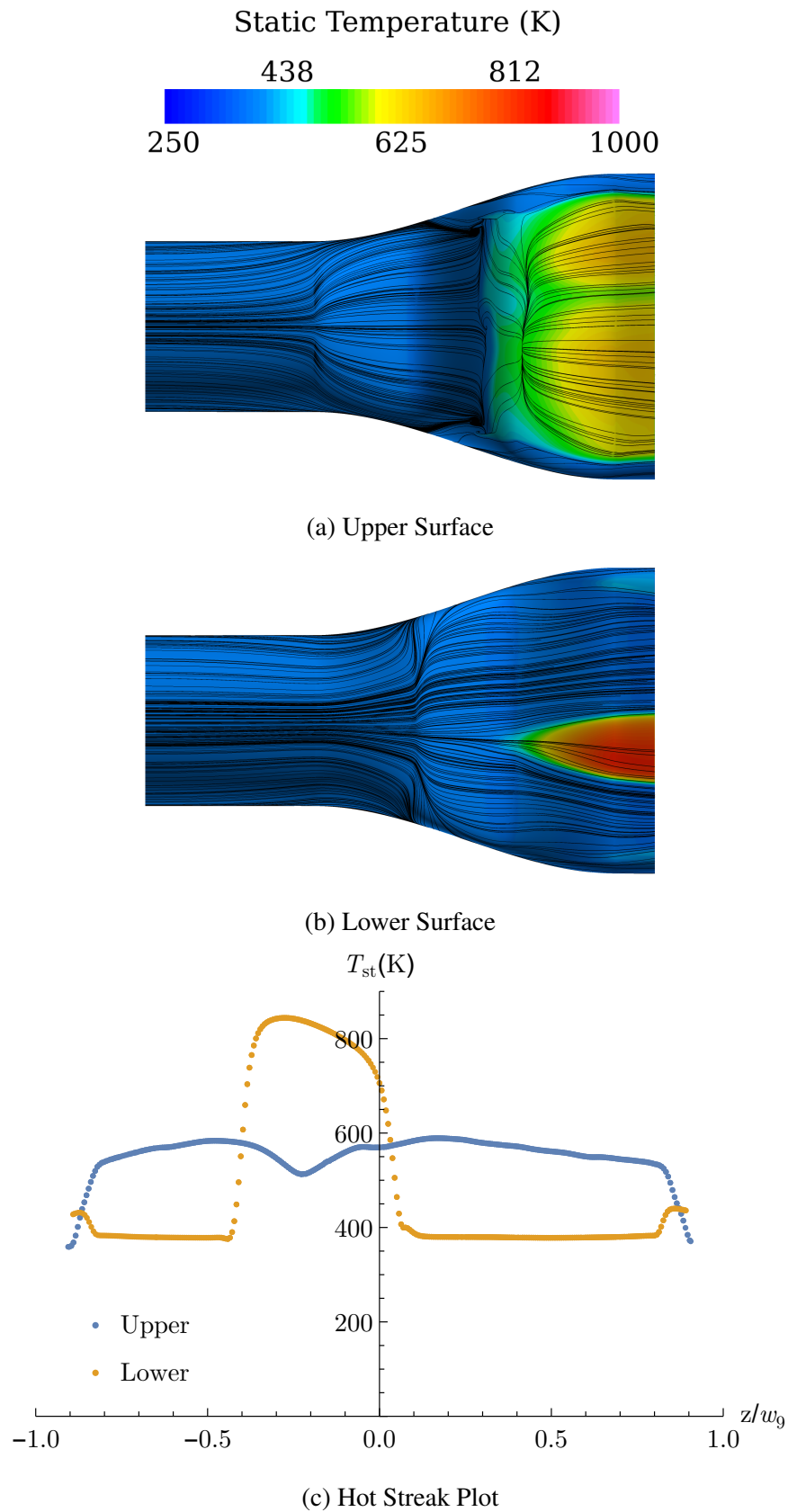
(a) Upper Surface

(b) Lower Surface

(c) Hot Streak Plot

Figure 4.134: No-swirl LD2_AR10 Exit Surface Temperature.

(a) Upper Surface

(b) Lower Surface

(c) Hot Streak Plot

Figure 4.135: Swirl LD2_AR10 Exit Surface Temperature.

243

Figures 4.136(a) and (b) show the upper and lower surface temperature with imposed surface flow for the LD2_AR4 nozzle. Again, a connection between the flow separation/reattachment and the impingement of hotter flow on the surface is observed. Unlike the LD2_AR10 nozzle, the lower surface stays cool, with no hot streak formation. The lack of a hot streak is due to flow separation at the lower surface, a feature unique to this nozzle. The exit surface temperature plot in Figure 4.136(c) displays asymmetry and the weak upper surface hot streak.

Figures 4.137(a) and (b) show the upper and lower surface temperature with imposed surface flow for the LD2_AR4 swirl case. Again, a distinctly different behavior results compared to the no-swirl case. The upper surface has hot flow impinged upon it, exactly at the reattachment line, where hot flow is buffered in the separated region. The second upper separation near the exit draws cooler flow towards the centerline, resulting in distinct decreases in surface temperature on either side of the centerline. The lower surface remains quite cool, a pattern observed in Figure 4.137(c). Also seen in this plot is the drop-off in temperature on the upper port side due to the second separation.

Figures 4.138(a) and (b) show the upper and lower surface temperature with imposed surface flow for the LD3_AR10 nozzle. The upper surface stays relatively cool compared to the lower surface, with a much more symmetry surface temperature distribution compared to the shorter nozzles. The lower surface experiences a much larger hot streak compared to the LD2_AR10 nozzle, almost directly along the centerline. The streak begins upstream of the second bend, where the hot core flow in the lower portion of the duct that was previously unaffected by the change in upper streamline curvature of the the first bend impacts the second bend, as seen by the splitting of the surface flow lines. This behavior is shown in Figure 4.138(c) as a sharp increase in temperature near the centerline of the duct at the exit. Some asymmetry is present in the distribution on lower surface due to the entrainment of the asymmetric tailcone vortices, while the upper surface is more symmetric.

Static Temperature (K)

(a) Upper Surface

(b) Lower Surface

(c) Hot Streak Plot

Figure 4.136: No-swirl LD2_AR4 Exit Surface Temperature.

(a) Upper Surface

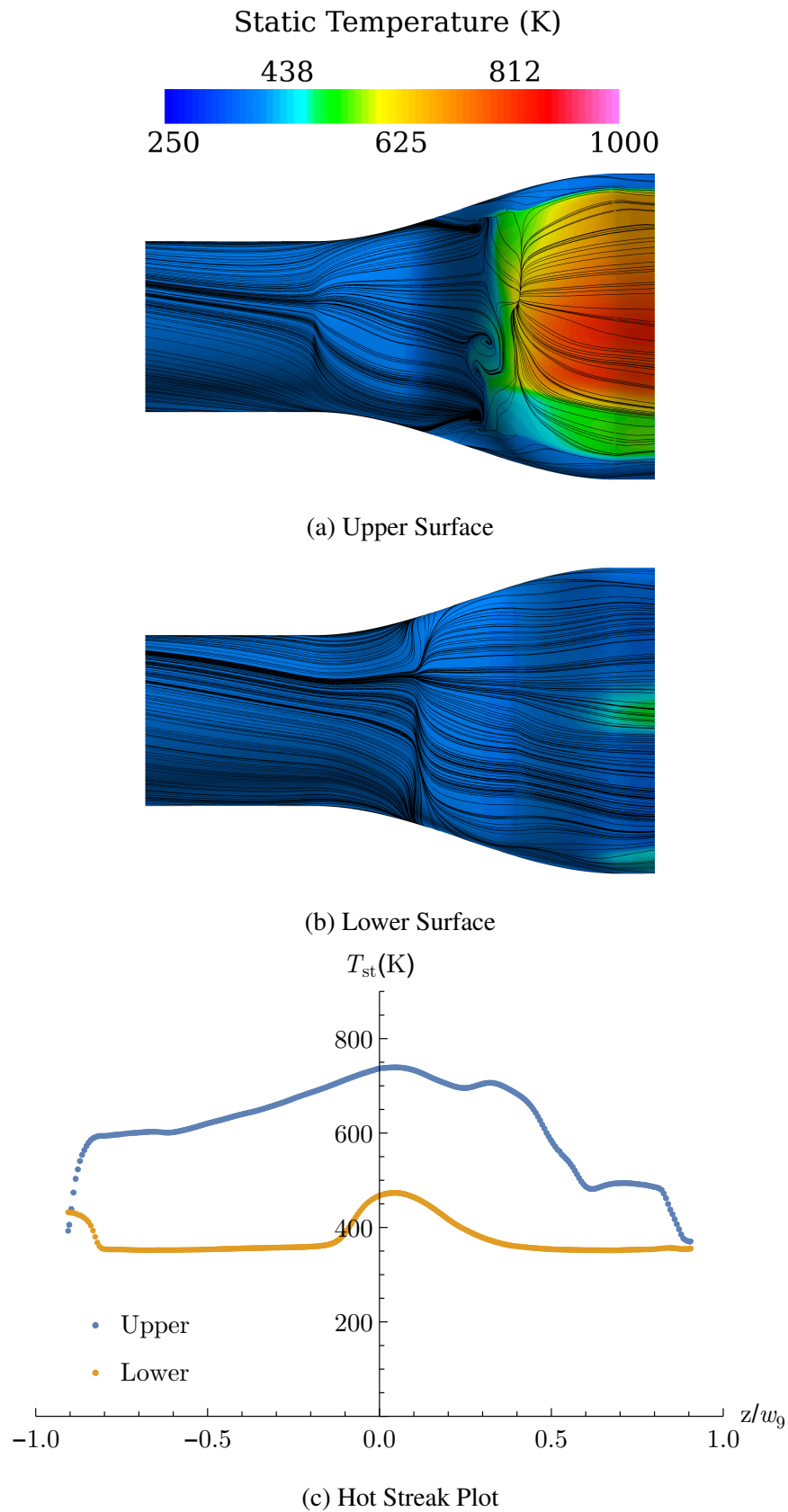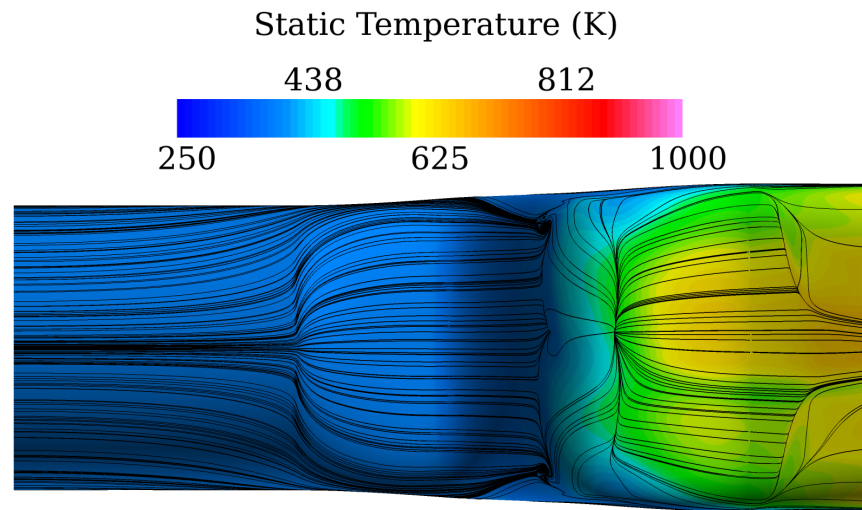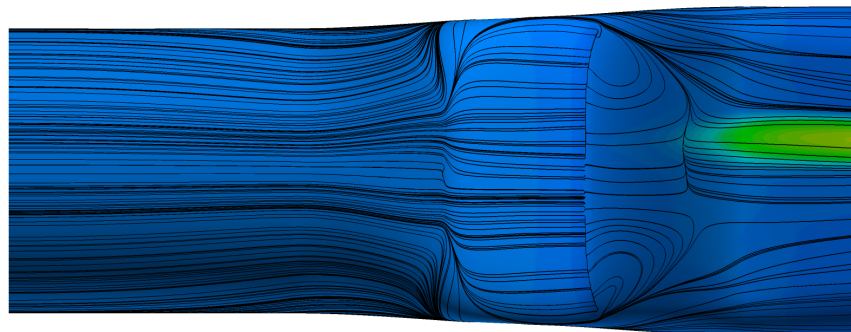(b) Lower Surface

(c) Hot Streak Plot

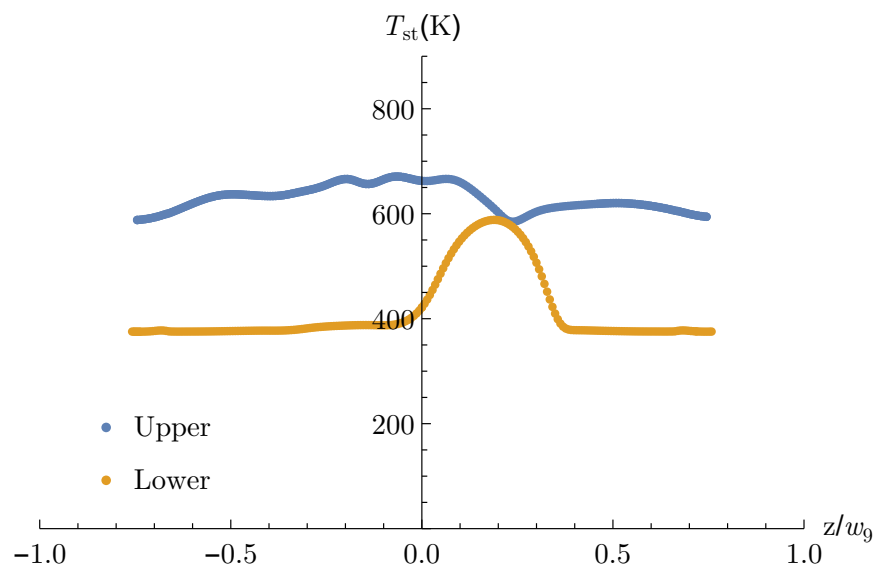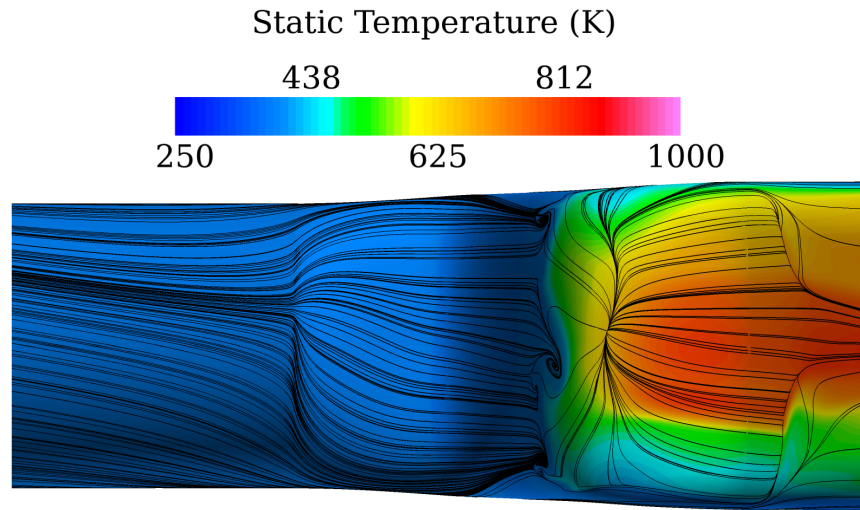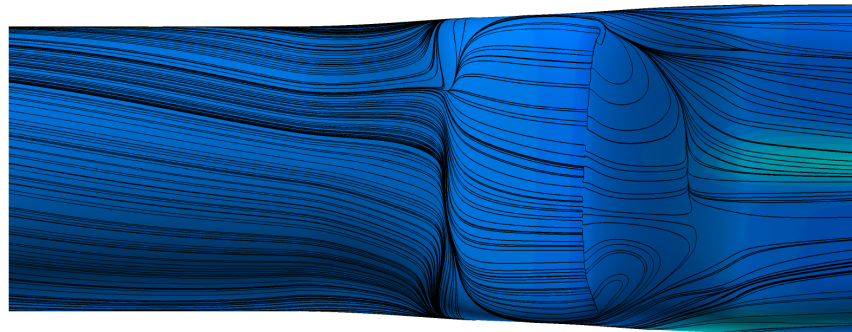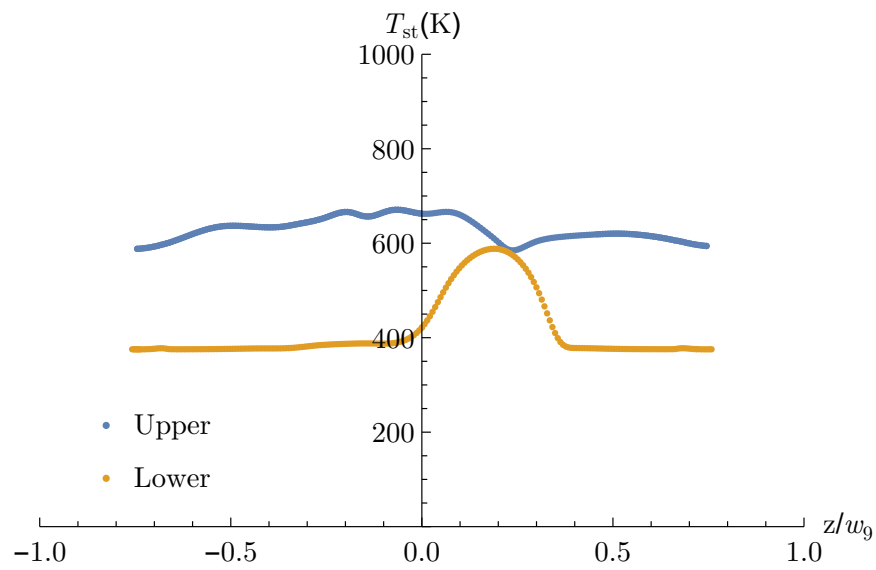Figure 4.137: Swirl LD2_AR4 Exit Surface Temperature.

246

Figures 4.139(a) and (b) show the upper and lower surface temperature with imposed surface flow for the LD3_AR10 swirl case. The upper surface shows a distinct barrier between the hot streak and cool flow due to the upper surface swirl-induced vortex. The lower surface remains cool, with a small increase in temperature near the centerline. Figure 4.139(c) shows the distinct rise in temperature due to the presence of the hot streak.

Figures 4.140(a) and (b) show the upper and lower surface temperature with imposed surface flow for the LD3_AR4 nozzle. Similar to the LD3_AR10 nozzle, the upper surface remains relatively cool, with a symmetry distribution. The lower surface has a long hot streak that begins downstream of the first bend along the centerline and continues to the exit. The distinct streak is seen in the exit surface temperature plot in Figure 4.140(c).

Figures 4.141(a) and (b) show the upper and lower surface temperature with imposed surface flow for the LD3_AR4 swirl case. The upper surface again shows a distinct barrier between the hot streak and cold flow at the coalescence location, although the hot streak is lower in temperature than the LD3_AR10 nozzle. The lower surface remains almost completely cool, with very little influence from the core flow. This behavior is shown in Figure 4.141(c) where the lower exit surface is almost completely at the bypass flow temperature. The hot streak location is also clearly observed.

Figures 4.142(a) and (b) show the upper and lower surface temperature with imposed surface flow for the LD4_AR10 nozzle. The upper surface is very similar to the LD3_AR10 nozzle, with a symmetric temperature distribution warmed by mixing. The lower surface is also similar, with a large hot streak symmetrically down the centerline. The symmetry is displayed in Figure 4.142(c).

Figures 4.143(a) and (b) show the upper and lower surface temperature with imposed surface flow for the LD4_AR10 swirl case. Again, the distinct hot streak barrier is observed on the upper surface. Some heating does occur on the starboard side of the lower surface,

(a) Upper Surface

(b) Lower Surface

(c) Hot Streak Plot

Figure 4.138: No-swirl LD3_AR10 Exit Surface Temperature.

248

(a) Upper Surface

(b) Lower Surface

(c) Hot Streak Plot

Figure 4.139: Swirl LD3_AR10 Exit Surface Temperature.

249

Static Temperature (K)

(a) Upper Surface

(b) Lower Surface

(c) Hot Streak Plot

Figure 4.140: No-swirl LD3_AR4 Exit Surface Temperature.

Static Temperature (K)

438   812

250   625   1000

(a) Upper Surface

(b) Lower Surface

T_{st}(K)
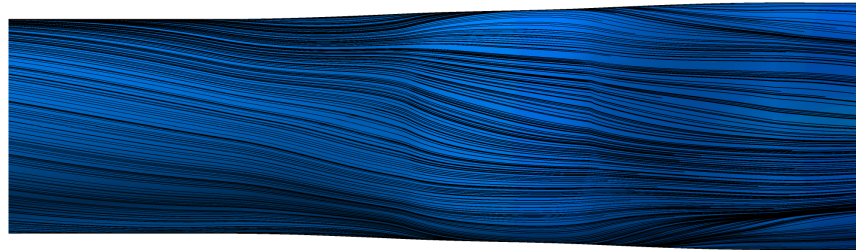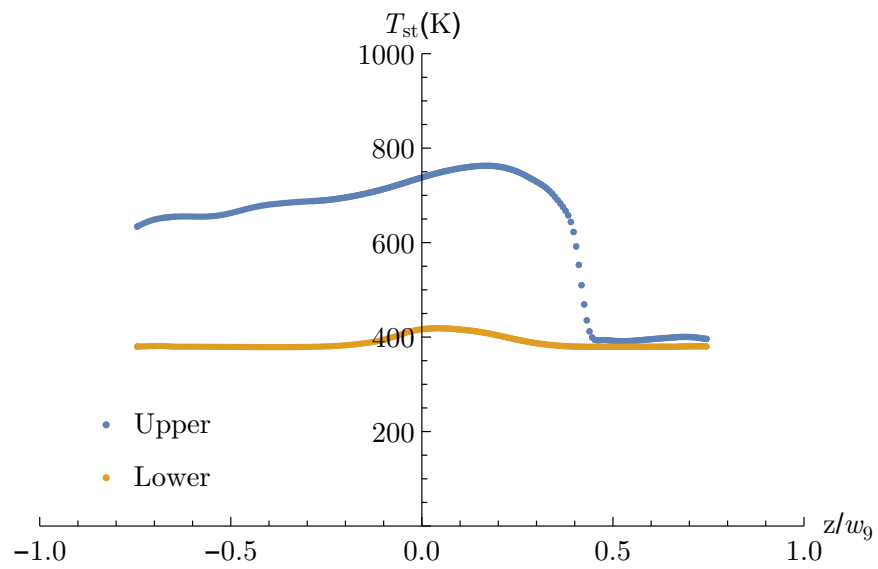
(c) Hot Streak Plot

Figure 4.141: Swirl LD3_AR4 Exit Surface Temperature.

251
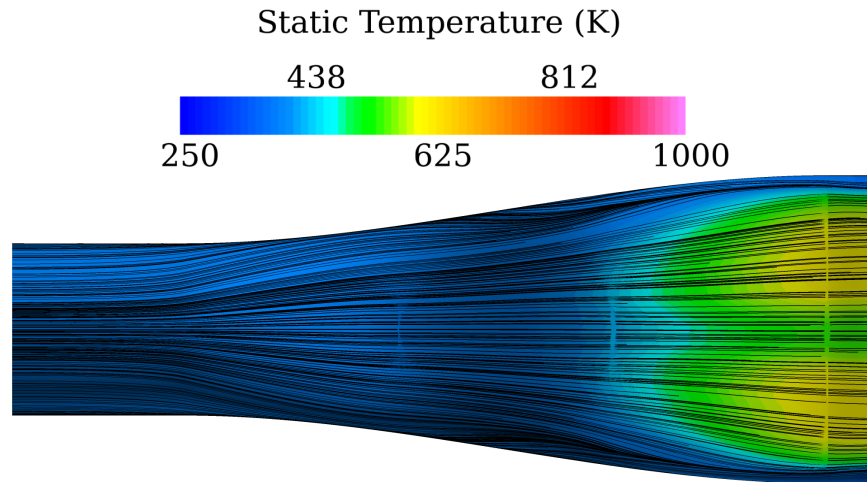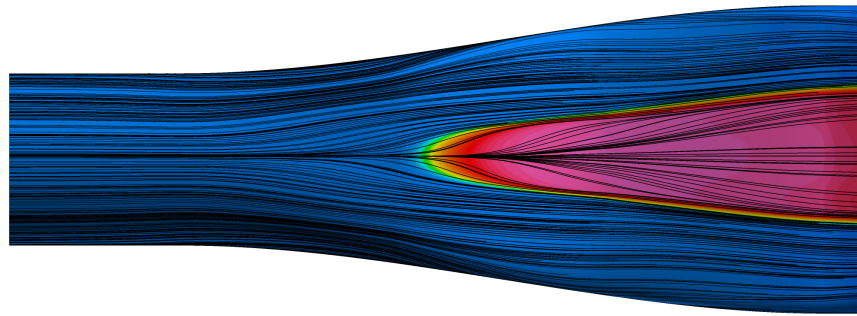
(a) Upper Surface
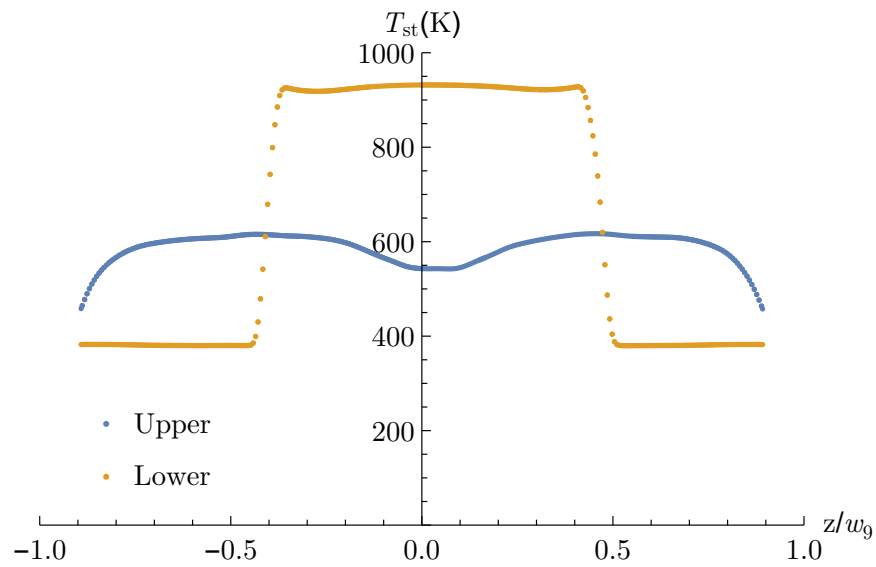
(b) Lower Surface

(c) Hot Streak Plot

Figure 4.142: No-swirl LD4_AR10 Exit Surface Temperature.

more so than the shorter swirl cases. This asymmetric heating is also seen on the exit surface in Figure 4.143(c).

Figures 4.144(a) and (b) show the upper and lower surface temperature with imposed surface flow for the LD4_AR4 nozzle. The upper surface is relatively cool compared to the shorter nozzles. The lower surface shows a long hot streak originating just downstream of the first bend, more upstream than any other nozzle due to the lack of influence from the upper curvature. The exit surface plot in Figure 4.144(c) shows a similar plot as the LD4_AR10 nozzle.

Figures 4.145(a) and (b) show the upper and lower surface temperature with imposed surface flow for the LD4_AR4 swirl case. The upper surface shows a strong coalescence of flow at the edge of the hot streak. The lower surface remains relatively cool. Figure 4.145(c) reflects these observations at the exit.

Next, the effect of geometry on hot streak phenomena at the nozzle exit is discussed. The surface temperature data at the nozzle exit shown above is plotted together. Figure 4.146 shows the upper surface exit temperature distribution for the no-swirl cases. As previously discussed for each nozzle, some heating does occur at the upper surface but the surfaces remains relatively uniform. Most nozzles experience a slight dip in temperature along the centerline due to the bypass flow at the top-dead-center of the nozzle, which does not migrate away from the centerline flowpath (as shown in every surface flow figure) and provides a buffer from warmer flow. The exceptions are the two $L/D = 2$ nozzles, which are the only nozzles to experience a large degree of flow separation. The asymmetric nature of the flow reattachment and the interaction with the strong central counter-rotating vortex pair results in temperature dips near ± 0.25 z/w_9.

Figure 4.147 shows a somewhat unexpected result. As previously seen, most cases experience a large hot streak along nearly 50% of the duct length. The exceptions are again the nozzle that experience flow separation. The separation is shown to lift hot flow from

253

Static Temperature (K)

438   812

250   625   1000
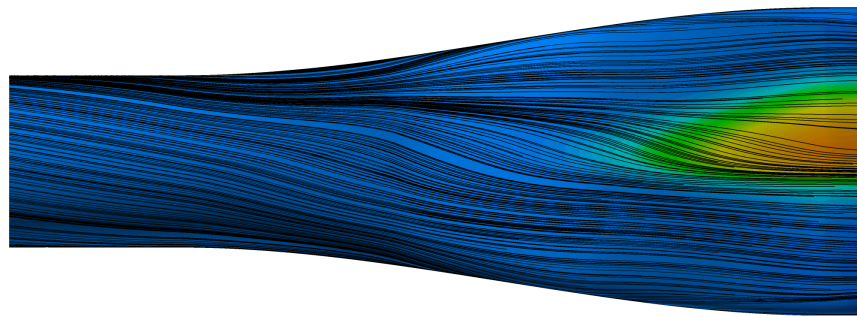
(a) Upper Surface
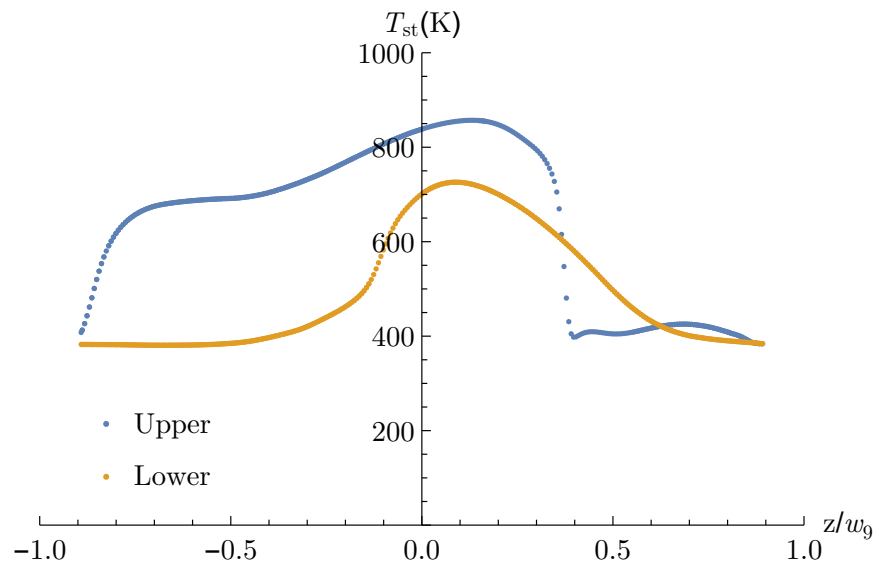
(b) Lower Surface

(c) Hot Streak Plot
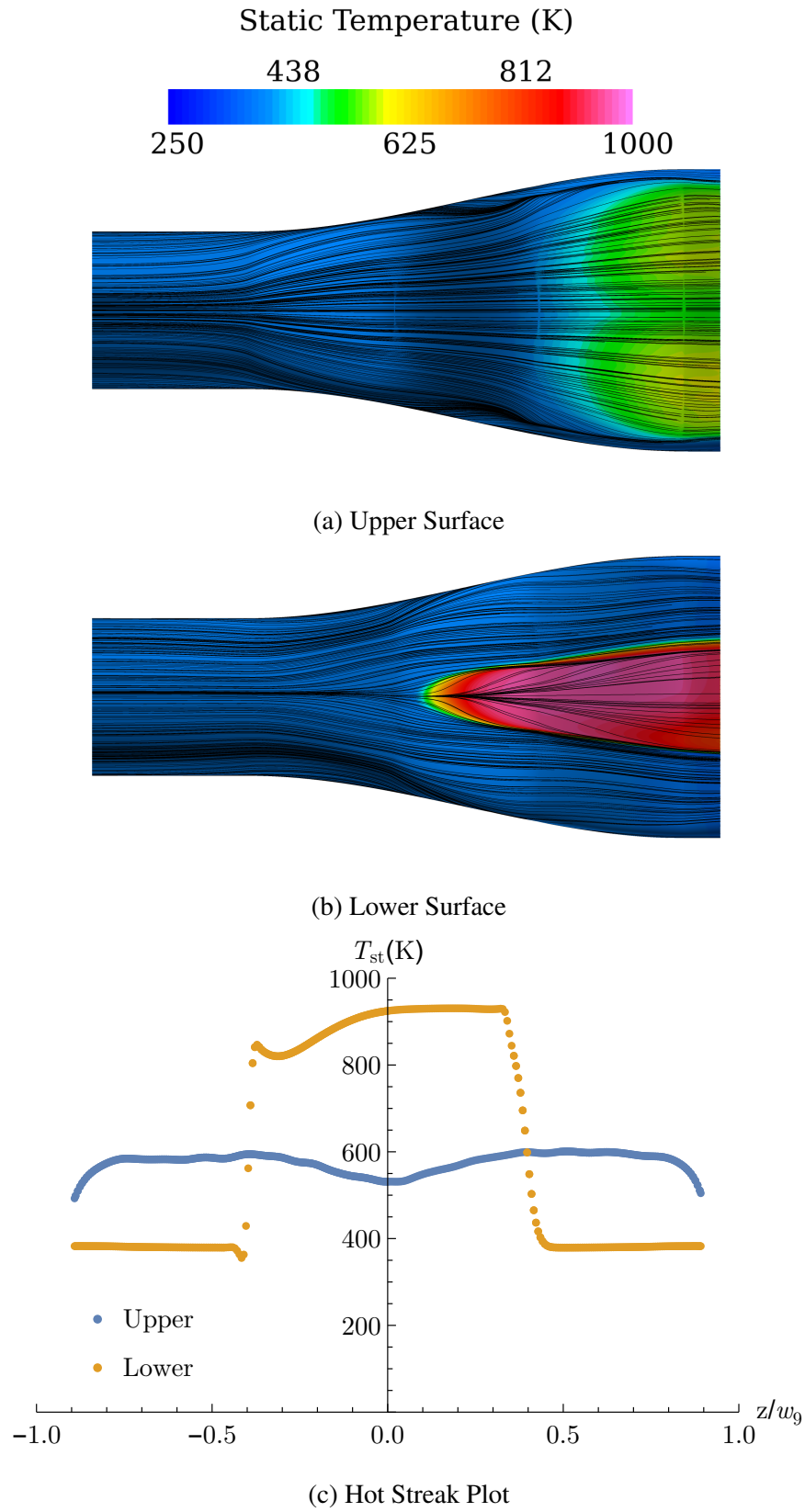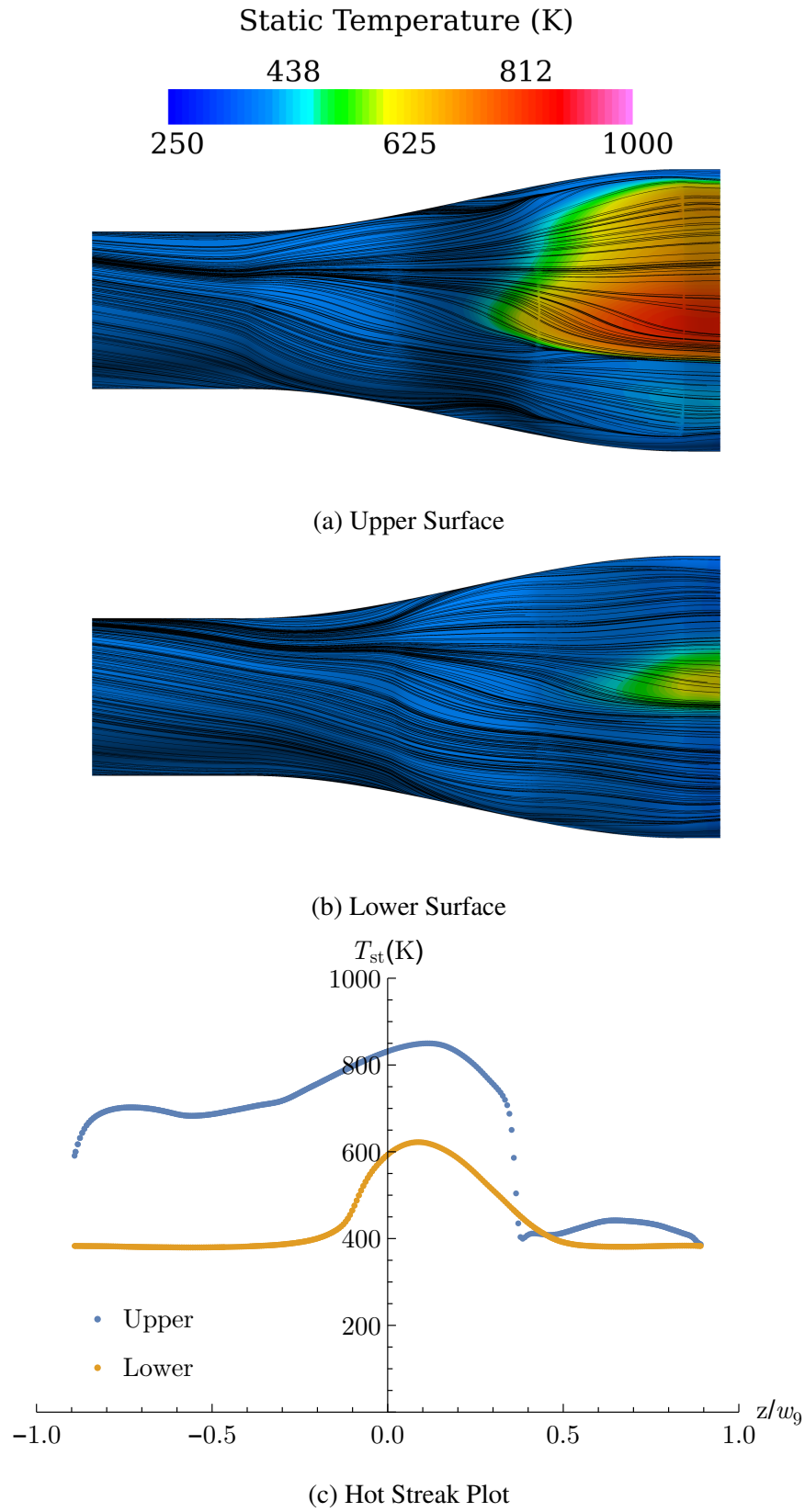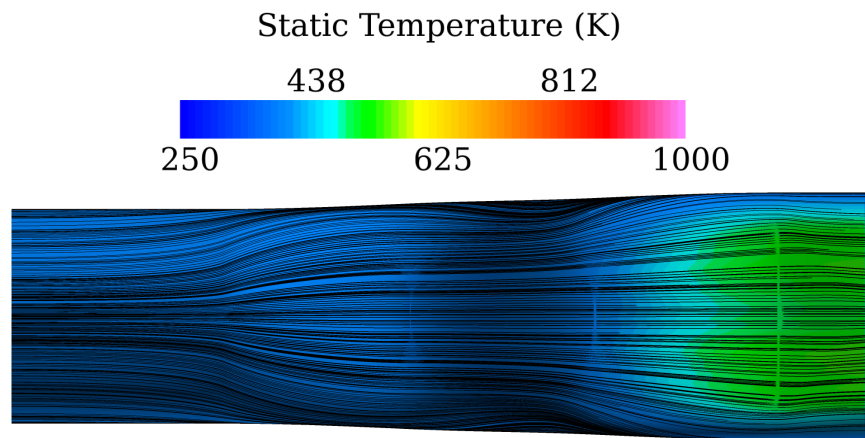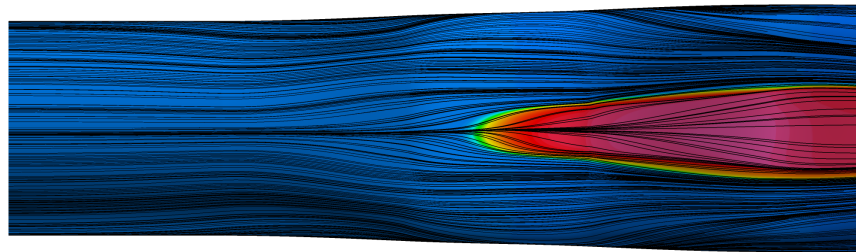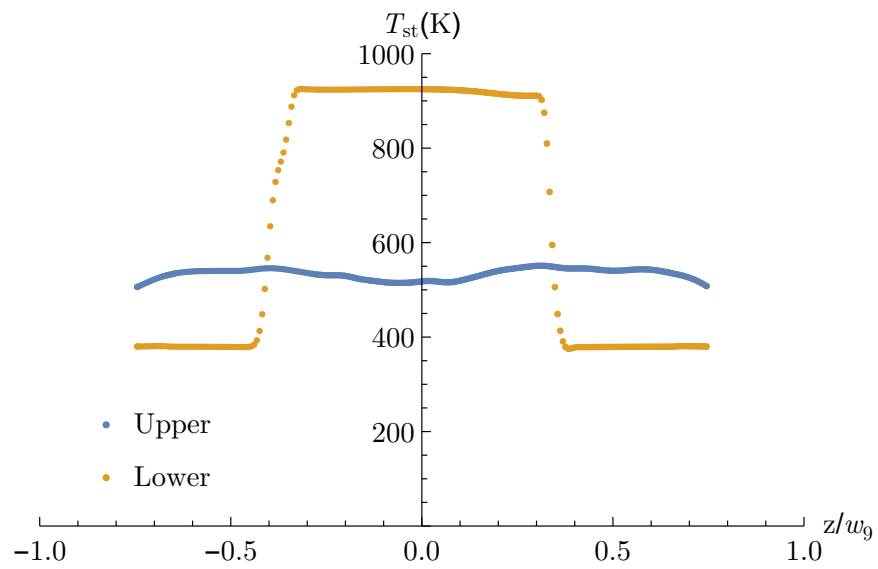
Figure 4.143: Swirl LD4_AR10 Exit Surface Temperature.
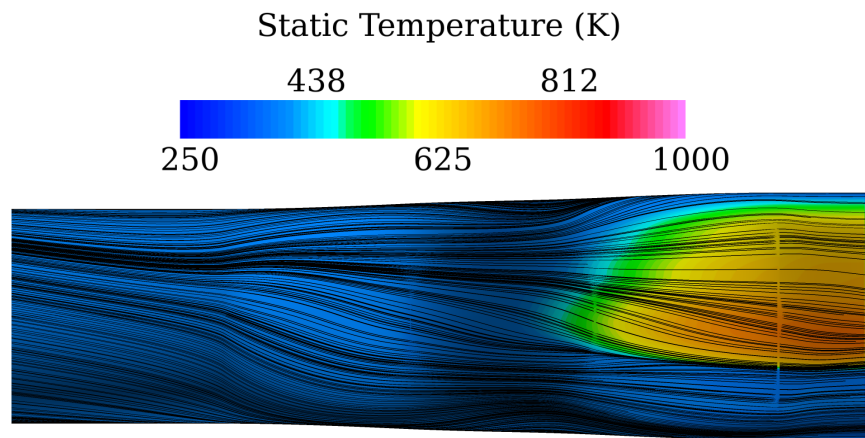
254

Static Temperature (K)
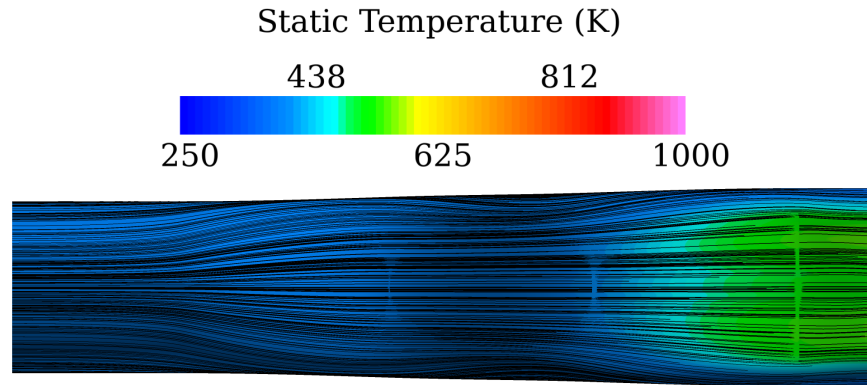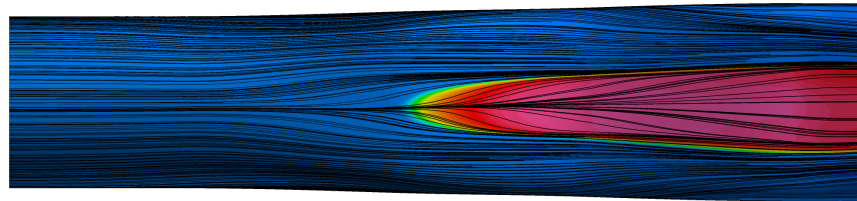
(a) Upper Surface
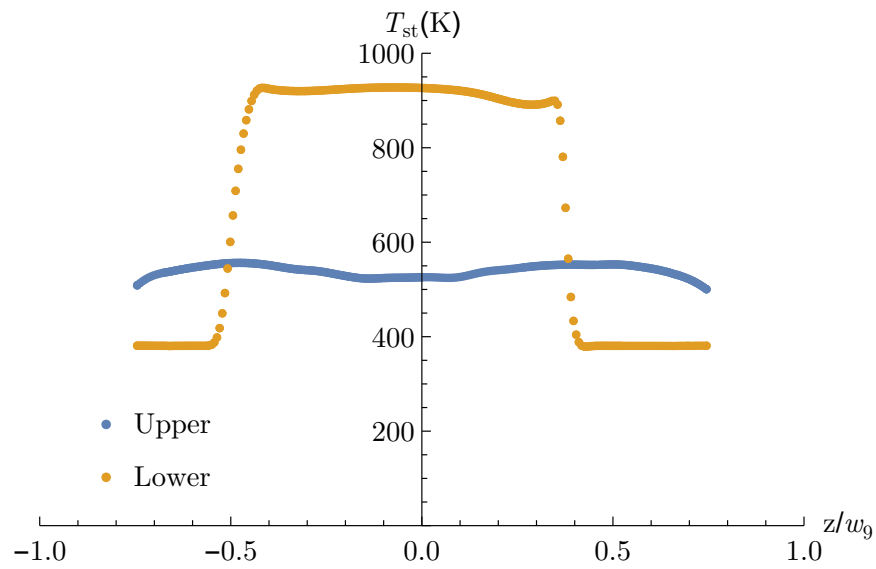
(b) Lower Surface

(c) Hot Streak Plot

Figure 4.144: No-swirl LD4_AR4 Exit Surface Temperature.

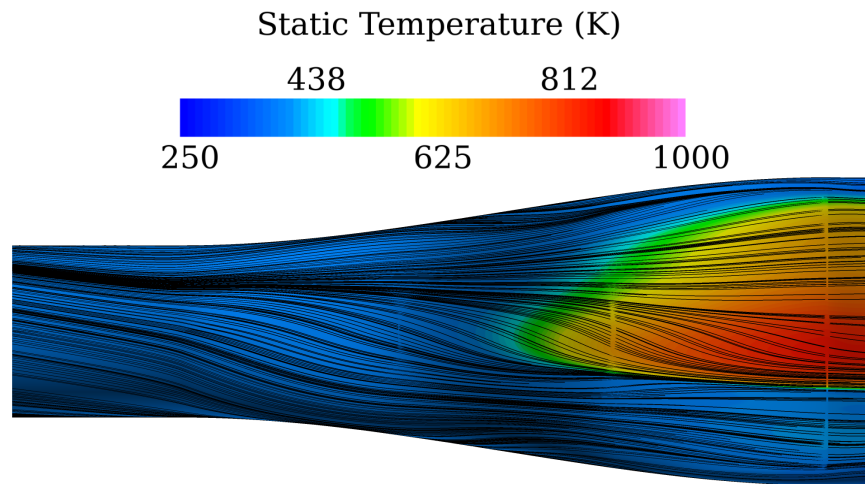# Static Temperature (K)
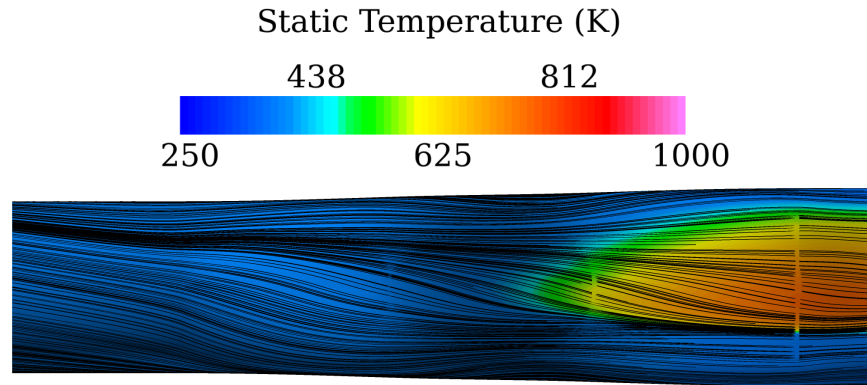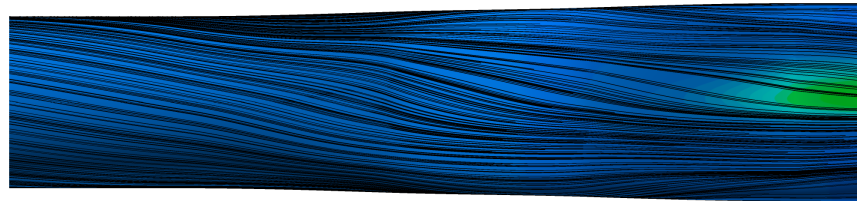
(a) Upper Surface

(b) Lower Surface
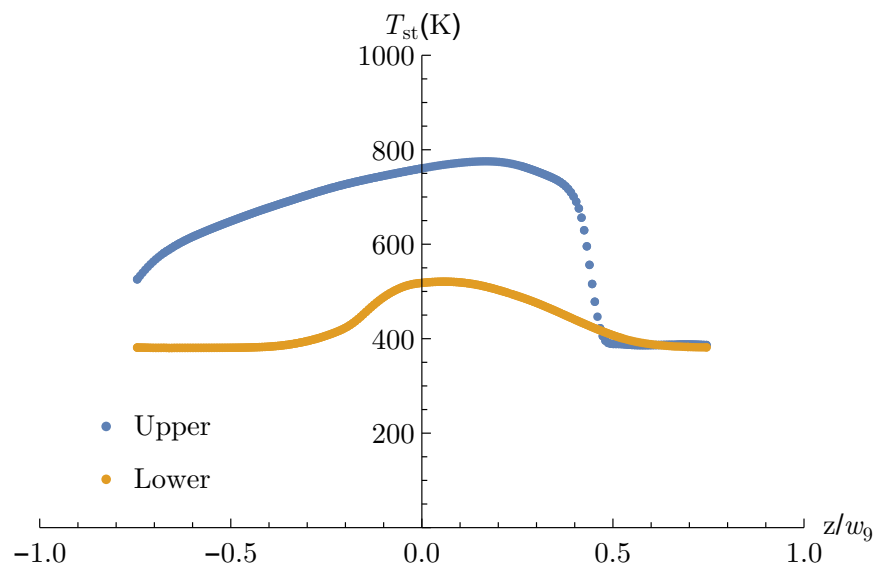
(c) Hot Streak Plot

Figure 4.145: Swirl LD4_AR4 Exit Surface Temperature.
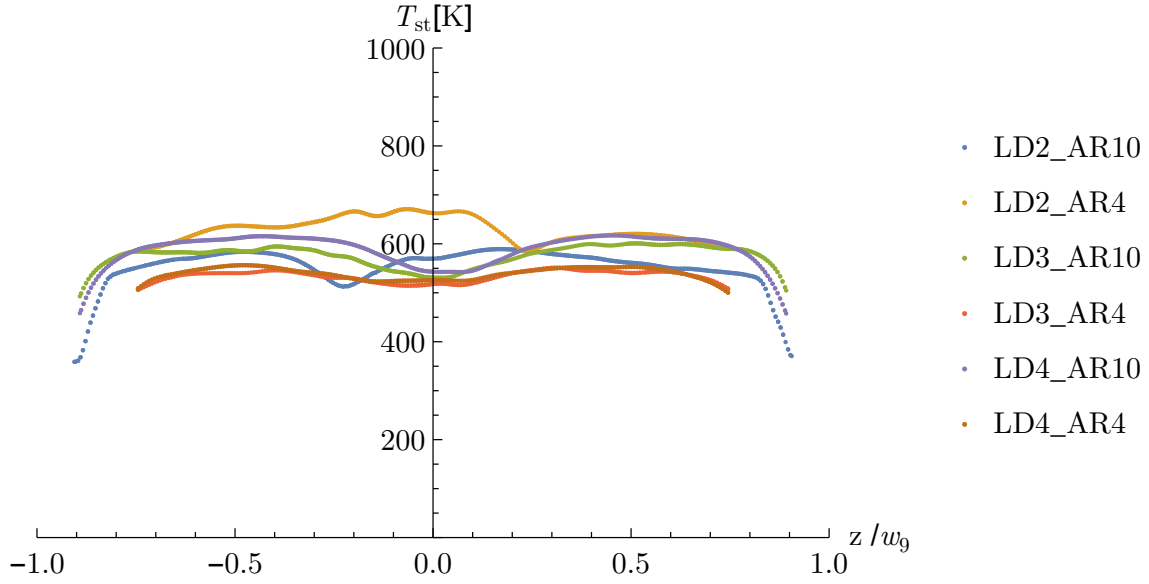
Figure 4.146: Temperature Distribution at Upper Exit Surface, No-swirl Cases.

the surface and encourage mixing near the bottom edge, effectively reducing the surface temperature dramatically. The opposite asymmetry in the two $L/D = 2$ nozzle is again seen at the lower surface. The LD2_AR4 nozzle is the only case to experience flow separation at the lower surface downstream of the second bend, and this phenomenon seems to further buffer the lower surface from hot flow.

Figure 4.148 shows the upper surface temperature distribution for the swirl cases. This figure displays the heating of the starboard side and the sharp barrier at the port side due to the upper swirl vortex. This barrier is more effective at cooling the surface for the nozzles that do not experience upper surface flow separation. For the $L/D = 2$ nozzles, the presence of the upper port-side counter-rotating vortex pair draws core flow from the center up to the surface. For the other nozzles, the presence of the coalesced flow with negative vorticity moves bypass flow toward the nozzle center.

Figure 4.149 shows the lower surface temperature distribution for the swirl cases. All cases display a similar pattern of asymmetric heating in the swirl direction. A decrease in surface temperature is seen with an increase in De_S. The increase in De_S essentially
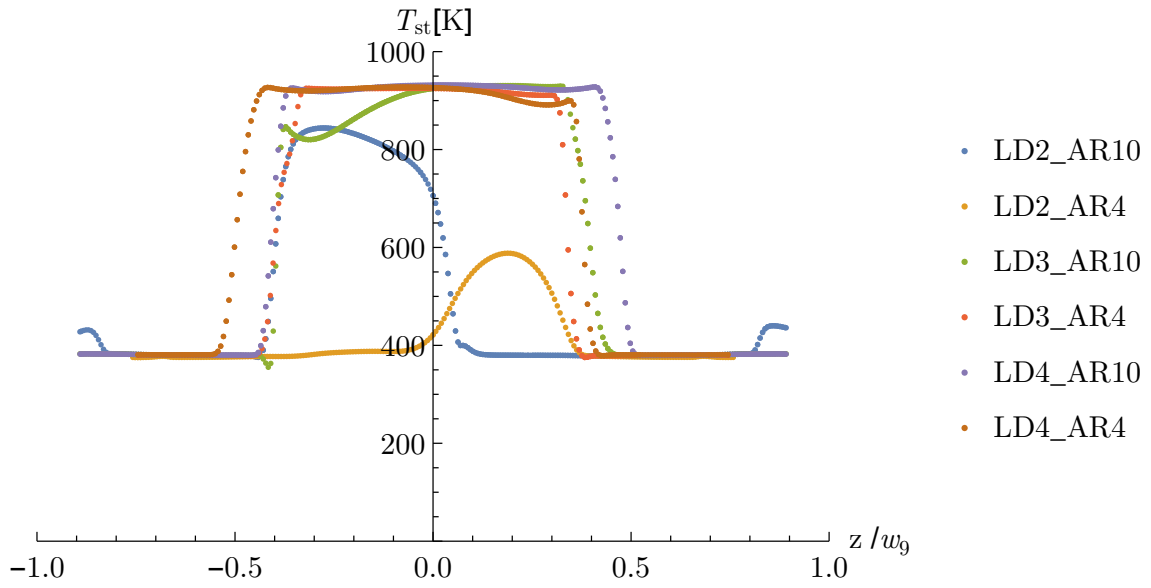
Figure 4.147: Temperature Distribution at Lower Exit Surface, No-swirl Cases.
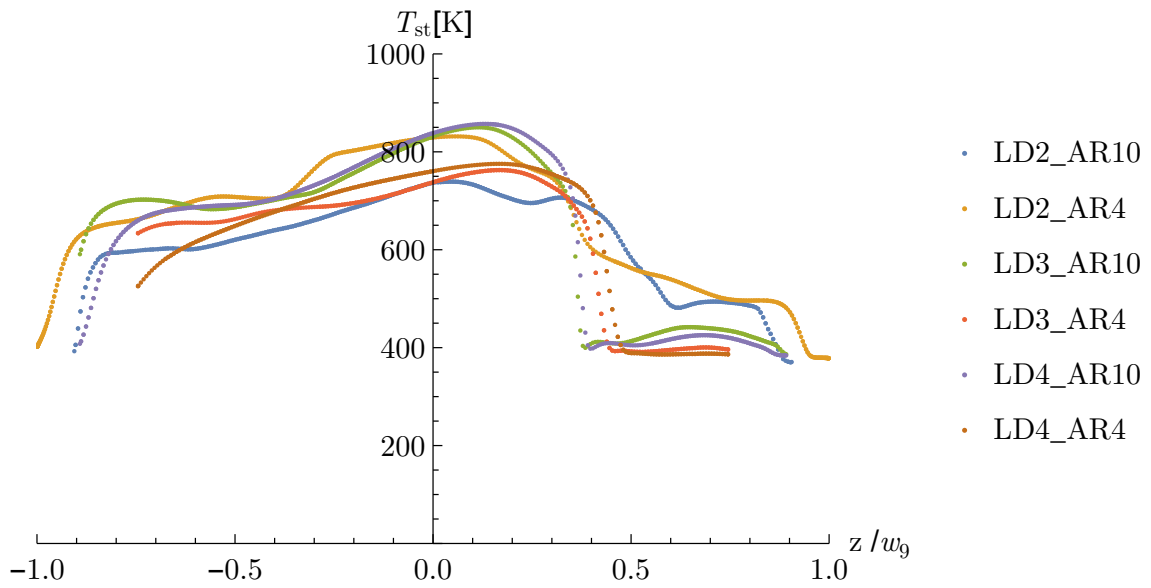
Figure 4.148: Temperature Distribution at Upper Exit Surface, Swirl Cases.

prevents the warmer flow from reaching the surface due to a higher degree of turning. The lower De_s flows tend to have more lateral migration, which spreads the lower bypass flow out at the lower surface, allowing more mixing with warmer core flow.
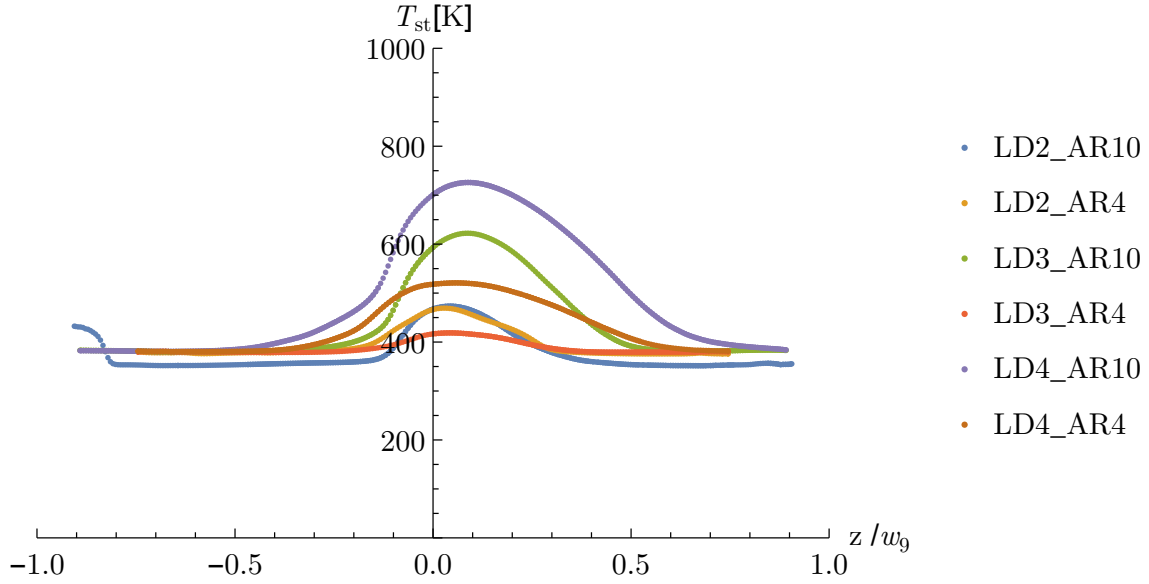
Figure 4.149: Temperature Distribution at Lower Exit Surface, Swirl Cases.

Table 4.7 summarizes the results in Figures 4.146 and 4.147 by giving the average and maximum static temperatures for the upper and lower surface of each nozzle and the maximum static temperature difference between any two nozzles. For the no-swirl cases, changing geometry increases average surface temperature by 11% on the upper surface and 33% on the lower surface. Differences in nozzle geometry increase the maximum surface temperature by 13% on the upper surface and 28% on the lower surface. In order to determine which nozzle maintains the coolest surface (and thus minimizes the effects of hot streaks), the minimum temperature values are highlighted.

Table 4.8 summarizes the results in Figures 4.148 and 4.149 by giving the average and maximum static temperatures for the upper and lower surface of each nozzle and the maximum static temperature difference between any two nozzles. For the swirl cases,

Table 4.7: No-Swirl Surface Temperatures (K)

Nozzle	Lower Avg	Lower Max	Upper Avg	Upper Max
LD2_AR10	496	844	551	589
LD3_AR10	576	931	575	601
LD4_AR10	636	932	586	617
LD2_AR4	**414**	**588**	630	671
LD3_AR4	634	926	**533**	**551**
LD4_AR4	715	928	540	556
Max Difference	32.7%	28.0%	10.8%	12.7%

changing geometry increases average surface temperature by only 3% on the upper surface and 16% on the lower surface. Differences in nozzle geometry increase the maximum surface temperature by 10% on the upper surface and 33% on the lower surface. It should be noted that while the reversal of hot flow from the lower to upper surfaces due to the presence of swirl has been discussed in the above sections, Table 4.8 shows that no upper surface maximum temperature is above the threshold temperature of 880 K. In order to determine which nozzle maintains the coolest surface (and thus minimizes the effects of hot streaks), the minimum temperature values are highlighted.

Table 4.9 gives the effect of swirl on the average and maximum upper and lower surface temperature for each nozzle. As noted in the plot of surface temperature for each nozzle, swirl tends to decrease the lower surface temperature—26% for the average temperature and 36% for the maximum temperature. Swirl increases the average upper surface temperature by 11% and increases the maximum upper surface temperature by 35%. The largest changes due to swirl are highlighted.

Table 4.8: Swirl Surface Temperatures (K)

Nozzle	Lower Avg	Lower Max	Upper Avg	Upper Max
LD2_AR10	**378**	473	620	**739**
LD3_AR10	421	622	640	850
LD4_AR10	487	726	636	857
LD2_AR4	396	469	**614**	832
LD3_AR4	389	**419**	627	763
LD4_AR4	434	521	628	775
Max Difference	16.1%	32.9%	2.8%	9.6%

Table 4.9: Effect of Swirl on Surface Temperatures (%)

Nozzle	Lower Avg	Lower Max	Upper Avg	Upper Max
LD2_AR10	-23.8	-43.9	+12.4	+25.4
LD3_AR10	-26.9	-33.1	+11.3	**+41.4**
LD4_AR10	-23.4	-22.1	+8.5	+38.9
LD2_AR4	-4.3	-20.2	-2.46	+23.9
LD3_AR4	-38.7	**-54.8**	**+17.7**	+38.4
LD4_AR4	**-39.3**	-43.9	+16.4	+39.4

V. Summary and Conclusions

For the foreseeable future, it is expected that embedded engine designs will continue to gain in popularity as a response to the increasingly stringent cost, weight, and performance requirements facing modern and future USAF weapons systems. These exhaust systems incorporate an aft deck into the airframe downstream of the nozzle to provide denial of line-of-sight into the hot section of the engine. Recent issues with material degradation and failure along the aft deck of some USAF weapon systems are caused by hot streaks—portions of the hot core flow which impinge upon the aft deck surface. The desire to reduce material failure due to hot streaks by maximizing the effectiveness of current cooling schemes has lead to the need for a detailed investigation of hot streak phenomena. This research attempts to fulfill that need by accomplishing a computational study involving serpentine exhaust nozzles of various representative geometries. The goal of this research is to observe and characterize the underlying flow physics of hot streak phenomena by determining how and why the temperature distribution within a serpentine nozzle changes when the nozzle geometry is altered. This research goal was accomplished by fulfilling the following research objectives:

1. Perform CFD validation of existing computational methods proposed for the research.

2. Establish a design methodology to create serpentine exhaust nozzle geometries which vary L/D (2, 3, and 4) and AR (4 and 10).

3. Achieve a grid-independent solution on a serpentine exhaust nozzle by means of a grid convergence study.

4. Investigate the application of a second-order closure turbulence model to the increase fidelity of the CFD simulations.

5. Perform CFD simulations on each nozzle designed in Research Objective 2 for two swirl conditions (0°and 10°). Describe the changes in flow physics for each solution.

6. Develop a set of parameters to characterize hot streak phenomena and relate the changes in temperature distribution and hot streak formation with changes in nozzle geometry.

5.1 Summary of Results

5.1.1 Research Objective 1: Validation Study.

The commercial CFD code Fluent was chosen to accomplish the research objectives due to its extensive application to aero-propulsion flows, including serpentine ducts, and its inclusion of an RSM turbulence model (Research Objective 4). Since an extensive search of the available literature failed to yield any useful data pertaining to serpentine exhaust nozzles, a problem involving serpentine inlets was chosen to validate the computational methods used in this research. The validation study was based on the first AIAA PAW and used the same geometry, experimental data, and computational methods as ANSYS participants, with improved fluid properties. Two simulations were performed corresponding to the two experimental conditions presented at the workshop. Table 5.1 gives the maximum error compared to experimental data.

Table 5.1: Validation Study Results

Parameter	Test Case 1	Test Case 2
Mach	1.53%	1.43%
Boundary Layer Height	< 1%	< 1%
Streamwise P_i/P_{i_0}	5.76%	1.58%
Circumferential P_i/P_{i_0}	2.22%	1.16%
Pressure Recovery	0.05%	0.13%

The CFD simulations matched experimental data well, with the largest errors in the regions of flow separation—a continuing area of improvement for steady CFD simulations. The inclusion of variable air properties resulted in errors smaller than the ANSYS participants for Test Case 1, whose results were noted by workshop organizers as matching the experimental data very well. Errors for Test Case 2 were similar to PAW participants, whose results were also noted as matching experimental data well. Therefore, the computational methods were validated for the serpentine duct problem.

5.1.2   Research Objective 2: Design Methodology.

After several iterations, a methodology was established to design the set of serpentine exhaust nozzles used in this research. Initial flow conditions and isentropic relations were used to determine exit and throat areas and the divergent section length. An exit shape in the form of a rectangle capped by semi-circles was defined in terms of *AR*. Inflection points were established at thirds of the nozzle length between the mixing plane and throat to provide denial of line-of-sight into the engine core. Bézier curves were used to create a smooth nozzle geometry.

The design methodology is based on sound nozzle design principles used for conventional exhaust nozzles. The methodology is scalable and applicable to nozzles in a wide range of lengths, aspect ratios, inflection point locations, and exit shapes. However, there are limits to the methodology for certain L/D and *AR* combinations in terms of preventing flow separation and nozzle choking upstream of the throat (namely, $L/D = 2$ and $AR = 4, 10$). The limitations can be mitigated by loosening restrictions on the inflections points, either by placing them at unequal lengths along the centerline or relaxing the 0.5/0.5 offset requirement used in this research.

5.1.3   Research Objective 3: Grid Independence.

Three grids were generated for the LD2_AR10 nozzle to determine a grid-independent average axial and circumferential surface grid spacing. The GCI method of Roache was

264

used to determine the error and uncertainty of the grid-independent solution. Three figures of merit were used: hot flow size, $TAVHOT$, and $TFAV$. Thresholds of 2.5% and 5% were established for error and uncertainty to determine when grid independence was achieved. The fine grid with 0.2 inch (0.0052 m) average surface spacing met the error and uncertainty thresholds for all figures of merit with hot flow size as the limiting factor. The fine grid solution exhibited second-order convergence in p and via a linearity test that yielded high goodness-of-fit values.

5.1.4   Research Objective 4: Second-Order Closure Turbulence Model.

The RSM second-order closure turbulence model was applied to the LD3_AR4 and LD3_AR10 nozzles. In both cases, a stable solution was obtainable only by limiting the turbulent transport equations to first-order accuracy. Both solutions exhibited the same general trends compared to the respective K-ω SST solutions. There was little difference in surface centerline non-dimensional total pressure, Mach contours, and nozzle surface flows; however, there was a distinct difference in the separated tailcone surface flows, with the RSM solutions exhibiting stronger vortex foci. Differences in the streamwise vorticity distribution were observed for both cases, with the RSM solutions containing higher levels of vorticity and tighter vortical structures. Changes in the total temperature distribution resulted from the different vorticity fields. The RSM solutions were more symmetric and encouraged more mixing of the two streams due to an increase in entrainment of bypass into the core by the central counter-rotating vortices. The increase in mixing resulted in a higher temperature at the upper surfaces for both nozzles.

While the RSM solutions demonstrated the increased ability to capture swirling flow physics, first-order accurate turbulent quantities are unacceptable for academic research or practical applications. Therefore, an investigation involving other CFD codes with RSM capability is necessary to determine the differences between first- and second-order closure turbulence models when applied to serpentine exhaust nozzles in terms of numerical

accuracy and increased computational expense. This investigation could also include codes that contain a two-equation Algebraic Reynolds Stress Model (ARSM), which represents a bridge between conventional two-equation models and RSM.

5.1.5   *Research Objective 5: Nozzle Simulations* .

Five additional models were designed using the methods in Research Objective 2. Two swirl conditions were simulated for each nozzle. The no-swirl solutions shared the following general flow development features:

- Core flow separated off the tailcone and propagated downstream in the form of two counter-rotating vortices.

- From the mixing plane to the first inflection point, flow at the upper portion of the nozzle was forced down and around the sides due to the upper streamline curvature change and resulting centrifugal forces.

- From the first to second inflection points, flow at the lower portion of the nozzle was forced up and around the sides due to the streamline curvature change and resulting centrifugal forces. The upward-migrating flow met the lower-migrating flow near the second inflection point. This coalescence of streamlines induced vortex formation at the sidewalls.

- From the second inflection point to the throat, the sidewall vortices assisted in pulling hot core flow to the sidewalls as the nozzle experienced lateral divergence.

- From the throat to the exit, nozzle expansion resulted in a decrease in streamwise vorticity strength.

- Throughout the center of the nozzle, the counter-rotating vortex pair from the tailcone separation persisted and entrained cooler bypass flow to the center.

- The strength of streamwise vorticity decreased with an increase in nozzle length.

266

The swirl solutions accomplished for this research objective shared the following flow development features unique from the no-swirl solutions:

- A single, strong, separation-induced vortex propagated downstream of the tailcone.

- The vorticity and temperature distributions were more asymmetric throughout the nozzle due to the swirl direction assisting in lateral divergence on the port side and competing against lateral divergence on the starboard side.

- From the first to second inflection points, the combination of streamline curvature change and swirl caused coalescence of flow at the upper port-side portion of the nozzle, generating additional streamwise vorticity in this region. This vortex drew cooler bypass flow toward the nozzle core.

The $L/D = 2$ nozzle solutions produced distinct differences from the longer nozzles:

- Flow separation occurred at the upper surface for both nozzles upstream of the second inflection point. The flow reattached between the second inflection point and the throat. The separation induced a pair of counter-rotating vortices at each sidewall.

- Flow separation occurred at the lower surface for LD2_AR4 nozzle at the second inflection point.

- Additional separation occurred for the LD2_AR4 nozzle at the upper surface in the divergent section.

- The LD2_AR4 nozzle was choked far upstream of the throat as the flow passed around the lower bend of the second inflection point.

5.1.6 Research Objective 6: Hot Streak Characterization.

The solutions were compared by introducing a new non-dimensional parameter: a modified Dean number, which accounts for flow conditions via Reynolds number and

nozzle geometry via serpentinity. The nozzles were analyzed using the characterization parameters size, magnitude, and location. These parameters represent how the total temperature distribution at the exit plane varies with changes in nozzle geometry. Size was found to vary in an approximately quadratic manner with Dean number, with the maximum size in the mid-Dean number ranges equating to lower levels of mixing, although the quadratic curve fit was poor. Size differed between nozzles by up to 11% for the no-swirl cases and 8% for the swirl cases. Swirl increased size by an average of 3%. Magnitude also varied in an approximately quadratic manner with modified Dean number and exhibited a general upward trend, with higher Dean number equating to higher magnitude, or less mixing. Magnitude differed between nozzles by up to 19% for the no-swirl cases and 14% for the swirl cases. Swirl increased magnitude by an average of 4%. Hot flow centroid location showed various trends. For the no-swirl cases, high modified Dean number kept the centroid nearer the lateral centerline, and the vertical centroid decreased with length. For the swirl cases, two groups emerged based on modified Dean number. The three lowest Dean number nozzlse had positive lateral centroid, while the three highest Dean number nozzles had a negative lateral centroid. The vertical centroid trended positively with Dean number.

Temperature distortion was characterized in the circumferential and radial directions by probing 40 locations which form 5 rings around the exit plane. Distortion is another indicator of changes in the exit total temperature distribution for the various nozzle geometries. Circumferential distortion increased with ring distance from the center for the no-swirl cases. For the swirl cases, circumferential distortion increased until the outermost ring, which had a slightly lower value than Ring 4. Circumferential distortion coefficient differed between nozzles by up to 15% for the no-swirl cases and 19% for the swirl cases. Swirl increased circumferential distortion coefficient by an average of 19%. Radial distortion decreased from positive to negative with distance from the center for both no-

swirl and swirl cases. Rings 3 and 4 experienced the greatest differences between nozzles: up to 69% for Ring 3 of the no-swirl cases and 84% for Ring 4 of the swirl cases. The maximum change due to swirl occurred at Ring 4, where swirl increased radial distortion by 25%.

Discharge and thrust performance were examined for each nozzle to determine the practical effects of altering nozzle geometry. Discharge coefficient decreased with modified Dean number, increased with L/D, increased with AR, and decreased with swirl. Excluding the choked LD2_AR4 nozzle, the differences in discharge performance between the nozzles was an average of 0.05%, meaning changes in nozzle geometry had little effect on C_d. The same trends were apparent for thrust performance as well.

An alternate characterization of the flow changes due to nozzle geometry was accomplished by comparing each nozzle solution to a corresponding straight nozzle case of the same L/D. These comparisons revealed further information regarding the relationship between nozzle geometry and dwell time. Size, magnitude, C_d, C_{F_g}, and F_g were reexamined by normalizing the previous serpentine nozzle solutions by the corresponding straight nozzle solution, the ratio of which representing the relative effect of the serpentine geometry on the straight nozzle solution. The nozzles were grouped by aspect ratio and plotted against L/D. In terms of normalized hot flow size, shorter nozzles were more affected by the serpentine geometry, with swirl reducing the effect of geometry changes. Normalized magnitude peaked at $L/D = 3$, except for the LD2_AR4 nozzle, and again swirl reduced the impact of serpentine nozzle geometry. All normalized performance parameters exhibited the same trend: increasing length decreased the effect of serpentine geometry. Swirl slightly reduced the geometry effect for C_d, but slightly increased the effect for thrust performance.

Examination of total temperature on the upper and lower surfaces revealed critical information about how hot streak phenomena is affected by changes in nozzle geometry.

269

Flow asymmetry in the no-swirl cases was displayed most prominently for the $L/D = 2$ nozzles. The upper surfaces of the no-swirl cases remained below the hot flow threshold temperature, although some streaking behavior in the cooler flow was evident. Except for LD2_AR4 case, the lower surfaces of the no-swirl cases contained large hot streaks at or near the centerline, with increases in L/D causing larger hot streaks along nearly half the nozzle length. The swirl cases presented a completely different hot streak behavior. In these solutions, the upper surface experienced the hot streak with a distinct barrier between the hot and cold flow on the port side. The lower surface experienced some asymmetric heating, which increased with modified Dean number.

5.2 Conclusions and Recommendations

Changes in serpentine nozzle geometry produce distinct differences in flow physics. The change in flow physics is especially true in terms of flow separation, where there exists some L/D between 2 and 3 where the reduction in upper surface curvature would keep the flow attached. The separation-induced vortices from the tailcone have a large impact on the temperature distribution at the exit, as do the sidewall vortices. Therefore, a connection can be made between the vorticity field and the exit total temperature distribution. Examination of centerline surface non-dimensional static pressure and Mach contours shows the design methodology produces close to ideally expanded flow that reaches supersonic flow near the designed throat, except for the LD2_AR4 case. Thus, the parameters for the LD2_AR4 nozzle represent a design limitation to the methodology. The introduction of swirl into the nozzle produces distinct differences from the no-swirl cases primarily due to the interaction between the swirl direction and the direction of lateral divergence.

Characterization of hot streak phenomena by hot flow size, magnitude, location, distortion, and performance provides valuable insight into the relationship between changes in nozzle geometry and flow physics. The alternate characterization using values normalized by straight nozzle solutions provides further insight by revealing a trend related

270

to the relative change of the characterization parameters. Namely, shorter nozzles are more affected by changes in nozzle geometry than longer nozzles. Hot streaks are more prominent on the lower surface of longer nozzles for no-swirl cases. For the swirl cases, hot streaks appear on the port-side upper surface next to the vortex barrier. The hot flow on the upper surface of the swirl cases was below the threshold temperature used in this research, effectively preventing "hot" flow from impacting the nozzle surface. Thus, a distinct connection is observed between the vorticity generated within the nozzle and the temperature distribution on the nozzle surface.

Based on these conclusions the following general design guidelines are recommended:

1. If flow separation is to be avoided, a nozzle with $L/D > 3$ should be considered.

2. If a shorter nozzle is necessary, an investigation of nozzle designs with L/D between 2 and 3 is needed to determine the L/D limit for separation (e.g. $L/D = 2.75$).

3. Designs similar to the LD2_AR4 nozzle should be avoided. If an L/D near 2 is necessary with $AR < 10$, several design iterations could be necessary to prevent the nozzle from choking upstream of the throat.

4. If the nozzle is expected to experience swirl above 10°, a down-first flowpath could reduce the effects of hot streaks on the lower surface.

5. If swirl is expected to be below 10°, an up-first flowpath would likely produce hot streaks on the upper surface, again reducing the amount of hot flow impinging upon the lower surface and aft deck.

The final conclusion to be made concerns determining which of the nozzles used for this research represents a design that minimizes hot streaks while maximizing performance, i.e., which nozzle represents the "best" design in terms of fulfilling the purpose of a serpentine exhaust nozzle. Tables 4.7 and 4.8 gave average and maximum surface

271

temperatures for the upper and lower surfaces of all nozzles. The minimum values were highlighted and revealed three nozzles which exhibited the "best" behavior across the eight categories: LD2_AR10, LD2_AR4, and LD3_AR4. The design limitations and their effects on nozzle performance for the LD2_AR4 nozzle were discussed above and in Chapter 4, therefore this nozzle will not be considered a "best" design even though it exhibited the minimum lower surface temperature for the no-swirl solutions. The surface temperature and performance results for the LD2_AR10 and LD3_AR4 nozzles are summarized in Table 5.2. The "best" value (lowest temperature or highest coefficient) is highlighted and the difference between the two results is given.

Table 5.2: "Best" Nozzles for Hot Streak Mitigation and Performance

	LD2_AR10	LD3_AR4	% Diff
No-Swirl Lower T Avg	**496 K**	634 K	24.4
No-Swirl Lower T Max	**844 K**	925 K	9.2
No-Swirl Upper T Avg	551 K	**533 K**	3.3
No-Swirl Upper T Max	589 K	**551 K**	6.7
Swirl Lower T Avg	**378 K**	389 K	2.8
Swirl Lower T Max	473 K	**419 K**	12.3
Swirl Upper T Avg	**620 K**	627 K	1.3
Swirl Upper T Max	**739 K**	763 K	3.1
No-Swirl C_d	**0.959**	0.949	1.0
Swirl C_d	**0.957**	0.946	1.2
No-Swirl C_{F_g}	0.973	**0.978**	0.5
Swirl C_{F_g}	0.973	**0.976**	0.3

Based on the information in Table 5.2, the LD2_AR10 nozzle offers a better balance between hot streak mitigation and performance than the LD3_AR4 nozzle. The LD2_AR10 nozzle exhibits the lowest temperature in five of the eight categories and provides slightly better discharge performance, while only reducing thrust performance by less than 1%.

5.3   Future Work

The results and conclusions stated above accomplish the goal of this research. The work described in this document is among the first academic forays into the field of serpentine exhaust nozzle aerodynamics. While satisfactorily addressing the present research objectives, this research effort has also uncovered many questions and new lines of investigation to pursue. An experiment using the nozzles designed in this research would provide a valuable source of validation data. Nozzles designed by slightly altering or relaxing some of the design restraints would provide further confirmation of the scalability of the design methodology, especially in regards to the LD2_AR4 nozzle. A different grid topology (i.e., triangular surface meshes) could be tested to determine any differences from the hybrid grid topology used in this research. Further turbulence model investigations could include unsteady simulations using Detached Eddy Simulation (DES) and Large Eddy Simulation (LES) to ascertain the unsteady effects in serpentine exhaust nozzle flow. The effects of a variable turbulent Prandtl number could be considered to determine the impact of improving the traditional assumption of a constant value. Future nozzle designs might include an aft deck in the geometry to determine if the streaking behavior on the lower surface would extend to an external aft deck, and if so, how the hot streaks change downstream of the nozzle exit. This design could be further investigated for cases with swirl by flipping the nozzle about the axial direction to produce an "up-first" design, where the hot streaks would appear on the lower surface and aft deck. More flow physics could be incorporated into future simulations, to include modeling the core flow as a mixture of combustion products, introducing external freestream velocity to determine the interaction

273

with the nozzle exhaust, and computing the heat transfer at the nozzle surface and aft deck to determine the effect on hot streak temperature. Serpentine exhaust nozzle research is a new and interesting field of study that has potential for large returns on investment in improving the mission capability of future USAF weapons systems.

Bibliography

[1] *A Current Assessment of the Inlet/Engine Temperature Distortion Problem.* SAE ARD 50015, January 1991.

[2] "B-2 Bomber Tailpipe Cracks Compel New Spare Parts Production", June 2012. http://www.nti.org/gsn/article/b-2-bomber-tailpipe-cracks-compel-new-spare-parts-production/.

[3] Abbott, J. M., B. H. Anderson, and E. J. Rice. "INLETS, DUCTS, AND NOZZLES". *Aeropropulsion*, 157–174, 1987.

[4] Anderson, J. D. *Modern Compressible Flow with Historical Perspective*. McGraw Hill, 1990.

[5] ANSYS, Inc. *ANSYS FLUENT 14.5 Theory Guide*. Canonsburg, PA, 2012.

[6] Baker, R., 2013. NASA Glenn Research Center.

[7] Bansod, P. and P. Bradshaw. "The Flow in S-shaped Ducts". *Aeronautical Quarterly*, 23(2):131–140, 1972.

[8] Blazek, J. *Computational Fluid Dynamics: Principles and Applications*. Elsevier, 2005.

[9] Bradshaw, P., T. Cebeci, and J. H. Whitelaw. *Engineering Calculation Methods for Turbulent Flow*. Academic Press, 1981.

[10] Brear, M. J., Z. W., J. F. Mangus, S. Braddom, J. D. Paduano, and J. S. Philhower. "Flow Separation Within the Engine Inlet of an Uninhabited Combat Air Vehicle (UCAV)". *Journal Of Fluids Engineering*, 126(2):266–272, 2004.

[11] Brear, Michael J., Howard P. Hodson, Paloma Gonzalez, and Neil W. Harvey. "Pressure Surface Separations in Low-Pressure Turbine—Part 2: Interactions with the Secondary Flow". *Journal of Turbomachinery*, 123(3):402–409, 2002.

[12] Burley, J. R. and J. R. Carlson. *Circular-to-Rectangular Transition Ducts for High-Aspect Ratio Nonaxisymmetric Nozzles*. AIAA paper 85–1346, July 1985.

[13] Cavicchi, R. H. *Application of the RNS3D Code to a Circular-Rectangular Transition Duct With and Without Inlet Swirl and Comparison With Experiments*. NASA TM 209394, October 1999.

[14] Celik, I. B., U. Ghia, P. J. Roache, C. J. Freitas, H. Coleman, and P. E. Raad. "Procedure for Estimation and Reporting of Uncertainty Due to Discretization in CFD Applications". *Journal of Fluids Engineering*, 130(7), 2008.

[15] Chawner, J. "Quality and Control—Two Reasons Why Structured Grids Aren't Going Away", March 2013. http://www.pointwise.com/theconnector/March-2013/Structured-Grids-in-Pointwise.shtml.

[16] Constantinescu, G. and K. Squires. "Numerical investigations of flow over a sphere in the subcritical and supercritical regimes". *Physics of Fluids*, 16(5):1449–1466, 2004.

[17] Constantinescu, G. S., H. Pasinato, Y.-Q. Wang, and K. D. Squires. *Numerical Investigation of Flow Past a Prolate Spheroid*. AIAA paper 2002–0588, January 2002.

[18] Davis, D. O. and F. B. Gessner. "Experimental Investigation of Turbulent Flow Through a Circular-to-Rectangular Transition Duct". *AIAA Journal*, 30(2):367–375, 1992.

[19] Deaton, J. D. and R. V. Grandhi. *Thermal-Structural Analysis of Engine Exhaust-Washed Structures*. AIAA paper 2010–9236, September 2010.

[20] Delot, A. and R. K. Scharnhorst. *A Comparison of Several CFD Codes with Experimental Data in a Diffusing S-Duct*. AIAA paper 2013–3796, July 2013.

[21] Domel, N. D. and D. Baruzzini. *Inlet CFD Results: Comparison of Solver, Turbulence Model, Grid Density and Topology*. AIAA paper 2013–3793, July 2013.

[22] Dorgan, A. J. and C. M. Winkler. *BCFD Analysis for the 1st AIAA Propulsion Workshop: S-Duct Results*. AIAA paper 2013–3792, July 2013.

[23] Gea, L. M. and S. Nyugen. *CFD Simulation of S-Duct Test Case Using Overset Grids*. AIAA paper 2013–3795, July 2013.

[24] Gerolymos, G.A., S. Joly, M. Mallet, and I. Vallet. "Reynolds-Stress Model Flow Prediction in Aircraft-Engine Intake Double-S-Shaped Duct". *Journal of Aircraft*, 47(4):1368–1381, July 2010.

[25] Gonzalez, O. and J. H. Maddocks. "Global curvature, thickness, and the ideal shapes of knots". *Preceedings of the National Academy of Sciences*, 96:4769–4773, April 1999.

[26] Gopaliya, M. Kumar, M. Kumar, S. Kumar, and S. M. Gopaliya. "Analysis of performance characteristics of S-shaped diffuser with offset". *Aerospace Science and Technology*, 11:130–135, November 2007.

[27] Hamstra, J. W., D. N. Miller, and P. P. Truax. *ACTIVE INLET FLOW CONTROL TECHNOLOGY DEMONSTRATION*. ICAS–2000–6112, August 2000.

[28] Haney, M. A. *Topology Optimization of Engine Exhaust-Washed Structures*. Ph.D. thesis, Wright State University, November 2006.

276

[29] Harloff, G. J., C. F. Smith, J. E. Burns, and J. R. DeBonis. "Navier-Stokes Analysis of Three-Dimensional S-Ducts". *Journal of Aircraft*, 30(4):526–533, August 1993.

[30] Hill, P. and C. Peterson. *Mechanics and Thermodynamics of Propulsion*. Addison-Wesley, 1992.

[31] Karvinen, A. and H. Ahlstedt. "Comparison of turbulence models in case of three-dimensional diffuser", 2008. Tampere University of Technology, Tampere.

[32] Keating, M. "Accelerating CFD Solutions". *ANSYS Advantage*, V(1):48–49, 2011.

[33] Kirk, A. M., J. I. Gargoloff, O. K. Rediniotis, and P. G. A. Cizmas. "Numerical and experimental investigation of a serpentine inlet duct". *International Journal of Computational Fluid Dynamics*, 23(3):245–258, 2009.

[34] Kumar, S., B. Sasanapuri, K. Kurbatskii, and A. Lestari. *Pressure-based Coupled Simulation of Pressure Recovery and Distortion in an S-shaped Intake Diffuser*. AIAA paper 2013–3794, July 2013.

[35] Kurbatskii, K. A. and A. Lestari. *Pressure-based Coupled Numberical Approach to the Problem of Compressible Flow through Convergent Conical Nozzles*. AIAA paper 2013–2543, June 2013.

[36] Kutner, M. H., C. J. Nachtsheim, J. Neter, and W. Li. *Applied Linear Statistical Models*. McGraw-Hill/Irwin, 2005.

[37] Malecki, R. E. and W. K. Lord. *Parabolized Navier-Stokes Analysis of Circular-to-Rectangular Transistion Duct Flows*. SAE paper 881480, October 1988.

[38] Mattingly, J. D. *Elements of Gas Turbine Propulsion*. AIAA, 2005.

[39] Mayer, E. *Effect of Transition in Cross-Sectional Shape on the Development of the Velocity and Pressure Distribution of the Turbulent Flow in Pipes*. NACA TM 903, August 1939.

[40] McMurty, P. A. "University of Utah Lectures on Vorticity Dynamics", 2014.

[41] Miau, J. J., E. C. Lin, Q. S. Chen, J. H. Chou, D. Pan, and C. K. Lin. "Swirling Flows in Circular-to-Rectangular Transition Ducts". *Experiments in Fluids*, 20(6):401–409, 1996.

[42] Patrick, W. P. and D. C. McCormick. *Circular-to-Rectangular Duct Flows: A Benchmark Experimental Study*. SAE paper 89–1776, October 1987.

[43] Pointwise, Inc. *Pointwise User Manual*. Fort Worth, TX, 2014.

[44] Prandtl, L. *Essentials of Fluid Dynamics*. Hafner, 1952.

[45] Rabe, A. C. *Effectiveness of a Serpentine Inlet Duct Flow Control Scheme at Design and Off-Design Simulated Flight Conditions*. Ph.D. thesis, Virginia Polytechnic Institute and State University, August 2003.

[46] Reichert, B. A. and W. R. Hingst. *An Experimental Comparison of Nonswirling and Swirling Flow in a Circular-to-Rectangular Transition Duct*. AIAA paper 91–0342, January 1991.

[47] Reynolds, T. *Flow Control Application in a Submerged Inlet Characterized by Three-Component LDV*. Ph.D. thesis, Air Force Institute of Technology, December 2010.

[48] Roache, P. J. "Quantification of uncertainty in computational fluid dynamics". *Annual Review of Fluid Mechanics*, 29(1):123–160, 1997.

[49] Sasanapuri, B., M. Kumar, S. Wirogo, and K. A. Kurbatskii. *Numerical Simulation of a Supersonic Cruise Nozzle*. AIAA paper 2013–0492, January 2013.

[50] Sobota, T. H. and F. E. Marble. "Swirling Flows in an Annular-to-Rectangular Transition Section". *Journal of Propulsion and Power*, 5(3):334–340, 1989.

[51] Sotiropoulos, F. and V. C. Patel. "Prediction of Turbulent Flow Through a Transition Duct Using a Second-Moment Closure". *AIAA Journal*, 32(11):2194–2204, 1994.

[52] Sullivan, K. M. *Numerical Investigation of S-Duct Geometric Effects on Inlet Performance Using Sequential Design of Experiments*. Master's thesis, Air Force Institute of Technology, March 2009.

[53] Taneda, S. "Visual observations of the flow past a sphere at Reynolds numbers between 10^4 and 10^6". *Journal of Fluid Mechanics*, 85(1):187–192, 1978.

[54] Tannehill, J. C., D. A. Anderson, and R. H. Pletcher. *Computational Fluid Mechanics and Heat Transfer*. Taylor & Francis, 1997.

[55] Taskinoglu, E. S. and D. D. Knight. "Multi-Objective Shape Optimization Study for a Subsonic Submerged Inlet". *Journal of Propulsion and Power*, 20(4):620–633, August 2004.

[56] Tormalm, M. *Design and Analysis of Compact UAV Ducts*. AIAA paper 2006–2828, June 2006.

[57] Turns, S. R. *An Introduction to Combustion*. McGraw-Hill, 1996.

[58] Vassberg, J. C., M. A. DeHaan, and T. J. Sclafani. *Grid Generation Requirements for Accurate Drag Predictions Based on OVERFLOW Calculations*. AIAA paper 2003–4124, June 2003.

[59] Wellborn, S. R., B. A. Reichert, and T. H. Okiishi. "Study of the Compressible Flow in a Diffusing S-Duct". *Journal of Propulsion and Power*, 10(5):668–675, 1994.

[60] White, F. M. *Viscous Fluid Flow*. McGraw-Hill, 1996.

[61] Wilcox, D. C. *Turbulence Modeling for CFD*. DCW Industries, 2006.

[62] Wilson, D. G. and T. Korakianitis. *The Design of High-Efficiency Turbomachinery and Gas Turbines*. Prentice Hall, 1998.

[63] Wu, C., S. Farokhi, and R. Taghavi. *A Computational Study of Advanced Exhaust System Transition Ducts with Experimental Validation*. AIAA paper 1992–3794, July 1992.

[64] Wu, J.-Z., H.-Y. Ma, and M.-D. Zhou. *Vorticity and Vortex Dynamics*. Springer, 2006.

Vita

Darrell S. Crowe grew up in various small Texas towns and graduated from Alice High School in April 1998. He then attended Texas A&M University in College Station, Texas. He earned a Bachelor of Science in Aerospace Engineering in May 2003. He attended Officer Training School and was commissioned in the United States Air Force in September 2003. His first assignment was to Tinker Air Force Base, Oklahoma, where he served as a reliability engineer for the KC-10 tanker and F100 engine. He then entered the Graduate School of Engineering and Management at the Air Force Institute of Technology (AFIT) at Wright-Patterson Air Force Base, Ohio. In March of 2008, he earned a Master of Science in Aeronautical Engineering. His next assignment was to Eglin Air Force Base, Florida, where he served as a computational fluid dynamics engineer at the Air Force SEEK EAGLE Office. In September of 2011, he entered AFIT as a PhD student where he studied Aeronautical Engineering. Upon graduation he will join the Department of Aeronautics and Astronautics faculty at AFIT.

REPORT DOCUMENTATION PAGE

1. REPORT DATE *(DD–MM–YYYY)*	2. REPORT TYPE	3. DATES COVERED *(From — To)*
26–12–2014	Doctoral Dissertation	Oct 2011–Dec 2014

4. TITLE AND SUBTITLE

Hot Streak Characterization in Serpentine Exhaust Nozzles

5a. CONTRACT NUMBER

5b. GRANT NUMBER

5c. PROGRAM ELEMENT NUMBER

6. AUTHOR(S)

Crowe, Darrell S., Major, USAF

5d. PROJECT NUMBER

5e. TASK NUMBER

5f. WORK UNIT NUMBER

7. PERFORMING ORGANIZATION NAME(S) AND ADDRESS(ES)

Air Force Institute of Technology
Graduate School of Engineering and Management (AFIT/EN)
2950 Hobson Way
WPAFB, OH 45433-7765

8. PERFORMING ORGANIZATION REPORT NUMBER

AFIT-ENY-DS-14-D-32

9. SPONSORING / MONITORING AGENCY NAME(S) AND ADDRESS(ES)

Air Force Research Laboratory
Sensors Directorate, Systems Technology Office
2241 Avionics Circle
Area B, Building 254
WPAFB, OH 45433-7765

10. SPONSOR/MONITOR'S ACRONYM(S)

AFRL/RYS

11. SPONSOR/MONITOR'S REPORT NUMBER(S)

12. DISTRIBUTION / AVAILABILITY STATEMENT

DISTRIBUTION STATEMENT A.
APPROVED FOR PUBLIC RELEASE; DISTRIBUTION UNLIMITED.

13. SUPPLEMENTARY NOTES

This work is declared a work of the U.S. Government and is not subject to copyright protection in the United States.

14. ABSTRACT

Modern aircraft of the United States Air Force face increasingly demanding cost, weight, and survivability requirements. Serpentine exhaust nozzles within an embedded engine allow a weapon system to fulfill mission survivability requirements by providing denial of direct line-of-sight into the high-temperature components of the engine. Recently, aircraft have experienced material degradation and failure along the aft deck due to extreme thermal loading. Failure has occurred in specific regions along the aft deck where concentrations of hot gas have come in contact with the surface causing hot streaks. The prevention of these failures will be aided by the accurate prediction of hot streaks. Additionally, hot streak prediction will improve future designs by identifying areas of the nozzle and aft deck surfaces that require thermal management. To this end, the goal of this research is to observe and characterize the underlying flow physics of hot streak phenomena. The goal is accomplished by applying computational fluid dynamics to determine how hot streak phenomena is affected by changes in nozzle geometry. The present research first validates the computational methods using serpentine inlet experimental and computational studies. A design methodology is then established for creating six serpentine exhaust nozzles investigated in this research. A grid independent solution is obtained on a nozzle using several figures of merit and the grid-convergence index method. An investigation into the application of a second-order closure turbulence model is accomplished. Simulations are performed for all serpentine nozzles at two flow conditions. The research introduces a set of characterization and performance parameters based on the temperature distribution and flow conditions at the nozzle throat and exit. Examination of the temperature distribution on the upper and lower nozzle surfaces reveals critical information concerning changes in hot streak phenomena due to changes in nozzle geometry.

15. SUBJECT TERMS

Serpentine Exhaust Nozzle, Computational Fluid Dynamics, Hot Streak

16. SECURITY CLASSIFICATION OF:			17. LIMITATION OF ABSTRACT	18. NUMBER OF PAGES	19a. NAME OF RESPONSIBLE PERSON
a. REPORT	b. ABSTRACT	c. THIS PAGE			Christopher L. Martin, Jr.
U	U	U	UU	310	19b. TELEPHONE NUMBER *(include area code)* (937)255-3636x4403 christopher.martin@afit.edu